Oil & Natural Gas Technology

DOE Award No.: DE-FC26-06NT42242
Reporting Period: October 2004 to June 2008

Final Report

ADVANCED SEISMIC WHILE DRILLING SYSTEM

Submitted by:
Technology International, Inc.
2103 River Falls Drive
Kingwood, Texas 77339-3154
bradtke@technologyinternationalinc.com

Prepared by:
Principal Investigator
Robert P. Radtke

Dr. John E. Fontenot
David A. Glowka
Robert H. Stokes
Jeffery Sutherland

Ron Evans
Dr. Jim Musser
ION Geophysical, Inc.

Prepared for:
United States Department of Energy
National Energy Technology Laboratory

June 2008

Office of Fossil Energy

DISCLAIMER

Preface

The objective of this project was to develop an acoustically augmented drill bit that can be deployed in deep (15,000+ feet [ft]) high temperature and high-pressure (HTHP) wells to perform advanced Drill Bit Seismic While Drilling Services (SWD). A key element that has been needed for decades is a seismic source that can be located at the drill bit to create and transmit a suitable signal to the surface without interrupting the drilling process.

Through scientific research, Technology International, Inc. (TII) has discovered patent pending SeismicPULSER™ technology that meets the needs of the petroleum industry. The technical path is reported herein, beginning with testing in a Seismic Borehole Rock Simulator, a flow loop, and, finally, field boreholes with both wireline and drillstring tools.

Detailed test data and analysis is reported in four Appendices. Appendix A contains test results on conventional high frequency sparker source testing in the TII Seismic Borehole Rock Simulator. Appendix B provides the results of seismic testing of a high-frequency sparker on a wireline in boreholes at the University of Texas Devine Test Site near Devine, Texas. Subsequent to the high-frequency sparker testing at Devine, the low-frequency SeismicPULSER™ methodology was discovered during testing in the TII Borehole Rock Simulator. Appendix C provides the data and analysis from tests performed in the TII laboratory to determine sparker bubble dynamics in a low-pressure flowing fluid. Testing Appendix D is the report of the surface recordings and analysis of the newly discovered low frequency signals generated by the SeismicPULSER™ on a drillstring in a borehole at the Department of Energy Rocky Mountain Oilfield Test Center (DOE RMOTC) field test site near Casper, Wyoming.

Table of Contents

List of Figures

List of Appendices

This page intentionally left blank

EXECUTIVE SUMMARY

A breakthrough has been discovered for controlling seismic sources to generate selectable low frequencies. Conventional seismic sources, including sparkers, rotary mechanical, hydraulic, air guns, and explosives, by their very nature produce high-frequencies. This is counter to the need for long signal transmission through rock. The patent pending SeismicPULSER™ methodology has been developed for controlling otherwise high-frequency seismic sources to generate selectable low-frequency peak spectra applicable to many seismic applications.

Specifically, we have demonstrated the application of a low-frequency sparker source which can be incorporated into a drill bit for Drill Bit Seismic While Drilling (SWD). To create the methodology of a controllable low-frequency sparker seismic source, it was necessary to learn how to maximize sparker efficiencies to couple to, and transmit through, rock with the study of sparker designs and mechanisms for a) coupling the sparker-generated gas bubble expansion and contraction to the rock, b) the effects of fluid properties and dynamics, c) linear and non-linear acoustics, and d) imparted force directionality. After extensive seismic modeling, the design of high-efficiency sparkers, laboratory high frequency sparker testing, and field tests were performed at the University of Texas Devine seismic test site. The conclusion of the field test was that extremely high power levels would be required to have the range required for deep, 15,000+ ft, high-temperature, high-pressure (HTHP) wells. Thereafter, more modeling and laboratory testing led to the discovery of a method to control a sparker that could generate low frequencies required for deep wells. The low frequency sparker was successfully tested at the Department of Energy Rocky Mountain Oilfield Test Center (DOE RMOTC) field test site in Casper, Wyoming.

An 8-in diameter by 26-ft long SeismicPULSER™ drill string tool was designed and manufactured by TII. An APS Turbine Alternator powered the SeismicPULSER™ to produce two Hz frequency peak signals repeated every 20 seconds. Since the ION Geophysical, Inc. (ION) seismic survey surface recording system was designed to detect a minimum downhole signal of three Hz, successful performance was confirmed with a 5.3 Hz recording with the pumps running. The two Hz signal generated by the sparker was modulated with the 3.3 Hz signal produced by the mud pumps to create an intense 5.3 Hz peak frequency signal.

The low frequency sparker source is ultimately capable of generating selectable peak frequencies of 1 to 40 Hz with high-frequency spectra content to 10 kHz. The lower frequencies and, perhaps, low-frequency sweeps, are needed to achieve sufficient range and resolution for realtime imaging in deep (15,000 ft+), high-temperature (150°C) wells for a) geosteering, b) accurate seismic hole depth, c) accurate pore pressure determinations ahead of the bit, d) near wellbore diagnostics with a downhole receiver and wired drill pipe, and e) reservoir model verification. Furthermore, the pressure of the sparker bubble will disintegrate rock resulting in an increased overall rates of penetration. Other applications for the SeismicPULSER™ technology are to deploy a low-frequency source for greater range on a wireline for Reverse Vertical Seismic Profiling (RVSP) and Cross-Well Tomography.

Commercialization of the technology is being undertaken by first contacting stakeholders to define the value proposition for rig site services utilizing SeismicPULSER™ technologies.

Stakeholders include national oil companies, independent oil companies, independents, service companies, and commercial investors. Service companies will introduce a new Drill Bit SWD service for deep HTHP wells. Collaboration will be encouraged between stakeholders in the form of joint industry projects to develop prototype tools and initial field trials. No barriers have been

identified for developing, utilizing, and exploiting the low-frequency SeismicPULSER™ source in a variety of applications. Risks will be minimized since Drill Bit SWD will not interfere with the drilling operation, and can be performed in a relatively quiet environment when the pumps are turned off. The new source must be integrated with other Measurement While Drilling (MWD) tools. To date, each of the oil companies and service companies contacted have shown interest in participating in the commercialization of the low-frequency SeismicPULSER™ source. A technical paper has been accepted for presentation at the 2009 Offshore Technology Conference (OTC) in a Society of Exploration Geologists/American Association of Petroleum Geophysists (SEG/AAPG) technical session.

1.0 INTRODUCTION

Drill Bit SWD equates to data normally obtained by conventional vertical seismic profiling (VSP) or RVSP methods. That is, seismic data is obtained with the receiver in the drill string and the source at the surface: VSP methods are costly since they interrupt the drilling process. A Drill Bit SWD seismic method is needed that provides competent downhole acoustic energy without interruption of the drilling process.

Conventional VSP surveying techniques use wireline systems with recording tools in the borehole. Drill Bit SWD helps overcome the higher costs and risks, and provides the geophysicists and drillers with valuable information to optimize drilling efficiency and to steer to the target with the ability to predict pore pressure ahead of the bit and verify reservoir models in real-time. In this way, the renewed application of Drill Bit SWD by the petroleum industry can offer an economic, as well as technological, advantage.

A review of recent applications of SWD is given by Meehan et al. The drill bit as a source of vibrations has been studied extensively since the 1960s, first to monitor the vibrations produced by the drilling process, and later to obtain seismic-while-drilling measurements. However, reliable while-drilling geophysical results have only been obtained in the last 10 years. The preprocessing of the acquired time-incoherent raw field data is required to obtain impulsive shaped seismograms with known zero times. This is accomplished using very long recording intervals that require several tens of minutes of passive listening for each depth point. The reliability of this technology follows from the actual availability of new generation computers, such as PCs and workstations, with processors having computational power of hundreds of megaflops and storage disk memory of gigabytes, which have greatly increased reprocessing capability in the field.

The idea of measuring the drill bit vibrations during drilling was proposed for a number of reasons; in addition various approaches have been considered to solve the problem of identifying the drill bit signal. Guy[2] proposed a new method for the geological control of drilling, which takes into account the various technical maneuvers and interventions occurring during the course of drilling. This method uses the amplitudes measured by seismometers located at the surface of the ground to record the level of drilling vibrations and obtain information about the nature of the drilled formation. Measured drill bit vibrations were also used to analyze the status of the bit. For example, methods for determining the state of wear of a multi-cone bit were proposed by Stuart, as well as Jardine et. al.[4] Another reason for investigating the drill-string vibrations was to determine the precise bit position during the drilling operations. Several authors studied the use of impulsive sources to obtain results with minimum effort and interruption to the drilling process. Bailey[5] proposed a (non-passive) continuous bit-positioning system using motion sensors on the drilling rig and a plurality of geophones on the surface of the earth to make a measurement from which the position of the bit can be determined.

Drawing on the advantages of many of these while-drilling methods, Staron et al.[6] proposed the idea of using the drill bit vibrations recorded on the top end of the drill string as a sort of reference Vibroseis™ sweep to obtain while-drilling seismograms. The method consists of obtaining drill string and ground recordings corresponding to the same depth levels, grouping these elementary recordings in pairs and correlating and stacking them to produce a correlated signal which is representative of the acoustic energy produced and of the travel times of the waves transmitted in the formation. A particular application of this method is the VSP that is obtained after correcting the correlated seismograms for the travel time of the reference signal recorded on the drill string. This method of instantaneous acoustic logging within a wellbore was the basic idea as well as the first effective approach of using the seismic drill bit technology, notwithstanding the initially low quality of the results.

After Staron, other researchers studied the seismic drill bit signal. In particular, Rector and Marion[7] demonstrated, with results of good quality, the use of the drill bit reverse RVSP, using roller-cone correlated data. Rector[8] proposed methods of deconvoluting the drill-string multiples by spiking the drill-string pilot autocorrelation. From the promising results obtained by Rector and Marion[7], the technology of the first SWD commercial system, the TOMEX® system, was developed. Rector and Hardage[9] studied the bit signal to characterize the radiation pattern of the roller-cone-bit wave fields, as well as the noisy conditions. Using a different approach, which does not use pilot recordings at the rig, Widrow[10] proposed a method to extract the drill bit signature and signal by means of adaptive filters. These filters are connected to each of the sensors used to acquire a plurality of traces, located in different positions in the earth near the surface, in order to measure drill bit signals with different travel paths. The drill bit signature and the reflections are calculated after the convergence of the adaptive filters (Widrow[10]), obtained by optimizing the cross-correlation function of the output traces. In the same period, Rocca et. al.[11] investigated the use of the drill bit signal for borehole seismic purposes, by using a plurality of pilot sensors in the rig assembly and adjacent areas. They developed a method that enabled them to perform the statistical separation of the pilot signal starting from the noisy traces obtained by the plurality of sensors placed in the different locations.

Following these works and experience in exploration wells (Miranda et al.[12]), ENI E&P Division and OGS (National Institute of Oceanography and Applied Geophysics) developed their own system, SEISBIT®. This system performs automated acquisition, data quality control, and uses a method of selective data processing based on diagnosis of drilling conditions (Miranda et al.[13]). Furthermore, the investigation extended the SWD to unfavorable conditions, such as downhole-motor and diamond-bit drilling. This was done with the support of downhole tools to acquire improved pilot traces using a local downhole storage memory.

A method for the determination and deconvolution of the drill bit signature was proposed by Miller et al.[14] This method uses an array of receivers positioned at the earth's surface to record the seismic signals produced by the drill bit source. These traces are time-shifted on the basis of analysis of coherence and weighted to estimate the signal (beam forming). A deconvolution filter is computed and applied to the data. A multi-offset application is discussed by Haldorsen et al.[15] The state-of-the-art of Drill Bit SWD as of 2004 can be found in the text by Poletto and Miranda.[16]

The significant replacement of the roller bit by the quieter PDC (polycrystalline diamond drill bit) bit in the 1980s due to higher rates of penetration all but eliminated Drill Bit SWD. An alternative seismic source for the roller bit is something oil and service companies have sought since then. It was said by Mike Tweedy, Chevron Oil Company, in 1989, “The time is coming when we will not drill without looking ahead of the bit any more than we would drive at night without headlights—occasionally shining a lamp to see what we hit.”

Once reliable and detailed information can be obtained about the formations ahead of the bit, significant improvements to the economics of oil and gas drilling are foreseen. This enhanced knowledge will a) facilitate geosteering and verification of pre-drill reservoir models to “look ahead” and efficiently reach desired targets, b) increase safety and cost savings by detecting unexpected high pore pressure ahead of the bit, c) eliminate contingent casing strings, d) reduce flat time, and e) create new operational capabilities when drilling HTHP wells.

2.0 RESULTS

The initial testing of the sparker acoustic source was performed in the TII Seismic Borehole Rock Simulator in 2002. During this first series of tests, the performances of various high-frequency sparker configurations were measured, and the best performing configuration was selected for field testing at the University of Texas Devine Seismic Test Site near Hondo, Texas. While surface recordings at Devine showed success in demonstrating that the sparker at 1,800 ft would provide sufficient surface signal strength when powered with 2,200 Joules (J), it was apparent that extreme power levels would be necessary to achieve the goal for operating at depths greater than 15,000 ft. Thereafter, flow tests were performed to determine whether there could be power enhancement when the sparker is placed in the mud flow of a drill bit. After being unable to demonstrate sufficient enhancement, the project came to a standstill. Fortunately, since “need is the mother of invention,” the developers embarked on developing a better basic understanding of the sparker bubble formation physics. A second set of laboratory tests were performed, again with the desired sparker configuration in the TII Seismic Borehole Rock Simulator. The objective was to generate lower frequencies and, thus less acoustic attenuation in rock, at sensible power levels. It was discovered that with proper control of the sparker input power, one, two, three, four, five, and six Hz peak frequencies were produced. Thereafter, with a fraction of the power used for the Devine wireline high-frequency sparker test, the low-frequency sparker was proved to be capable of operating on a drill string as a downhole source at the RMOTC field test site.

2.1 High-Frequency Sparker Laboratory Testing

A single sparker pulse will first create a gas bubble as illustrated in Figure 1a. Then, milliseconds later, the bubble collapses with a second response. The theoretical model for the event is given by the modified Rayleigh-Willis equation, with results illustrated in Figure 1b.

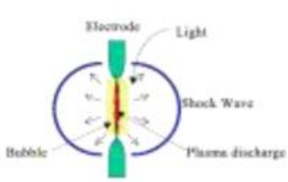

Figure 1a – Gas Bubble Formation

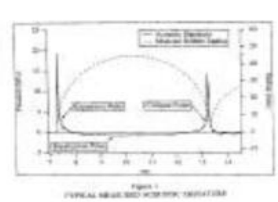

Figure 1b – Gas Bubble Formation-Collapse

When an underwater high-energy spark impulse occurs, a bubble is formed that expands outward until the pressure inside the bubble reaches ambient pressure, and then the bubble collapses. The process produces two high-energy pressure pulses, one at the initial impulse and one upon bubble collapse. The time between these two pressure pulses is referred to as the bubble period. The bubble period is a function of the energy involved in the initial impulse and the operating pressure.

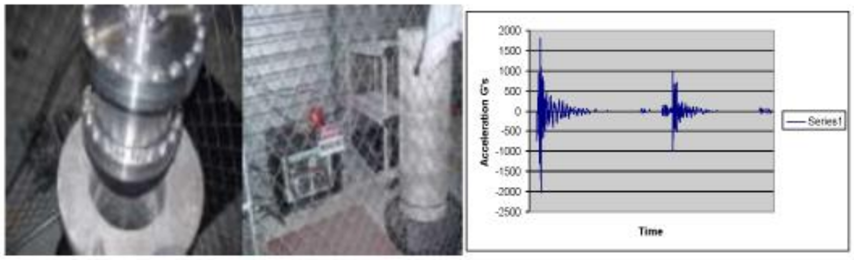

Figure 2 – TII Seismic Borehole Rock Simulator

Shown in Figure 2 is an electrical spark device that was used as the seismic sound source for tests conducted with the device suspended in the TII Seismic Borehole Rock Simulator — a 16 in diameter by 40 in long cylindrical White Sierra Granite rock sample with an 8.5 in borehole. Rock acceleration measurements are also shown that correspond to the formation and collapse of the bubble. The sparker was suspended at different heights above the bottom of the hole in two feet of fresh tap water. The purpose of the testing was to demonstrate that the sparker energy was in agreement when both a) a calibrated hydrophone suspended into the water are in agreement, and b) the values measured with vertical and horizontal accelerometers affixed to the outside of the test rock. The output measurements of the hydrophone and accelerometer were then compared and found to agree with the theoretical values.

Acoustic data was collected at a transmit power level of 400 J. The peak amplitude out of the hydrophone was 248 dB with reference to 1 micro Pascal (ref1 µPa). For these test conditions in the laboratory with a 400 J sparker in 2 ft of water, the measured period of 12 msec agreed with the theoretical predictions. This double impulse produces a very broad acoustic spectrum that

peaks at a frequency that is approximately the reciprocal of the bubble period. Spectrum analysis of the received signal from the horizontal accelerometer output for the 400 J pulse agreed with

theoretical predictions. Higher levels were not measured with the hydrophone because of the fear of damaging the hydrophone. However, accelerometer measurements were made with input power levels up to 2,200 J. Tests were made to compare the output of the two accelerometer outputs with the sparker fitted with several different coupling devices. Special shaped couplers provided more vertical accelerometer output and, thus, more directionality than the plain sparker.

These laboratory tests have shown that the sparker performed as theory predicts and validates the model. Therefore, this model can be used to predict the performance in field tests with confidence. The calculations indicate that a 2,200 J sparker operating at 1,800 ft depth at the Devine Test Site could produce sufficient power over a bandwidth of 50 to 1,111 Hz to be detected on the surface to a range of quarter mile. Details of the high-frequency sparker laboratory testing can be found in Appendix A – Design and Testing of a High-frequency Sparker.

2.2 High-Frequency Sparker Devine Field Test

An optimized high-frequency sparker configuration was tested on a wireline at the University of Texas Devine Test Site near Hondo, Texas. The sparker was lowered on a wireline as shown in Figure 3 below.

Figure 3 – Devine Field Test

The overall objective of this test program was to demonstrate the potential of the acoustic source as a downhole seismic source in known lithology to a depth of 1,800 ft. The specific objectives of the Devine well tests were:

1. To successfully demonstrate the operation of the acoustic source to depths of 1,800 ft in a fiberglass-cased wellbore.
2. Using the results obtained above, to determine at what energy level the acoustic source must be operated in order to successfully obtain surface seismic information at depths to 15,000 ft.
3. To demonstrate the utility of the acoustic source for cross-well seismic operations.

Three wells were used for these tests. Wells No. 2 and No. 4 are approximately 363 ft apart and are steel cased to a depth of approximately 400 ft and cased with fiberglass to 3,000 ft. A shallow (150 ft) steel-cased hole next to Well No. 2 was also used. The approach taken in this test program was to begin testing with the acoustic source at the bottom of the shallow well (150± ft), with a hydrophone in deep Well No. 4 at the same depth and proceed to ever increasing depths to 1,800 ft. A single hydrophone was used to collect cross-well data in each formation type present at the Devine Test Site. Also two surface seismic arrays were deployed orthogonally out to a distance of ½ mile to receive and record direct transit through and reflected signals from the various formations present. A total of seven tests were run with the acoustic source in the shallow hole. A single hydrophone was lowered in Well No. 4 to prescribed depths of 80, 110, 622, 1,200, 1,590, and 1,800 ft, roughly in the middle of each layer to record cross-well seismic signals. Each test was repeated eight times.

The original intent was to lower a 10 hydrophone string in Well No. 4 to record the cross-well coupling at 10 depths simultaneously, but the 10 hydrophone string was not available. Therefore a single hydrophone was lowered to discreet depths of 80, 110, 622, 1,200 and 1,500 ft, roughly in the middle of each geological layer. The data that is recorded shows the direct arrival energy from the acoustic source in the shallow well to the hydrophone in Well No. 4. Only limited cross-well data was collected with the acoustic source at the 1,800 ft depth because the tests were terminated during this run due to equipment problems.

The sound velocity of the direct arriving ray was calculated by dividing the slant range distance by the measured seismic travel time. The calculated velocities agree very closely to the archival data furnished by The Bureau of Economic Geology at the University of Texas in Austin. The shallow well tests demonstrated that the Z-Seis hydrophone was able to detect the direct path cross-well signal to depths of 1,590 ft This demonstrated the utility of the acoustic source for cross-well seismic operations.

An additional 7 tests were conducted with the acoustic source lowered to various depths in Well No. 2. The single hydrophone was lowered to the same depths in Well No. 4, to record cross-well seismic signals. Simultaneously two orthogonal digital surface arrays recorded the seismic signals received at the surface. Cross-well coupling was measured at the 622 ft depth but wasn't recorded at the deeper depths. Cross-well coupling worked between the shallow hole and Well No. 4, and was expected to work just as well from Well No. 2. The Cross-Well coupling was not detected at the depths greater than 622 ft due to sound ray refraction, a problem typically encountered by commercial cross-well tomography services. The detailed analysis of sound ray refraction shows that when the acoustic source and a single hydrophone are placed at the same deep depth it is possible that the signal will not be received. This analysis shows that a small change in sound velocity with depth creates a velocity gradient, which bends the sound ray upward about a radius that can force the horizontal ray to miss the hydrophone. If the 10 hydrophone string, as earlier planned, had been available there may have been a different result, because there would have been hydrophones above and below the acoustic source depth.

The digital surface sensor data plots showed the sensor output on a typical seismic plot with the frequency of the received signal from 0 to 500 Hz. Data below 100 Hz was contaminated by noise from the diesel generator operating near the recording trailer. The anti-aliasing filter rolls off above 350 Hz. Therefore, the useful data is in the frequency band from 100 to 350 Hz. Visual inspection of the frequency response showed that the signal in this area is cleaner (less noise) than data outside this band. The digital surface sensor data demonstrated that the acoustic source signal could be received from 1,800 ft depths. The horizontal range was limited because the low frequencies (below 100 Hz) were obscured by the diesel power generator noise. The results of the deep well test with the surface array were encouraging. The acoustic source demonstrated that it generated a pulse that could be received with the surface array from a depth of 1,800 ft. This verified our calculations that the acoustic source would produce a signal level that could be detected from 1,800 ft depth with the surface array. Detailed field test data and data analysis can be found in Appendix B – High-frequency Sparker Demonstration at the University of Texas Devine Test Site near Hondo, Texas.

2.3 Laboratory Flow Testing

A series of hydraulic tests were performed to understand the fluid dynamics of spark-generated steam bubbles in a pressurized, flowing fluid. These tests were conducted in a specially built flow loop shown in Figure 4.

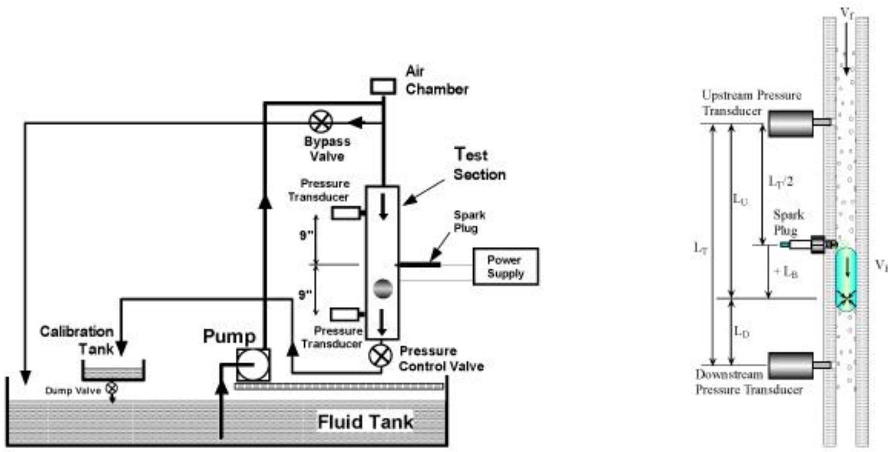

Figure 4 – Sparker Low-Pressure Flow Loop

The purpose of the testing was two-fold: 1) to confirm that spark-induced bubbles under pressurized flowing conditions will not destroy the hardware involved, and 2) to determine the effects of ambient pressure and fluid velocity on the measured pressure pulses resulting from the expansion and collapse of the bubbles. Each test was run with fresh tap water.

The first series of tests were run in straight sections of 1½, 2, and 2½ in steel pipe, with the intent of investigating the effects of creating spark-generated bubbles within the confined space of a straight tube of various diameters. The second series of tests was run with different nozzle and orifice configurations. The spark plug was placed upstream of the nozzle or orifice in some cases, downstream in others, with the intent of investigating the effects of sparker placement relative to a drilling fluid jet stream. Spark plugs function well for test conditions, but do not have the life or efficiency required for a seismic application. The tests were run with ambient pressures ranging from 17 to 58 psi and mean fluid velocities ranging from 0 to 34 ft/sec. A conventional spark plug, threaded into the side of the test section, was used with a standard charge amplifier to generate the sparks. Pressure gauges both upstream and downstream of the spark plug were used to measure the resulting pressure pulses. Bubbles were successfully generated and recorded under ambient pressures that would have created spherical bubbles ranging from 1.2 to 2.4 in diameter in open water. Pressure pulses as high as 510 psi were measured 9 in away from the spark during bubble expansion. Pulses up to 400 psi were measured during bubble collapse. Details of the data collected and the analysis can be found in Appendix C – Effects of Low-pressure Flow on Spark-generated Bubbles. The results obtained in these tests have provided significant insight into the bit hydraulic and mechanical design parameters for a drill bit incorporating a sparker for Drill Bit SWD applications. In particular, the following conclusions have been reached:

1) Spark-induced bubbles can be generated in water within a confined, pressurized space, either with or without fluid flow; and can be done at power levels low enough to avoid destruction of the hardware involved. Pressure pulses resulting from the expansion and collapse of the bubbles produce fluid pressures of extremely short duration (tens to

hundreds of microseconds) and several hundred psi. nearly a foot away from the sparker. Such pressure pulses should be an effective acoustic source for downhole applications.

2) Bubble lifetime was found to decrease with ambient pressure, as predicted by the modified Rayleigh-Willis equation for a spherical bubble, with significant effects found due to the confining effect of the tube and any nozzles or orifices near the bubble during expansion. Bubble lifetime was found to generally increase with fluid velocity and to increase with a reduction in test-section diameter. This is thought to be a geometry effect, where a long cylindrical bubble apparently takes longer to collapse than a spherical bubble of the same volume.

3) The measured bubble-expansion and bubble-collapse pressure peaks were found to increase with a reduction in test-section diameter. This could be because the pressure peaks generated at the bubble wall are geometrically attenuated to a smaller degree in a smaller tube. In the presence of a nozzle or orifice, the bubbles were found to collapse with greatly reduced peak pressures. This may be due to distortion of the bubbles in the reduced fluid cross-section, which causes them to collapse asymmetrically and with less concentrated force than either a spherical or cylindrical bubble.

4) The bubble-expansion and bubble-collapse pressure peaks in both the straight-tube and nozzle/orifice tests were found to be unaffected by either the initial ambient pressure or the velocity of the fluid.

2.4 Low-Frequency Laboratory Testing

A technique to generate a low-frequency seismic signal using spark gap technology was first discovered in the TII Seismic Borehole Rock Simulator, shown in Figure 2. The acoustic frequency spectrum measurements were conducted in an enclosed rock chamber. A strain gauge accelerometer was attached for axial measurements at the bottom the rock, and horizontal measurements were made with an accelerometer attached to the side of the rock in line with the sparker. The development of a non-conventional sparker control method lead to the SeismicPULSER™ technology employed to generate peak low frequencies (one, two, three, four, five, and six Hz) with an otherwise high-frequency sparker source at power levels useful for Drill Bit SWD.

For example, Figure 5a is a broadband spectrum of a conventional sparker measured in the test rock. Figure 5b is the frequency spectrum of the same sparker operating in the low frequency SeismicPULSER™ mode. Figure 5a shows that the single pulse fundamental frequency is centered between 40 and 500 Hz or about 150 Hz. Figure 5b shows the same sparker operating in the low-frequency mode at the same power level, but the fundamental frequency is now shifted to five Hz. Both spectra have high-frequency content extending to 10 kHz.

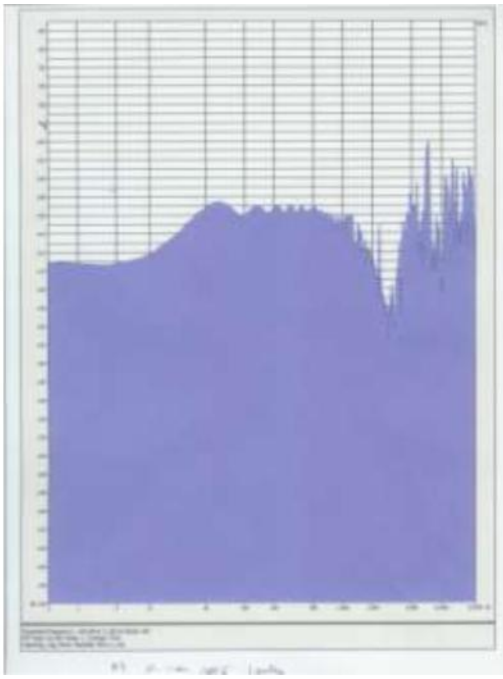

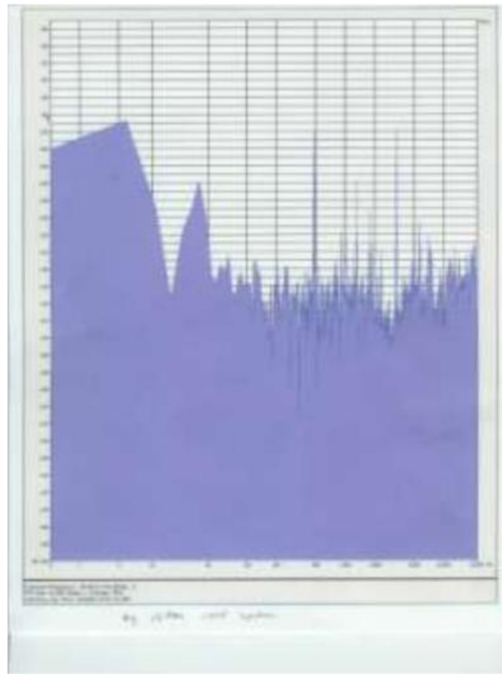

Figure 5a – High-frequency Conventional Sparker 40 Hz to 10 kHz

Figure 5b – Low-frequency SeismicPULSER™ 5 Hz Peak to 10 kHz

The frequency spectrum measured was of a peak waveform with a very broad spectrum. Electrical feed-over peaks from the spark are present at the start of the accelerometer signal. These sharp peaks also distort the measured spectrum. In spite of these known distortions these tests demonstrate that the SeismicPULSER™ technique produces a low peak frequency seismic signal.

2.5 RMOTC Sparker Field Drill Mode Test

The main objective of the field test of a deployable drill string sparker tool was to fire and record the seismic energy generated by the low-frequency sparker down-hole source in a well site environment. Field demonstration with a prototype 26 ft long x 8 in diameter sparker tool, shown in Figure 6, was performed at the 10,000-acre U.S. DOE RMOTC facility located within the U.S. Naval Petroleum Reserve No. 3 (NPR-3) near Casper, Wyoming.

Figure 6 – Prototype Low-Frequency Sparker Tool

The well was lined with casing to approximately 650 ft, with open hole to 5,665 ft. However, due to hole conditions, tests could only be conducted to 4,000 ft. Directly below the casing was the Steele Shale formation, containing thin sandstone channels, the Sussex and Shannon sands. The deeper sandstone formations were the first, second, and third Wall Creek, the Dakota and the Lakota.

The seismic recording system monitored and recorded the seismic signal generated by the down-hole low-frequency sparker. Two orthogonal receiver lines were laid out close to the well head location. Each of the two lines employed 48 receivers at 55 ft spacings. The lines crossed close to the surface total depth location of the bore-hole at approximately 500 ft west of the well-head location. The seismic data were recorded in SEG-Y format, and re-formatted for use of a seismic processing software package.

The rig environment, contained many sources of background noise including mud pumps with a 3.3 Hz and 6.6 Hz frequency as a function of the 350 gpm pumping rate, as shown in Figure 7a. The rationale was to program the low frequency sparker at a low peak frequency (two Hz), since it was assumed to be below the bandwidth range of the background noise. Seismic records show that the sensors recorded no coherent energy below three Hz. With the receiving sensors and recording system damping all signals below three Hz, it was not possible to see the two Hz signal. However, it was discovered that the two Hz signal modulated with the 3.3 Hz mud flow signal, creating the combined signal of 5.3 Hz, as shown in Figure 7b.

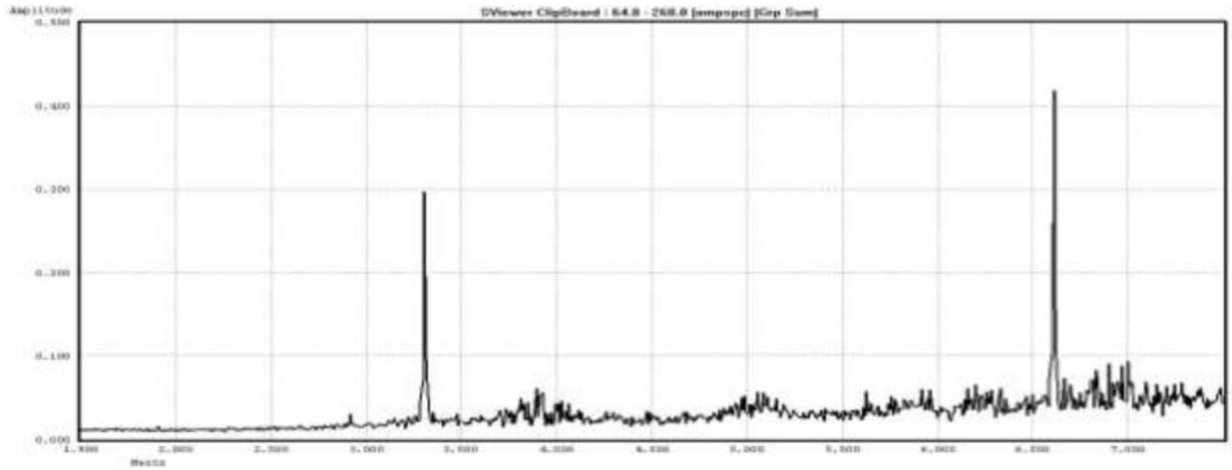

Figure 7a – Flow Noise With Mudflow @ 350 gpm, No Sparker

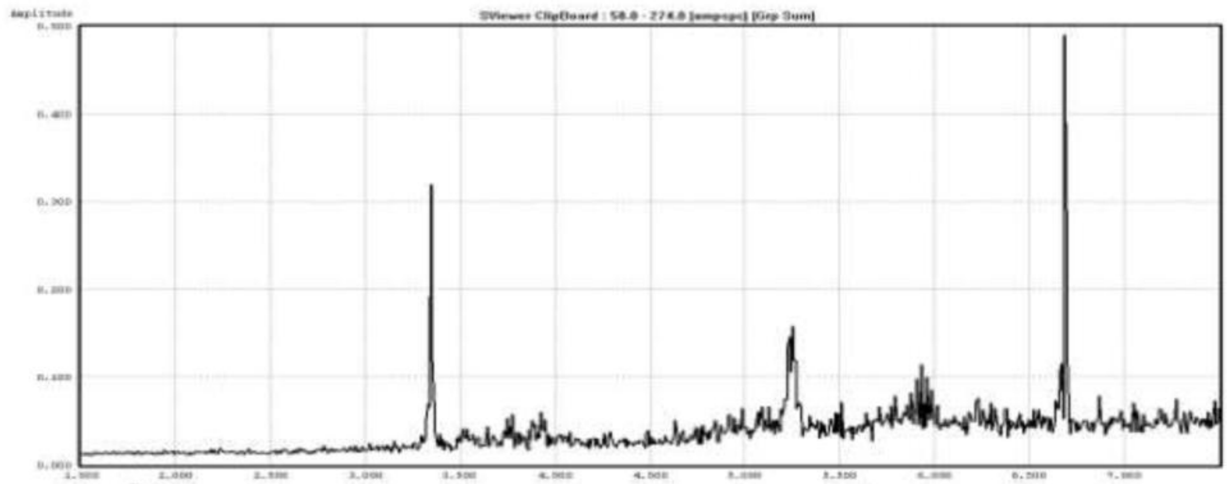

Figure 7b – Sparker Operating With Mudflow @ 350gpm

When utilized in the drilling mode, the energy generated by the low-frequency sparker would normally have to compete with all the coherent noise energy generated at the rig site while the pumps are running and drill string rotating. However, with high-voltage electrical energy stored in the capacitors, the sparker can be programmed, for example, to generate a four Hz peak signal every 20 seconds with the pumps turned off. When utilized in the drilling mode, the additional energy at the drill bit may increase rate of penetration. Detailed test data and analysis may be found in Appendix D – RMOTC Downhole SeismicPULSER™ Source Test.

1. Discovered during laboratory seismic borehole simulation testing and demonstrated in the field, low frequencies can be generated by an otherwise high frequency sparker.
2. Static fluid laboratory rock tests showed that bubble formation and collapse were found to be consistent with the modified Rayleigh-Willis formula for bubble dynamics, while flow tests showed pressure pulses higher than predicted.
3. The unique sparker control system has the ability to adjust power and frequency as needed from the surface to meet varying demands of depth, rock properties, and other geological variances.

4. At 15,000+ ft, 150°C rated capacitors, charged with only a 13 hydraulic horsepower turbine alternator, can create low frequencies peak spectra (1 to 40 Hz) that reflect from formations ahead of the bit to the surface.
5. The sparker can also be controlled as a conventional sparker producing high frequencies desirable for near wellbore diagnostics for use with wired drill pipe.
6. The new low-frequency sparker source output is independent of depth/pressure.
7. The low frequency Drill Bit SWD system will not interfere with the drilling process, thus avoiding unacceptable cost implications.
8. In deep HTHP wells, low-frequency Drill Bit SWD can provide “look ahead” imaging with a selectable and surface adjustable power and frequency source that can be fired when the pumps are turned off.
9. Velocity profiles can be created in real-time at the rig site for employing existing service company pore pressure diagnostic capabilities.
10. The low-frequency sparker can be fired when pulling out of the hole for seismic data verification.
11. New hydrocarbon reservoir and salt dome seismic applications can be performed with increased control of Drill Bit SWD source spectra.
12. The addition of a downhole clock that is synchronized with the surface recordings is required to perform commercial Drill Bit SWD services.
13. The control system can be designed to have a selectable frequency tuned to operate in the quiet zone of the ambient noise environment created by the rig and surrounding noise sources.
14. Commercial Drill Bit SWD services can be designed to operate when the mud pumps are turned off.
15. Integration of the low-frequency sparker with the drill bit may provide increased rate of penetration.

3.0 CONCLUSIONS

1. Discovered during laboratory seismic borehole simulation testing and demonstrated in the field, low frequencies can be generated by an otherwise high frequency sparker.
2. Static fluid laboratory rock tests showed that bubble formation and collapse were found to be consistent with the modified Rayleigh-Willis formula for bubble dynamics, while flow tests showed pressure pulses higher than predicted.
3. The unique sparker control system has the ability to adjust power and frequency as needed from the surface to meet varying demands of depth, rock properties, and other geological variances.
4. At 15,000+ ft, 150°C rated capacitors, charged with only a 13 hydraulic horsepower turbine alternator, can create low frequencies peak spectra (1 to 40 Hz) that reflect from formations ahead of the bit to the surface.
5. The sparker can also be controlled as a conventional sparker producing high frequencies desirable for near wellbore diagnostics for use with wired drill pipe.
6. The new low frequency sparker source output is independent of depth/pressure.
7. The low frequency Drill Bit SWD system will not interfere with the drilling process, thus avoiding unacceptable cost implications.

8. In deep HTHP wells, low frequency Drill Bit SWD can provide "look ahead" imaging with a selectable and surface adjustable power and frequency source that can be fired when the pumps are turned off.
9. Velocity profiles can be created in real-time at the rig site for employing existing service company pore pressure diagnostic capabilities.
10. The low frequency sparker can be fired when pulling out of the hole for seismic data verification.
11. New hydrocarbon reservoir and salt dome seismic applications can be performed with increased control of Drill Bit SWD source spectra.
12. The addition of a downhole clock that is synchronized with the surface recordings is required to perform commercial Drill Bit Seismic While Drilling services.
13. The control system can be designed to have a selectable frequency tuned to operate in the quite zone of the ambient noise environment created by the rig and surrounding noise sources.
14. Commercial Drill Bit Seismic While Drilling services can be designed to operate when the mud pumps are turned-off. 15. Integration of the low frequency sparker with the drill bit may provide increased rate of penetration.

4.0 REFERENCES

1. Meehan, R., Nutt, L., Dutta, N., and Menzies, J., (1998) Drill Bit Seismic: A Drilling Optimization Tool, IADC/SPE Paper No. 39312.
2. Guy, M.M., (1961) NOUVELLE METHODE DE CONTROLE GEOLOGIQUE DE FORAGE, Brevet d‟Invention No. 1,584,951, Ministere du Développement Industriel et Scientifique, Republique Francoise.
3. Stuart, J., (1989) METHOD FOR DETERMINING DRILL BIT WEAR, European Patent Application, EP 0 336 477 A1.
4. Jardine, S.I., Lesage, M.L. and McCann, D.P., (1990) Estimating Tooth Wear from Roller Cone Bit Vibration, IADC/SPE Paper No. 19966.
5. Bailey, J.R., (1974), CONTINUOUS BIT POSITIONING SYSTEM, U.S. patent No. 3,817,345.
6. Staron, P., Arens, G. and Gros, P., (1998) METHOD OF INSTANTANEOUS ACOUSTIC LOGGING WITHIN A WELLBORE: U.S. Patent No. 4,718,048.
7. Rector, III J. W., and Marion. B. P., (1991) The Use of Drill bit Energy as a Downhole Seismic Source, Geophysics, 56, 628-634.
8. Rector, III J. W., (1989) SYSTEM FOR REDUCING DRILL STRING MULTIPLES IN FIELD SIGNALS, U.S. Patent No. 4,862,423.
9. Rector III, J. W., and Hardage, B. A., (1992) Radiation Pattern and Seismic Waves Generated by a Working Roller-cone Drill Bit, Geophysics, 57, 1319-1333.
10. Widrow, B., (1990) SEISMIC PROCESSING AND IMAGING WITH A DRILL BIT SOURCE, U.S. Patent No. 4,964,087.
11. Rocca, F., Persoglia, S., Poletto, F., and Craglietto, A., (1990) Use of Drilling Noise to Generate a Reciprocal VSP, CEE Contract DGXII/TH-0113-87, Final Report of the Project.
12. Miranda, F., Aleotti. L., Abramo, F., Poletto, F., Craglietto, A., Persoglia, S., and Rocca, F., (1996) Impact of Seismic While Drilling Technique on Exploration Wells, First Break, 14, 55-68.

13. Miranda. F., Abramo, F. Poletto, F., and Comelli, P., (2000) PROCESS FOR IMPROVING THE BIT SEISMIC SIGNAL USING DRILLING PARAMETERS, European Patent Application 00201332.4-2213.
14. Miller, D., Haldorsen, J., and Kostov, C., (1990) METHODS FOR DECONVOLUTION OF UNKNOWN SOURCE SIGNATURES FROM UNKNOWN WAVEFORM DATA, U.S. Patent No. 4,922,362. 15. Haldorsen, J.B.U., Miller, D.E. and Walsh, J.J., (1995) Walk-Away VSP Using Drill Noise as a Source, Geophysics, 60, 978-997.
15. Poletto, F. and Miranda, F., (2004) Seismic While Drilling – Fundamentals of Drill bit Seismic for Exploration, HANDBOOK OF GEOPHYSICAL EXPLORATION, 35.

5.0 ACKNOWLEDGEMENTS

TII acknowledges the significant contributions to the success of this project by the Principal Investigator, Robert P. Radtke, and project participants Dr. John E. Fontenot, David A. Glowka, Bill Grant, A.J. Kucera, Richard Riedel, Robert H. Stokes, Jeffery Sutherland, Sheila Underreiner, and Virlen Wagner, Technology International, Inc.; Ron Evans, Bjarte Fabergas and Dr. Jim Musser, ION Geophysical, Inc.; James Mento, Z-Seis, Inc. (now Schlumberger); and Brian Black, DOE RMOTC. A special thank you to the many subcontractors for manufacturing the prototype tools that performed flawlessly. The investigation was performed with funding from the U.S. Department of Energy (DOE) National Energy Technology Laboratory (NETL), under technical monitors William Gwilliam and John Terneus, plus cost-sharing contributions by ION Geophysical, Inc., and TII.

This page intentionally left blank

APPENDIX A – DESIGN AND TESTING OF A HIGH-FREQUENCY SPARKER

Principal Investigator
Robert P. Radtke
Technology International, Inc.

Prepared by:
Robert H. Stokes
Jeff Sutherland

This page intentionally left blank

Table of Contents

List of Figures

List of Tables

This page intentionally left blank

EXECUTIVE SUMMARY

TII developed an electrical spark device to be used as the seismic sound source for their SWD program. Tests were conducted of the SWD sparker in the TII laboratory in Kingwood, Texas. The sparker was suspended in a 16 in. diameter by 40 in. long cylindrical rock sample with an 8.5 in hole bored in the center. The hole was partially filled with fresh water and the sparker was suspended two in. above the bottom of the hole in two ft of water. The purpose of the test were to demonstrate that the sparker could generate reliable sparks over power ranges of 400 – 2,200 J and measure the output with a calibrated hydrophone suspended in the water and with vertical and horizontal accelerometers affixed to the outside of the test rock. The output measurements of the hydrophone and accelerometer were then compared to theoretical values for a sparker operating in two feet of water.

Acoustic data was collected at a transmit power level of 400 J. The peak amplitude out of the hydrophone was 248 dB ref 1 µPa. Higher levels were not measured with the hydrophone because of the fear of damaging the hydrophone. However, accelerometer measurements were made with input power levels up to 2,200 J.

When an underwater high-energy spark impulse occurs a bubble is formed that expands outward until the pressure inside the bubble reaches ambient pressure and then the bubble collapses. This process produces two high-energy pressure pulses, one at the initial impulse and one on bubble collapse. The time between these two pressure pulses is referred to as the bubble period. The bubble period is a function of the energy involved in the initial impulse and the operating depth. For the test conditions in the lab with a 400 J sparker at two foot depth, the measured period of 12 ms agreed with the theoretical predictions.

This double impulse produces a very broad acoustic spectrum that peaks at a frequency that is approximately the reciprocal of the bubble period. Spectrum analysis of the received signal from the horizontal accelerometer output for the 400 J pulse agreed with theory theoretical predictions.

Tests were made to compare the two accelerometer outputs with the sparker fitted with several different coupling devices. It was shown that the funnel shaped coupler provided more vertical accelerometer output than the plain sparker; therefore, it will be the recommended device to use in future tests.

These laboratory tests have shown that the sparker performed as theory predicts and validates the model. Therefore, this model can be used to predict the performance at the Devine Test Site with confidence. These calculations indicate that the 2.2 kJ sparker, operating at 1,800 ft depth, will produce sufficient power over a bandwidth of 50–1,111 Hz to be detected on the surface to a range of a half mile.

1.0 INTRODUCTION

Tests were conducted with a sparker in the Seismic Borehole Rock Simulator Laboratory at the TII Laboratory located in Kingwood, Texas. The sparker was suspended in a 16 in. diameter by 40 in long cylindrical White Sierra Granite rock sample with an 8.5 in hole bored in the center. The side wall and bottom thickness was 3.5 in. The hole was filled with fresh water and the sparker was suspended 2.0 in. above the bottom of the hole. The purpose of the tests were to demonstrate that the sparker could generate reliable sparks over power ranges of 400 – 2,200 J and measure the output with a calibrated hydrophone suspended in the water and the output of a vertical and horizontal accelerometers affixed to the outside of the test rock. The output measurements of the hydrophone and accelerometer were then compared to theoretical values for a sparker operating in water at approximately two ft depth.

The measured outputs agreed with the theoretical predictions, therefore the model was validated and this model can be used to predict the performance of the sparker at much deeper depths at the Devine test site. Below is a summary discussion of the results.

When an underwater high-energy impulse occurs, a bubble is formed that expands outward until the pressure inside the bubble reaches ambient pressure and then the bubble collapses. This process produces two high-energy pressure pulses, one at the initial impulse and one on bubble collapse as illustrated in Figure 1a.

The time between these two pulses shown is referred to as the bubble period. The bubble period is a function of the energy involved in the initial impulse and the depth. Theoretical calculations of the bubble period are based on the Rayleigh-Willis[1] formula shown below.

$$\text{Bubble Period } (T) = \frac{0.000209(KQ)^{1/3}}{(d + 33)^{5/6}}$$

where: K = constant = 1×10^{10} when Q is in kJ
d = depth in feet

The spectrum produced by this impulse peaks at a frequency that is the reciprocal of the time difference between the two pressure maxima is illustrated in Figure 2b.

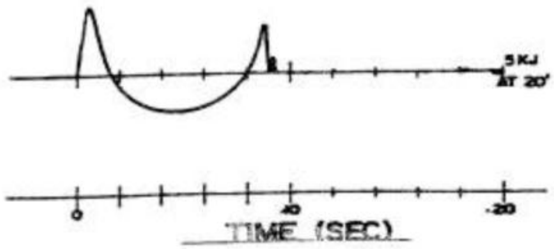

Figure 1a – Pressure Pulse

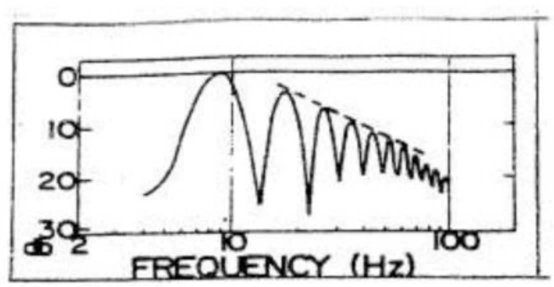

Figure 1b – Spectrum

2.0 RESULTS

2.1 Laboratory Tests

Figure 2 shows the calculated bubble period in msec for different power levels at 4.5 ft depth based on the Rayleigh-Willis formula. Also shown are the results of prior experiments[2] that show that sparker sources produce periods that are approximately 70 percent of the theoretical value because of the electrical and other losses that are not accounted for in the Rayleigh-Willis formula.

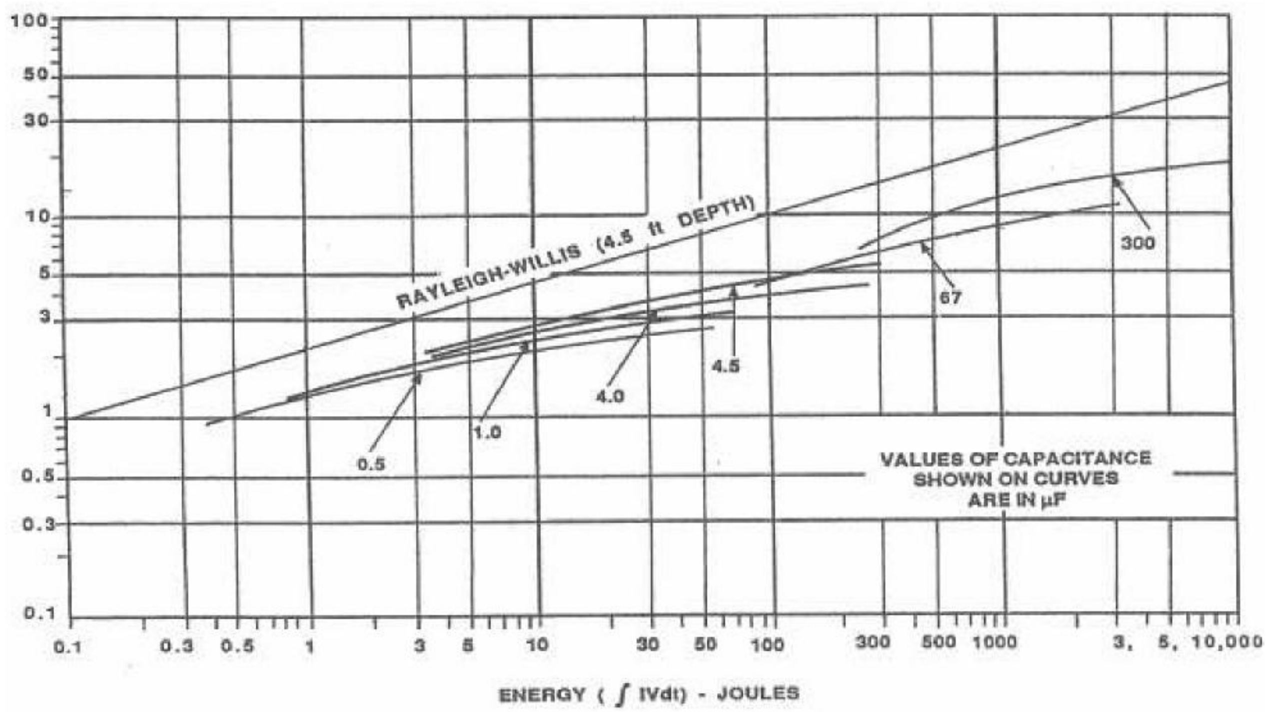

Figure 2 – Bubble Period as a Function of Input Electrical Energy

Figure 3 on the next page shows the calculated bubble period for different power levels and depths based on the modified Rayleigh-Willis formula.

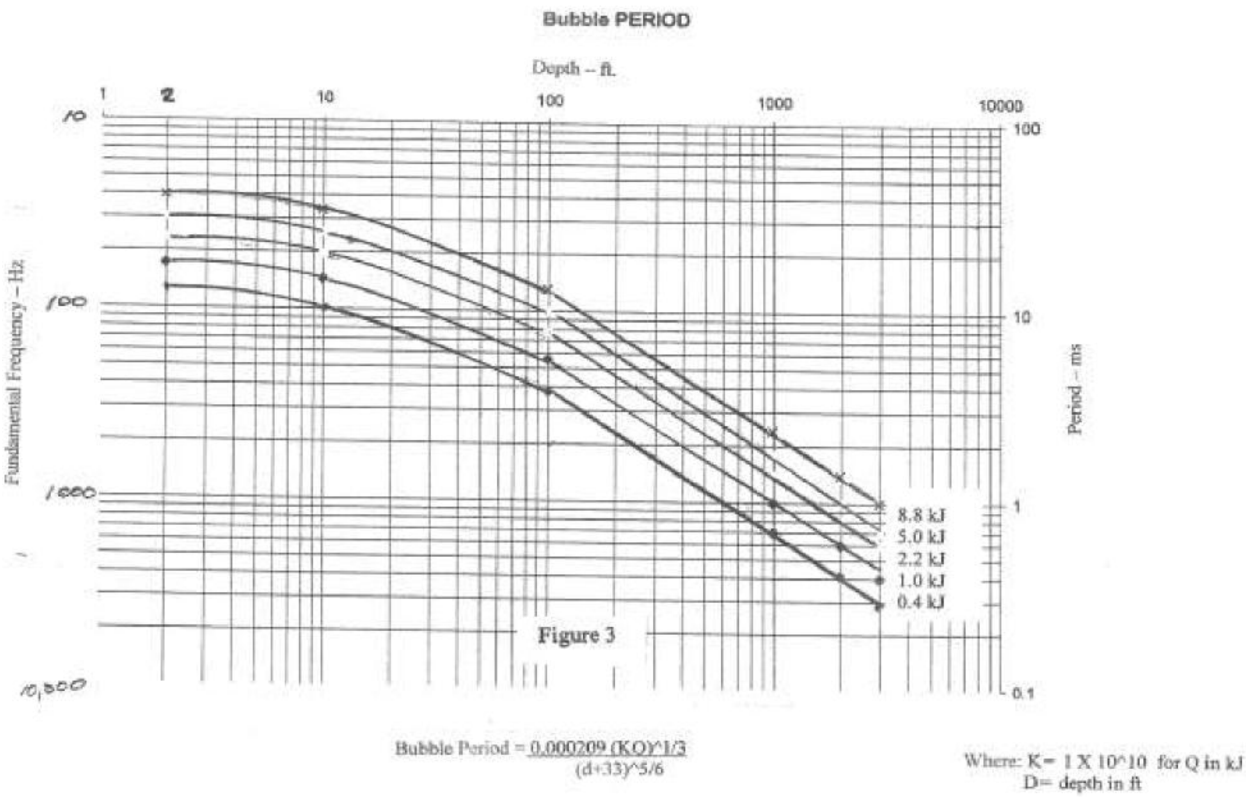

Figure 3 – Fundamental Frequency as a Function of Bubble Period

Acoustic data was collected at 400 J levels. The peak amplitude out of the hydrophone was 250 V, which corresponds to a source level of 248 dB ref 1 µPa. Higher levels were not measured because of the fear of damaging the hydrophone. These unit calculations used a reference of µPa because that is an industry standard and the hydrophone is calibrated in µPa. However, it is straightforward to convert µPa to more familiar seismic units such as MPa or psi.

1 MPa = 240 db re 1
µPa 1 MPa = 140 psi

Two accelerometers were clamped to the test rock, one on the bottom to measure vertical acceleration and one on the side to measure horizontal acceleration. The accelerometers have a sensitivity of 5mV/g and a maximum input of 10,000 g. Figure 4 is a trace of the vertical and horizontal accelerometer outputs from a 400 J spark. As can be seen, there is 12 ms between the initial pulse and the bubble collapse pulse. From the vertical scale calibration, it was determined that for the 400 J pulse there was a peak value of 4.4 V, or 800 g acceleration. The minimum sensitivity of the receiving accelerometer is 0.00 1 g; the ratio of the 400 J measured signal to the minimum detectable signal will be 800 g/0.001g = 800,000 or 20 Log 800,000 = 118 db. Attenuation can exist between the transmitted and received signal and still have a detectable signal. This attenuation will consist of spreading and absorption losses.

4003_10

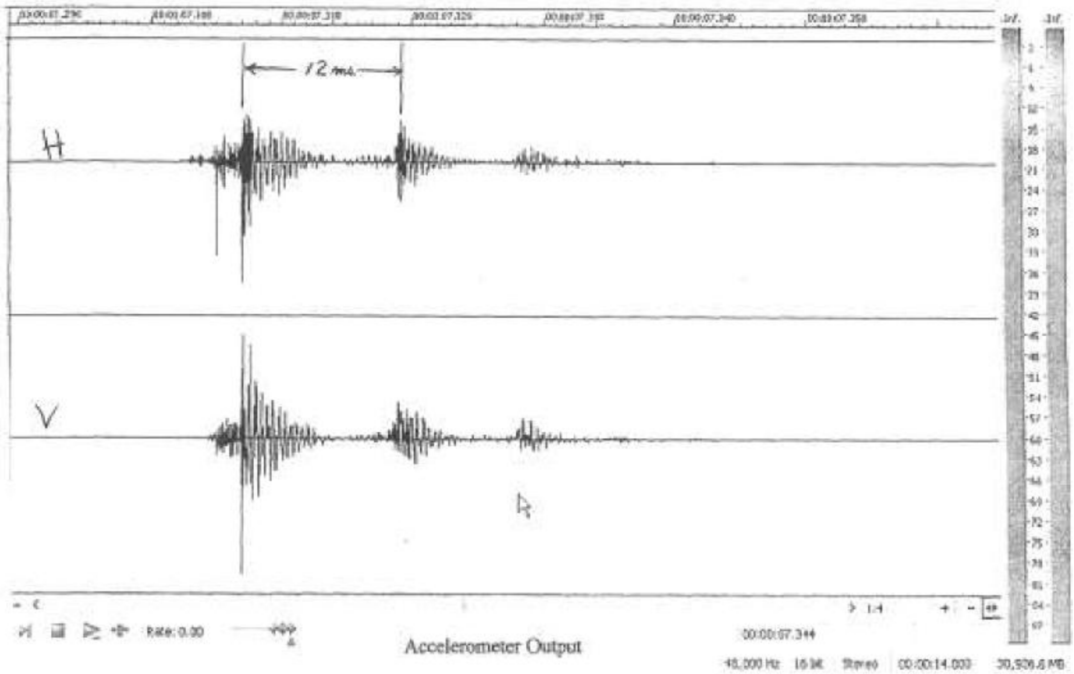

Figure 4 – Bubble Period

2.2 Acoustic Tests

Figure 5 is a Spectrum Analysis using Sound Forge analysis software of the horizontal accelerometer output from the 400 J pulse. The fundamental frequency in the spectrum corresponds roughly to the inverse of the bubble period (F = 1/T). For T = 12 msec the fundamental frequency is 1/T = 83 Hz. As can be seen the output level starts to decrease above the fundamental frequency as expected. Even though the amplitude is decreasing, there is still significant signal at 1,000 Hz and higher. Consistently in all the data there was a peak in the frequency response at approximately 2,200 Hz. Because this peak was in all data regardless of the output power or the Fast Fourier Transform (FFT) filter, it is felt that it is a resonant phenomenon based on the rock size and the placement of the accelerometers; therefore it should not be present in the Devine tests.

For the 400 J Spectrum shown in Figure 5, the frequency ranges from 0 – 22,000 Hz along the horizontal axis and relative amplitude in dB on the vertical axis. The spectrum shows that the output level decreases as the frequency decreases from 83 Hz to 0 Hz. This low-frequency response should roll off below the fundamental frequency at approximately 12dB/octave, similar to the spectrum shown in Figure 5. However, the spectrum does not roll off as steeply from 83–0 Hz as predicted. It was suspected that this response was a function of the FFT sample rate and smoothing filter of the Sound Forge analysis software rather than the actual signal level. Several filters were tried such as Blackman-Harris, Hamming, Hanning, Rectangle and Triangle. When the spectrum analysis was made with the Blackman-Harris filter, the frequency response was essentially flat from one Hz to the fundamental frequency but when the same data was analyzed with the Hamming filter, the frequency rolls off below the fundamental frequency at approximately six dB/octave. The theoretical spectrum shown in Figure 3 assumes free field conditions and two single, very sharp and well defined pressure pulses. The two pulses in the laboratory were made in an enclosed chamber in a rock cylinder and certainly did not have the free field conditions upon which the theoretical calculations are based.

For the test conditions in the lab with a 400 J sparker at two ft depth, the measured period is 12 msec This is good agreement between the measured period of 12 msec and theoretical period of 12 msec shown in Figure 3 and summarized in Table 1.

Table 1 – Summary of Laboratory Measurements

Power	Modified Rayleigh-Willis Period	Measured Period	Fund. Freq. 1/T
400 J	12 ms	12 ms	83 Hz
1000 J	16 ms	18 ms	55 Hz
2200 J	21 ms	25 ms	40 Hz

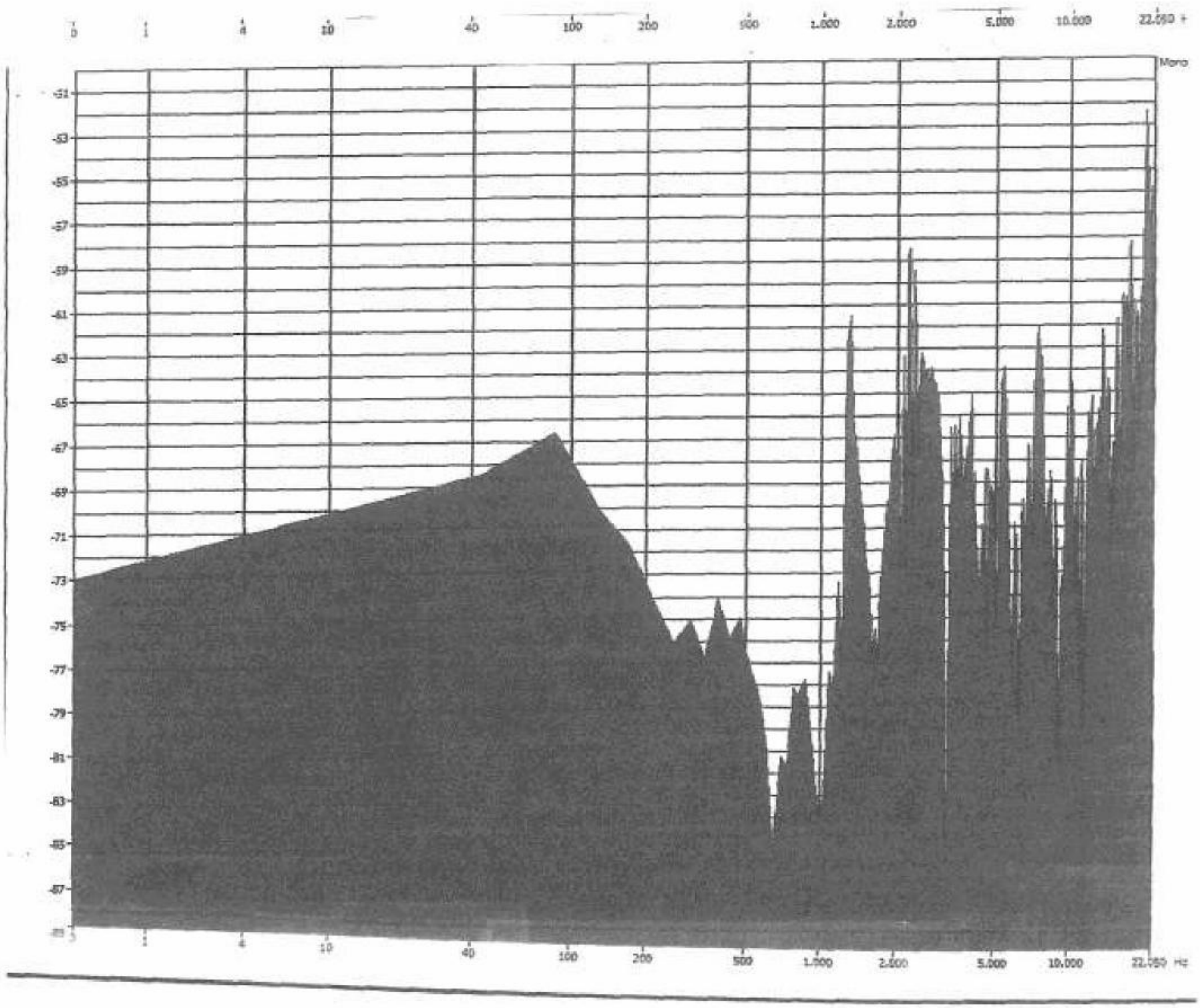

Figure 5 – Spectrum for 400 Joule Pulse

2.3 Accelerometer Tests

Testing was performed in the TII laboratory. Figure 6 is a comparison of the horizontal and vertical accelerometer outputs for the sparker with no coupler (plain) and two different couplers. The sparker power for each test was 400 J. The output amplitude shown on the vertical axis is the digital output count from an Analog to Digital converter and is summarized in Table 2. The horizontal "Time" axis shows the typical 12 msec pulse for the 400 J spark.

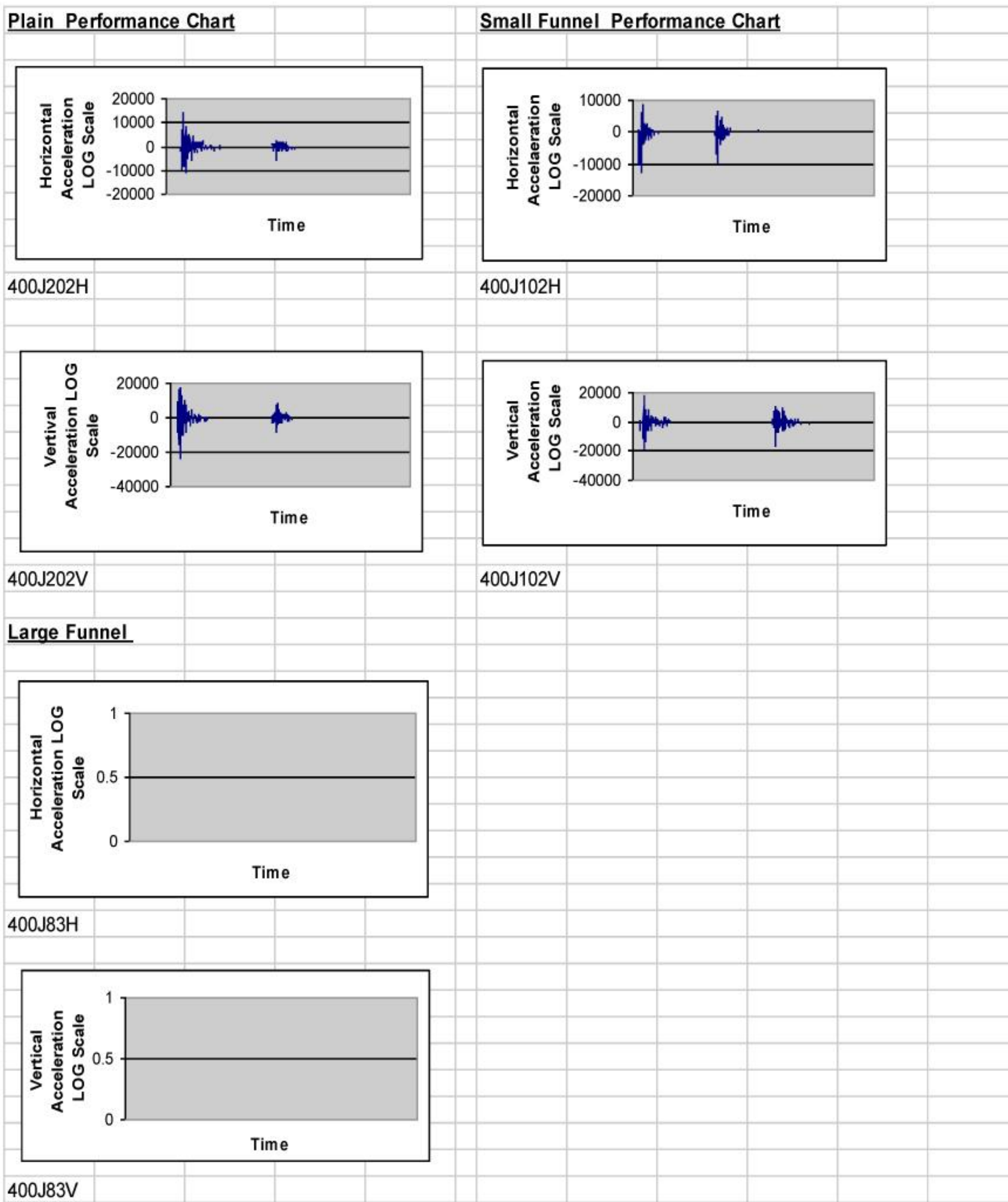

Figure 6 – Accelerometer Output from Plain and Cone Couplers

Table 2 – Accelerometer Outputs with Different Sparker Designs

Coupler	Plain	Small Funnel	Large Funnel
Hor. Acc.			
+peak	13,000	9,000	12,000
-peak	-10,000	-13,000	-13,000
Vert. Acc.			
+peak	19,000	19,000	22,000
-peak	23,000	-20,000	-20,000

1. As can be seen in the above data, the vertical accelerometer achieved the highest outputs. Also, the vertical accelerometer was not coupled to the test rock as tightly as the horizontal accelerometer and the amplitude difference may be even greater. The + vertical amplitude for the large funnel is greater than the small funnel.
2. For the small and large funnel coupler, the + horizontal output is less than the +plain unit output, and the +vertical output is higher, indicating the wall of the coupler decreased the horizontal signal and increased the vertical signal as expected.
3. The mounting hardware for the parabolic and elliptical coupler was not rugged enough to withstand the high power conditions of the test. These couplers were made of aluminum and the screws would loosen and cause inconsistencies in the data. Therefore, data from the parabolic and elliptical couplers are invalid and not presented. The small and large funnels were made of stainless steel and were more rugged and did not shift around during the tests and their data is more consistent.
4. Based on these observations, it is recommend the large funnel be the first choice for the coupler with the small funnel as the second choice.

The power supplied to the sparker was varied from 400 to 2,200 J and the outputs from the accelerometers were recorded. The output of the + Vertical Accelerometer as a function of the input power is shown in Table 3.

Table 3 – Accelerometer Output vs. Power

Power	Plain	Small Funnel	Large Funnel
400 J	13,000	19,000	22,000
600 J	26,000	15,000	
1000 J	20,000	21,000	
1200 J	20,000	20,000	
1600 J	22,000	10,000	
1800 J	18,000	21,000	
2200 J	20,000	23,000	

1. General observation of the data shows that as the input power increases, the output from the accelerometer increases. As an example, the plain unit output goes up from 13,000 to 20,000 as the power goes up from 400 J to 2,200 J and the small funnel increases from 19,000 to 23,000. However, there are a few unexplained wild data points, such as, the 400 to 600 J output actually went down for the Small Funnel and the 600 to 1,000 J.
2. The output decreased for the plain unit. A plot of this data in Figure 7, shows this trend when these wild data points are omitted.

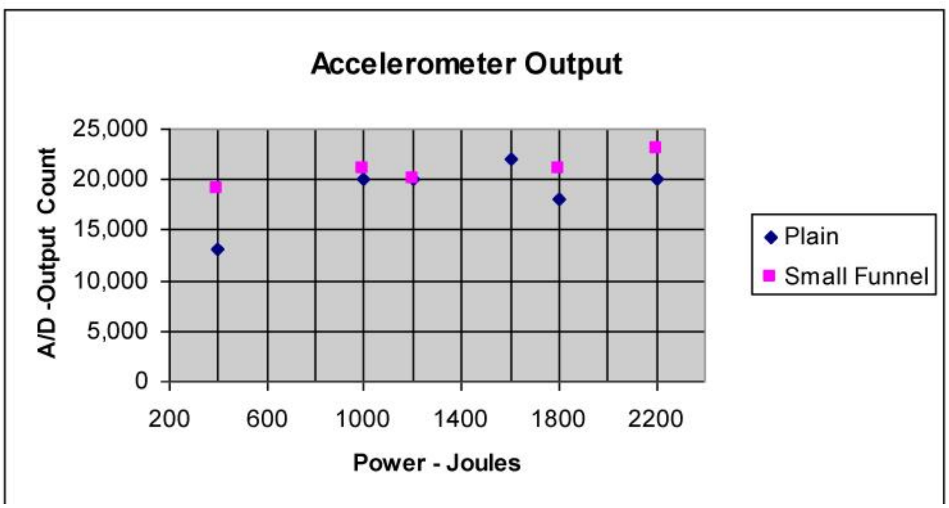

Figure 7 – Accelerometer Output

3. Too much focus should not be put on the absolute numbers because these tests were made in a small cylinder of water at about 2 ft deep. Acoustic measurements at 400 J produced a Sound Pressure Level of 248 dB//1uPa. At these high-power levels, the system will be producing cavitation bubbles or will be operating in a nonlinear shock mode. In either case, the output will not be linear and as the input power is increased, the output energy mostly goes into generating higher harmonic frequencies rather than increasing the output energy. Cavitation problems will be eliminated as the hydrostatic pressure is increased. At depths equal to 10 atmospheres or 300 ft, cavitation should not be a problem.

2.4 Field Test Conditions

What will happen in field testing will be entirely different than what was measured at the laboratory. The laboratory data was used to validate the model to predict what the spectrum will be at any depth of operation at Devine. The Sound Forge spectrum is in reasonable agreement with the theoretical spectrum for the expected results at the laboratory depth of about two ft. To predict the spectrum at any other depth, the spectrum produced at two ft has to be translated to the predicted fundamental frequency at the operating depth and determine what the spectrum will be. As an example, we know that the 400 J fundamental frequency is 83 Hz at two ft, and analysis with the Sony Sound Forge software application agrees with that. We also know that theoretically the amplitude will roll off at six dB per octave above 83 Hz and Sound Forge agrees with that. Theoretically the signal should roll off below 83 Hz at 12 dB per octave. Sound Forge with Hamming filtering shows the output rolling off about 6 dB per octave rather than 12 dB. This is not perfect agreement with theoretical, but at least trending in the right direction. The theoretical calculation is for free field conditions in water and not for a cylindrical rock with an 8.5 in hole bored in the cylinder, therefore some differences are expected.

Calculations were made to predict sparker performance in field conditions. As an example, consider a 400 J pulse at 10 ft depth and from Figure 3 it is seen that the period will be 10 ms and a fundamental frequency of approximately 100 Hz. If it is assumed the velocity of sound in the rock is 3,000 m/sec, the wavelength of 100 Hz will be 30 m. From Liner[3] page 147 the absorption coefficient of most rock lies in the range of 0.2–0.5 dB/wavelength. If we assume a depth and slant range of operation of 4,000 ft, or 1,212 meters, the range is 40 wavelengths.

The Liner absorption will decrease the fundamental frequency signal by:

$A = e^{-(0.25dB/wl)}(\text{range}) = e_{-(0.25)(40)} = e_{-10} = 0.0000454$

Absorption expressed in dB = 10 log 0.0000454 = -43.4 dB

Spherical spreading loss is 20 Log 1212 = 61.6 db, the total attenuation (A) will be: Total Attenuation = Spreading + Absorption = 61.6 dB + 43.4 dB = 105 dB.

A 400 J pulse produces 118 dB of signal dynamic range. Therefore the Signal to Noise ratio (S/N) at the receiver will be:

S/N = Dynamic Range - Total Attenuation
S/N = 118 dB - 105 dB = 13 dB

Also seen from Figure 3, as the sparker source is lowered to deeper depths, the bubble period gets smaller and the fundamental frequency gets higher. Some of the increase in frequency can be compensated for by increasing the sparker power from 400 J to 2.2 kJ, for 7.4 dB increase. As seen from Figure 3, for 2.2 kJ at 250 ft depth the period is 4 ms, which is the same as 400 J at 10 ft depth. Therefore the same absorption and spreading loss at a range of 1,212 m, will still occur but because of the increase in output power, the signal to noise will actually be greater.

$A = e^{-(0.25dB/wl)}(\text{range}) = e_{-(0.25)(40)} = e_{-10} = 0.0000454$

Absorption expressed in dB = 10 log 0.0000454 = -43.4 dB

Attenuation = 61.6 dB + 43.4 dB = 105 dB S/N = 118 dB + 7.4 dB - 105 dB = 20.4 dB

However, if the 2.2 k J sparker is lowered to 1,500 ft, the bubble period decreases to 1 ms and the fundamental frequency is increased to 1,000 Hz and the wavelength is 3 meter. For the same 1,212 m range, there would be 400 wavelengths rather than 40 wavelengths and the absorption of the fundamental would be much greater, about 400 dB and this is not acceptable. However the spectrum of the 2.2 kJ pulse at 1,500 ft depth is not constrained to just the fundamental. It is very broad and has considerable energy at lower frequencies. As demonstrated below, the low frequency content of the spectrum is adequate to be detected on the surface from 1,500 ft depth.

If the 2.2 k J sparker is placed at 1,800 ft, it will produce a bubble period of 0.9 ms or a fundamental frequency of approximately 1,111 Hz. A worst case calculation uses the spectrum seen in Figure 5 where the low frequency rolls off from the fundamental at approximately 12 dB per octave. This will result in a 50 Hz signal that is 54 db below the peak at the fundamental of 1,111 Hz. The 50 Hz wavelength in rock will be 60 m. A range of 1,212 m will result in a range of 20.2 wavelengths. The Liner[3] absorption for a 20.2 wavelength range is 22 dB.

$$A = e^{-(.25)(20.2)} = e^{-5.05} = 0.0064$$

Absorption in dB = 10 Log 0.0064 = 22 dB

Total Attenuation = Spreading + Absorption + Roll Off = 61.6 + 22 + 54 = 137.6 dB.

Since we had 118 dB +7.4 dB of signal dynamic range to work with, there will be a S/N ratio of 5.4 dB at a range of 1,212 meters.

S/N = 104 dB + 7.4 dB - 137.6 dB = -12.2 dB

Therefore, there will not be adequate signal to detect the 2.2 k J sparker operating at a depth of 1,800 ft on the surface at one-half mile.

However if the horizontal range on the surface is a quarter of a mile and the depth is 1,800 ft, the slant range will be 680.35 m. The Absorption at 50 Hz will be:

$$A = e^{-(.25)(680.35/60)} = e^{-(.25)(11.3)} = e^{-2.8} = 0.05\ 88$$

Absorption in dB = 10 Log 0.05 88 = 12.3 dB

Total Attenuation = Spreading + Absorption + Roll Off = 56.6 + 12.3 + 54 = 122.9 dB.
S/N = 118 db + 7.4 dB - 122.9 dB = 2.5 dB

This indicates that the 2.2 kJ signal transmitted at a depth of 1,800 ft will be detectable at a horizontal surface range of quarter mile. This agrees very well with what was measured at the Devine test site.

A best case calculation assumed the Sound Forge Hamming spectrum was accurate and we got very good detection at 1,800 ft depth at ranges of 4,000 ft. The worst case calculation assumed 12 dB/octave roll off and we still predict detection at 4,000 ft but not as good as the best case.

3.0 CONCLUSIONS

1. These laboratory tests have shown that the sparker performed as theory predicts and validates the model. Therefore, this model can be used to predict the performance in Devine with confidence.
2. These tests show that the 2.2 kJ sparker operating at 200 ft depth will produce sufficient power over a bandwidth of 50 – 1,000 Hz to operate to a range of 4,000 ft or greater.
3. Even though the fundamental frequency is 250 Hz there will be considerable energy produced over a bandwidth of 50 – 1,000 Hz.
4. With the sparker operated at 1,800 ft depth, it will produce sufficient power over a bandwidth of 50 – 1,111 Hz to operate to a horizontal surface range of a quarter mile.
5. Based on these tests, the SWD sparker should perform at the Devine tests extremely well in the shallow 200 ft test whole for surface monitoring out to ranges of 1,212 m and greater.
6. The sparker should also perform extremely well for cross-well logging in the two 1,800 foot deep wells.

4.0 REFERENCES

7. Rayleigh, Lord "On the Pressure Developed in a Liquid During the Collapse of a Spherical Cavity" Phil. Mag. 34, 94-98 (1917).
8. Rolleigh, Richard, Gleeson, Austin and Holly Arthur, "Results of Work on Plasma Sound Source (PSS), GR-AS-90-1, Applied Research Laboratories: University of Texas, Feb 1990.
9. Liner, C. L., Elements of 3D Seismology, 2nd Edition, Penn Well Corp, Tulsa, OK, 2004.

APPENDIX B – HIGH-FREQUENCY SPARKER DEMONSTRATION AT THE UNIVERSITY OF TEXAS SEISMIC TEST SITE DEVINE, TEXAS

Principal Investigator
Robert P. Radtke
Technology International, Inc.

Prepared by:
Robert H. Stokes
Jeffrey Sutherland

Dr. James Musser
ION Geophysical, Inc.

This page intentionally left blank

Table of Contents

List of Figures

List of Tables

EXECUTIVE SUMMARY

An acoustic source developed as part of an Advanced SWD Demonstration System was tested at the University of Texas Devine Test Site. The overall objective of this test program was to demonstrate the potential of the acoustic source as a downhole seismic source in known lithology to a depth of 1,800 feet.

The specific objectives of the Devine well tests were:

1. To successfully demonstrate the operation of the acoustic source to depths of 1,800 ft in a fiberglass-cased wellbore.
2. To demonstrate that the acoustic source produces detectable seismic signals at the surface to distances within ½ mile of the test well.
3. To determine the magnitude of the seismic signals received at the surface when the acoustic source is located at a depth of 1,800 ft and is operated at various energy levels.
4. Using the results obtained above; determine at what energy level the acoustic source must be operated in order to successfully obtain surface seismic information at the field test site at depths to 15,000 ft.
5. To demonstrate the utility of the acoustic source for inter-well seismic operations.
6. To post calculate velocity profiles (VPs) from the seismic data obtained at the surface using I ONS AZIM software.
7. To compare the calculated VPs with previously obtained data and demonstrate the ability to obtain small spatial profiles.
8. To successfully demonstrate the operation of the acoustic source to depths of 1,800 ft in a fiberglass-cased wellbore.
9. Using the results obtained above, determine at what energy level the acoustic source must be operated in order to successfully obtain surface seismic information at depths to 15,000 ft.
10. To demonstrate the utility of the acoustic source for cross-well seismic operations.

Three wells were used for these tests. Wells No. 2 and No. 4 are approximately 363 ft apart and are steel cased to a depth of approximately 400 feet and cased with fiberglass to 3,000 ft. A shallow (150 ft) steel-cased hole next to Well No. 2 was also used. The approach taken in this test program was to begin testing with the acoustic source at the bottom of the shallow well (150± ft), with a hydrophone in deep Well No. 4 at the same depth and proceed to ever increasing depths to 1,800 ft. A single hydrophone was used to collect cross-well data in each formation type present at the Devine Test Site. Two surface seismic arrays were deployed orthogonally out to a distance of ½ mile to receive and record direct transit through and reflected signals from the various formations present.

A total of seven tests were run with the acoustic source in the shallow hole. A single hydrophone was lowered in Well No. 4 to prescribed depths of 80, 110, 622, 1,200, 1,590, and 1,800 ft, roughly in the middle of each layer to record cross-well seismic signals. Each test was repeated eight times.

The original intent was to lower a Z-Seis 10 hydrophone string in Well No. 4 to record the Cross-Well coupling at 10 depths simultaneously, but the 10 hydrophone string was not available.

Therefore a single hydrophone was lowered to discreet depths of 80, 110, 622, 1,200 and 1,590 ft, roughly in the middle of each geological layer. The data that is recorded shows the direct arrival energy from the acoustic source in the shallow well to the hydrophone in Well No. 4. Only limited cross-well data was collected with the acoustic source at the 1,800 ft depth because the tests were terminated during this run due to equipment problems.

The sound velocity of the direct arriving ray was calculated by dividing the slant range distance by the measured seismic travel time. The calculated velocities agree very closely to the archival data furnished by the Bureau of Economic Geology at University of Texas at Austin. The shallow well tests demonstrated that the Z-Seis hydrophone was able to detect the direct path cross-well signal to depths of 1,590 ft This demonstrated the utility of the acoustic source for cross-well seismic operations.

An additional seven tests were conducted with the acoustic source lowered to various depths in Well No. 2. The single hydrophone was lowered to the same depths in Well No. 4, to record cross-well seismic signals. Two orthogonal VectorSeis™ surface arrays recorded the seismic signals received at the surface. Cross-well coupling was measured at the 622 ft depth but was not recorded at the deeper depths. Cross-well coupling worked between the shallow hole and Well No. 4, and was expected to work just as well from Well No. 2. One explanation of why the Cross-Well coupling was not measured at the deeper depths might be due to sound ray refraction, a problem typically occurring by commercial cross-well tomography service.

A detailed analysis of sound ray refraction is presented. It shows that when the acoustic source and a single hydrophone are placed at the same deep depth, it is possible that the signal will not be received. This analysis shows that a very small change in density creates a velocity gradient, which bends the sound ray upward about a radius that can force the horizontal ray to miss the hydrophone. If the 10 hydrophone string, as earlier planned, had been available there may have been a different result, because there would have been hydrophones above and below the acoustic source depth. This was not known at the time, and, consequently, all data was recorded with the hydrophone set at the same depth as the acoustic source.

The ION VectorSeis™ surface sensor data plots showed the VectorSeis™ sensor output on a typical seismic plot on top of the page and the frequency of the received signal from 0– 500 Hz is shown in the data presented at the bottom of the page. Data below 100 Hz is contaminated by noise from the diesel generator operating near the recording trailer. The anti-aliasing filter rolls off above 350 Hz. Therefore, the useful data is in the frequency band from 100–350 Hz. Visual inspection of the frequency response shows that the signal in this area is cleaner (less noise) than data outside this band.

The VectorSeis™ surface sensor data demonstrated that the acoustic source signal could be received from 1,800 ft depths. The horizontal range was limited because the low frequencies (below 100 Hz) were obscured by the diesel power generator noise.

The results of the deep well test with the ION surface array were encouraging. The acoustic source demonstrated that it generated a pulse that could be received with the ION surface array from a depth of 1,800 ft. This verified our calculations that the acoustic source would produce a signal level that could be detected from 1,800 ft depth with the ION surface array.

1.0 INTRODUCTION

An acoustic source developed as part of an Advanced SWD Demonstration System was tested at the University of Texas Devine Seismic Test area, near Hondo, Texas. This site is managed by the Exploration Geophysics Laboratory (EGL), an Industrial Associate Program at the Bureau of Economic Geology of The University of Texas at Austin.

The initial testing of the acoustic source was performed in a laboratory environment. In this laboratory testing, the performance of various acoustic source configurations was measured and the best performing configuration was selected for further testing under realistic downhole conditions.

Testing was conducted by Robert Radtke, Robert Stokes, Jeff Sutherland, TII, with the assistance of Jim Musser, ION Geophysical, Inc., leading the surface seismic monitoring crew, and Jim Minto, Z-Seis, Inc. (now Schlumberger), leading the wireline crew.

2.0 TEST OBJECTIVES

The overall objective of this test program was to demonstrate the potential of the acoustic source as a downhole seismic source in known lithology to a depth of 1,800 ft. The specific objectives of the Devine well tests are as follows:

1. To successfully demonstrate the operation of the acoustic source to depths of 1800 ft in a fiberglass-cased wellbore.
2. To demonstrate that the acoustic source produces detectable seismic signals at the surface to distances within ½ mile of the test well.
3. To determine the magnitude of the seismic signals received at the surface when the acoustic source is located at a depth of 1,800 ft and is operated at various energy levels.
4. Using the results obtained above, determine at what energy level the acoustic source must be operated in order to successfully obtain surface seismic information at the field test site at depths to 15,000 ft.
5. To demonstrate the utility of the acoustic source for inter-well seismic operations.
6. To post calculate velocity profiles (VPs) from the seismic data obtained at the surface using IONs AZIM software.
7. To compare the calculated VPs with previously obtained data and demonstrate the ability to obtain small spatial profiles.

3.0 DESCRIPTION OF DEVINE TEST SITE

The site is managed by the EGL, an Industrial Associate Program at the Bureau of Economic Geology of the University of Texas at Austin.

3.1 Devine Location

The 100-acre Devine Test Site (DTS) is located less than 50 miles southwest of San Antonio, Texas, in Medina County, Texas (Figures 1 and 2, below). The test site is used for surface-based seismic and potential-field experiments performed in conjunction with downhole and cross-well experiments.

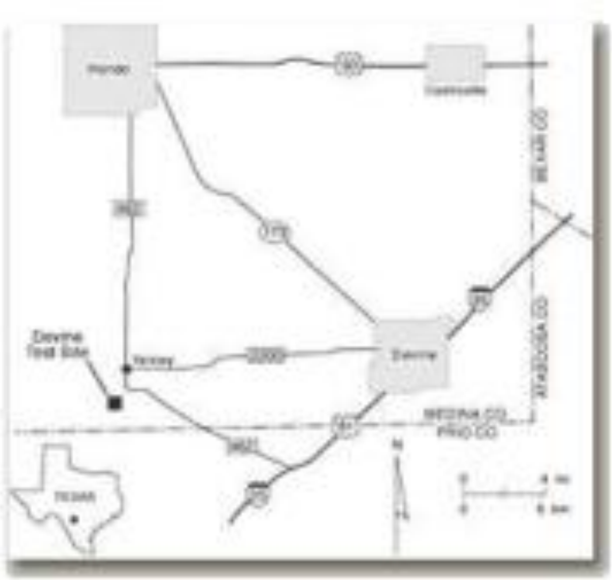

Figure 1 – Location of Devine Test Site in Medina County

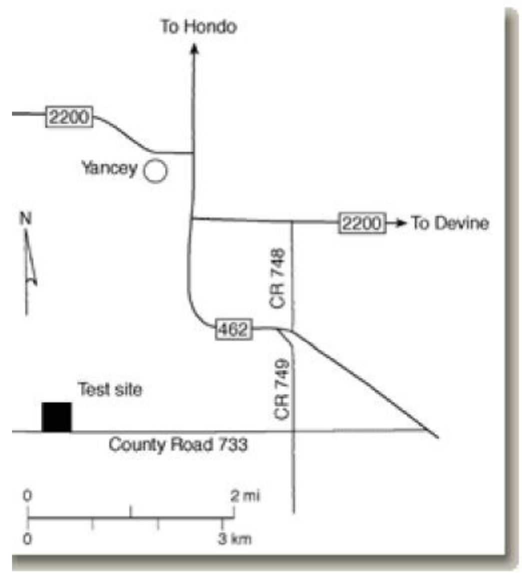

Figure 2 – Local Map of Devine Area

3.2 Test Site and Available Test Wells

The size and shape of the 100-acre field laboratory and the adjacent area for which surface-access rights can be negotiated with property owners is shown in Figure 3. Figure 4 shows the relative locations of the 3 test wells (2, 4, and 9) which are cased with 5½ in casing to 3,000 ft. Wells No. 2 and No. 4 are completed with fiberglass casing. Four shallow (100 – 200 ft) steel-cased holes are available for borehole-based seismic energy sources and other instrumentation. The site has electricity, flood lights for nighttime use, a water well and water lines, and storage sheds.

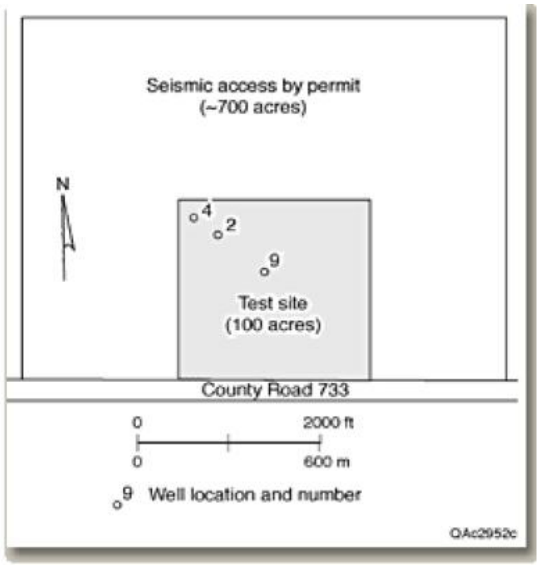

Figure 3 – Test Area and Deep Boreholes

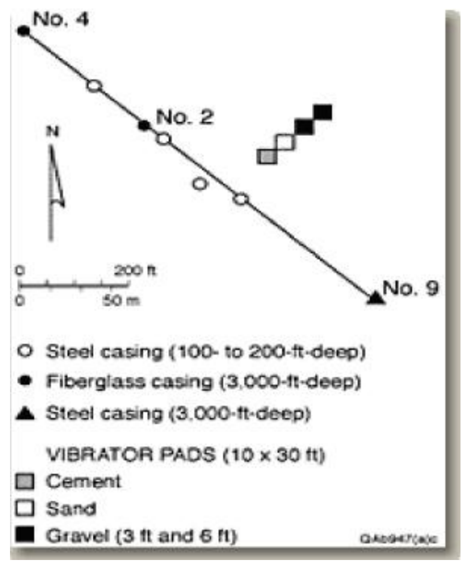

Figure 4 – Detail of Deep and Auxiliary Boreholes

The test wells to be employed in this test program are shown in Figures 5 through 8.

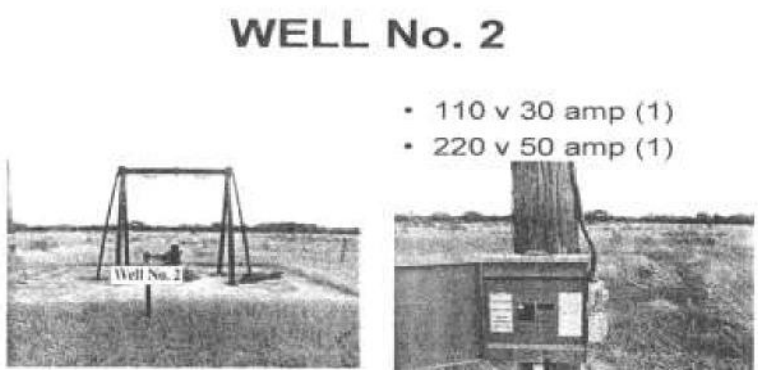

Figure 5 – Devine Well No. 2

Figure 6 – Devine Well No. 2 Wellhead

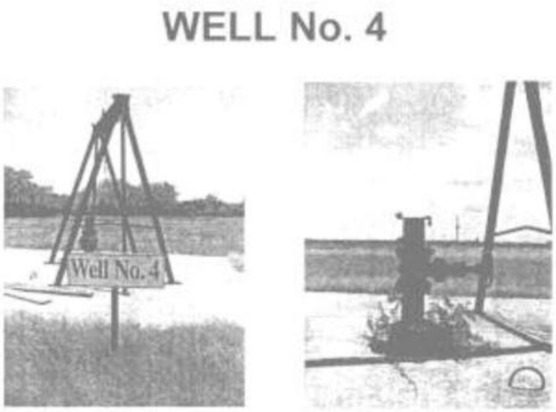

Figure 7 – Devine Well No. 4

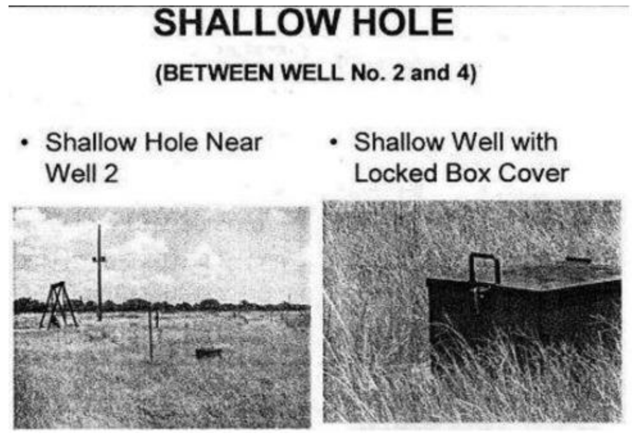

Figure 8 – Devine Shallow Hole Near Well No. 2

3.3 Stratigraphy for Test Wells

The stratigraphic section breached by the site's 3,000 ft wells is shown in Figure 9. A key attribute of the site is its stable geologic condition. The nearest oil and gas production is several miles away, which ensures that no fluid-exchange processes are occurring in rock faces immediately around the wellbores. Petrophysical properties of the formations; therefore, are well calibrated by numerous historical well logs preserved in the public database.

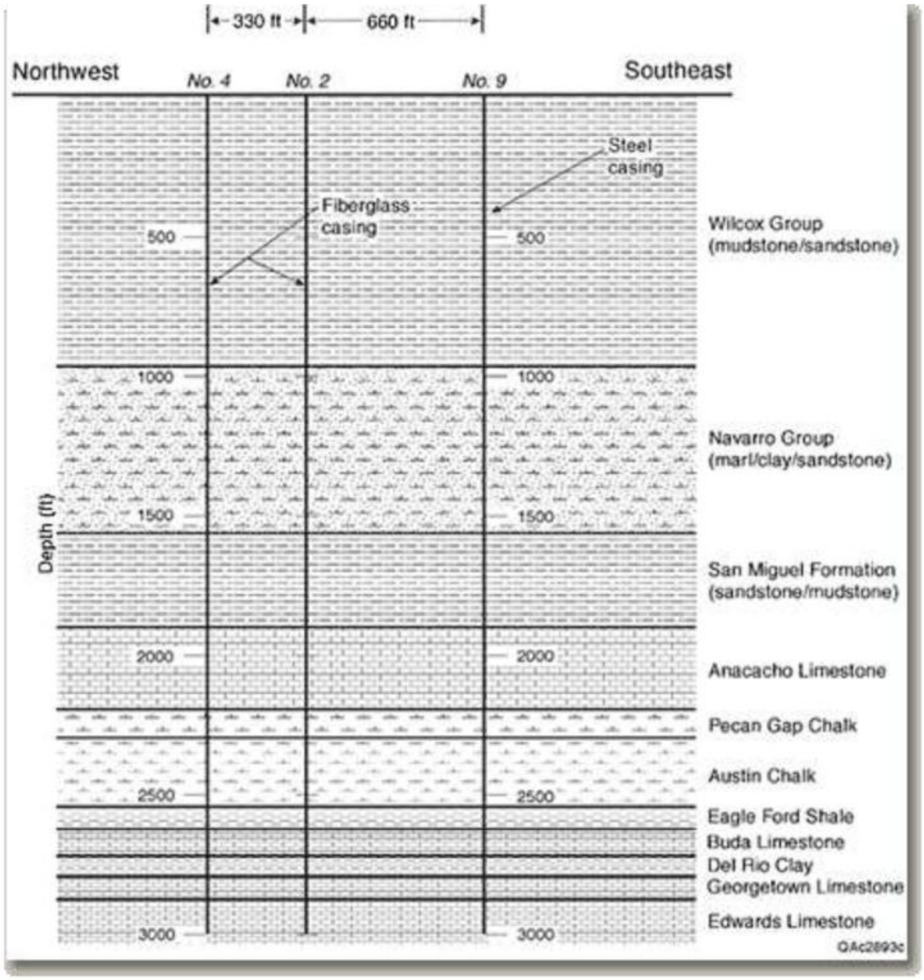

Figure 9 – Formations and Rock Types at Devine

3.4 Available Test Site Formation Data

There are records of experimental data recorded in test wells by British Petroleum during its 12 years of ownership of the DTS. This information is available for review and copy at the EGL public-access data room at the Bureau's headquarters in Austin, Texas. This data will be used to compare with the acoustic source data obtained during these tests.

4.0 TEST REQUIREMENTS

1. Access to Wells No. 2, No. 4 and shallow, steel-cased hole adjacent to Well No. 2.
2. Access to surface locations needed for deploying the seismic array.
3. A high-voltage and high-current cable that can supply power to the acoustic source.
4. Acoustic source hardware consisting of:
   a. Acoustic source in configuration to be tested.
   b. Steel housing for acoustic source and required downhole electronics.
   c. Downhole electronics package.

5. Surface seismic arrays and associated recording and processing equipment.
6. A hydrophone for use in Well No. 4.
7. Communication equipment for members of test team.
8. Test procedures and check lists.

5.0 SUMMARY OF TEST STRATEGY

The approach taken in this test program was to begin testing at a shallow depth (150± feet), and proceed to ever-increasing depths to 1,800 ft. A single hydrophone was used to collect Cross-Well data in each formation type present at the DTS. Two surface seismic arrays were deployed orthogonally out to a distance of ½ mile to receive and record direct transit through and reflected signals from the various formations present. Post-well analysis will be used to calculate formation velocity profiles and compare them to historical information.

5.1 Location of Signal Sources and Receivers

1. The acoustic source was initially to be tested at the bottom (150± ft) of the Shallow Hole near Well No.2, but due to debris in the hole the depth was limited to 80 ft.
2. The acoustic source was placed at various depths in Well No. 2 per the list below:
    a. 80 ft in the Wilcox formation
    b. 622 ft in the Wilcox formation
    c. 1,200 ft in the Navarro formation
    d. 1,590 ft in the San Miguel Formation
    e. 1,800 ft in the San Miguel Formation
3. A single hydrophone was placed at various depths in Well No.4, as shown in Table 1.
4. VectorSeis™ surface arrays were deployed at Well No. 2, as shown in Figure 10.

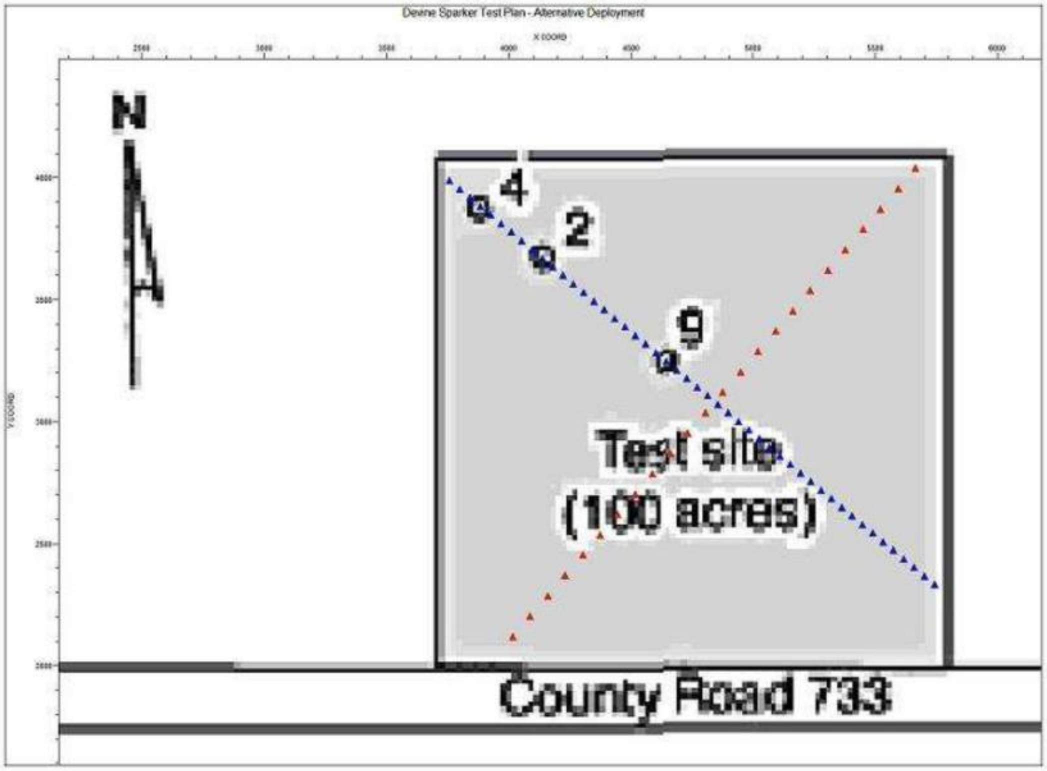

Figure 10 – Schematic of Seismic Surface Array to be Deployed by ION

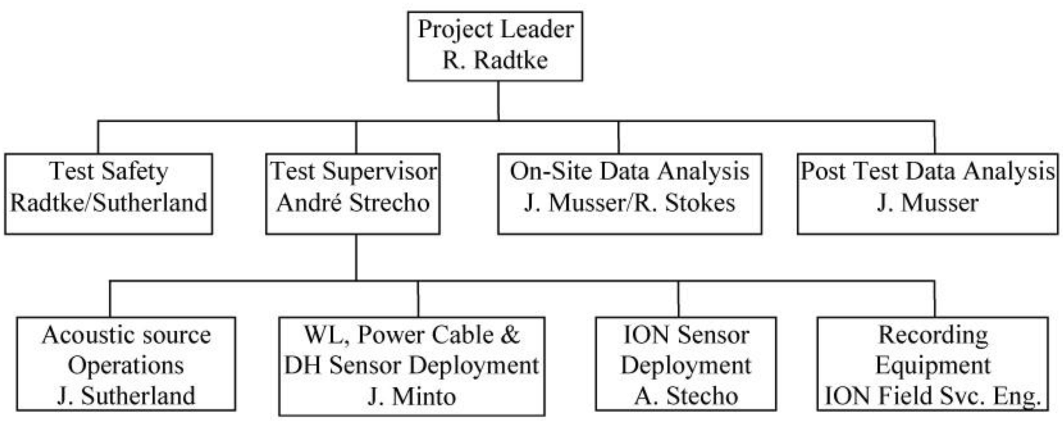

Figure 11 – Organization Chart for Devine Testing

5.2 Description of Downhole and Surface Support Equipment

5.*2.1* *Well Test System*

A Z-Seis Wireline Truck suspended a hydrophone at prescribed depths to 1,800 ft. The wireline truck also contained recording equipment for 75 ION VectorSeis™ surface sensors and the Z-SEIS downhole Hydrophone. The VectorSeis™ sensors were located both laterally and perpendicular to Well No. 2, and up to ½ mile away. Well No. 2 is located 363 ft southeast of Well No. 4. A Z-Seis Wireline Truck suspended the first TII Acoustic source at various depths to

1,800 ft. A hand lowered nylon line was used to suspend a second Acoustic source at 80 feet in the steel cased (100 to 200 ft deep) hole located next to Well No. 2. A TII RV was located near the wireline truck and contained the power supply to operate each Acoustic source.

5.2.2 Acoustic Source Configurations

Two Acoustic source configurations were tested based on the Laboratory Test Program. In Well No. 2, the Acoustic source had a 45-degree conical reflector to simulate the bottom of the hole. In the Shallow Hole, the acoustic source housing had a 3 in standoff to hold it up from the bottom of the hole.

Figure 12 – Photograph of Acoustic Source

6.0 SUMMARY TABLE OF TESTS AND DATA TO BE RECORDED

A total of seven tests were run with the Acoustic source in the shallow hole adjacent to Well No. 2. A single hydrophone was lowered in Well No. 4 to prescribed depths to record Cross-Well seismic signals. An additional 7 tests were conducted with the Acoustic source at various depths in Well No. 2. A single hydrophone to record cross-well seismic signals was positioned in Well No. 4 at the same depths as the Acoustic source in Well No. 2. Two orthogonal VectorSeis™ surface arrays recorded the seismic signals received at the surface. The Acoustic source was tested at two levels of input power in the shallow hole and at 80 and 622 ft in Well No. 2. For tests at 1,200, 1,590 and 1,800 ft in Well No. 2, the acoustic source was tested only at one power level. Each test was repeated eight times. The schedule of tests and data to be recorded are shown in Table 2. The test numbers shown in this table was used to mark the data recordings for correlation with test conditions.

7.0 DATA PROCESSING BY ION GEOPHYSICAL, INC.

Post-test analysis was conducted by ION. They will convert the VectorSeis™ data to formation velocity profiles and will compare to previously obtained results at Devine.

8.0 REPORT OF TEST RESULTS

Table 1 – Schedule of Acoustic Source Tests and Data to be Recorded

TESTS					DATA TO BE RECORDED		
No.	Power Level	Test Repetitions	Well Location	Depth (feet)	Hydrophones Location	Depth of Hydrophone (feet)	VectorSeis Stations
1	X	8	Shallow Hole*	150± (TBD)	Well No. 4	150± (TBD)	All 72
2	2X	8	" " "	" " "	" " "	" " "	" " "
3	X	8	Shallow Hole	150± (TBD)	Well No. 4	622	All 72
4	2X	8	" " "	" " "	" " "	" " "	" " "
5	2X	8	Shallow Hole*	150± (TBD)	Well No. 4	1200	All 72
6	2X	8	Shallow Hole	150± (TBD)	Well No. 4	1590	All 72
7	2X	8	Shallow Hole*	150± (TBD)	Well No. 4	1800	All 72
8	X	8	Well No. 2	150± (TBD)	Well No. 4	150± (TBD)	All 72
9	2X	8	" " "	" " "	" " "	" " "	" " "
10	X	8	Well No. 2	622	Well No. 4	622	All 72
11	2X	8	" " "	" " "	" " "	" " "	" " "
12	2X	8	Well No. 2	1200	Well No. 4	1200	All 72

8.1 Shallow Well Test (Tests #1 – #7)

The steel-encased shallow well adjacent to Well No. 2 was used for this test. The acoustic source was tested in a five gallon bucket of fresh water prior to deploying the acoustic source in the shallow well, and it appeared to be working properly. The acoustic source was lowered into the shallow hole by hand with the RG-8 coaxial cable taped to a nylon line. This shallow hole is approximately 150 ft deep; however, it was found to be full of rust and debris up to a depth of about 115 ft. Because of this debris, the depth of the acoustic source was set to 110 ft. The acoustic source worked as expected at the 110 ft depth for the Test #1. There was a significant "bang" at the top of the well hole when the acoustic source transmitted. When trying to run test #2 it was discovered that the acoustic source would not transmit. The problem was identified and the equipment repaired.

The acoustic source was then set to a depth of 80 ft to get more spacing between the acoustic source and the debris and the system appeared to be working properly. Data test #2 – #6 were completed with the system working properly. When test #7 was conducted, the same short circuit problem with the power supply was discovered after one transmission. The acoustic source was raised and it was covered with rust particles that apparently were shorting out the acoustic source electrodes. The shallow well tests were then terminated.

During these tests, surface seismic data was recorded by ION Geophysical, Inc. and Cross-Well acoustic data was recorded by Z-Seis.

8.2 Cross-Well Coupling from Shallow Well (Tests #1–#7)

The original intent entailed lowering a Z-Seis ten hydrophone string in well No. 4 to record the Cross-Well coupling, but the 10 hydrophone string was not available. Therefore a single hydrophone was lowered to different depths as shown in the test matrix to be roughly in the middle of each layer when the acoustic source was fired. The original intent of the shallow well test was to place the acoustic source four in above the bottom of the hole so that there was good acoustic coupling into the rock bottom. However, the large amounts of debris in the hole prevented placing the acoustic source at this depth and most of the data was recorded with the acoustic source operating at 80 ft depth, but one set of data was recorded at 110 ft. Therefore, the large amount of separation between the bottom of the hole and the debris in the hole reduced the vertical coupling into the rock layer. At this 80 ft depth the acoustic source was inside the steel casing; therefore, much of the acoustic energy would have been attenuate as it was transmitted horizontally into the rock formation. Also, Well No. 4 is steel cased to a depth of approximately 400 ft which would have further reduced any Cross-Well data above 400 ft during test runs #3–#7 the Z-Seis hydrophone was set to a depth below the steel casing and better acoustic conditions were present.

8.3 Shallow Well Data Analysis

The single Z-Seis hydrophone data is shown in Appendix Ba. The data presented shows the Z-Seis hydrophone output on the left side of the page in files 1,000–1,073 with the hydrophone at various depths. The data that is encircled shows the direct arrival energy from the acoustic source in the shallow well to the hydrophone in Well No. 4 about 363 ft away. These figures show the energy detected by the Z-Seis hydrophone at various depths of 80, 110, 622, 1,200, and 1,590 ft with various frequency bands. In all but the 110 ft, data the acoustic source was at 80 ft depth in the shallow well. No data was collected from the 1,800 ft depth because the tests were terminated after Run #7. The sound velocity of the direct arriving ray was calculated by dividing the slant range distance by the measured seismic travel time.

As stated earlier, the acoustic source was placed inside the water filled steel casing at 80 ft depth. The bottom of the hole was at 150 ft. The steel casing acted as a funnel to couple the sound produced at 80 ft to the rock bottom at 150 ft. This 70 ft distance through the water would require approximately 14.7 msec.

The velocities shown in the figures of Appendix Ba varied from 1,457 ft/sec for the shallow depth to 3,045 ft/sec for the 1,590 ft depth. This is obviously a too low velocity for the sandstone in this area. An investigation of archival data at the Bureau of Economic Geology at University of Texas at Austin produced velocity-depth profiles as shown in Figure 13. The previously measured velocity varied from 6,000 ft/sec at shallow depth to 14,000 ft/sec at 2,000 ft depth. Based on these velocities there apparently was a 200 msec delay in all of the recordings and when this delay is factored into the velocity calculations the new velocity calculations agree very closely to the archived data as shown in Table 2.

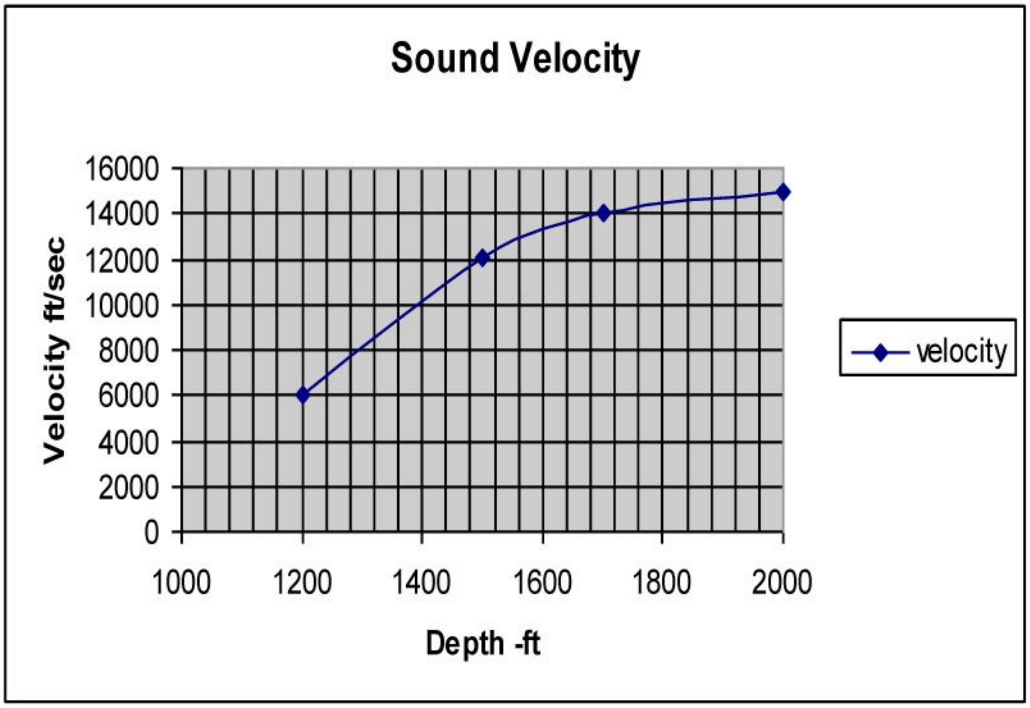

Figure 13 – Velocity-Depth Profile

Table 2 – Direct Arrival Velocity Calculation

Hydrophone Depth	Direct Path	Z-Seis Measured Travel Time	Calculated Travel Time	Corrected Travel Time	% Difference
80 ft	363 ft	200 msec.	51.8 msec.	251 msec	25 %
110	363	240	52	252	13
622	595	280	85.1	285	1.8
1,200	1,105	385	165	365	5.2
1,590	1,475	500	213	413	17

8.4 Cross-Well Coupling from Deep Well No. 2 (Tests #8–#14)

A second acoustic source was connected to two 2,000 ft high voltage, high current cables. Prior to lowering the acoustic source into Well No. 2, it was tested in a five gallon bucket of fresh water. It was noted that the acoustic source fired as expected and there was a ring of bubbles rising to the surface around the canister. This verified that the 45° cone was working as designed and deflected the acoustic source energy out horizontally and evenly around the cone. The acoustic source was then lowered into Well No. 2. The two cables were rolled off the two spools and taped together and then taped to the wire line deployed by Z-Seis. Test #8 at 1,200 J power was conducted using an 80 ft depth rather than 150 ft, to be consistent with the depth used in the shallow well tests. There was an audible sound out of the well when the acoustic source transmitted but it was not as loud as the shallow well. This was possibly due to the increased loss down the 2,000 ft cable. The Z-Seis hydrophone was lowered in Well No. 4 to the same depth as the acoustic source in Well No. 2.

As can be seen in the figures in Appendix Ba, cross-well coupling was measured at the 622 ft depth but not seen at the deeper depths. Calculations of the expected signal levels at the Z-Seis hydrophone are very high and should have been easily detected. One explanation of why the Cross-Well coupling cannot be measured at the deeper depths might be due to sound ray refraction.

8.5 Sound Ray Refraction

Figure 14 below shows how the acoustic rays from the acoustic source reflect off of the 45-degree cone horizontally into the rock layer. As seen from the velocity depth data in Figure 13, the sound velocity increases linearly as depth increases from 6,000 ft/sec at 1,200 ft to 12,000 ft/sec at 1,500 ft. Urick[1] has shown that in a medium in which the velocity of sound changes linearly with depth, the sound rays can be shown to refract, or bend, in arcs of circles.

The radius of curvature is given by:

R = C0 /g where C0 = velocity at the depth of source ft/sec
g = sound velocity gradient (ft/sec)/ft

If the hydrophone is initially placed at the same depth as the acoustic source, the sound rays from the acoustic source will all be refracted or bent upward and the hydrophone will receive less signal strength than if the rays were not bent.

As an example, most of the rock formations at Devine are sandstone, and the speed of sound in this sandstone at 1,200 ft is 6,000 ft/sec and at 1,500 ft the velocity is 12,000 ft/sec.

The sound velocity gradient calculated from the velocity data in Figure 13 is:

g = Change in velocity / Change in depth = (12,000 – 6,000) / (1,500 – 1,200) = 6,000 ft/sec / 300 ft= 20 /sec

The radius of curvature of the horizontal ray is calculated as:

R = C0 /g = (6,000 ft/sec)
/ (20 /sec) R = 300 ft

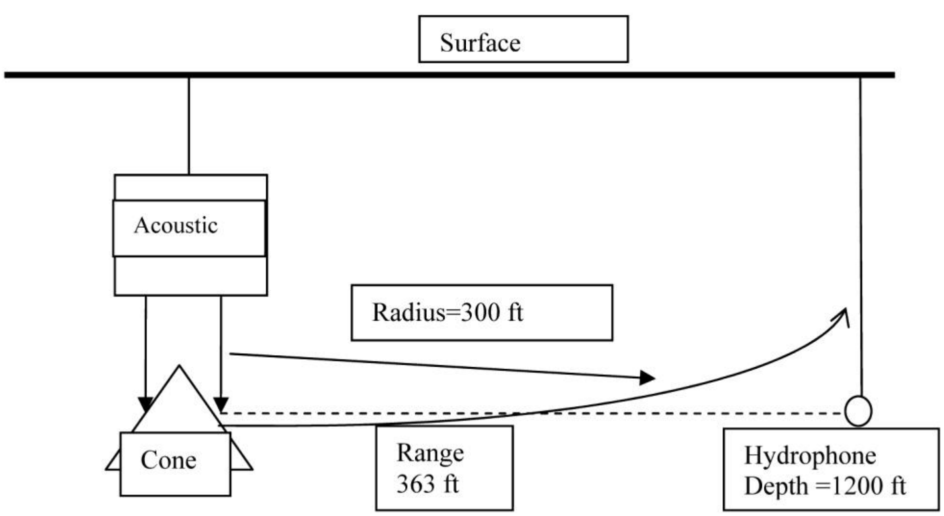

Figure 14 – Ray Bending of Horizontal Ray

Of course there are many other rays than the one shown in Figure 14, but the conical reflector also reflects them horizontally and they will all have the same upward bending radius. This might explain why there was very little signal detected at the hydrophone when it was put at the same depth as the acoustic source for the deeper depths. If the 10 hydrophone string, as earlier planned, had been available there may have been a different result because there would have been hydrophones above and below the acoustic source depth. If the hydrophone had been placed at a depth of 1,100 ft rather than 1,200 ft the refracted ray may have been received. This was not known at the time and consequently all data was recorded with the hydrophone set at the same depth as the acoustic source.

This cross-well problem is analogous to a common sonar problem known as the "Afternoon Effect." If sonar operating near the surface is trying to detect a surface target, there is usually no problem until the afternoon sun heats up the surface a few degrees and then all the acoustic rays are bent downward and targets that are easily detected in the morning cannot be detected in the afternoon. If the target goes to a slightly deeper depth, then it again becomes detectable.

8.6 Z-Seis Hydrophone Calculations

The range from Well No. 2 to the Z-Seis hydrophone at Well No. 4 was 115 m.

The acoustic source and hydrophone were placed at the same depth within each rock formation. The depths used were 80, 622, 1,200, 1,590 and 1,800 ft.

From Liner[2] the approximate absorption in rock is:

A = e-(0.25) R where R = the range in wavelengths

Note: Assuming the average speed of sound in the rock at Devine is 2,400 m/s

Table 3 lists the calculated bubble period, fundamental frequency, wavelength, range in wavelengths, and the exponent:

Table 3 – The Effect of Depth on Bubble Period, Fundamental Frequency, Wave Length, and Range in Wave Length

Depth	Period	Fund. Freq.	Bubble Diameter	Wavelength	Slant Range (w l)	(0.25)R
80 ft	8 ms	125 Hz	4.8 in	24 m	5.9	1.5
622	2	500	1.2	6	23.9	5.9
1,200	1.2	833	0.65	3.6	39.6	9.9
1,590	1.0	1,000	0.6	2.4	47.9	11.9
1,800	0.9	1,111	0.54	2.1	54.7	13.7

The transmitted signal is a very broad band signal centered on the fundamental frequency. The signal level rolls off in amplitude 12 dB per octave below the fundamental frequency and six dB per octave above the fundamental frequency. There are also multiple peaks in the amplitude at higher harmonic frequencies. For example, at a depth of 622 ft the bandwidth of the signal in the major band would be from 25–1,000 Hz with additional signals at higher harmonics.

Table 4 – The Effect of Depth on the Absorption

Depth	$e^{-(.25)R}$	Absorption=10 Log
80 ft	0.22	-6.6 dB
622	0.0027	-25.7
1200	0.00005	-43.0
1590	0.0000068	-51.5
1800	0.0000011	-59.6

The calculated signal level at the Z-Seis hydrophone is:

Signal = Transmit Level - Absorption - Attenuation – Spreading Loss

We know from laboratory tests that for 3000 J the Transmit Level = 260 dB ref 1µPa

Spherical Spreading Loss = 20 Log 115 = 41.2 dB

Table 5 – The Effect of Depth on Absorption, Spreading Loss, and Total Attenuation

Depth	Absorption	Spreading Loss	Total Attenuation	Signal at hydro.
80 feet	6.6 dB	41.2 dB	47.8 dB	212.2dBref 1µPa
622	25.7	41.2	66.9	193.1
1,200	43.0	41.2	84.2	175.8
1,590	51.5	41.2	92.9	167.1
1,800	59.6	41.2	100.8	159.2

Notes: The Z-Seis hydrophone has a sensitivity of -179 d BV /µPa, and the Voltage out of the hydrophone = Signal at hydrophone – 179 d BV.

Table 6 – The Effect of Depth on Signal at Hydrophone and Voltage

Depth	Signal at Hydro	V out	Volts
80 feet	212.2 dB ref 1µPa	33.2 d BV	46 Volts
622	193.1	14.1	5.0
1,200	175.8	-3.2	0.7
1,590	167.1	-11.9	0.25
1,800	159.2	-19.8	0.1

As seen from these calculations, the voltage out of the hydrophone has a very high range from 0.1 V to 46 V. This does not include the 83 dB of gain in the preamp. Even the worst case where the fundamental frequency is 1,111 Hz, there is + 159.2 dB ref 1µPa at the Z-Seis hydrophone and it is probably clipping. Z-Seis says that their hydrophone is set to handle over voltage and just clips the signal so they do not think that is a problem.

These calculations were for the fundamental frequency only. As stated earlier the transmitted signal is very broad band and there is significant energy at lower frequencies, which would have had less attenuation. As seen in the data in Appendix Ba, the frequency bands from 100 Hz to 300 Hz detected signals from the shallow well. Any signals below 100 Hz were masked by the 60 Hz diesel generator operating on site.

8.7 Deep Well VectorSeis™ Recording at the Surface

The second acoustic source was connected to the two 2,000 ft high voltage, high current cables. Prior to lowering the acoustic source into Well No. 2, it was tested in a five gallon bucket of fresh water. It was noted that the acoustic source fired as expected but that there was a ring of bubbles coming to the surface around the canister. This verified that the 45° cone was working as designed and deflected the acoustic source energy out horizontally and evenly around the cone. The acoustic source was lowered by hand into Well No. 2. The two cables were rolled off the two spools and taped together and then taped to the wire line deployed by Z-Seis. Tests #8 and #9 at 1,200 J and 3,000 J power were completed using an 80 ft depth rather than 150 ft, to be consistent with the depth used in the shallow well. There was an audible sound out of the well when the acoustic source transmitted but it was not as loud as the shallow well. In both tests the ION surface seismic sensors and the Z-Seis hydrophone data were received. There was some problem with synchronizing the acoustic source transmission with the start of the ION recording but this was worked out with a simple radio link to give ION a “ready”-“set”-“fire” command. ION would then turn on their receiver to start recording data.

The acoustic source was then attempted to be lowered to 622 ft for Test #10. This worked smoothly until the acoustic source hung up in the hole at a depth of 400 ft. The acoustic source was raised and lowered several times with the hopes it would untangle itself, but it would still hang up at 400 ft. The acoustic source was then recovered and the cables rolled back up on the reels. Inspection of the acoustic source did not provide any clues as to why it was hanging. The acoustic source from the shallow well test along with a heavy weight was attached to the wire line and lowered to 400 ft. There was a momentary stall at 400 ft but the weight and acoustic source passed this depth without hanging up. There was a clanking sound when the acoustic source passed by the obstruction as if some concrete broke off and fell down the hole. It was assumed that was where the fiberglass and steel casings met and some of the concrete had leaked into the hole.

After this, the 45° cone acoustic source and the two power cables were lowered into Well No. 2 with no problem. The interval of taping the cables to the wire line was increased from every 100 ft to every 25 ft to minimize any slack cable that might hang up on whatever might be left of the original obstruction.

Tests #10, #11 and #12 showed large electrical noise interference on the ION VectorSeis™ data. Radiation from the reel of high power cable connecting the acoustic source apparently was causing the interference. The ION VectorSeis™ sensors inter-connect cables, which were lying along the ground near Well No. 2, were moved to a greater distance from Well No. 2 and the noise level was reduced to levels that did not interfere with the data recording. However, the background noise level for all the data was high due to the diesel power generator in the vicinity of the data collection trailer. Test #10 was repeated and Tests #11, #12, #13 and #14 were completed with acceptable noise levels. After the tests were completed, the equipment was removed and shipped back to Houston, Texas.

8.8 Deep Well VectorSeis™ Data Analysis

The ION VectorSeis™ surface data is shown in Appendix Bb. The data plots presented show the VectorSeis™ sensor output on the top of the page. The frequency of the received signal from 0 to 500 Hz is shown in the data presented at the bottom of the page. Data below 100 Hz is contaminated with the 60 Hz noise from the diesel generator operating near the recording trailer. The anti-aliasing filter rolls off above 350 Hz. Therefore, the useful data is in the frequency band from 100 to 350 Hz. Visual inspection of the frequency response shows that the signal in this area is cleaner (less noise) than data outside this band.

The acoustic source produces a bubble when it fires and the expansion and collapse of the bubble produces a broad band acoustic signal that is centered at a fundamental frequency of 1/T of the bubble period. As the acoustic source operates at deeper depths the higher ambient pressure causes the bubble period to be shorter and consequently the fundamental frequency to be higher. Even though the fundamental frequency becomes 1,000 Hz or higher at deep depths, there is still considerable energy at the low frequency part of the spectrum, which allows seismic detection from the 1,800 ft depth. Table 7 shows the fundamental frequency of the 3,000 J acoustic source for the different operating depths.

Table 7 – Fundamental Frequency vs. Depth

Depth	Power Level	Fundamental Frequency
80 ft	3,000 J	111 Hz
622	3,000	500
1,200	3,000	666
1,590	3,000	1,000
1,800	3,000	1,428

The surface data demonstrated that the acoustic source signal could be received from 1,800 ft depths. The range was limited because the low frequencies needed to achieve long range were obscured by the diesel power generator noise.

9.0 OVERALL SUMMARY AND CONCLUSIONS

The shallow well tests were modified because of the debris in the hole and the acoustic source could not be placed at the bottom of the hole where it would have good coupling with the rock formation. The acoustic source was set at a depth of 80 ft, which was inside the steel casing and about 70 feet above the bottom of the hole. This was not optimum positioning for Cross-Well coupling but that that was all that was possible due to the circumstances.

The Z-Seis hydrophone was able to detect the direct path Cross-Well signal to depths of 1,590 ft with the acoustic source operating at 80 ft. The 1,800 ft test was not performed due to equipment problems. The ION VectorSeis™ surface receivers were able to record surface data from the shallow hole tests with the acoustic source operating at 80 ft.

The Cross-Well test did not work very well from the deep well where the hydrophone was placed at the same depth as the acoustic source. Only for Test Run #10 at 622 ft depth did the Z-Seis hydrophone detect a signal from the deep hole. The 622 ft depth was in the upper layer where the velocity-depth profile was constant and there was little or no ray bending. Also at 622 ft, both the acoustic source and hydrophone were below the steel casing and the acoustic source signal could get better horizontal coupling into the rock layer. The calculation of Cross-Well coupling shows that there should have been sufficient signal level at the Z-Seis hydrophone to be easily detected. One explanation for the poor Cross-Well performance was upward ray bending and the Z-Seis hydrophone was not at the proper depth to receive any significant signal. If the 10 hydrophone string had been available, as originally planned, the hydrophones would have been at depths above and below the acoustic source depth and probably would have been able to detect the signal.

The results of the deep well test with the ION surface array were much more encouraging. The acoustic source demonstrated that it could generate a pulse that could be received with the ION surface array from a depth of 1,800 ft. Previous calculations showed that the acoustic source would produce a signal level that could be detected from 1,800 ft depth with the ION surface array and this was verified. The ION surface array was able to detect signals from 1,800 ft depths even though there was high background noise that limited the performance at the low frequencies.

10.0 REFERENCES

1. Urick, Robert J., Principles of Underwater Sound for Engineers, p119, McGraw-Hill, 1967.
2. Liner, C. L., Elements of 3D Seismology, 2nd Edition, Penn Well Corp, Tulsa, OK, 2004.

APPENDIX Ba – SINGLE Z-SEIS HYDROPHONE DATA

The data presented in Appendix Ba are from the slide presentation of Dr. James Musser, ION Geophysical, Inc., of his analysis of the Devine test data.

SLIDE NO. 1

Single ZSeis Hydrophone in Adjacent Well

- The following records show the single ZSeis hydrophone record for all test shots.
  - These traces are recorded with a sampling interval of 0.125 ms and an anti-aliasing filter of about 3000 hertz.
- The hydrophone well is located about 363 feet from the source well.
- Files 1000-1073 were recorded with the source in the shallow well and the hydrophone at various depths.
  - Files 1069-1073 are invalid due to source misfires.
- Files 1074-1169 were recorded with the source at various depths in the deep well and the hydrophone at the corresponding depths in the hydrophone well.
- Different frequency bands up to 1000 hertz are shown to illustrate the bandwidth of the downhole source.
- Coherent source energy with frequencies above about 400 hertz are not observed.

SLIDE NO. 2

Single ZSeis Hydrophone in Adjacent Well

- The ellipses in the preceding and following slides indicate the direct arrival energy from the sparker source to the hydrophone in the adjacent well.
- The hydrophone well is located about 363 feet from the source well.
- The direct arrival velocity for the seismic waves propagating from the source to the hydrophone can be determined simply from the source-to-receiver slant range distance divided by the seismic travel time.
- These velocities are shown in the preceding slides.
- It is interesting to note that not all arrivals are observed for the various frequency bands.

SLIDE NO. 3

Single Hydrophone Data for All Tests – 5-10-300-350 hz

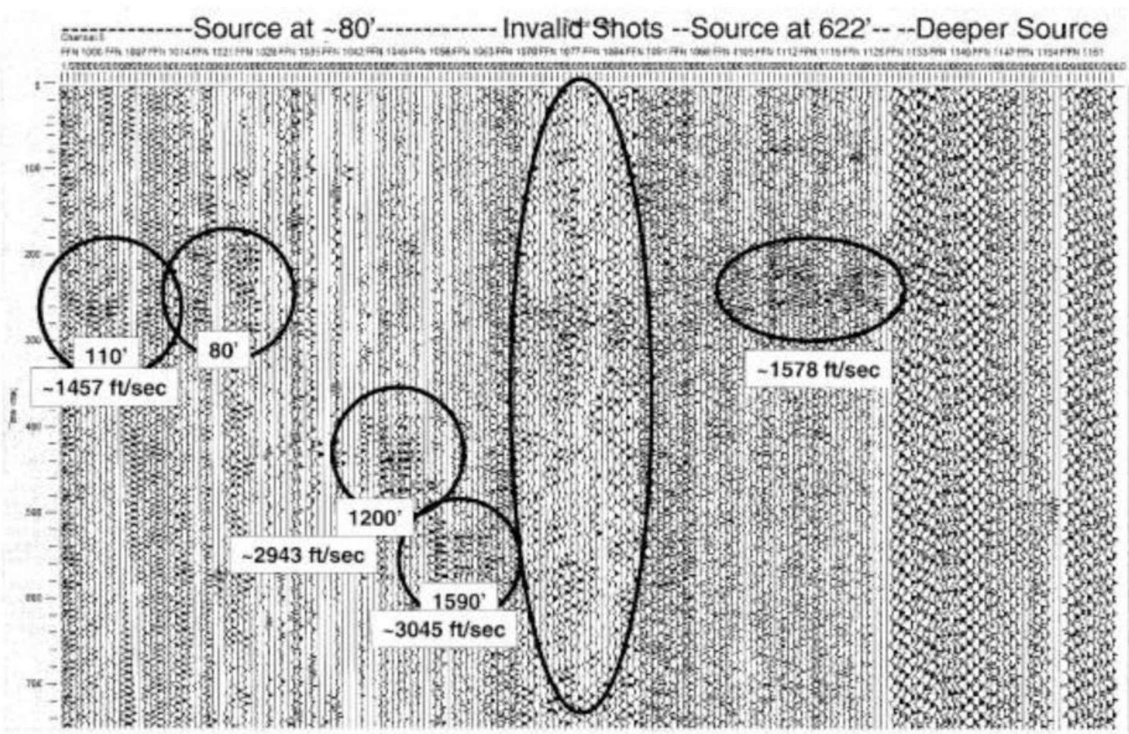

SLIDE NO. 4

Single Hydrophone Data for All Tests – 5-10-100-120 hz

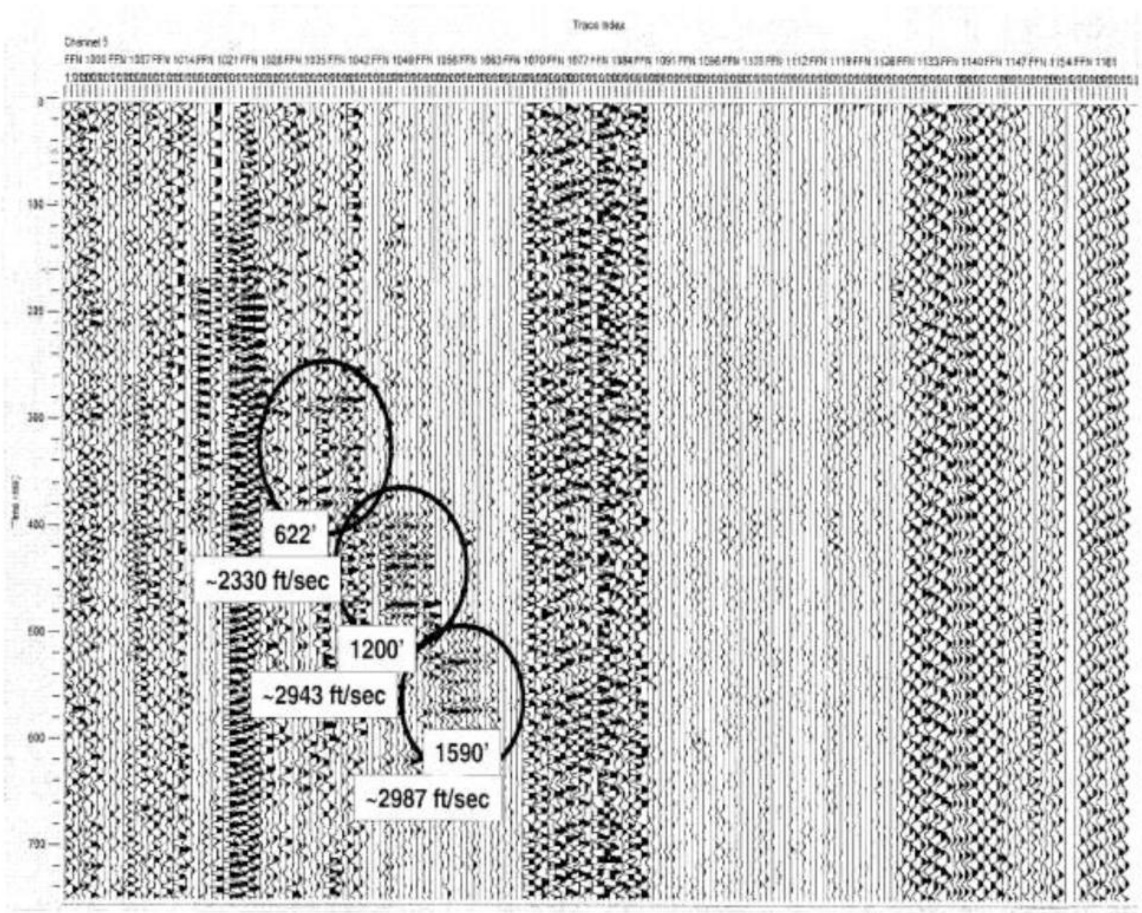

SLIDE NO. 5

Single Hydrophone Data for All Tests – 80-100-200-220 hz

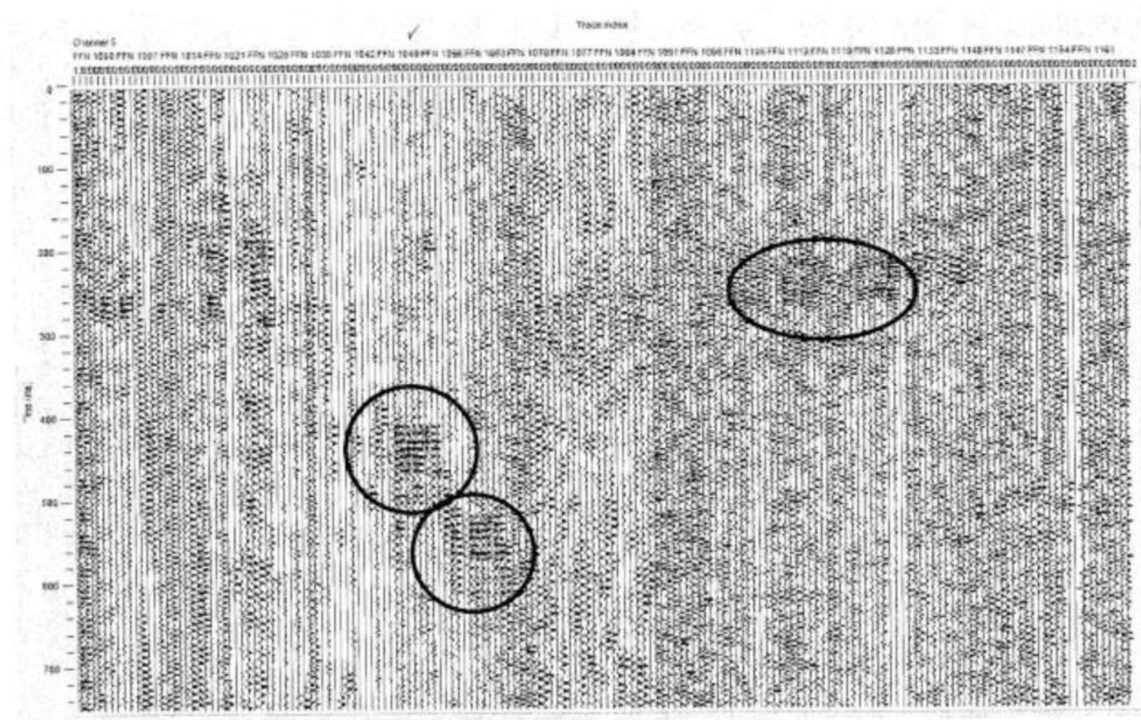

SLIDE NO. 6

VectorSeis Records at Surface

- The following records show the vertical component of the VectorSeis accelerometer records and corresponding spectra for summed and selected test shots.
  - These traces are recorded with a sampling interval of 1 ms and an anti-aliasing filter of 375 hertz.
- The primary VectorSeis line runs between and beyond hydrophone and source wells with 48 stations on 55' spacings for a total length of ½ mile.
- The secondary VectorSeis line is perpendicular to the primary line crossing at a distance of about 950' from the source well (at channel #87).
- Coherent seismic energy was not observed on the secondary cross-line at a distance of ~950' feet from the source well.

APPENDIX Bb – SURFACE SEISMIC RECORDINGS

SLIDE NO. 1

1.2 kJ Source at 80' in Deep Well

Spectrum for Nearest Offset Trace – Vertical Component

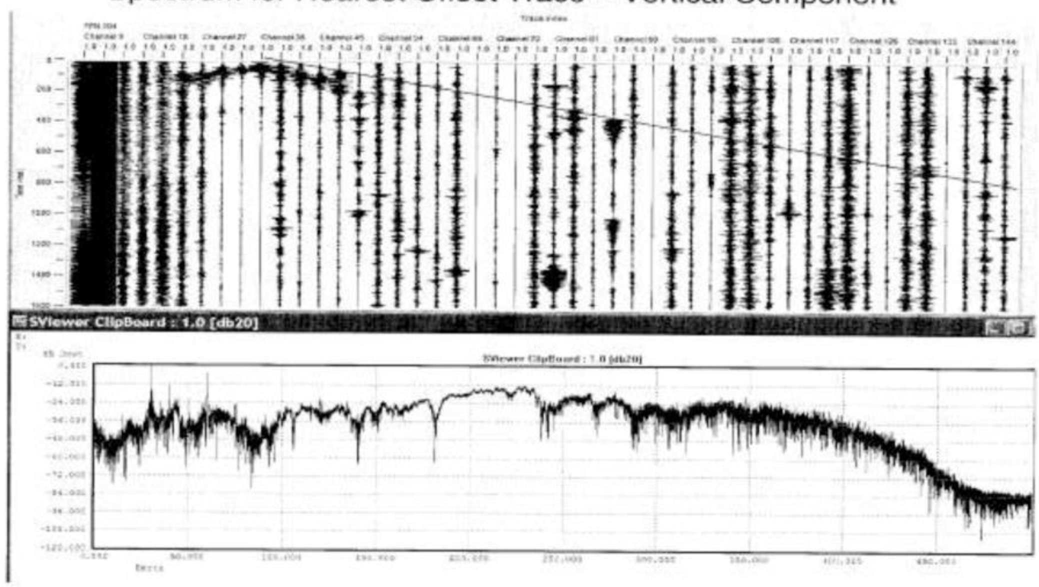

SLIDE NO. 2

3.0 kJ Source at 80' in Deep Well

Spectrum for Nearest Offset Trace – Vertical Component

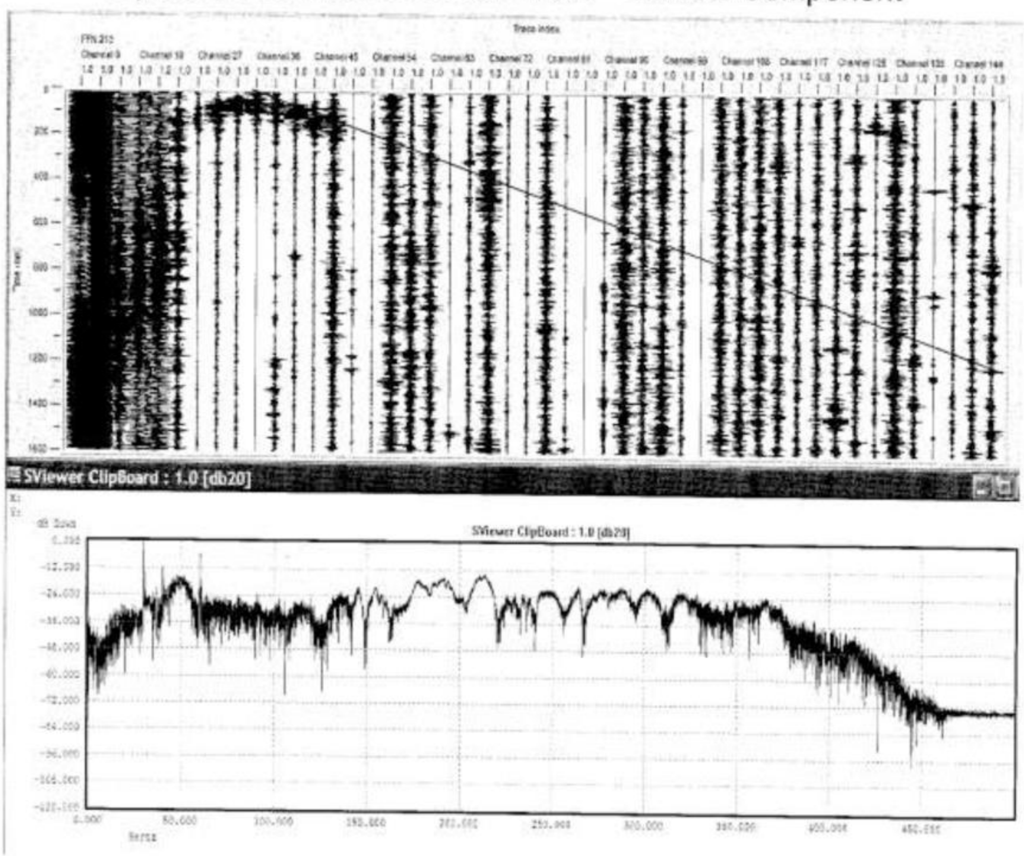

SLIDE NO. 3

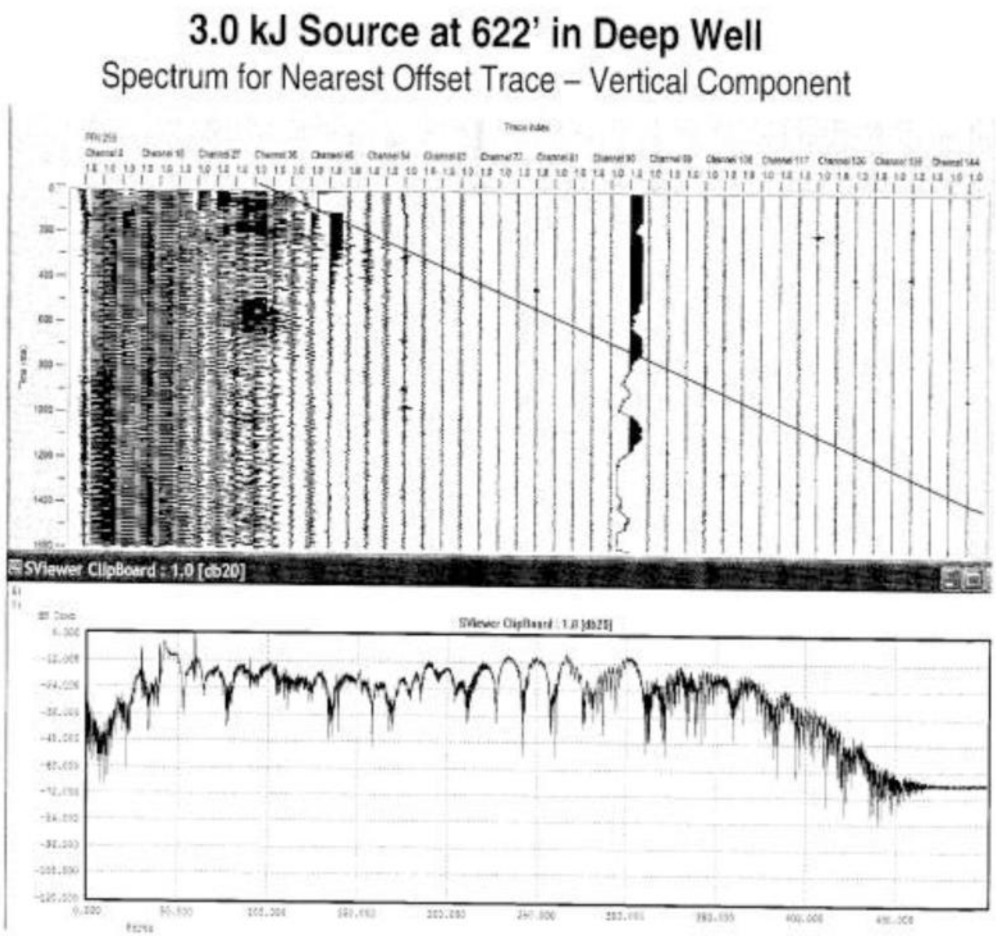
3.0 kJ Source at 622' in Deep Well
Spectrum for Nearest Offset Trace – Vertical Component
SViewer ClipBoard : 1.0 [db20]

SLIDE NO. 4

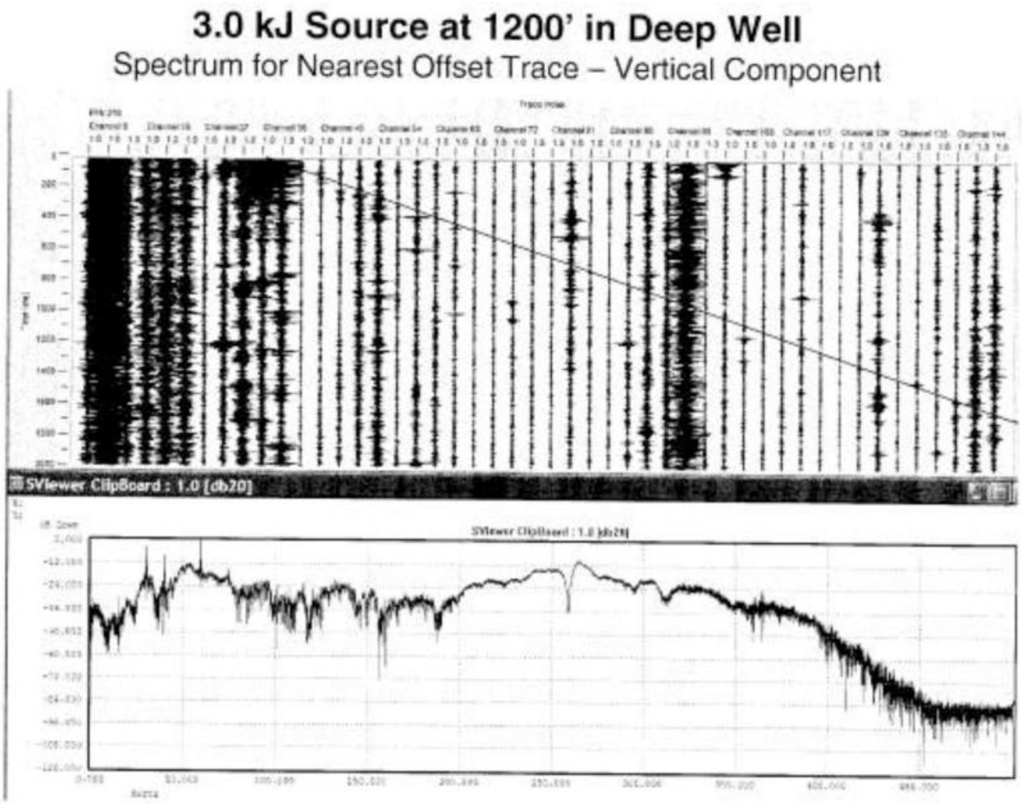
3.0 kJ Source at 1200' in Deep Well
Spectrum for Nearest Offset Trace – Vertical Component
SViewer ClipBoard : 1.0 [db20]

SLIDE NO. 5

3.0 kJ Source at 1590' in Deep Well

Spectrum for Nearest Offset Trace – Vertical Component

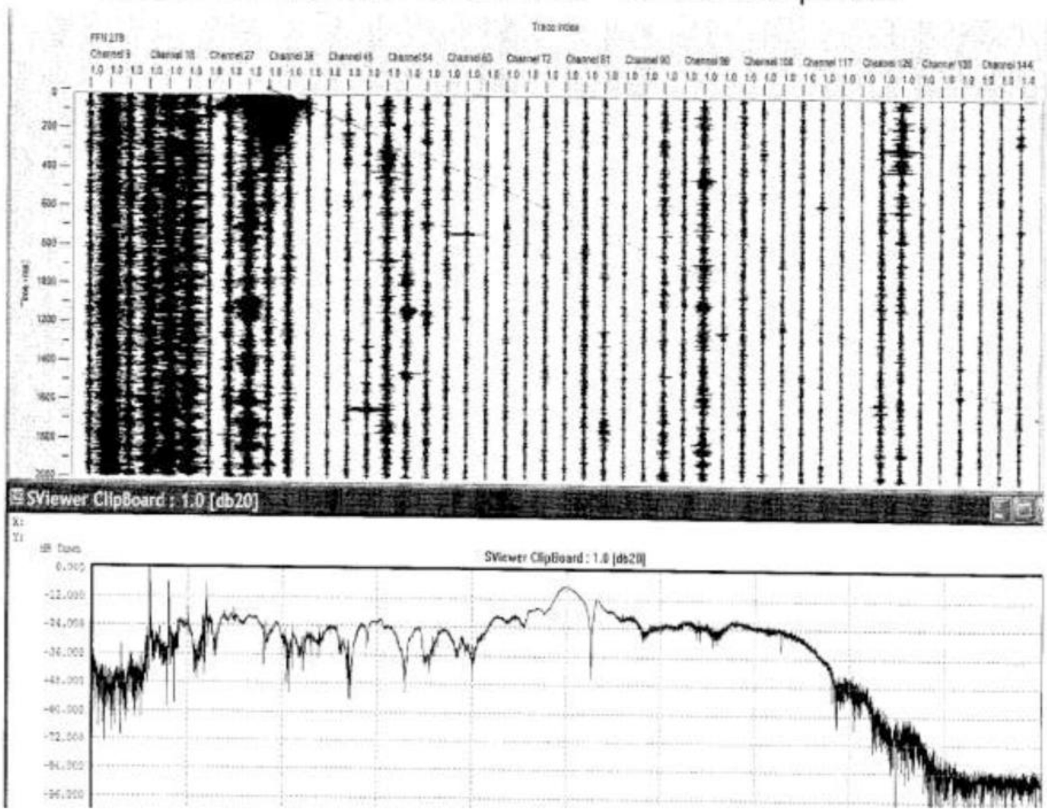

SLIDE NO. 6

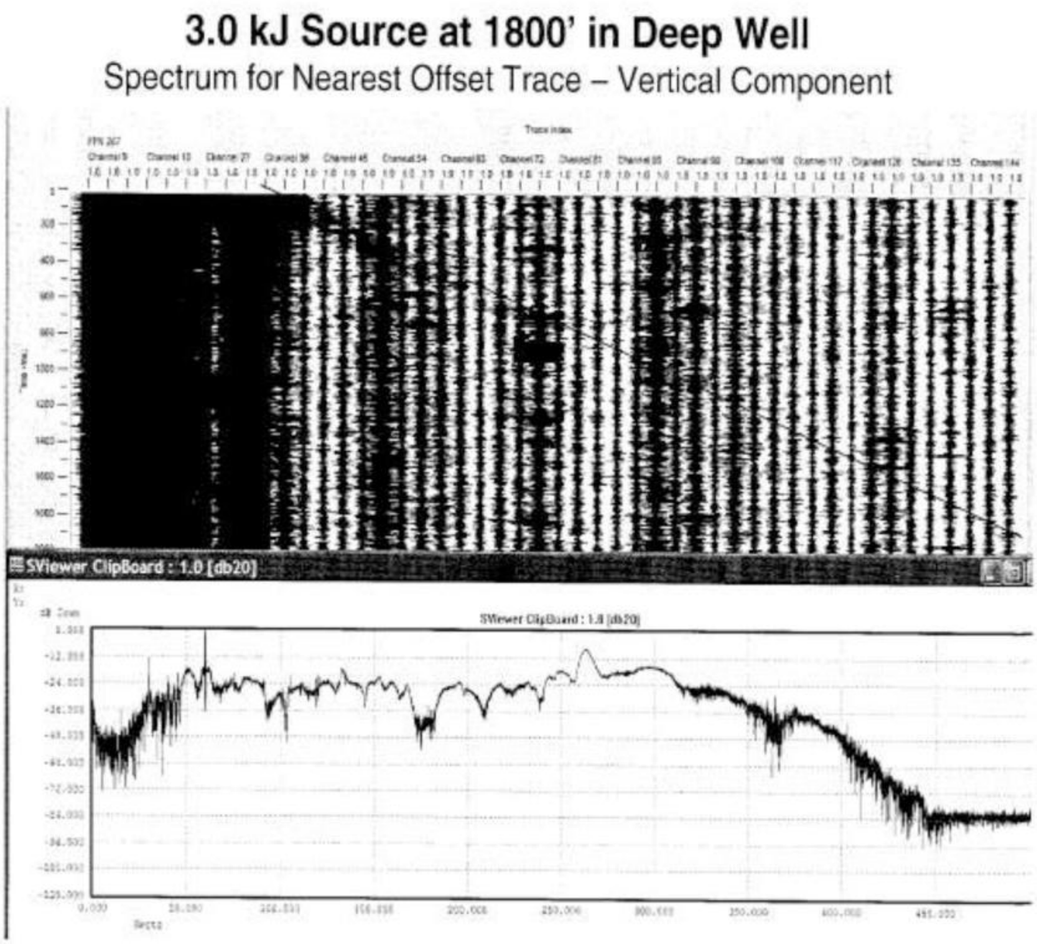
3.0 kJ Source at 1800' in Deep Well
Spectrum for Nearest Offset Trace – Vertical Component
SViewer ClipBoard : 1.0 [db20]

APPENDIX C – EFFECTS OF LOW-PRESSURE FLOW ON SPARK-GENERATED BUBBLES

Principal Investigator
Robert Radtke
Technology International, Inc.

Prepared by:
David A. Glowka

Investigators:
Dr. John E. Fontenot
Robert H. Stokes

This page intentionally left blank

Table of Contents

List of Figures

List of Tables

List of Graphs

This page intentionally left blank

EXECUTIVE SUMMARY

TTI has completed an initial series of tests examining spark-generated steam bubbles in a pressurized flowing fluid. These tests were conducted in a specially built low-pressure flow loop. The purpose of the testing was two-fold: 1) to confirm that we can generate spark-induced bubbles under pressurized, flowing conditions without destroying the hardware involved; 2) to determine the effects of ambient pressure and fluid velocity on the measured pressure pulses resulting from the expansion and collapse of the bubbles.

The first series of tests was run in straight sections of 1½, 2, and 2½ in steel pipe, with the intent of investigating the effects of creating spark-generated bubbles within the confined space of a straight tube of various diameters. The second series of tests was run with different nozzle and orifice configurations. The spark plug was placed upstream of the nozzle or orifice in some cases, downstream in others, with the intent of investigating the effects of sparker placement relative to a drilling fluid jet stream.

The tests were run with ambient pressures ranging from 17 to 58 psi and mean fluid velocities ranging from 0 to 34 ft/sec. The maximum fluid velocity achieved in these low-pressure laboratory tests was 1/7 to ½ of the velocities expected downhole in a drill bit.

A conventional lawnmower spark plug, threaded into the side of the test section, was used with a standard charge amplifier to generate the sparks. Pressure gages both upstream and downstream of the spark plug were used to measure the resulting pressure pulses. Bubbles were successfully generated and recorded under ambient pressures that would have created spherical bubbles ranging from 1.2 to 2.4 in diameter in open water. Pressure pulses as high as 510 psi was measured 9 in away from the spark during bubble expansion. Pulses up to 400 psi were measured during bubble collapse.

The results obtained in these tests have provided significant insight into the bit hydraulic and mechanical design parameters for a drill bit incorporating a sparker for SWD applications. In particular, the following conclusions have been reached:

1) We can generate spark-induced bubbles in water within a confined, pressurized space, either with or without fluid flow; and we can do it at power levels low enough to avoid destruction of the hardware involved. Pressure pulses resulting from the expansion and collapse of the bubbles produce fluid pressures of extremely short duration (tens to hundreds of micro seconds) and several hundred psi. magnitude nearly a foot away from the sparker. Such pressure pulses should act as an effective acoustic source for downhole applications.
2) Bubble lifetime was found to decrease with ambient pressure, as predicted by the modified Rayleigh-Willis equation for a spherical bubble, with significant effects found due to the confining effect of the tube and any nozzles or orifices near the bubble during expansion. Bubble lifetime was found to generally increase with fluid velocity and to increase with a reduction in test-section diameter. This is thought to be a geometry effect, where a long cylindrical bubble apparently takes longer to collapse than a spherical bubble of the same volume.
3) The measured bubble-expansion and bubble-collapse pressure peaks were found to increase with a reduction in test-section diameter. This could be because the pressure peaks generated at the bubble wall are geometrically attenuated to a smaller degree in a smaller

tube. In the presence of a nozzle or orifice, the bubbles were found to collapse with greatly reduced peak pressures. This may be due to distortion of the bubbles in the reduced fluid cross-section, which causes them to collapse asymmetrically and with less concentrated force than either a spherical or cylindrical bubble.

4) The bubble-expansion and bubble-collapse pressure peaks in both the straight-tube and nozzle/orifice tests were found to be unaffected by either the initial ambient pressure or the velocity of the fluid.

Based on these conclusions, there seems to be no compelling reason to locate the sparker within a flow tube on the bit while the pumps are running. This will help ensure more spherical bubbles that may expand and collapse with higher peak pressures.

The surprising strength of reflected pressure waves in the low-pressure lab tests further suggest that placing a reflector above the sparker could improve the quality of the bubble as an acoustic source. It may be possible to tune the reflector so that the reflected bubble-expansion pressure wave arrives at the rock surface simultaneously with the bubble-collapse pressure peak. The resulting superposition of amplitudes should further improve the acoustic-source quality of the bubble. This concept is explored in this report, and simple design considerations for a tuned reflector are developed and discussed.

1.0 INTRODUCTION

TII has completed an initial series of tests examining spark-generated steam bubbles in a pressurized, flowing fluid. These tests were designed and conducted in a specially built, low-pressure flow loop in support of the Borehole Seismic Measurement and Diagnostics System under development with funding from the U.S. Department of Energy. The tests were conducted by Robert P. Radtke, Robert H. Stokes, and David A. Glowka. Data analysis and reporting were completed by David A. Glowka. Technical review was provided by Dr. John Fontenot.

The purpose of the testing was two-fold: 1) to confirm that we can generate spark-induced bubbles under pressurized, flowing conditions without destroying the hardware involved; and 2) to determine the effects of ambient pressure and fluid velocity on the measured pressure pulses resulting from the growth and collapse of the bubbles.

2.0 LABORATORY TEST CONFIGURATION

A schematic and two photographs of the flow loop are shown in Figure 1a and 1b, respectively, showing the PVC test section used to calibrate the control valves and a close-up of the 2.5-inch steel section used for in testing. A 3-hp centrifugal pump was used to provide water flow rates up to 120 gpm and test-section pressures up to 60 psi. A bypass valve and a pressure control valve were used to set the pressure and flow rate conditions specified for each test.

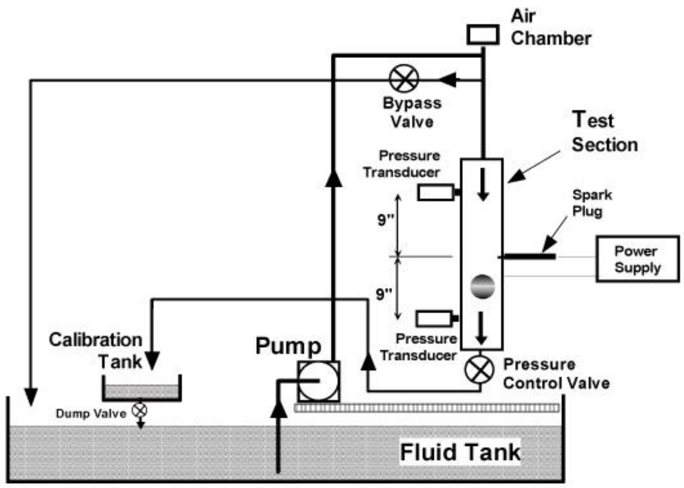

Figure 1a – Schematic of the Low-Pressure Flow Loop

Figure 1b – Photographs of the Low-Pressure Flow Loop and Test Section

A 24-in straight-tube test section consisting of either 1.5 in, 2.0 in, or 2.5 in XXS stainless steel pipe was threaded to fit a spark plug and 2 pressure transducers as shown, one upstream (above) the spark plug and one downstream (below) it. With the exception of the test section, all other piping in the flow loop was composed of 2-inch Schedule 40 PVC pipe and fittings.

In addition to these straight-tube test sections, several sections using different nozzle or orifice configurations between the two pressure transducers were also tested. The spark plug was upstream of the nozzle/orifice in some cases, downstream in others. The intent was to examine the effects of spark placement relative to the drilling fluid jet stream.

The pressure transducers used in the flow loop were Omega Engineering Model PX303, which boast a full-scale accuracy of 0.25 percent, a maximum pressure rating of 1,000 psi, and a "response time" of 1 msec. This response time means that the sensors were barely adequate for the msec-range signals we anticipated. Although the transducers were expected to respond to pressure changes that occur over a period on the order of 1 msec, it was recognized that they may not accurately measure the magnitudes of any peaks shorter than several milliseconds in duration.

Time and cost constraints discouraged the use of more expensive, more rapid-response transducers, and it was believed that absolute accuracy of the measured pressure peak magnitudes was not as important as the timing of the peaks, which could be reliably determined from the data.

A 300-gallon polyethylene stock tank was used as the fluid tank and base for the piping support structure. Two (blue) 55-gallon drums were used inside the tank: one was fitted with a calibrated sight tube and dump valve for measuring flow rates through the test section, and the other was used as a stilling well for calming the returning water in order to prevent the pump from drawing air at the higher flow rates.

An air chamber above the test section was used to absorb or attenuate pressure waves traveling back upstream to the pump. It was designed to be twice the size of the largest bubble theoretically predicted in these tests.

A typical test consisted of setting the desired test section pressure and flow rate, then signaling the power supply to energize the spark plug. A snapping noise about as loud as a child's cap gun was accompanied by pressure surges that were measured with the two pressure transducers. The transducer signals were captured and displayed on a recording oscilloscope screen, where they were photographed using a digital camera for later analysis.

For the first test series, a test matrix consisting of the 3 straight-tube test-section diameters, three test-section pressures, and 6 different fluid flow rates was developed, leading to a total of 24 different sets of test conditions spanning the matrix. Tests were repeated at each set of conditions at least 4 times, resulting in a total of 97 recorded tests. All data were obtained at a nominal power-supply charge setting of 100 J.

For the second test series, a test matrix consisting of two nozzle/orifice configurations, two sparker locations (upstream/downstream), three test-section pressures, and 16 different fluid flow rates was exercised, leading to a total of 42 different sets of test conditions spanning the matrix. Tests were repeated at each set of conditions at least 3 times, resulting in a total of 125 recorded tests. All data were again obtained at a nominal power-supply charge setting of 100 J.

3.0 TYPICAL LABORATORY TEST DATA

A typical photograph of the oscilloscope screen is shown in Figure 2 for a typical straight-tube test (Test #38). The upper scope trace is the pressure reading from the upstream transducer, and the lower trace is from the downstream pressure transducer.

Also shown are the reference lines that were drawn on each photo as aids in measuring the waveform characteristics. A set of dividers was used to scale the pertinent readings from the scope's grid marks and the scaling factors printed on the screen (e.g., “2V ” = two volts/division; and “2ms” = 2 msec/division.)

The pressure transducers had a linear voltage output, ranging from 1 volt at 0 psi to 11 volts at 1,000 psi; thus,

> Pressure = [Volts] * 100 psi/V, where [Volts] is measured from the 1-volt reference line drawn at 0 psi for each channel.

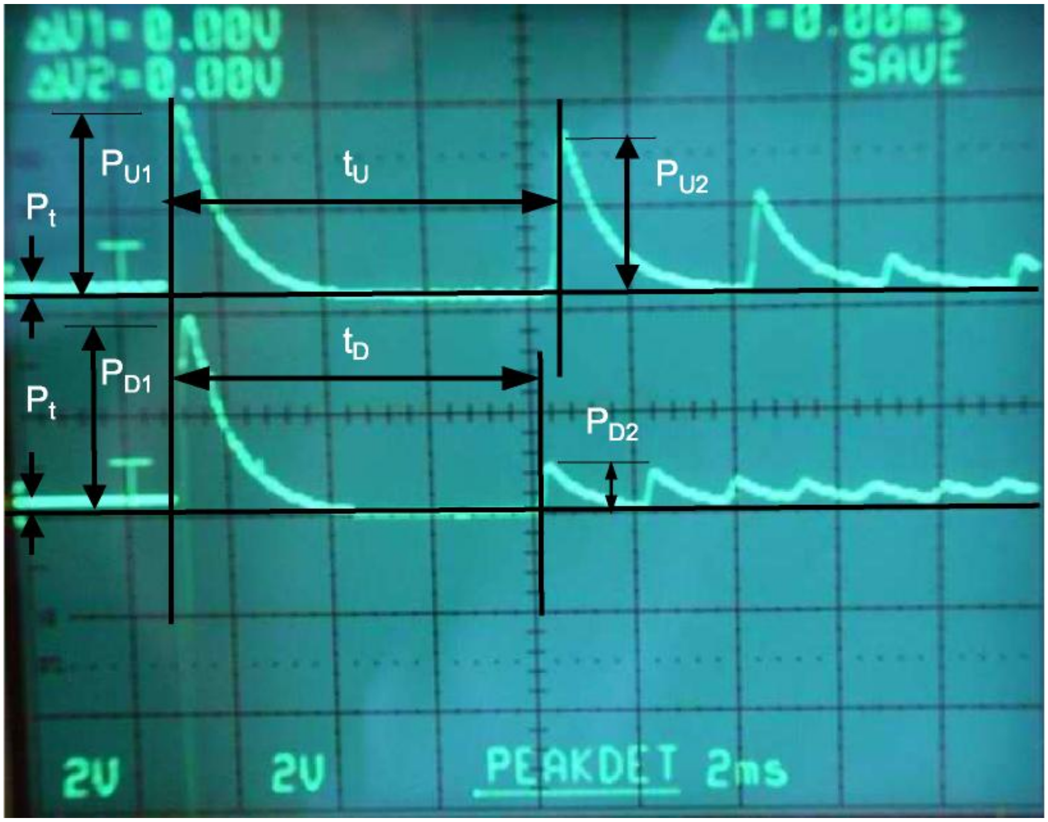

Figure 2 – Photograph of Oscilloscope Display

Note: The reference lines drawn on this photograph are not parallel to the oscilloscope grid lines because of limitations in the drawing software used in this figure. Actual reference lines used for measurement were hand-drawn on each photograph.

For example, P_{U1} in this figure is 1.8 divisions above the zero-volt reference line, so: P_{U1} = [1.8 divisions * 2 V/division] * 100 psi/V= <u>360 psi.</u>

The parameters scaled from each photograph are defined as follows:

P_t = test section pressure just prior to energizing the spark plug, psi;

P_{U1} = peak pressure at <u>upstream</u> transducer during bubble <u>expansion,</u> psi;

P_{U2} = peak pressure at <u>upstream</u> transducer during bubble <u>collapse,</u> psi;

PD1= peak pressure at <u>downstream</u> transducer during bubble <u>expansion,</u> psi;

PD2= peak pressure at <u>downstream</u> transducer during bubble <u>collapse,</u> psi; t_U = time to bubble collapse as measured at <u>upstream</u> transducer, msec.; and t_D = time to bubble collapse as measured at <u>downstream</u> transducer, msec.

This photograph illustrates the classic pressure response for spark-generated bubbles, albeit somewhat dampened by the slow response of our pressure transducers. The first peak corresponds to the formation and growth of the bubble shortly after the spark is initiated, and the second peak corresponds to collapse of the bubble. Subsequent peaks are thought to be pressure waves reflecting from elbows and valves in the piping system. No attempt has been made to analyze these subsequent peaks, as they are more of an artifact of the flow loop than of the bubble itself.

Other interesting tests are shown in Figure 3 below. These figures are used to further illustrate important characteristics of the signals and their interpretations relative to the underlying physical phenomena.

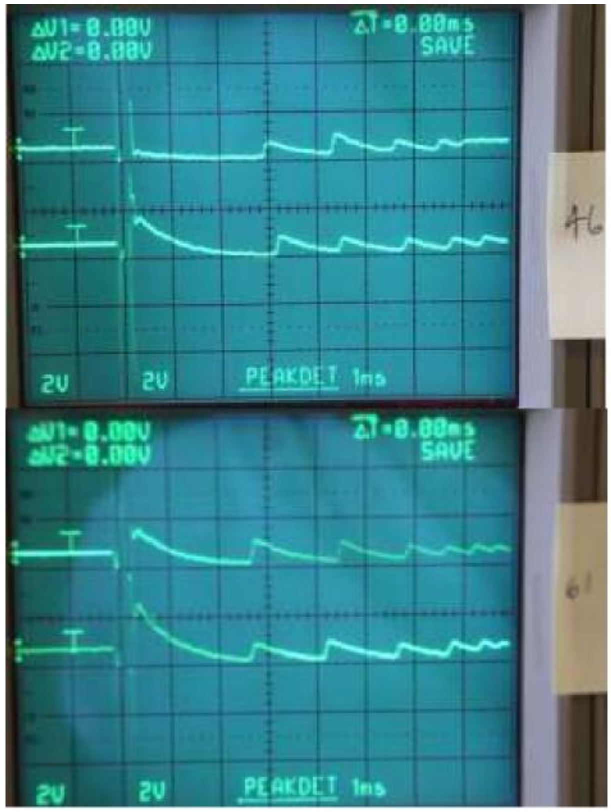

Figure 3a – Oscilloscope Readings for Various Straight-Tube Tests

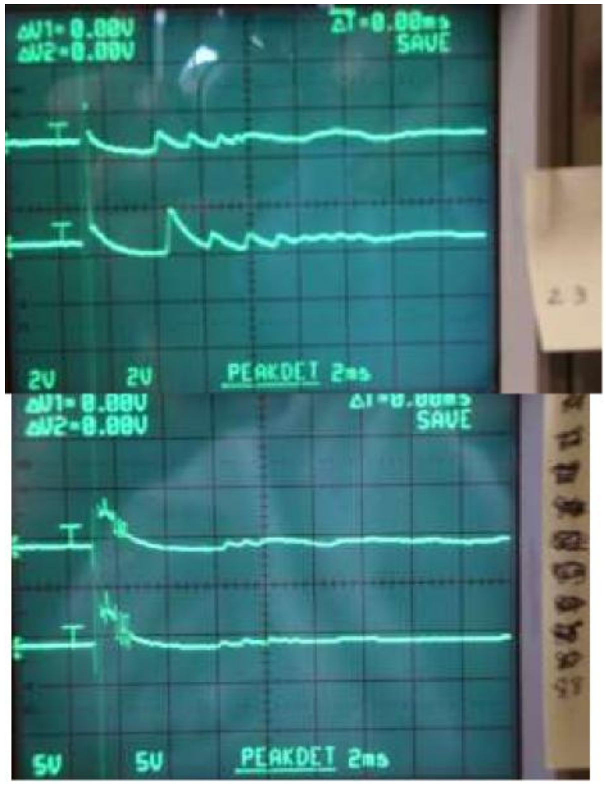

Figure 3b – Oscilloscope Readings for Various Straight-Tube Tests

Notes: The test number is shown on right side of each photograph. There are various differences in peak amplitudes and timing of the second pressure pulse. Also, an unusual pressure response was observed during Test 88, when the ceramic around the spark plugs anode shattered.

The initiation of the spark is clearly seen on each trace as a sudden discontinuity in the test-section pressure. The signals typically bounce around wildly for a fraction of a millisecond because of electromagnetic inductance (EMI) picked up by the signal wires. These spurious signals sometimes settled down in time to catch the true transducer readings of the peak pressures, but this was not always the case. Consequently, reading the initial pressure peaks was sometimes challenging, particularly in the second test series.

In general, however, it can be concluded that the initial pressure peaks occur about 0.4 msec after spark initiation. Given that the pressure wave associated with bubble formation should take about 0.15 msec to travel the 9 in from the spark plug to each pressure transducer, this leaves about 0.25 msec for the bubble to reach its maximum size (and hence pressure on the surrounding fluid) after spark initiation. This is in line with previous experimental data for spherical bubbles in an unconfined fluid.

After the bubble reaches its maximum size, it begins to collapse as the steam inside it begins to condense. As the bubble shrinks, the pressure on the surrounding fluid subsides. Often the bubble collapse process is so fast that it creates zones of zero pressure on both sides of the bubble, which propagate upstream and downstream prior to final bubble collapse. Upon final collapse, the collision and rapid momentum change of the fluid rushing into the center from all sides create the second pressure peak.

Again, the subsequent pressure peaks are most likely reflections from other boundaries and discontinuities in the flow loop piping. Note how the nature of these peaks can vary from test to test. The surprising strength of these reflections is one important finding of this test program that could have significant implications for the design of a downhole bit that utilizes spark-generated bubbles.

4.0 STRAIGHT-TUBE TEST RESULTS

The results for the straight-tube test sections are presented and analyzed first.

4.1 Raw, Straight-Tube Test Data

A total of 130 tests were conducted in straight tubes, using 3 different test-section diameters as previously described. Two series of tests were run with the 1.5-in pipe, one of which had the spark plug extending much farther into the flow than with the other pipe sizes. Because of this and the fact that the additional extension caused more variability in the results, only the second test series data for that pipe size were analyzed. A total of 97 straight-tube tests are therefore presented in this report.

The measured results for the 97 tests are listed in Table I of the attached Excel file "LP Flow Test Data.xls." In addition to the raw data, several other calculated and derived parameters are shown in Table II of the same file. Most of these parameters will be discussed in a subsequent section of this report.

The raw straight-tube test results are plotted in Graphs 1 and 2, respectively, of the Word file "LP Flow Test Graphs.doc." In these two graphs, all data points connected to each other by a continuous line represent tests conducted under identical conditions, i.e., repeat tests.

4.2 Conceptual Model for Evaluating the Test Data

A conceptual schematic of spark-generated bubble expansion and collapse in a straight-tube test section is shown in Figure 4. Experimental evidence suggests that the spark and bubble-expansion process is so energetic that a substantial velocity can be imparted to the bubble in a direction away from the electrode. This was seen, for instance, in the relatively unconfined, atmospheric-pressure tests conducted in the TII, Seismic Rock Test Simulator, where it was reported in Appendix II, that the bubble could be seen to travel a substantial distance (inches) from the electrode within its 12 msec lifetime [Ref. 1]. Given that water expands roughly 1,700 times when it vaporizes at atmospheric pressure, it is easy to see how a bubble could be motivated to move one way or another if it is asymmetrically confined or obstructed.

Inside a tube, substantial movement away from the electrode can mean only one thing: moving axially, either upstream or downstream. Figure 4 shows the downstream case, where the distance the bubble moves before collapsing is L_B, defined as positive in the downstream case and negative if the bubble moves upstream prior to collapse.

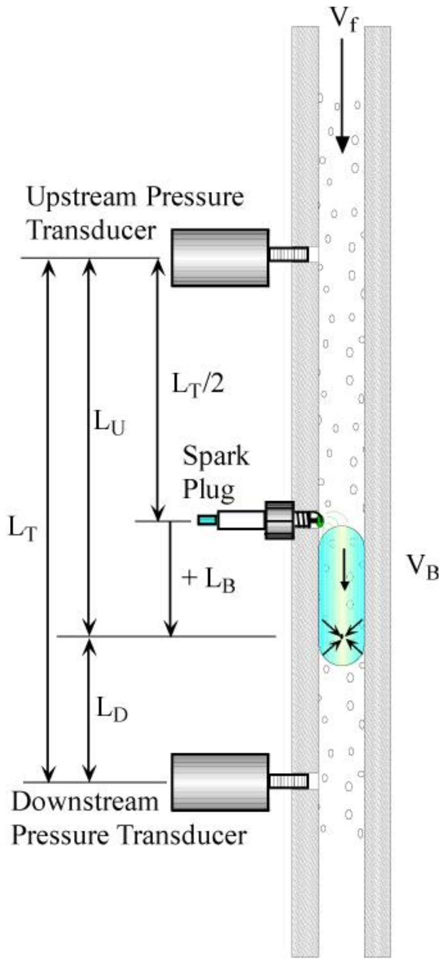

Figure 4 – Conceptual Model for Bubble Formation and Collapse in a Straight-Tube Test

The pressure wave generated upon bubble collapse travels both upstream and downstream. If the bubble collapses at the electrode ($L_B = 0$), then the pressure wave should reach the upstream and downstream pressure transducers almost simultaneously, given that the fluid velocity was much smaller than the acoustic velocity in all the lab tests. If the pressure wave reaches the downstream transducer first, it can be concluded that the bubble collapsed downstream of the electrode ($L_B > 0$). If the upstream transducer responds first, logic dictates that the bubble must have collapsed upstream of the electrode ($L_B < 0$). The difference in the response time of the two transducers should, therefore, provide a clue as to where the bubble collapses in each test.

The time to bubble collapse, as measured by each of the two pressure transducers, can be expressed in terms of the actual bubble lifetime and the lengths shown in Figure 4.

and ....(1)

$$t_U = T + L_U/c \text{ , } t_D = T + L_D/c \text{ ,}$$

............(2)

where T is the bubble lifetime (seconds) and c is the sonic velocity (ft/sec) of the pressure wave traveling from the bubble collapse point to the transducers.

Note that bubble lifetime as defined here is the time from spark initiation to bubble collapse. This differs slightly from the definition of the bubble period, which is the time difference between the formation and collapse pressure peaks. Since the formation pressure peaks in these tests generally occurred about 0.25 msec. after the spark initiation, as previously shown, the bubble lifetime is about 0.25 msec. longer than the bubble period in these tests.

Subtracting Eq. 2 from Eq. 1 gives an equation relating the time difference with the sonic travel distances to each transducer:

$$t_U - t_D = (L_U - L_D)/c \,, \qquad (3)$$

These distances are also related by the equation

$$L_T = L_U + L_D \,, \qquad (4)$$

as long as the bubble collapses somewhere between the two transducers, as shown in the figure (either above or below the spark plug). Combining Eqs. 3 and 4 produces the following equations of interest:

$$L_U = ½ \, [c \, (t_U – t_D) + L_T] \,, \qquad (5)$$

$$L_D = L_T - L_U \,. \qquad (6)$$

Substituting Eq. 5 into Eq. 1 yields the measured bubble lifetime

$$T = ½ \, [t_U + t_D – L_T/c] \,. \qquad (7)$$

Finally, it should be noted that

$$L_B = L_T /2 - L_D. \qquad (8)$$

Before using these equations on the experimental data, consider another possible location of the bubble collapse: below the downstream pressure transducer. In this case, Eqs. 1–3 are still valid as long as L_U and L_D are both still considered as positive distances (i.e., scalar, not vector, quantities).

Eq. 4, however, changes to

$$L_U = L_T + L_D \,, \qquad (9)$$

so Eq. 3 becomes simply

$$t_U - t_D = L_T /c \,. \qquad (10)$$

This means that the difference in time to bubble collapse as measured by the two pressure transducers is simply a function of the distance between the two transducers and the sonic velocity, and it provides no information about L_U and L_D. In other words, it is impossible to locate the position of the collapse based on time measurements alone when the bubble does not collapse between the transducers. This fact is undoubtedly related to a basic principle of triangulation.

Inserting L_T = 1.5 ft and c = 4,904 ft/sec (for fresh water at 75°F) into Eq. 10, we get $t_U - t_D$ = 0.31 msec

In other words, the time difference between the two transducer readings for bubble collapse should never exceed 0.31 msec for the given transducer spacing and assumed sonic velocity. Yet we routinely measured time differences greater than this value in the straight-tube tests, many in the range of 0.4–0.6 msec with some up to 1.1 msec.

The only way Eq. 10 could be correct, then, is if the sonic velocity in the water were much lower than that of fresh water at 75°F. It is possible that enough long-lived, very small bubbles were created during the spark event that the sonic velocity in the water is significantly reduced. This seems particularly possible given the existence of the zero- or low-pressure condition consistently seen in the test section after bubble expansion and just prior to collapse of the main bubble. Such a low-pressure could easily bring out of solution any dissolved air in the water. Notice now the tiny subliminal bubbles shown in Figure 4.

If this aeration concept has any merit, then the actual sonic velocity in the bubbly water can be estimated using Eq. 10 and the maximum time difference measured in the lab:

$$c_{min} = 1.5 \text{ ft/sec} / 1.1 \text{ msec.} = 1{,}364 \text{ ft/sec.,} \qquad (11)$$

which compares favorably with a sonic velocity of 1,088 ft/sec in 32^{o}F air and the sonic velocity of 1,328 ft/sec in 212^{o}F water vapor [Ref. 2]. It is possible that the density of the small bubbles could vary from test to test, so the actual sonic velocity in each test could also vary.

This aeration concept is supported by the following equation for the sonic velocity in aerated water, c_{aw} [Ref. 3]:

$$c_{aw} = c\ [1 / (1+ 2.5 \text{ X } 10_4 \qquad {}^{1/2,} \qquad (12)$$

It is where c is the sonic velocity in water and β is the volume fraction of air in the water. It, therefore, takes only 0.048 percent air by volume (β = 0.00048) to reduce the sonic velocity in water from 4,904 ft/sec (for fresh water at 75°F) to the 1,364 ft/sec value calculated in Eq. 11. Although we have no way of knowing what the equivalent air fraction was in these tests, it is not unreasonable to imagine it was at least that high.

The value of c that is used in Eqs. 5–8 has a large impact on the calculated distance the bubble travels before it collapses, but not on its net direction (i.e., upstream or downstream of the spark plug), which is only dependent on the sign of $t_U - t_D$. The value of c we use also has an impact on the calculated bubble lifetime, according to Eq. 7.

So what value of cash would be used? Using the 4,904 ft/sec value for water does not make sense because so many bubbles are thereby predicted to collapse either above the upstream transducer or below the downstream transducer. Using the minimum value calculated above in Eq. 11 results in all calculated bubble collapse locations falling between the two transducers. The main interest is in trends; therefore, examination of this case is very instructive, regardless of the actual value of the sonic velocity that developed prior to bubble collapse.

4.3 Bubble Collapse Locations

The measured bubble collapse locations based on the minimum sonic velocity calculated in Eq. 11 are shown in Figure 3. All 97 straight-tube tests are shown. A separate curve is plotted for each of the three test section sizes and three test section pressures, resulting in nine different trendlines for the bubble collapse location as a function of fluid velocity.

Examine first the data for the 2.5 in test section (black data points and trendlines). It appears that all the bubbles in this test section collapsed above the spark plug (L_B<0). Although there is no strong trend in the data, there appears to be a slight increase (downstream movement) in the bubble collapse location as fluid velocity increases. The fluid in the pipe moves an average of 0.6 in over the predicted life of the bubble at the maximum fluid velocity (12.5 ft/sec) and minimum pressure (17 psi) for this pipe size.

The (blue) data for the 2.0 in test section indicate that bubbles again collapsed upstream of the spark plug (L_B<0) when there was no or little fluid velocity. As fluid velocity increased, the collapse point again moved downstream, generally passing the spark plug at fluid velocities greater than about eight ft/sec. The predicted average fluid movement at the maximum fluid velocity of 18.3 ft/sec for this pipe size is 0.9 in.

Finally, the bubbles in the 1.5 in test section (red data points and lines) all collapse downstream of the spark plug (LB<0), even at zero fluid velocity. Again, a trend for additional downstream movement with increased fluid velocity is clearly seen. The predicted fluid movement at the maximum fluid velocity of 33.8 ft/sec for this pipe size is 1.5 in.

It can thus be concluded that regardless of the preferred direction of bubble travel at zero fluid velocity, the movement of the fluid superimposes a downstream velocity component on the bubble. The above conclusion means only that there is not total slip between the bubble and the fluid, which leaves only total and partial slip as the remaining possible options to examine. Zero bubble slip would exist if the superimposed downstream component was equal to the velocity of the fluid, which is plausible based on the scattered experimental data. In other words, the data would not dispute the theory that the relative bubble collapse location should move downstream the <u>same</u> amount as the fluid moves during the bubble's lifetime. Nor would the data dispute a theory of partial slip, where the relative bubble collapse location moves downstream an amount that is somewhat less than the amount the fluid moves during the bubble's lifetime.

At zero fluid velocity, why did the bubbles apparently collapse upstream of the spark plug in the 2.5 in and 2.0 in pipes, but downstream of the spark plug in the 1.5 in pipe? Perhaps the direction the spark plug faced after it was threaded into the test section played a role; but the cathode faced upstream (12:00 position) in the pipe and downstream (6:00 position) in the pipes. Perhaps slight departures in the perpendicularity of the threaded spark plug hole to the axis of the pipe section played a role, but any differences had to be minute. Perhaps the design of the spark plug played a role: one brand of plug was used in the 2.5 in and 2 in pipes, and a different brand of plug was used in the 1.5-inch pipe. Whatever the cause, the bubble at zero fluid velocity was consistently thrown in one direction or the other, depending on the straight-tube pipe size, and the bubble collapse point generally moved downstream with increasing fluid velocity.

4.4 Effects of Ambient Pressure on Bubble Characteristics

The measured bubble lifetimes, based on the minimum sonic velocity previously calculated, are shown in Figure 4. A trend line is shown for all 97 straight-tube data points as well as for each test-section diameter individually. In addition, the data points for the zero-velocity condition are plotted using a different marker type in order to emphasize the following point. In general, the bubble lifetime decreases with ambient pressure, and it is generally the lowest for the zero-velocity condition at each pressure. It is also seen that the bubble lifetime is significantly longer for the 1.5 in pipe compared with the larger-diameter test sections.

Also shown in Figure 4 is the modified Rayleigh-Willis equation for the lifetime of a spherical bubble in an unconfined water environment, which has been used extensively to predict bubble growth in this project [Ref. 4]. It is seen that the lowest values of the measured bubble lifetimes coincide extremely well with this equation.

It should again be noted that the bubble <u>lifetime</u> defined in this report is slightly longer than the bubble <u>period</u> defined by the Rayleigh-Willis equation because the peak of the bubble expansion pressure actually occurs slightly (about 0.25 msec in these tests) after the initiation of the spark. Thus, 0.25 msec have been added to the modified Rayleigh-Willis equation for the bubble period in order to predict the bubble lifetime shown in Figure 4.

The effects of ambient pressure on the measured peak pressures at both transducers during bubble expansion and collapse are shown in Graphs 5–8. Two conclusions can be drawn from these data: 1) the peak pressure response increases significantly with a reduction in test section diameter; and 2) the peak pressure response is not greatly affected by the initial ambient pressure in the test section, except in the cases of the upstream and downstream collapse pressures in the 1.5 in pipe, which do increase rather significantly with ambient pressure.

One question is why would the peak pressure response generally increase with smaller pipe size? As will be shown later, most of the pressure responses generally increase slightly with fluid velocity, and fluid velocities are generally higher in the smaller pipe sizes. However, this does not account for the full effect because the 1.5 in test section supports longer bubble lifetimes and higher pressure responses even at zero fluid velocity. There is something else about the pipe size other than pressures and velocities that influences bubble lifetime.

One hypothesis is that it is a geometry effect: A long cylindrical bubble takes longer to collapse than a spherical bubble of the same volume because the fluid pressures that help collapse the bubble act on only the two end faces of a cylindrical bubble confined within a tube and not on its cylindrical sides, which are in contact with the tube wall. Compared with a spherical bubble collapsing from all sides, the cylindrical bubble experiences overall lower collapse forces, leading to slower collapse. This effect is particularly pronounced at the lower ambient pressures, where the cylindrical bubbles are much longer relative to their maximum diameter inside the tube.

The finding that the peak pressure responses are not greatly affected in most cases by the initial ambient pressures is supported by our momentum-exchange model developed in an earlier report [Ref. 4], which predicts the pressure peaks to be a function of the fluid density and sonic velocity, neither of which are greatly affected by ambient pressure. This conclusion is further supported by a more comprehensive model and experimental data reported in Reference 5.

4.5 Effects of Fluid Velocity on Bubble Characteristics

The measured bubble periods are plotted as a function of fluid velocity in Figure 9. Compare different-length trendlines within a given color (pipe size) to see the effects of pressure; compare trendlines across colors to see the effects of pipe size. For a given trend line, the bubble lifetime generally increases slightly with velocity. The large increase in bubble lifetime at 33 ft/sec could signal the beginning of a significant trend; or, since the data are somewhat limited, they could be anomalous. It would be desirable to have additional data around 25 to 30 ft/sec in order to confirm this apparent trend in the data.

The measured peak pressure responses during bubble expansion and collapse are plotted as a function of fluid velocity in Figures 10–13. Although there are a few cases where the measured peak pressure responses seem to increase with fluid velocity, there are also many combinations of test section size and ambient pressure where the peak pressures dropped with increasing fluid velocity. Generally, then, it can be concluded that there is no strong, consistent effect of fluid velocity on the bubble formation or collapse pressures.

4.6 Correlation of Peak Pressures with Bubble Lifetime

It was argued in an earlier paper (Ref. 6) that larger bubbles, which have longer lifetimes, should produce higher pressure pulses. The validity of this assertion is examined in Figures 14–17, where the measured pressure peaks are plotted against bubble lifetime. It appears that, in general, the measured peak pressures do tend to increase with bubble lifetime; however, this is distinctly not true for some of the 1.5 in test section results, particularly at lower pressures and higher velocities. This suggests that the smaller the tube diameter relative to the size of the bubble, the more cylindrical and less spherical the bubble becomes, and this perhaps extends the life of the bubble relative to that of a more spherical bubble of the same volume.

4.7 Summary of Results, Straight-tube Tests

The following summary lists the findings derived from the low-pressure flow tests using the straight-tube test sections:

1) We now know that we can generate spark-induced bubbles in water within a confined, pressurized space, either with or without fluid flow, and we can do it at power levels low enough to avoid destruction of the hardware involved.

2) Spark plugs designed for small gasoline engines can be used to generate spark-induced bubbles in water, but they show significant consumption of cathode material and widening of the cathode-anode gap after only 30 sparks.

3) Significant variability in measured results was experienced from one test to the next. Some of this variability may have been due to variability in the charge delivered by the power supply from one shot to the next; however, the charge would need to change by a factor of two or more in order to single-handedly produce the typical differences we observed in the measured bubble lifetimes. Another likely culprit of the variability is the spark plug design and its orientation on the pipe. Furthermore, since each spark consumed significant cathode material, it is likely that the exact spark location, corona angle, and perhaps even shape of the corona changed from shot to shot. This could have affected the shape and initial velocity vector imparted to the resulting bubble, which may have significantly affected the magnitude and timing of the pressure waves that propagated upstream and downstream in the pipe.

4) For a given spark plug/pipe size combination, the bubble was consistently thrown in one direction or the other (either upstream or downstream) during its expansion under no-flow conditions. With increasing fluid velocity, the bubbles tended to move farther downstream prior to collapse.

5) Bubble lifetime was found to be a strong function of ambient pressure, as predicted by the modified Rayleigh-Willis equation, which has been used throughout this project. In fact, the lower end of the range in measured bubble lifetimes coincides remarkable well with the quantitative predictions of that equation. Increased departure from the equation (i.e., longer bubble life than the equation predicts) is generally observed in smaller pipes and at higher fluid velocities.

6) Bubble lifetime generally increases very slightly with fluid velocity. This effect is fairly weak over most of the velocity range tested but appears to be quite significant at the highest fluid velocity of 33 ft/sec. Whether this is anomalous or the beginning of a significant trend is not clear from the limited data available.

7) Bubble lifetime generally increases with a reduction in test-section diameter. This is thought to be a geometry effect, where a long cylindrical bubble apparently takes longer to collapse than a spherical bubble of the same volume. This effect is particularly pronounced at lower ambient pressures, where the cylindrical bubbles are much longer relative to their maximum diameter inside the tube.

8) All of the upstream and downstream, expansion and collapse peak pressure pulses significantly increase with a reduction in test-section diameter. This may be caused by the same effect that extends bubble life in smaller tubes, or it may just be that the peak pressures attenuate to a lesser degree in smaller tubes as they travel to the pressure transducer. There may be some way to correlate the results in terms of bubble size relative to tube diameter, but none of the simple relationships attempted has produced good correlation of the test data.

9) The magnitudes of the upstream and downstream pressure peaks during bubble expansion do not depend greatly on the initial ambient pressure in any of the test sections. The pressure peaks measured during bubble collapse are likewise not dependent on initial ambient pressure, except in the case of the 1.5 in test section. In that smaller test section, the collapse pressures curiously increase rather significantly with ambient pressure. Whether this trend is significant and would continue at higher pressures is unknown.

10) The magnitudes of the bubble expansion and collapse pressures do not depend to any significant extent on the fluid velocity.

5.0 NOZZLE/ORIFICE TEST RESULTS

The 1.5 in pipe (1.1 in ID) was modified to accommodate different nozzle configurations. Four configurations were tested. In first two of these, a rather abrupt reduction in flow tube diameter, from 1.10 in to 0.62 5 in, was achieved with a series of bell reducers and pipe bushings. The spark plug was placed just upstream (2.0 in) of the entrance to this orifice in one configuration and just downstream (2.0 inches) of the exit from the orifice in the other. In the second pair of configurations, a 30°-included angle (Leach and Walker) (L&W) nozzle was inserted into the pipe to achieve a gradual reduction in pipe size from 1.10 in to 0.375 in. Again, the spark plug was placed just upstream (2.0 in) of this L&W nozzle in one configuration and just downstream (2.0 in) of it in the other.

Although the set-up with the power-supply, spark-plug, pressure transducers, and oscilloscope was identical to that employed earlier with the straight-tube tests, problems were encountered obtaining usable pressure data during the nozzle/orifice tests. For some unknown reason during these tests, there was considerably more EMI imposed by the power supply on the pressure transducer signals. A typical shot is shown in Figure 5.

Note that the pressure peaks associated with the expansion of the bubble are completely masked by the EMI, which superimposes a large negative voltage on both channels for at least 2–3 msec. after firing of the spark. By the time the EMI dissipates, the pressure peaks have also dissipated and the bubble is beginning to collapse. In many cases, the signals were still distorted by the time the second pressure peak arrived, signaling final bubble collapse.

Consequently, it was not possible to accurately measure the bubble <u>expansion</u> pressure peaks for these tests. Furthermore, the bubble <u>collapse</u> pressure peaks had to be scaled from the data simply as departures from the baseline readings just prior to the peak pressures rather than from the true zero-pressure levels; otherwise negative pressures would be recorded, which is clearly impossible.

Other idiosyncrasies noted in the nozzle/orifice tests are shown in Figures 6 and 7. Nozzle/orifice Test #3 shows a pressure peak at 2.6 msec on the lower trace that is thought to be a reflection of the bubble-expansion pressure wave bouncing off a

Figure 5 – Photograph of Oscilloscope Display for a Typical Nozzle/Orifice Test

Note: The upper trace in this photo only is the downstream pressure transducer reading; the lower trace is the upstream pressure, transducer reading.

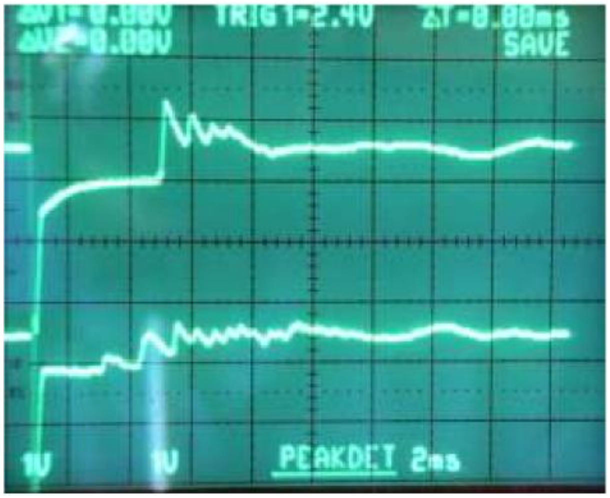

Figure 6 – Nozzle/Orifice Test #3

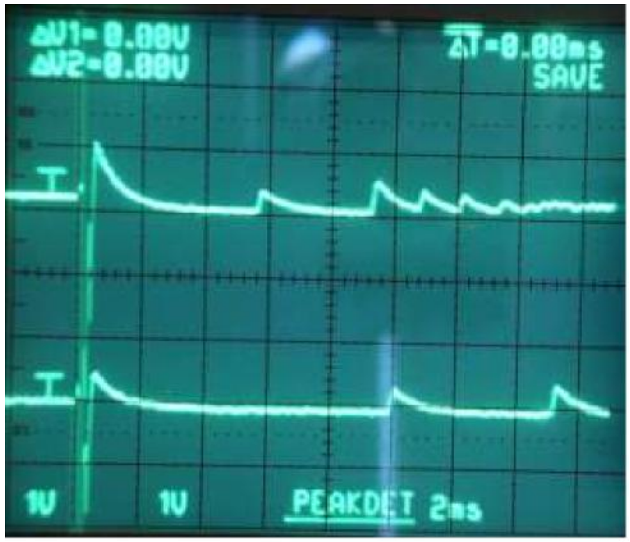

Figure 7 – Nozzle/Orifice Test #118

Note: This was the typical pressure wave on lower trace at 2.6 msec. when a gurgling sound was heard at the flow loop exit. Perhaps this was caused by the discontinuity in the flow area, such as the elbow in the pipe run below the test section. Such reflected wave signals often masquerade as the bubble-collapse pressure peaks, thereby confusing the analysis of the downstream pressure transducer readings.

Nozzle/orifice Test #118 in Figure 7 shows a pressure pattern that was typical of about six different runs with the sparker located upstream of the Leach and Walker nozzle. In these runs, a distinct gurgling sound was heard coming from the end of the flow loop after the spark plug was fired. Although the end of the flow loop was over 10 ft downstream of the spark plug, with an intervening nozzle in the way, the pressure wave seen in the lower trace evidently survived strongly enough to make an audible sound coming out the end of the flow loop.

The lower traces from all six of these tests were similar in that they were all exceptionally smooth except for a few distinct, well-organized peaks. It is possible that the bubble lifetimes in these tests were "in tune" with the flow loop, such that the reflected wave from the bubble <u>expansion</u> peak constructively superimposed with the bubble <u>collapse</u> pressure peak. This could have produced a coherent pressure pulse traveling downstream that was able to survive longer than that coming from bubbles generated under the other test conditions.

Using a set of dividers, one can find several periodic structures in many of the traces recorded during these tests. Although a comprehensive study of these structures might produce a clearer understanding of the acoustics involved, it is well beyond the scope of this project. The conclusion that can be reached at this point, however, is that reflected pressure waves have the potential to complicate not only the analysis of this laboratory data but also the use of these acoustic signals in field.

One other notable visual feature of the nozzle/orifice test data is that many of the collapse pressure peaks are much less distinct than those seen in the straight-tube tests. This indicates, perhaps, that the bubbles are being deformed by the nozzle or orifice, so that the bubble collapse is then spread out over a longer period than that associated with the collapse of a spherical bubble. This also, perhaps, accounts for the lower collapse pressures measured in the nozzle/orifice tests, as discussed below.

5.1 Nozzle/Orifice Test Data

A total of 125 tests were conducted with the four nozzle/Orifice configurations. The measured results are listed in Table III of the attached MS Excel file “LP Flow Test Data.xls”. The calculated and derived parameters are shown in Table IV of the same file. The raw nozzle/orifice test results are plotted in Graphs 18 and 19 of the Word file “LP Flow Test Graphs.doc”. As with the straight-tube data, all data points connected to each other by a continuous line represent tests conducted under identical conditions, i.e., repeat tests. Comparing these figures with Graphs 1 and 2, several conclusions can be immediately drawn. First, the variability in the nozzle/orifice test data is actually slightly smaller overall than that of the straight-tube test data. Second, the measured times to bubble collapse, t_U and t_D, are slightly longer in the nozzle/orifice tests than in most straight-tube tests.

Finally, the measured bubble-collapse peak pressures, P_{U2} and $_{PD2,}$ are significantly lower overall in the nozzle/orifice tests — generally less than 100 psi. with a few exceptions. Although the pressure measurements in these tests are somewhat more uncertain because of the prevailing EMI effect, it is believed that most of the measured drop in peak pressures is real. Limited tests were runs with the 2.5-inch straight-tube on the same day as the first nozzle/orifice tests as part of a debugging procedure, and the one recorded test produced significantly higher peak pressures (220 and 230 psi) than those measured with most of the nozzle and orifice configurations.

The measured bubble lifetimes with one of the nozzle/orifice configurations are shown in Graph 20 in comparison with the results from the straight-tube tests. In the tests shown here (Tests 1–30, shown in gray), the spark plug is located upstream of the 3/8-in orifice. It is seen that this configuration behaves in much the same manner as the 1.5-in straight tube, with bubble lifetime decreasing with ambient pressure. Bubble lifetime is significantly higher than the modified Rayleigh-Willis equation, but the presence of the nozzle has little effect beyond the apparent effect of using the smaller tube diameter. Similar results (plotted but not presented) were obtained with the other three nozzle/orifice configurations, where the measured bubble lifetimes were also very similar to those of the 1.5 in straight tube.

Comparison of the nozzle/orifice data with the straight-tube data continues in Figures 21–25. In each figure, the appropriate data for the same configuration (sparker upstream of 3/8-inch orifice) are plotted alongside the straight-tube data. It is remarkable how well the nozzle/orifice data fits in with the straight-tube data. The only notable difference between the two sets of data is that the measured bubble-collapse peak pressures are significantly lower than the 1.5 in straight-tube peak pressures, as noted earlier. The nozzle/orifice peak pressures are even lower in many cases than the 2.5 in straight-pipe pressures. Other than that, there appears to be no significant effect of the nozzle or orifice on measurable bubble dynamics. As with the straight-tube tests, neither the bubble lifetime nor the bubble collapse pressures depend greatly on fluid velocity.

Although not presented, the data for the other three nozzle/orifice configurations tested were also plotted in graphs similar to Figures 20–25. Although the data are far from identical to those presented, none of the observations made above are any different for the other configurations.

5.2 Summary of Results of the Nozzle/Orifice Tests

The following summary lists the findings derived from the low-pressure flow tests using the nozzle/orifice test sections:

1) The bubble-collapse pressure peaks are, in general, much less distinct than those seen in the straight-tube tests. It appears that the bubbles are being more greatly deformed by the nozzle or orifice than by the pipe cross-section alone, so that bubble collapse is spread out over a longer period than that associated with the collapse of a spherical bubble.

2) A more extended bubble collapse would tend to lessen the sudden shock that occurs when fluid rushes in from all sides and collides in the center of a perfectly spherical bubble. One would, therefore, expect a more highly deformed bubble to create lower peak pressures when it collapses. In general, significantly lower peak pressures were measured in the nozzle/orifice tests.

3) In all other respects, the presence of a nozzle or orifice in the flow section, either upstream or downstream of the sparker, has no apparent effect on measurable bubble behavior. Bubble lifetime generally decreases as the ambient pressure increases and is generally longer than that predicted by the modified Rayleigh-Willis equation for a spherical bubble. But bubble lifetime in the presence of a nozzle or orifice is essentially the same as that in the same size pipe without the nozzle or orifice.

4) As in the straight-tube tests, there is very little to no apparent effect of fluid velocity on bubble lifetime.

6.0 DISCUSSION AND RECOMMENDATIONS

The low-pressure flow tests have shown that, using relatively low electrical power levels, we can generate spark-generated bubbles in a tube, either one with a constant cross-section or upstream or downstream or a nozzle or orifice; and that these bubbles generate expansion- and collapse-pressure pulses on the order of tens to hundreds of pounds per square inch almost a foot away from the sparker. Such bubbles may, therefore, serve as an effective acoustic source for SWD applications. The question at hand is how best to configure the sparker to produce the highest-quality acoustic source possible.

6.1 Acoustic-Source Quality

The sketch shown in Figure 8 is used to explore the question of acoustic-source quality. Shown here is a sparker situated at the mouth of a reflector mounted on the lower face of the drill bit. The depth of the reflector cavity is D_R, and the stand-off height above the rock is H_S. After forming in the corona of the sparker, the bubble expands and moves away from the reflector. It eventually collapses, presumably somewhere near the rock surface. For discussion purposes, it is assumed that the bit is located at a depth of about 2,000 ft and that periodic bubbles are being generated by the sparker.

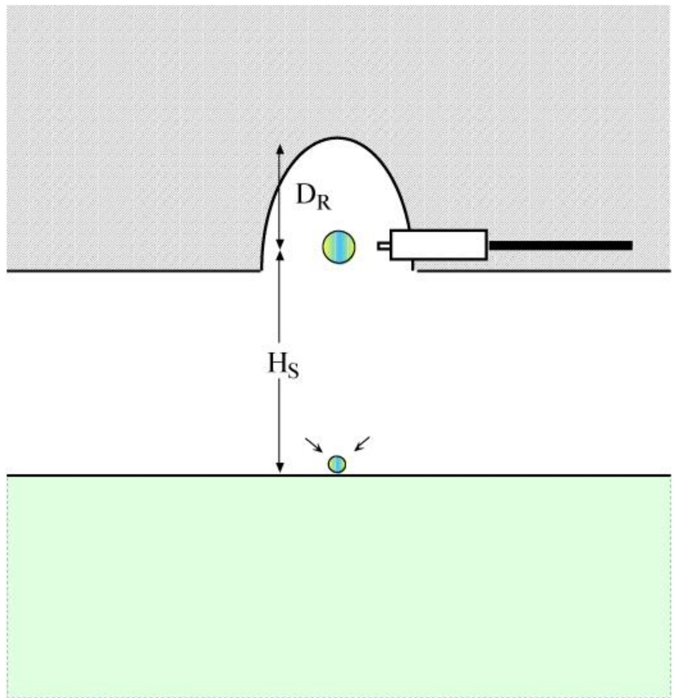

Figure 8 – Sparker Mounted in a Reflector on a Drill Bit at the Bottom of a Wellbore

A simplified view of the theoretical pressure peaks hitting the rock surface as a result of the expansion and collapse of the periodic bubbles is shown in Figure 9. (The form of these curves is based on the digitized readings from Test #38 of the straight-tube tests.)

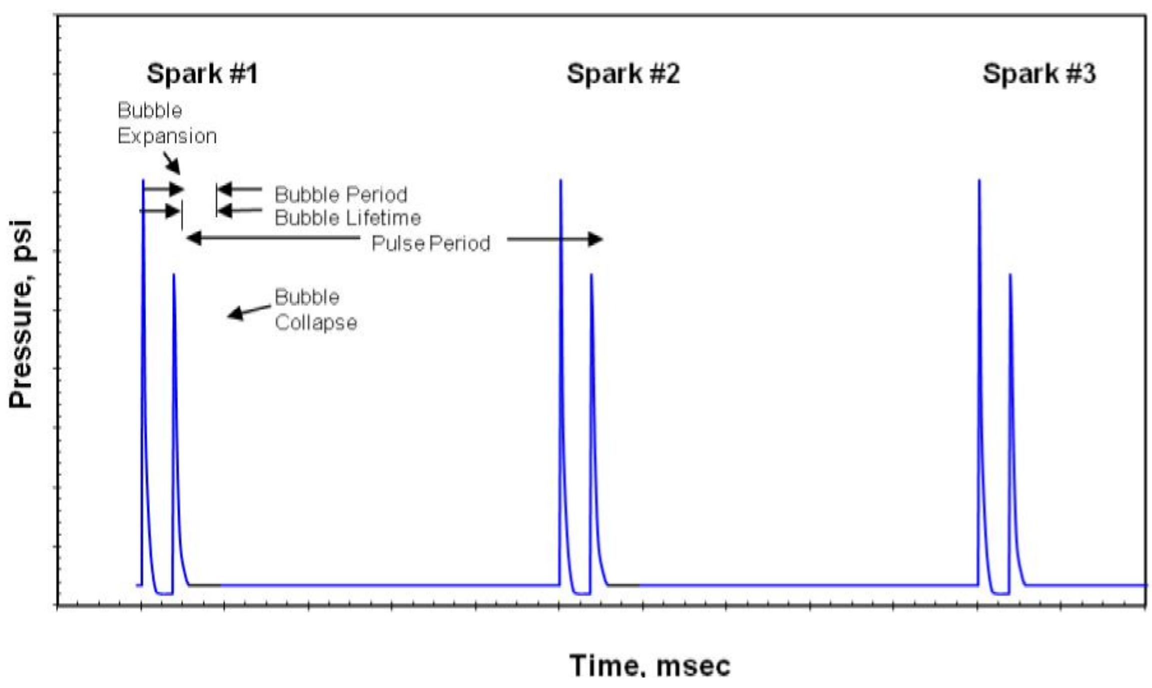

Figure 9 – Theoretical Bubble-Expansion and Bubble-Collapse Peak Pressures for Periodic Spherical Bubbles with No Reflections

Two distinct cycles are displayed in this acoustic signal. First is the major cycle governed by the pulse frequency or period, where the pulse period is the period between successive sparks? The second cycle is characterized by the bubble period, which is the time between the bubble-expansion and bubble-collapse pressure peaks.

Figure 9 actually illustrates the concept of linear acoustics proposed for use in the SWD system. The acoustic signals produced by each of the two pressure peaks associated with each spark event are very short-lived, on the order of tens to hundreds of *micro* seconds long. Furthermore, the bubble collapse period at 2,500 ft is on the order of 0.2 msec. Such high frequency (5-kHz) acoustic waves dampen quickly when traveling through rock and get quickly lost in the noise, so basing a seismic survey on an individual spark event is not practical.

On the other hand, pulsing the sparker periodically at a constant rate of, say, once every 40 msec. produces the same high frequency sound as before, but it does so every 40 msec. The levels of the acoustic waves reaching the geophones on the surface are no larger than they were before, but their arrival at a constant, known, and much lower frequency (25 Hz) allows the weak acoustic signal to be extracted from the noise much more reliably.

In this context, the individual expansion and collapse pressure peaks should be viewed as a single acoustic signal lasting about as long as the bubble period. The total acoustic wave energy striking the rock face is represented by the area under the time-pressure curve. The magnitude of the acoustic wave set up in the rock is probably also dependent on the magnitudes of the two pressure peaks.

If we assume, then, that a larger acoustic wavefront in the rock means that a larger signal is received at the surface, it follows that a higher-quality acoustic source is one where the acoustic energy is concentrated in one or two high-magnitude peaks rather than in multiple peaks of lower magnitude. This concept is illustrated with Figure 10, which is based on the collapse-pressure signals obtained in one of the nozzle/orifice tests (#1). Here the distorted bubble collapses over a longer period of time, with a more rounded and shorter peak than that seen in Figure 9. Although the acoustic energy associated with bubble collapse is approximately the same in both cases, the higher collapse pressure seen in Figure 9 should lead to a stronger acoustic signal arriving at the surface. These considerations suggest that more spherical, rather than distorted, bubbles are better because they may produce higher peak pressures upon collapse.

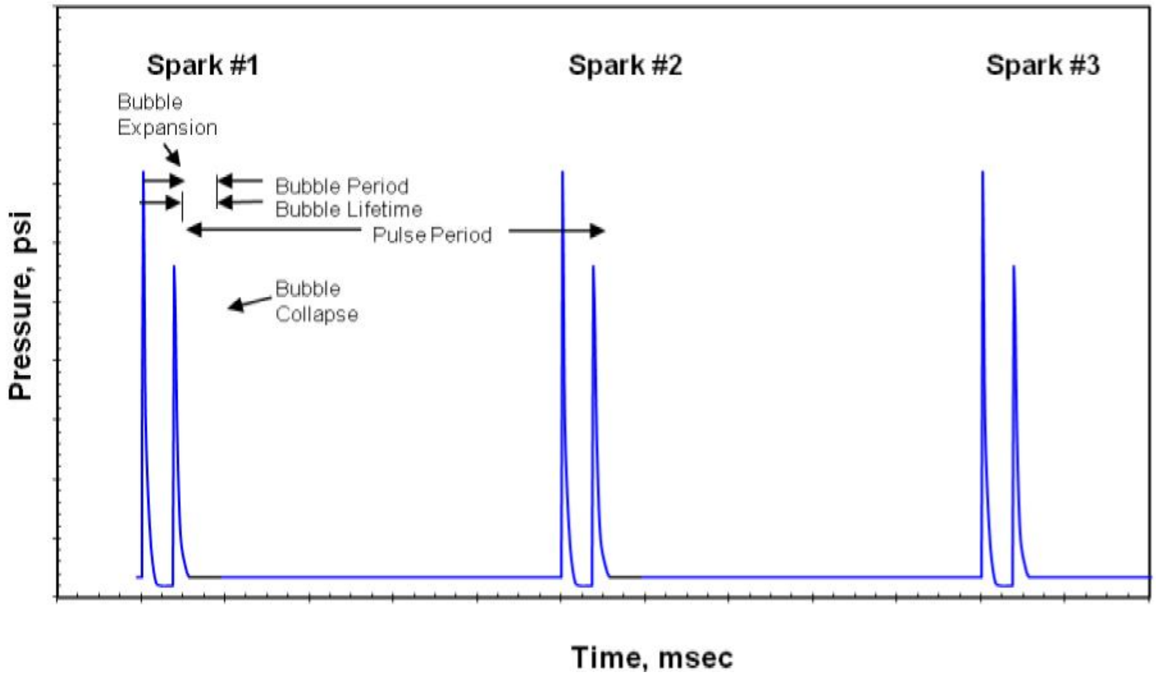

Figure 10 – Theoretical Bubble-Expansion and Bubble-Collapse Peak Pressures for Periodic Non-Spherical Bubbles with No Reflections

6.2 Optimizing Sparker Placement

There is significant evidence that obstruction to the growth of the bubble, such as that caused by a nearby nozzle or orifice, can distort the bubble and reduce its collapse pressure peak below that obtained with a more spherical bubble. Bubble distortion caused by velocity gradients within a fluid jet could have the same effect on collapse pressure.

Therefore, until more is understood about the highly complex dynamics involved in placing the sparker within a flow tube on a drill bit, no advantage and many disadvantages are seen with placing the sparker in such a location. It may instead be prudent to place the sparker on the outside surface of the drill bit, as illustrated in Figure 8, in a location that is as sheltered from the fluid jet streams as possible.

The reflector shown in this figure might serve as more than just a convenient recess in which to locate the sparker. If properly sized, it could act to amplify the bubble collapse pressure in such a way as to enhance the quality of the bubble as an acoustic source. This concept is illustrated in Figures 11 and 12. In the first case, the reflector depth (D_R) and stand-off distance (H_S) are such that the bubble-expansion pressure wave that reflects from the top of the reflector cavity reaches the rock surface just prior to the arrival of the bubble-collapse pressure peak. The reflected expansion pressure wave is, therefore, slightly out of phase with the bubble-collapse peak. The outward–radiating bubble-collapse pressure wave is also partially reflected back off the reflector and reaches the rock surface sometimes later, although greatly attenuated.

If the reflector depth, D_R, is increased by the right amount, as implied in Figure 12, the reflected bubble-expansion pressure wave will arrive at the rock surface at the same time as the bubble-collapse pressure peak. The principle of superposition suggests that the two pressure waves should be additive, resulting in a much higher collapse-pressure peaks as shown. A partial reflection of the single, superimposed pressure wave will then arrive at the rock surface some time later.

Comparing the acoustic signals of Figures 9–12 it can be seen that the reflector theoretically has the potential for greatly improving the quality of the acoustic source (i.e., higher overall acoustic energy and peak pressures striking the rock). It should be noted that the reflector actually increases the amount of acoustic energy striking the rock surface, regardless of its timing relative to bubble collapse, by turning around some of the energy that otherwise would travel away from the rock surface.

Whether or not the bubble-collapse pressure is amplified, of course, depends on the timing of the reflected energy, which in turn depends on the depth of the reflector and sparker stand-off distance. Referring to Figures 8 and 11, the time t_e for the bubble-expansion pressure wave to reach the rock surface is:

$$t_e = H_s / c \qquad (13)$$

where c is the sonic velocity and it is assumed that the bubble undergoes most of its expansion near the sparker. The time t_r for the reflected bubble-expansion wave to reach the rock surface is:

$$t_r = (2\,D_R + H_s) / c \qquad (14)$$

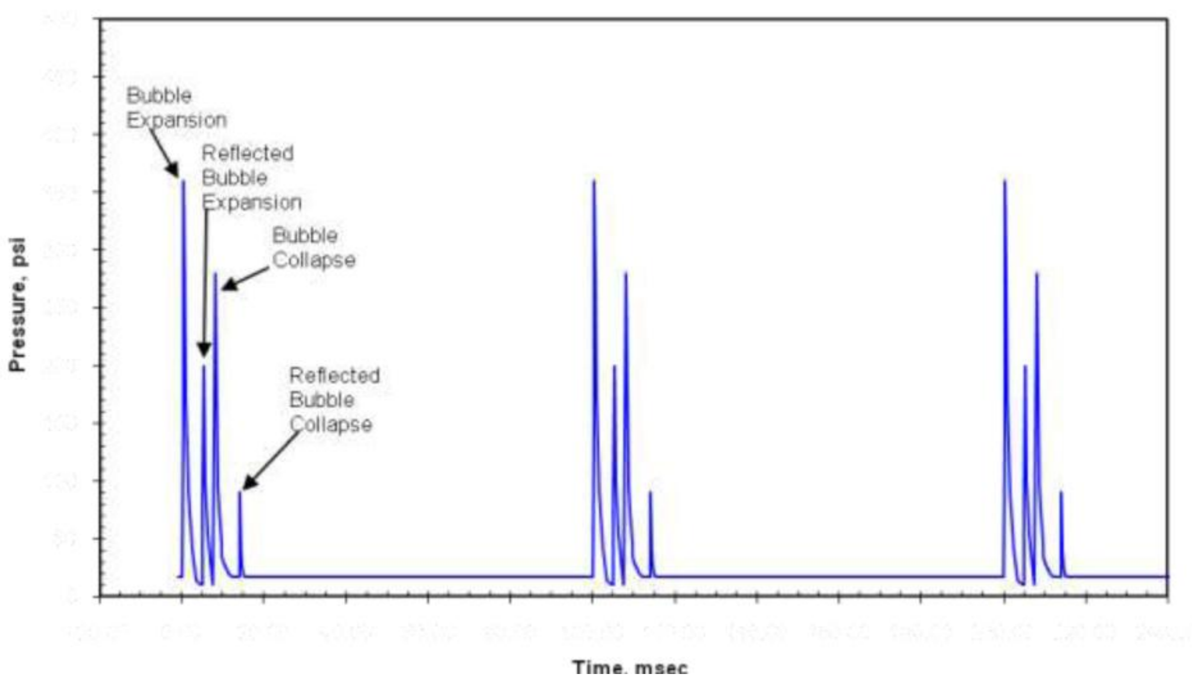

Figure 11 – Theoretical Bubble-Expansion and Bubble-Collapse Peak Pressures for Periodic Spherical Bubbles with Out-of-Phase Reflections

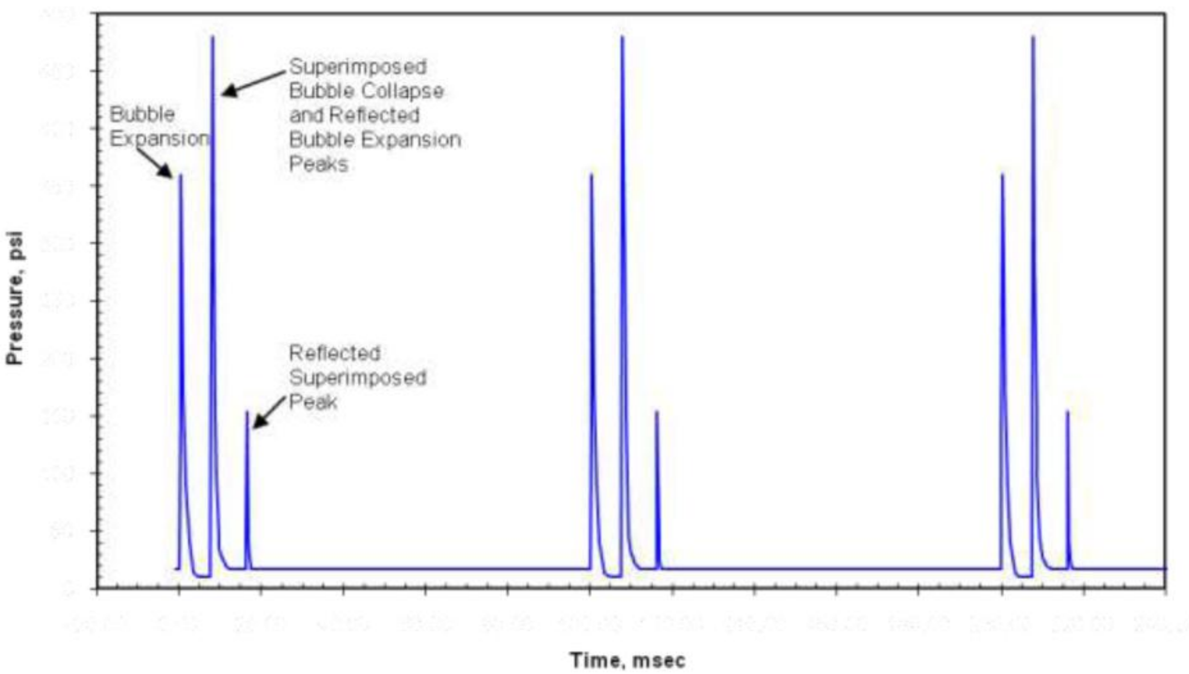

Figure 12 – Theoretical Bubble-Expansion and Bubble-Collapse Peak Pressures for Periodic Non-Spherical Bubbles with Timed Reflections.

If it is assumed that the bubble collapses near the rock surface, the collapse peak pressure occurs at time t_c:

$$t_c = T \qquad (15)$$

where T is the bubble period. For maximum amplification of the bubble-collapse pressure, the reflected expansion wave should arrive exactly at the time of bubble collapse, i.e.,

$$t_r = t_c \qquad (16)$$

Combining Eqs. 14–16, we get the relationship for the critical depth of the reflector to achieve maximum amplification of the bubble-collapse pressure:

$$(D_{R})_{crit} = (c\,T - H_s) / 2 \qquad (17)$$

The modified Rayleigh-Willis equation for the period of a spherical steam-generated bubble is

$$T = 0.7\ [0.000209\ (10^{10}Q_e)^{1/3} / (L_e + 33)^{5/6}] \ldots (18)$$

where Q_e is the energy delivered by the spark, in kJ; L_e is the effective well depth, in ft; and T is in seconds.

We thus see that the critical depth of the reflector is a function not only of the sparker stand-off distance, but also the sparker energy and the depth of the well.

For typical downhole conditions at 2,000 ft, with an acoustic velocity of 4,663 ft/sec, sparker energy of 100 J, and a sparker stand-off distance of 3 in, we calculate the bubble period and critical reflector depth to be:

$$T = 0.26 \text{ msec}$$

and

$$(D_{R})_{crit} = 5.7 \text{ in.}$$

A lower acoustic velocity, such as that inferred in some of the flow experiments reported in this document, would lead to smaller calculated values of $(D_{R})_{crit}$.

As the wellbore depth increases to 5,000 ft, the above parameters change to

$$T = 0.12 \text{ msec}$$

and

$$(D_{R})_{crit} = 1.9 \text{ in}$$

For maximum effect, the reflector depth would thus need to change with wellbore depth. Considering the other variables that affect the critical reflector depth, a system that adjusts the reflector depth to achieve maximum acoustic signal would be ideal. The practicality of such a concept is questionable, however, unless the effect is truly revolutionary, which is not anticipated.

Instead, it may be enough to design the reflector for the maximum wellbore depth expected. This would require a relatively shallow reflector, and the reflected waves would always arrive at the rock surface prior to or at the same time as bubble collapse. This would cause the reflected energy to return to the rock surface within the time window between the expansion and collapse pressure peaks, thereby improving the quality of the acoustic source even without timed superposition of the peaks at collapse.

7.0 REFERENCES

1. Stokes, Robert: private communication with Dave Glowka.
2. Marks, Lionel S. and Baumeister, Theodore: Standard Handbook for Mechanical Engineers, 7th Ed., McGraw-Hill Book Co., New York, 1967, p. 3-50.
3. Urick, Robert J.: Principles of Underwater Sound, McGraw-Hill Book Co., New York, 1975, p. 224.
4. Glowka, David A.: private communication with Robert Radtke
5. Cook, Jeffrey A., "Interaction of Multiple Spark-Generated Bubbles in a Compressible Liquid," Report ARL-TR-93-10, Applied Research Laboratories, University of Texas, June 1993, p. 78.
6. Glowka, Dave, private communication with Robert Radtke

APPENDIX Ca – LABORATORY DATA

Laboratory Data for "Effects of Low-Pressure Flow on Spark-Generated Bubbles"

					Table I - Raw Straight-Tube Test Data					
Test Numbers			1 thru 31	32 thru 63	64 thru 97		**Power Supply charge = 100 J in all tests**			
Test Section			2.5 inch XXS	2.0 inch XXS	1.5 inch XXS					
Test-Section ID, inches			1.771	1.503	1.100					
Spark Plug Manufacturer			Champion	Champion	E3					
Spark Plug Model			803C (N4C)	803C (N4C)	E3.10					
Spark Plug Gap, mm			1.0	1.0	1.0					
Spark Plug Extension, inches			0.75	0.75	0.625					
Cathode Orientation			12:00	6:00	6:00					
Test #	**Test Section ID, d_t, inches**	**Test Section Pressure, p_t, psi**	**Test Section Flow Rate, Q, gpm**	**Upstream Pressure Pulse 1, P_{U1}, psi**	**Downstream Pressure Pulse 1, P_{D1}, psi**	**Upstream Pressure Pulse 2, P_{U2}, psi**	**Downstream Pressure Pulse 2, P_{D2}, psi**	**Upstream Time to Collapse, t_U, msec**	**Downstream Time to Collapse, t_D, msec**	**Time Difference, $t_U - t_D$, msec**
1	1.771	17	0.0	280	320	200	140	5.95	5.75	0.20
2	1.771	17	0.0	320	270	120	120	4.50	5.00	-0.50
3	1.771	17	0.0	200	320	100	120	5.00	5.60	-0.60
4	1.771	17	0.0	350	380	80	100	4.70	5.30	-0.60
5	1.771	17	41.2	190	190	140	120	5.50	5.80	-0.30
6	1.771	17	41.2	110	290	80	100	4.55	4.95	-0.40
7	1.771	17	41.2	220	300	80	120	5.20	5.80	-0.60
8	1.771	17	41.2	430	420	180	220	6.40	6.80	-0.40
9	1.771	17	41.2	140	140	60	80	5.40	5.60	-0.20
10	1.771	17	96.0	200	200	100	110	5.30	5.75	-0.45
11	1.771	17	96.0	340	340	210	220	6.90	7.20	-0.30
12	1.771	17	96.0	220	380	80	100	5.35	5.70	-0.35
13	1.771	46	0.0	190	260	80	100	3.40	3.80	-0.40
14	1.771	46	0.0	300	300	60	100	2.80	3.40	-0.60
15	1.771	46	0.0	360	350	180	220	4.05	4.40	-0.35
16	1.771	46	22.0	180	320	80	180	3.35	3.85	-0.50
17	1.771	46	22.0	300	360	75	160	3.55	4.00	-0.45
18	1.771	46	22.0	360	360	260	200	4.30	4.40	-0.10
19	1.771	46	22.0	200	200	80	180	3.60	4.20	-0.60
20	1.771	46	42.0	200	180	100	160	3.35	3.80	-0.45
21	1.771	46	42.0	580	580	220	180	5.15	5.30	-0.15
22	1.771	46	42.0	290	300	130	270	4.00	4.35	-0.35
23	1.771	46	42.0	360	380	80	160	3.40	4.00	-0.60
24	1.771	58	0.0	340	440	100	120	3.25	3.50	-0.25
25	1.771	58	0.0	240	360	70	80	2.70	3.10	-0.40
26	1.771	58	0.0	340	400	80	100	3.00	3.15	-0.15
27	1.771	58	0.0	500	510	120	190	4.00	4.00	0.00
28	1.771	58	6.4	240	280	70	70	2.70	3.05	-0.35
29	1.771	58	6.4	430	430	240	200	4.20	4.20	0.00
30	1.771	58	6.4	260	260	80	110	3.00	3.30	-0.30
31	1.771	58	6.4	480	480	380	320	4.60	4.60	0.00

Table I - Raw Straight-Tube Test Data (cont'd)

Test #	Test Section ID, d_t, inches	Test Section Pressure, p_t, psi	Test Section Flow Rate, Q, gpm	Upstream Pressure Pulse 1, P_{U1}, psi	Downstream Pressure Pulse 1, P_{D1}, psi	Upstream Pressure Pulse 2, P_{U2}, psi	Downstream Pressure Pulse 2, P_{D2}, psi	Upstream Time to Collapse, t_U, msec	Downstream Time to Collapse, t_D, msec	Time Difference, $t_U - t_D$, msec
32	1.503	17	0	160	80	110	100	5.15	5.30	-0.15
33	1.503	17	0	180	240	95	80	6.10	6.30	-0.20
34	1.503	17	0	190	120	70	80	5.40	5.85	-0.45
35	1.503	17	0	190	190	90	60	6.60	6.60	0.00
36	1.503	17	42	280	310	200	70	7.20	6.80	0.40
37	1.503	17	42	180	180	65	65	6.00	6.00	0.00
38	1.503	17	42	360	370	320	80	7.80	7.40	0.40
39	1.503	17	42	150	150	70	60	6.00	5.80	0.20
40	1.503	17	101	200	300	65	65	5.05	5.20	-0.15
41	1.503	17	101	190	310	140	80	6.65	6.45	0.20
42	1.503	17	101	210	250	180	70	7.00	6.75	0.25
43	1.503	17	101	300	320	180	120	8.40	8.10	0.30
44	1.503	46	0	190	170	80	80	3.10	3.30	-0.20
45	1.503	46	0	170	210	90	80	3.45	3.65	-0.20
46	1.503	46	0	240	340	60	80	3.20	3.45	-0.25
47	1.503	46	0	130	130	80	80	3.20	3.40	-0.20
48	1.503	46	20	140	130	60	70	3.20	3.30	-0.10
49	1.503	46	20	280	300	75	60	3.80	3.85	-0.05
50	1.503	46	20	220	240	80	75	3.20	3.35	-0.15
51	1.503	46	20	130	180	60	60	3.25	3.35	-0.10
52	1.503	46	42	280	290	60	65	3.25	3.30	-0.05
53	1.503	46	42	190	120	60	80	3.15	3.25	-0.10
54	1.503	46	42	170	190	60	80	3.40	3.45	-0.05
55	1.503	46	42	240	200	90	80	3.30	3.30	0.00
56	1.503	58	0	120	140	100	80	3.00	3.00	0.00
57	1.503	58	0	200	200	80	60	3.00	3.00	0.00
58	1.503	58	0	300	300	80	100	3.15	3.15	0.00
59	1.503	58	0	270	270	100	80	3.50	3.50	0.00
60	1.503	58	12	350	380	100	110	3.15	3.15	0.00
61	1.503	58	12	140	230	90	60	2.95	2.95	0.00
62	1.503	58	12	290	290	100	95	2.80	2.80	0.00
63	1.503	58	12	480	480	80	120	3.50	3.50	0.00

Table I - Raw Straight-Tube Test Data (cont'd)

Test #	Test Section ID, d_t, inches	Test Section Pressure, p_t, psi	Test Section Flow Rate, Q, gpm	Upstream Pressure Pulse 1, P_{U1}, psi	Downstream Pressure Pulse 1, P_{D1}, psi	Upstream Pressure Pulse 2, P_{U2}, psi	Downstream Pressure Pulse 2, P_{D2}, psi	Upstream Time to Collapse, t_U, msec	Downstream Time to Collapse, t_D, msec	Time Difference, $t_U - t_D$, msec
64	1.100	17	0	450	450	250	175	6.60	6.00	0.60
65	1.100	17	0	475	475	225	150	6.40	6.00	0.40
66	1.100	17	0	475	475	200	200	5.80	5.40	0.40
67	1.100	17	0	425	425	350	100	8.40	8.10	0.30
68	1.100	17	40	400	375	200	125	6.70	6.40	0.30
69	1.100	17	40	450	400	200	150	7.20	6.80	0.40
70	1.100	17	40	450	400	300	125	8.00	7.40	0.60
71	1.100	17	40	425	400	275	100	7.70	7.30	0.40
72	1.100	17	100	450	450	125	150	10.80	10.10	0.70
73	1.100	17	100	475	475	125	275	11.00	10.40	0.60
74	1.100	17	100	500	500	200	125	11.70	10.60	1.10
75	1.100	17	100	475	450	125	100	11.70	10.70	1.00
76	1.100	17	100	400	400	50	100	10.00	10.50	-0.50
77	1.100	46	0	300	350	275	275	4.40	4.30	0.10
78	1.100	46	0	425	425	200	300	4.90	4.80	0.10
79	1.100	46	0	375	375	300	325	4.90	4.60	0.30
80	1.100	46	0	400	400	325	275	4.60	4.40	0.20
81	1.100	46	20	450	350	250	100	4.80	4.60	0.20
82	1.100	46	20	450	450	300	300	5.80	5.50	0.30
83	1.100	46	20	475	475	375	350	5.50	5.20	0.30
84	1.100	46	20	375	375	250	225	4.80	4.60	0.20
85	1.100	46	40	425	425	300	250	5.50	5.10	0.40
86	1.100	46	40	300	300	375	325	4.50	4.50	0.00
87	1.100	46	40	500	450	400	250	6.20	5.90	0.30
88	1.100	46	40	425	425	125	125	5.60	5.30	0.30
89	1.100	46	40	450	400	375	275	4.80	4.60	0.20
90	1.100	58	0	475	450	350	350	4.60	4.40	0.20
91	1.100	58	0	450	425	400	300	5.10	4.60	0.50
92	1.100	58	0	450	450	400	375	5.70	5.40	0.30
93	1.100	58	0	450	450	400	325	5.30	5.00	0.30
94	1.100	58	10	450	450	300	400	5.40	5.10	0.30
95	1.100	58	10	450	450	375	350	5.50	5.20	0.30
96	1.100	58	10	400	400	100	100	3.80	3.60	0.20
97	1.100	58	10	450	400	250	200	4.30	4.10	0.20

Table II - Calculated Straight-Tube Results

K_L, psi	323,000		μ_L, cP	0.92						
ρ_L, ppg	8.32		Q_{eL}, kJ	0.1						
c, ft/sec	4904		L_T, inches	18.00						
c_{min}, ft/sec	1364									
Test #	Test Section ID, d_t, inches	Test Section Pressure, p_t, psi	Test Section Flow Rate, Q, gpm	Test Section Fluid Velocity, V_f, ft/sec	Reynolds Number = $\rho_L V_f d_t / \mu_L$	Bubble Collapse Location, L_B, inches	Measured Bubble Lifetime, T, msec	Theoretical Bubble Lifetime, ms	Theoretical Bubble Diameter, inches	Theoretical Maximum Water-Hammer Pressure, psi
1	1.771	17	0	0.0	0.00E+00	1.64	5.30	4.38	2.43	0
2	1.771	17	0	0.0	0.00E+00	-4.09	4.20	4.38	2.43	0
3	1.771	17	0	0.0	0.00E+00	-4.91	4.75	4.38	2.43	0
4	1.771	17	0	0.0	0.00E+00	-4.91	4.45	4.38	2.43	0
5	1.771	17	41.2	5.4	7.97E+04	-2.46	5.10	4.38	2.43	98
6	1.771	17	41.2	5.4	7.97E+04	-3.27	4.20	4.38	2.43	98
7	1.771	17	41.2	5.4	7.97E+04	-4.91	4.95	4.38	2.43	98
8	1.771	17	41.2	5.4	7.97E+04	-3.27	6.05	4.38	2.43	98
9	1.771	17	41.2	5.4	7.97E+04	-1.64	4.95	4.38	2.43	98
10	1.771	17	96	12.5	1.86E+05	-3.68	4.98	4.38	2.43	229
11	1.771	17	96	12.5	1.86E+05	-2.46	6.50	4.38	2.43	229
12	1.771	17	96	12.5	1.86E+05	-2.86	4.98	4.38	2.43	229
13	1.771	46	0	0.0	0.00E+00	-3.27	3.05	2.64	1.41	0
14	1.771	46	0	0.0	0.00E+00	-4.91	2.55	2.64	1.41	0
15	1.771	46	0	0.0	0.00E+00	-2.86	3.68	2.64	1.41	0
16	1.771	46	22	2.9	4.26E+04	-4.09	3.05	2.64	1.41	53
17	1.771	46	22	2.9	4.26E+04	-3.68	3.23	2.64	1.41	53
18	1.771	46	22	2.9	4.26E+04	-0.82	3.80	2.64	1.41	53
19	1.771	46	22	2.9	4.26E+04	-4.91	3.35	2.64	1.41	53
20	1.771	46	42	5.5	8.12E+04	-3.68	3.03	2.64	1.41	100
21	1.771	46	42	5.5	8.12E+04	-1.23	4.68	2.64	1.41	100
22	1.771	46	42	5.5	8.12E+04	-2.86	3.63	2.64	1.41	100
23	1.771	46	42	5.5	8.12E+04	-4.91	3.15	2.64	1.41	100
24	1.771	58	0	0.0	0.00E+00	-2.05	2.83	2.31	1.21	0
25	1.771	58	0	0.0	0.00E+00	-3.27	2.35	2.31	1.21	0
26	1.771	58	0	0.0	0.00E+00	-1.23	2.53	2.31	1.21	0
27	1.771	58	0	0.0	0.00E+00	0.00	3.45	2.31	1.21	0
28	1.771	58	6.4	0.8	1.24E+04	-2.86	2.33	2.31	1.21	15
29	1.771	58	6.4	0.8	1.24E+04	0.00	3.65	2.31	1.21	15
30	1.771	58	6.4	0.8	1.24E+04	-2.46	2.60	2.31	1.21	15
31	1.771	58	6.4	0.8	1.24E+04	0.00	4.05	2.31	1.21	15

			Table II - Calculated Straight-Tube Results (cont'd)							
Test #	Test Section ID, d_t , inches	Test Section Pressure, p_t , psi	Test Section Flow Rate, Q , gpm	Test Section Fluid Velocity, V_f , ft/sec	Reynolds Number = $\rho_L V_f d_t / \mu_L$	Bubble Collapse Location, L_B , inches	Measured Bubble Lifetime, T , msec	Theoretical Bubble Lifetime, ms	Theoretical Bubble Diameter, inches	Theoretical Maximum Water-Hammer Pressure, psi
32	1.503	17	0	0.0	0.00E+00	-1.23	4.68	4.38	2.43	0
33	1.503	17	0	0.0	0.00E+00	-1.64	5.65	4.38	2.43	0
34	1.503	17	0	0.0	0.00E+00	-3.68	5.08	4.38	2.43	0
35	1.503	17	0	0.0	0.00E+00	0.00	6.05	4.38	2.43	0
36	1.503	17	42	7.6	9.57E+04	3.27	6.45	4.38	2.43	139
37	1.503	17	42	7.6	9.57E+04	0.00	5.45	4.38	2.43	139
38	1.503	17	42	7.6	9.57E+04	3.27	7.05	4.38	2.43	139
39	1.503	17	42	7.6	9.57E+04	1.64	5.35	4.38	2.43	139
40	1.503	17	101	18.3	2.30E+05	-1.23	4.58	4.38	2.43	335
41	1.503	17	101	18.3	2.30E+05	1.64	6.00	4.38	2.43	335
42	1.503	17	101	18.3	2.30E+05	2.05	6.33	4.38	2.43	335
43	1.503	17	101	18.3	2.30E+05	2.46	7.70	4.38	2.43	335
44	1.503	46	0	0.0	0.00E+00	-1.64	2.65	2.64	1.41	0
45	1.503	46	0	0.0	0.00E+00	-1.64	3.00	2.64	1.41	0
46	1.503	46	0	0.0	0.00E+00	-2.05	2.78	2.64	1.41	0
47	1.503	46	0	0.0	0.00E+00	-1.64	2.75	2.64	1.41	0
48	1.503	46	20	3.6	4.56E+04	-0.82	2.70	2.64	1.41	66
49	1.503	46	20	3.6	4.56E+04	-0.41	3.28	2.64	1.41	66
50	1.503	46	20	3.6	4.56E+04	-1.23	2.73	2.64	1.41	66
51	1.503	46	20	3.6	4.56E+04	-0.82	2.75	2.64	1.41	66
52	1.503	46	42	7.6	9.57E+04	-0.41	2.73	2.64	1.41	139
53	1.503	46	42	7.6	9.57E+04	-0.82	2.65	2.64	1.41	139
54	1.503	46	42	7.6	9.57E+04	-0.41	2.88	2.64	1.41	139
55	1.503	46	42	7.6	9.57E+04	0.00	2.75	2.64	1.41	139
56	1.503	58	0	0.0	0.00E+00	0.00	2.45	2.31	1.21	0
57	1.503	58	0	0.0	0.00E+00	0.00	2.45	2.31	1.21	0
58	1.503	58	0	0.0	0.00E+00	0.00	2.60	2.31	1.21	0
59	1.503	58	0	0.0	0.00E+00	0.00	2.95	2.31	1.21	0
60	1.503	58	11.6	2.1	2.64E+04	0.00	2.60	2.31	1.21	38
61	1.503	58	11.6	2.1	2.64E+04	0.00	2.40	2.31	1.21	38
62	1.503	58	11.6	2.1	2.64E+04	0.00	2.25	2.31	1.21	38
63	1.503	58	11.6	2.1	2.64E+04	0.00	2.95	2.31	1.21	38

			Table II - Calculated Straight-Tube Results (cont'd)							
Test #	Test Section ID, d_t , inches	Test Section Pressure, p_t , psi	Test Section Flow Rate, Q , gpm	Test Section Fluid Velocity, V_f , ft/sec	Reynolds Number = $\rho_L V_f d_t / \mu_L$	Bubble Collapse Location, L_B , inches	Measured Bubble Lifetime, T , msec	Theoretical Bubble Lifetime, ms	Theoretical Bubble Diameter, inches	Theoretical Maximum Water-Hammer Pressure, psi
64	1.100	17	0	0.0	0.00E+00	4.91	5.75	4.38	2.43	0
65	1.100	17	0	0.0	0.00E+00	3.27	5.65	4.38	2.43	0
66	1.100	17	0	0.0	0.00E+00	3.27	5.05	4.38	2.43	0
67	1.100	17	0	0.0	0.00E+00	2.46	7.70	4.38	2.43	0
68	1.100	17	40	13.5	1.25E+05	2.46	6.00	4.38	2.43	248
69	1.100	17	40	13.5	1.25E+05	3.27	6.45	4.38	2.43	248
70	1.100	17	40	13.5	1.25E+05	4.91	7.15	4.38	2.43	248
71	1.100	17	40	13.5	1.25E+05	3.27	6.95	4.38	2.43	248
72	1.100	17	100	33.8	3.11E+05	5.73	9.90	4.38	2.43	619
73	1.100	17	100	33.8	3.11E+05	4.91	10.15	4.38	2.43	619
74	1.100	17	100	33.8	3.11E+05	9.00	10.60	4.38	2.43	619
75	1.100	17	100	33.8	3.11E+05	8.18	10.65	4.38	2.43	619
76	1.100	17	100	33.8	3.11E+05	-4.09	9.70	4.38	2.43	619
77	1.100	46	0	0.0	0.00E+00	0.82	3.80	2.64	1.41	0
78	1.100	46	0	0.0	0.00E+00	0.82	4.30	2.64	1.41	0
79	1.100	46	0	0.0	0.00E+00	2.46	4.20	2.64	1.41	0
80	1.100	46	0	0.0	0.00E+00	1.64	3.95	2.64	1.41	0
81	1.100	46	20	6.8	6.23E+04	1.64	4.15	2.64	1.41	124
82	1.100	46	20	6.8	6.23E+04	2.46	5.10	2.64	1.41	124
83	1.100	46	20	6.8	6.23E+04	2.46	4.80	2.64	1.41	124
84	1.100	46	20	6.8	6.23E+04	1.64	4.15	2.64	1.41	124
85	1.100	46	40	13.5	1.25E+05	3.27	4.75	2.64	1.41	248
86	1.100	46	40	13.5	1.25E+05	0.00	3.95	2.64	1.41	248
87	1.100	46	40	13.5	1.25E+05	2.46	5.50	2.64	1.41	248
88	1.100	46	40	13.5	1.25E+05	2.46	4.90	2.64	1.41	248
89	1.100	46	40	13.5	1.25E+05	1.64	4.15	2.64	1.41	248
90	1.100	58	0	0.0	0.00E+00	1.64	3.95	2.31	1.21	0
91	1.100	58	0	0.0	0.00E+00	4.09	4.30	2.31	1.21	0
92	1.100	58	0	0.0	0.00E+00	2.46	5.00	2.31	1.21	0
93	1.100	58	0	0.0	0.00E+00	2.46	4.60	2.31	1.21	0
94	1.100	58	10	3.4	3.11E+04	2.46	4.70	2.31	1.21	62
95	1.100	58	10	3.4	3.11E+04	2.46	4.80	2.31	1.21	62
96	1.100	58	10	3.4	3.11E+04	1.64	3.15	2.31	1.21	62
97	1.100	58	10	3.4	3.11E+04	1.64	3.65	2.31	1.21	62

					Table III - Raw Nozzle/Orifice Test Data					
Test Numbers			1 thru 30	30 thru 67	68 thru 95	96 thru 125	**Power Supply charge = 100 J in all tests**			
Test Section			1.5 inch XXS	1.5 inch XXS	1.5 inch XXS	1.5 inch XXS				
Test-Section ID, inches			1.100	1.100	1.100	1.100				
Configuration			Spark Plug above Orifice	Spark Plug below Orifice	Spark Plug below L&W Nozzle	Spark Plug above L&W Nozzle				
Spark Plug Manufacturer			Champion	Champion	Champion	Champion				
Spark Plug Model			JBC	JBC	H10C	L86C(H)				
Spark Plug Gap, mm			1.0	1.0	1.0	1.0				
Spark Plug Extension, inches			5/16	5/16						
Cathode Orientation			3:00	2:00	7:00	12:00				
Test #	**Test Section ID, d_t, inches**	**Test Section Pressure, p_t, psi**	**Test Section Flow Rate, Q, gpm**	**Upstream Pressure Pulse 1, P_{U1}, psi**	**Downstream Pressure Pulse 1, P_{D1}, psi**	**Upstream Pressure Pulse 2, P_{U2}, psi**	**Downstream Pressure Pulse 2, P_{D2}, psi**	**Upstream Time to Collapse, t_U, msec**	**Downstream Time to Collapse, t_D, msec**	**Time Difference, $t_U - t_D$, msec**
1	1.100	50	0.0			180	70	5.00	4.50	0.50
2	1.100	50	0.0			80	50	4.80	4.20	0.60
3	1.100	50	0.0			130	55	4.50	3.90	0.60
4	1.100	50	45.6			195	30	4.80	3.80	1.00
5	1.100	50	45.6			95	50	3.80	5.40	-1.60
6	1.100	50	45.6			80	65	4.00	5.90	-1.90
7	1.100	50	5.0			50	50	5.70	4.90	0.80
8	1.100	50	5.0			80	40	4.60	4.20	0.40
9	1.100	50	5.0			70	50	4.20	3.90	0.30
10	1.100	50	20.0			80	40	4.65	4.60	0.05
11	1.100	50	20.0			50	50	4.30	4.30	0.00
12	1.100	50	20.0			60	50	5.20	5.40	-0.20
13	1.100	58	0.0			70	430	4.20	5.00	-0.80
14	1.100	58	0.0			65	85	5.10	5.30	-0.20
15	1.100	58	0.0			150	90	4.75	4.90	-0.15
16	1.100	58	12.8			75	270	4.25	5.25	-1.00
17	1.100	58	12.8			105	395	4.50	5.20	-0.70
18	1.100	58	12.8			70	370	4.05	4.80	-0.75
19	1.100	17	48.0			110	35	8.35	6.05	2.30
20	1.100	17	48.0							
21	1.100	17	48.0			140	40	10.50	8.70	1.80
22	1.100	17	8.0			80	50	9.40	9.00	0.40
23	1.100	17	8.0			50	60	10.00	9.20	0.80
24	1.100	17	8.0			60	50	9.30	8.70	0.60
25	1.100	17	0.0			50	50	10.20	8.80	1.40
26	1.100	17	0.0			50	40	9.40	8.60	0.80
27	1.100	17	0.0			70	30	8.90	8.10	0.80
28	1.100	17	34.0			150	40	8.20	10.60	-2.40
29	1.100	17	34.0			220	50	11.00	10.50	0.50
30	1.100	17	34.0			190	60	7.60	11.10	-3.50

Table III - Raw Nozzle/Orifice Test Data (cont'd)

Test #	Test Section ID, d_t, inches	Test Section Pressure, p_t, psi	Test Section Flow Rate, Q, gpm	Upstream Pressure Pulse 1, P_{U1}, psi	Downstream Pressure Pulse 1, P_{D1}, psi	Upstream Pressure Pulse 2, P_{U2}, psi	Downstream Pressure Pulse 2, P_{D2}, psi	Upstream Time to Collapse, t_U, msec	Downstream Time to Collapse, t_D, msec	Time Difference, $t_U - t_D$, msec
31	1.100	50	0.0			120	120	4.70	4.10	0.60
32	1.100	50	0.0			120	120	4.60	4.20	0.40
33	1.100	50	0.0			100	220	5.10	4.40	0.70
34	1.100	50	45.6			60	120	4.70	4.10	0.60
35	1.100	50	45.6			40	120	4.70	4.30	0.40
36	1.100	50	45.6			40	240	4.80	4.60	0.20
37	1.100	50	9.0			100	50	4.80	4.20	0.60
38	1.100	50	9.0			50	50	3.10	3.00	0.10
39	1.100	50	9.0			60	60	4.40	4.00	0.40
40	1.100	50	20.0			80	60	4.80	4.00	0.80
41	1.100	50	20.0			70	60	4.50	4.00	0.50
42	1.100	50	20.0			80	60	4.90	4.20	0.70
43	1.100	58	0.0			80	60	3.90	3.80	0.10
44	1.100	58	0.0			70	80	3.80	3.70	0.10
45	1.100	58	0.0			80	80	4.10	3.80	0.30
45.5	1.100	58	0.0			80	90	3.90	3.60	0.30
46	1.100	58	12.8			80	60	4.40	4.00	0.40
47	1.100	58	12.8			80	80	4.20	3.90	0.30
48	1.100	58	12.8			90	60	4.60	4.30	0.30
49	1.100	17	48.0					-		-
49.3	1.100	17	48.0			0	20	-	9.75	-
49.7	1.100	17	48.0			0	35	-	10.00	-
50	1.100	17	48.0			0	40	-	9.25	-
51	1.100	17	48.0			0	25	-	9.50	-
52	1.100	17	8.0			15	55	7.75	6.75	1.00
53	1.100	17	8.0			60	45	7.75	7.75	0.00
54	1.100	17	8.0			15	45	7.25	7.00	0.25
55	1.100	17	0.0			20	65	7.50	7.25	0.25
56	1.100	17	0.0			30	50	7.00	7.25	-0.25
57	1.100	17	0.0			30	65	7.00	7.00	0.00
58	1.100	17	0.0			20	60	7.20	7.20	0.00
59	1.100	17	36.0			0	55	-	7.70	-
60	1.100	17	36.0			0	60	-	8.20	-
61	1.100	17	36.0			25	80	7.30	6.90	0.40
62	1.100	50	0.0			80	60	5.40	4.60	0.80
63	1.100	50	0.0			75	95	5.00	4.60	0.40
64	1.100	50	0.0			80	60	5.20	4.50	0.70
65	1.100	50	30.0			0	20	-	5.80	-
66	1.100	50	30.0			-	-	-	-	-
67	1.100	50	30.0			0	25	-	5.40	-

Table III - Raw Nozzle/Orifice Test Data (cont'd)

Test #	Test Section ID, d_t, inches	Test Section Pressure, p_t, psi	Test Section Flow Rate, Q, gpm	Upstream Pressure Pulse 1, P_{U1}, psi	Downstream Pressure Pulse 1, P_{D1}, psi	Upstream Pressure Pulse 2, P_{U2}, psi	Downstream Pressure Pulse 2, P_{D2}, psi	Upstream Time to Collapse, t_U, msec	Downstream Time to Collapse, t_D, msec	Time Difference, $t_U - t_D$, msec
68	1.100	50	36.0	-	-	0	40	-	8.00	-
69	1.100	50	36.0	-	-	0	40	-	7.00	-
70	1.100	50	36.0	-	-	0	50	-	9.00	-
71	1.100	50	8.0	-	-	370	160	5.10	4.40	0.70
71.5	1.100	50	8.0	-	-	365	140	5.30	4.40	0.90
72.5	1.100	50	5.0	-	-	280	85	5.50	4.50	1.00
73	1.100	50	5.0	-	-	390	70	5.40	4.50	0.90
74	1.100	50	5.0	-	-	345	50	5.40	4.80	0.60
75	1.100	50	20.0	-	-	85	85	4.50	4.60	-0.10
76	1.100	50	20.0	-	-	90	55	4.40	4.40	0.00
77	1.100	50	20.0	-	-	145	70	5.40	5.20	0.20
78	1.100	58	0.0	-	-	260	110	4.30	3.80	0.50
79	1.100	58	0.0	-	-	245	80	4.20	3.60	0.60
80	1.100	58	0.0	-	-	190	100	4.40	3.80	0.60
81	1.100	58	18.0	-	-	80	100	4.00	4.60	-0.60
82	1.100	58	18.0	-	-	65	65	3.60	4.20	-0.60
83	1.100	58	18.0	-	-	40	65	3.60	4.10	-0.50
84	1.100	58	5.0	-	-	85	85	3.90	3.70	0.20
85	1.100	58	5.0	-	-	140	85	4.00	3.80	0.20
86	1.100	58	5.0	-	-	65	90	5.00	4.80	0.20
87	1.100	17	18.0	-	-	45	65	9.40	8.20	1.20
88	1.100	17	18.0	-	-	75	45	8.70	7.70	1.00
89	1.100	17	18.0	-	-	100	55	11.40	7.90	3.50
90	1.100	17	6.8	-	-	90	50	10.30	7.70	2.60
91	1.100	17	6.8	-	-	225	60	10.80	6.90	3.90
92	1.100	17	6.8	-	-	95	55	10.40	6.90	3.50
93	1.100	17	0.0	-	-	220	60	11.30	7.00	4.30
94	1.100	17	0.0	-	-	185	70	13.20	6.90	6.30
95	1.100	17	0.0	-	-	330	45	10.80	7.10	3.70

Table III - Raw Nozzle/Orifice Test Data (cont'd)

Test #	Test Section ID, d_t , inches	Test Section Pressure, p_t , psi	Test Section Flow Rate, Q , gpm	Upstream Pressure Pulse 1, P_{U1} , psi	Downstream Pressure Pulse 1, P_{D1} , psi	Upstream Pressure Pulse 2, P_{U2} , psi	Downstream Pressure Pulse 2, P_{D2} , psi	Upstream Time to Collapse, t_U , msec	Downstream Time to Collapse, t_D , msec	Time Difference, $t_U - t_D$, msec
96	1.100	50	0.0	-	-	115	45	4.80	4.00	0.80
97	1.100	50	0.0	-	-	60	30	4.90	4.00	0.90
98	1.100	50	0.0	-	-	85	55	5.00	5.00	0.00
99	1.100	50	34.0	-	-	80	15	4.80	4.40	0.40
100	1.100	50	34.0	-	-	60	25	4.20	4.00	0.20
101	1.100	50	34.0	-	-	0	25	-	4.60	-
102	1.100	50	20.0	-	-	0	25	-	6.90	-
103	1.100	50	20.0	-	-	45	55	5.90	5.00	0.90
104	1.100	50	20.0	-	-	65	50	5.60	5.00	0.60
105	1.100	50	5.0	-	-	55	60	4.50	4.50	0.00
106	1.100	50	5.0	-	-	30	70	4.60	4.40	0.20
107	1.100	50	5.0	-	-	50	55	6.20	6.00	0.20
108	1.100	58	0.0	-	-	50	75	5.70	5.70	0.00
109	1.100	58	0.0	-	-	25	70	5.20	5.70	-0.50
110	1.100	58	0.0	-	-					
111	1.100	58	20.8	-	-	50	40	4.00	4.60	-0.60
112	1.100	58	20.8	-	-	35	35	3.60	4.00	-0.40
113	1.100	58	20.8	-	-	50	20	4.30	4.00	0.30
114	1.100	58	6.8	-	-	40	40	4.10	4.20	-0.10
115	1.100	58	6.8	-	-	60	60	4.20	4.60	-0.40
116	1.100	58	6.8	-	-	45	60	4.20	3.70	0.50
117	1.100	17	22.0	-	-	80	0	10.20	-	-
118	1.100	17	22.0	-	-	50	40	9.70	10.10	-0.40
119	1.100	17	22.0	-	-					
120	1.100	17	4.0	-	-	50	40	7.50	8.90	-1.40
121	1.100	17	4.0	-	-	35	40	7.20	8.60	-1.40
122	1.100	17	4.0	-	-	30	40	7.20	8.60	-1.40
123	1.100	17	0.0	-	-	100	25	10.00	8.60	1.40
124	1.100	17	0.0	-	-	50	105	10.60	11.00	-0.40
125	1.100	17	0.0	-	-	30	70	10.60	11.80	-1.20

		Table IV - Calculated Nozzle/Orifice Results					
K_L , psi	323,000		μ_L , cP	0.92			
ρ_L , ppg	8.32		Q_{eL} , kJ	0.1			
c , ft/sec	4904		L_T , inches	18.00			
c_{min} , ft/sec	1364						
Test #	Test Section ID, d_t , inches	Test Section Pressure, p_t , psi	Test Section Flow Rate, Q , gpm	Test Section Fluid Velocity, V_f , ft/sec	Reynolds Number = $\rho_L V_f d_t / \mu_L$	Measured Bubble Lifetime, T , msec	Theoretical Bubble Lifetime, ms
1	1.100	50	0	0.0	0.00E+00	4.20	2.27
2	1.100	50	0	0.0	0.00E+00	3.95	2.27
3	1.100	50	0	0.0	0.00E+00	3.65	2.27
4	1.100	50	45.6	15.4	1.42E+05	3.75	2.27
5	1.100	50	45.6	15.4	1.42E+05	4.05	2.27
6	1.100	50	45.6	15.4	1.42E+05	4.40	2.27
7	1.100	50	5	1.7	1.56E+04	4.75	2.27
8	1.100	50	5	1.7	1.56E+04	3.85	2.27
9	1.100	50	5	1.7	1.56E+04	3.50	2.27
10	1.100	50	20	6.8	6.23E+04	4.08	2.27
11	1.100	50	20	6.8	6.23E+04	3.75	2.27
12	1.100	50	20	6.8	6.23E+04	4.75	2.27
13	1.100	58	0	0.0	0.00E+00	4.05	2.06
14	1.100	58	0	0.0	0.00E+00	4.65	2.06
15	1.100	58	0	0.0	0.00E+00	4.28	2.06
	1.100						
16	1.100	58	12.8	4.3	3.99E+04	4.20	2.06
17	1.100	58	12.8	4.3	3.99E+04	4.30	2.06
18	1.100	58	12.8	4.3	3.99E+04	3.88	2.06
19	1.100	17	48	16.2	1.49E+05	6.65	4.13
20	1.100	17	48	16.2	1.49E+05		4.13
21	1.100	17	48	16.2	1.49E+05	9.05	4.13
22	1.100	17	8	2.7	2.49E+04	8.65	4.13
23	1.100	17	8	2.7	2.49E+04	9.05	4.13
24	1.100	17	8	2.7	2.49E+04	8.45	4.13
25	1.100	17	0	0.0	0.00E+00	8.95	4.13
26	1.100	17	0	0.0	0.00E+00	8.45	4.13
27	1.100	17	0	0.0	0.00E+00	7.95	4.13
28	1.100	17	34	11.5	1.06E+05	8.85	4.13
29	1.100	17	34	11.5	1.06E+05	10.20	4.13
30	1.100	17	34	11.5	1.06E+05	8.80	4.13

Table IV - Calculated Nozzle/Orifice Results (cont'd)

Test #	Test Section ID, d_t, inches	Test Section Pressure, p_t, psi	Test Section Flow Rate, Q, gpm	Test Section Fluid Velocity, V_f, ft/sec	Reynolds Number = $\rho_L V_f d_t / \mu_L$	Measured Bubble Lifetime, T, msec	Theoretical Bubble Lifetime, ms
31	1.100	50	0	0.0	0.00E+00	3.85	2.27
32	1.100	50	0	0.0	0.00E+00	3.85	2.27
33	1.100	50	0	0.0	0.00E+00	4.20	2.27
34	1.100	50	45.6	15.4	1.42E+05	3.85	2.27
35	1.100	50	45.6	15.4	1.42E+05	3.95	2.27
36	1.100	50	45.6	15.4	1.42E+05	4.15	2.27
37	1.100	50	9	3.0	2.80E+04	3.95	2.27
38	1.100	50	9	3.0	2.80E+04	2.50	2.27
39	1.100	50	9	3.0	2.80E+04	3.65	2.27
	1.100			0.0	0.00E+00		
40	1.100	50	20	6.8	6.23E+04	3.85	2.27
41	1.100	50	20	6.8	6.23E+04	3.70	2.27
42	1.100	50	20	6.8	6.23E+04	4.00	2.27
43	1.100	58	0	0.0	0.00E+00	3.30	2.06
44	1.100	58	0	0.0	0.00E+00	3.20	2.06
45	1.100	58	0	0.0	0.00E+00	3.40	2.06
45R	1.100	58	0	0.0	0.00E+00	3.20	2.06
46	1.100	58	12.8	4.3	3.99E+04	3.65	2.06
47	1.100	58	12.8	4.3	3.99E+04	3.50	2.06
48	1.100	58	12.8	4.3	3.99E+04	3.90	2.06
49	1.100	17	48	16.2	1.49E+05	-	4.13
49R	1.100	17	48	16.2	1.49E+05	-	4.13
49R2	1.100	17	48	16.2	1.49E+05	-	4.13
50	1.100	17	48	16.2	1.49E+05	-	4.13
51	1.100	17	48	16.2	1.49E+05	-	4.13
52	1.100	17	8	2.7	2.49E+04	6.70	4.13
53	1.100	17	8	2.7	2.49E+04	7.20	4.13
54	1.100	17	8	2.7	2.49E+04	6.58	4.13
55	1.100	17	0	0.0	0.00E+00	6.83	4.13
56	1.100	17	0	0.0	0.00E+00	6.58	4.13
57	1.100	17	0	0.0	0.00E+00	6.45	4.13
58	1.100	17	0	0.0	0.00E+00	6.65	4.13
59	1.100	17	36	12.2	1.12E+05	-	4.13
60	1.100	17	36	12.2	1.12E+05	-	4.13
61	1.100	17	36	12.2	1.12E+05	6.55	4.13
62	1.100	50	0	0.0	0.00E+00	4.45	2.27
63	1.100	50	0	0.0	0.00E+00	4.25	2.27
64	1.100	50	0	0.0	0.00E+00	4.30	2.27
65	1.100	50	30	10.1	9.34E+04	-	2.27
66	1.100	50	30	10.1	9.34E+04	-	-
67	1.100	50	30	10.1	9.34E+04	-	2.27

	Table IV - Calculated Nozzle/Orifice Results (cont'd)						
Test #	Test Section ID, d_t, inches	Test Section Pressure, p_t, psi	Test Section Flow Rate, Q, gpm	Test Section Fluid Velocity, V_f, ft/sec	Reynolds Number = $\rho_L V_f d_t / \mu_L$	Measured Bubble Lifetime, T, msec	Theoretical Bubble Lifetime, ms
68	1.100	50	36	12.2	1.12E+05	-	2.27
69	1.100	50	36	12.2	1.12E+05	-	2.27
70	1.100	50	36	12.2	1.12E+05	-	2.27
71	1.100	50	8	2.7	2.49E+04	4.20	2.27
71R	1.100	50	8	2.7	2.49E+04	4.30	2.27
72R	1.100	50	5	1.7	1.56E+04	4.45	2.27
73	1.100	50	5	1.7	1.56E+04	4.40	2.27
74	1.100	50	5	1.7	1.56E+04	4.55	2.27
75	1.100	50	20	6.8	6.23E+04	4.00	2.27
76	1.100	50	20	6.8	6.23E+04	3.85	2.27
77	1.100	50	20	6.8	6.23E+04	4.75	2.27
78	1.100	58	0	0.0	0.00E+00	3.50	2.06
79	1.100	58	0	0.0	0.00E+00	3.35	2.06
80	1.100	58	0	0.0	0.00E+00	3.55	2.06
81	1.100	58	18	6.1	5.61E+04	3.75	2.06
82	1.100	58	18	6.1	5.61E+04	3.35	2.06
83	1.100	58	18	6.1	5.61E+04	3.30	2.06
84	1.100	58	5	1.7	1.56E+04	3.25	2.06
85	1.100	58	5	1.7	1.56E+04	3.35	2.06
86	1.100	58	5	1.7	1.56E+04	4.35	2.06
87	1.100	17	18	6.1	5.61E+04	8.25	4.13
88	1.100	17	18	6.1	5.61E+04	7.65	4.13
89	1.100	17	18	6.1	5.61E+04	9.10	4.13
90	1.100	17	6.8	2.3	2.12E+04	8.45	4.13
91	1.100	17	6.8	2.3	2.12E+04	8.30	4.13
92	1.100	17	6.8	2.3	2.12E+04	8.10	4.13
93	1.100	17	0	0.0	0.00E+00	8.60	4.13
94	1.100	17	0	0.0	0.00E+00	9.50	4.13
95	1.100	17	0	0.0	0.00E+00	8.40	4.13

Table IV - Calculated Nozzle/Orifice Results (cont'd)

Test #	Test Section ID, d_t , inches	Test Section Pressure, p_t , psi	Test Section Flow Rate, Q , gpm	Test Section Fluid Velocity, V_f , ft/sec	Reynolds Number = $\rho_L V_f d_t / \mu_L$	Measured Bubble Lifetime, T , msec	Theoretical Bubble Lifetime, ms
96	1.100	50	0	0.0	0.00E+00	3.85	2.27
97	1.100	50	0	0.0	0.00E+00	3.90	2.27
98	1.100	50	0	0.0	0.00E+00	4.45	2.27
99	1.100	50	34	11.5	1.06E+05	4.05	2.27
100	1.100	50	34	11.5	1.06E+05	3.55	2.27
101	1.100	50	34	11.5	1.06E+05	-	2.27
102	1.100	50	20	6.8	6.23E+04		2.27
103	1.100	50	20	6.8	6.23E+04	4.90	2.27
104	1.100	50	20	6.8	6.23E+04	4.75	2.27
105	1.100	50	5	1.7	1.56E+04	3.95	2.27
106	1.100	50	5	1.7	1.56E+04	3.95	2.27
107	1.100	50	5	1.7	1.56E+04	5.55	2.27
108	1.100	58	0	0.0	0.00E+00	5.15	2.06
109	1.100	58	0	0.0	0.00E+00	4.90	2.06
110	1.100	58	0	0.0	0.00E+00	-0.55	2.06
111	1.100	58	20.8	7.0	6.48E+04	3.75	2.06
112	1.100	58	20.8	7.0	6.48E+04	3.25	2.06
113	1.100	58	20.8	7.0	6.48E+04	3.60	2.06
114	1.100	58	6.8	2.3	2.12E+04	3.60	2.06
115	1.100	58	6.8	2.3	2.12E+04	3.85	2.06
116	1.100	58	6.8	2.3	2.12E+04	3.40	2.06
117	1.100	17	22	7.4	6.85E+04	-	4.13
118	1.100	17	22	7.4	6.85E+04	9.35	4.13
119	1.100	17	22	7.4	6.85E+04	-0.55	4.13
120	1.100	17	4	1.4	1.25E+04	7.65	4.13
121	1.100	17	4	1.4	1.25E+04	7.35	4.13
122	1.100	17	4	1.4	1.25E+04	7.35	4.13
123	1.100	17	0	0.0	0.00E+00	8.75	4.13
124	1.100	17	0	0.0	0.00E+00	10.25	4.13
125	1.100	17	0	0.0	0.00E+00	10.65	4.13

APPENDIX Cb – GRAPHS

Graph 1 – Upstream pressure transducer readings for all straight-tube tests.
(t_U = black diamonds; P_{U1} = blue squares; P_{U2} = red triangles)

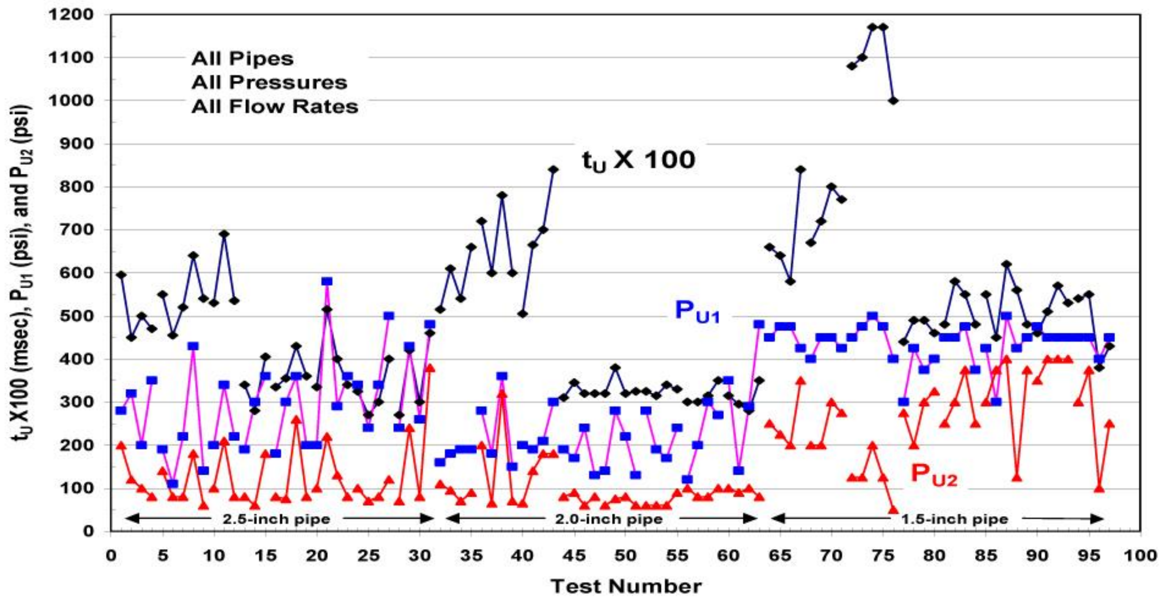

Graph 2 – Downstream pressure transducer readings for all straight-tube tests.
(t_D = black diamonds; P_{D1} = blue squares; P_{D2} = red triangles)

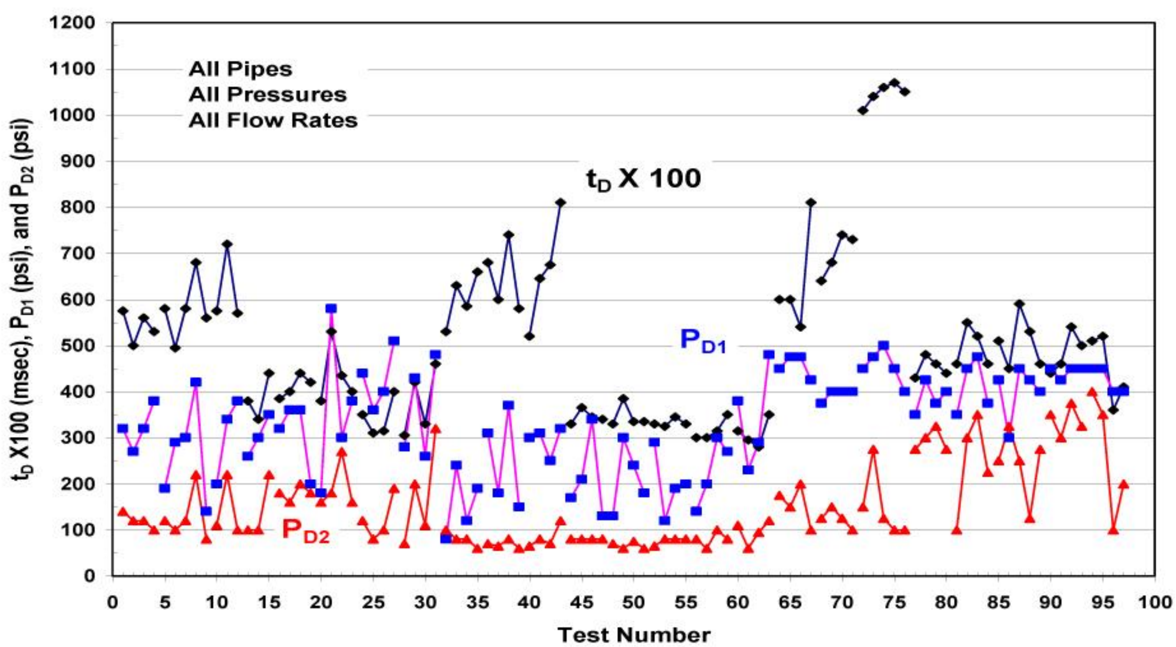

Graph 3 – Measured straight-tube bubble collapse locations based on minimum sonic velocity.

(Ambient pressure: 17 psi = squares and long lines; 42 psi = diamonds and medium lines; 58 psi = triangles and short lines)

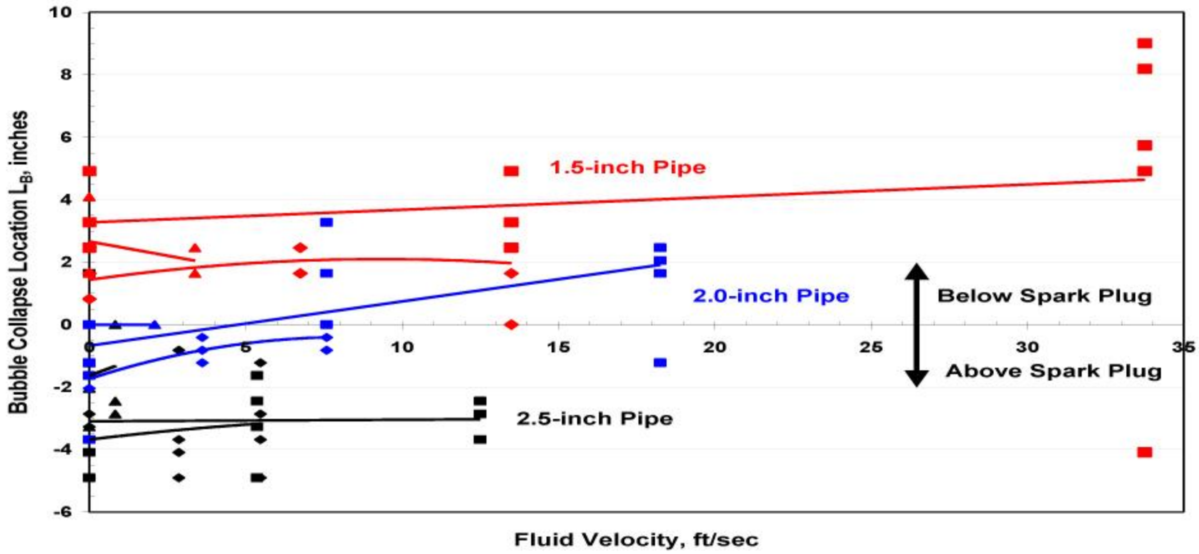

Graph 4 – Effects of test section pressure on bubble lifetime in straight-tube tests.

(2.5- inch test section @ 0 ft/sec = black bars; 2.0-inch test section @ 0 ft/sec = blue bars; 1.5-inch test section @ 0 ft/sec = red bars; all other data = green diamonds)

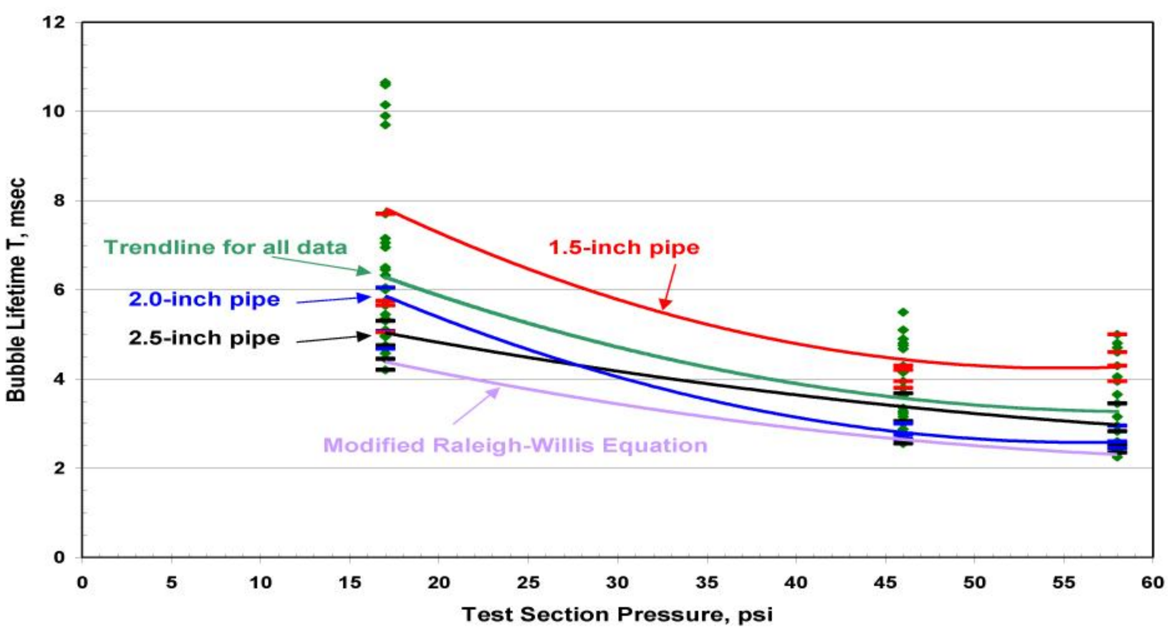

Graph 5 – Maximum upstream pressure transducer readings during bubble expansion in straight-tube tests.

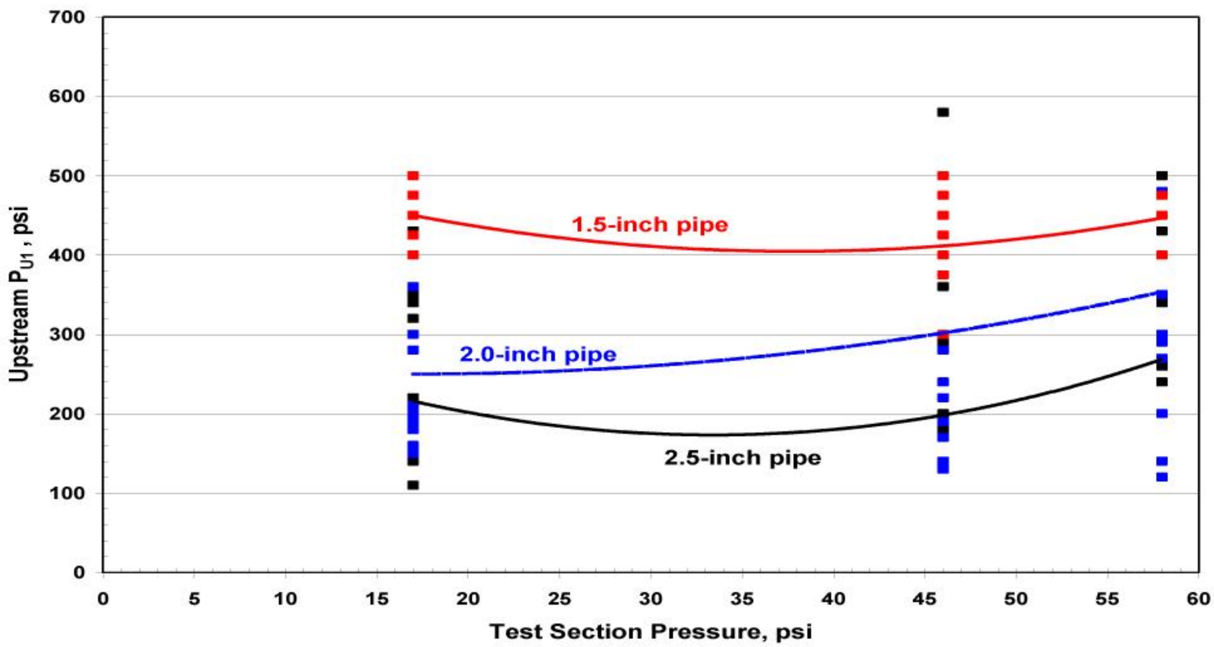

Graph 6 – Maximum upstream pressure transducer readings during bubble collapse in straight-tube tests.

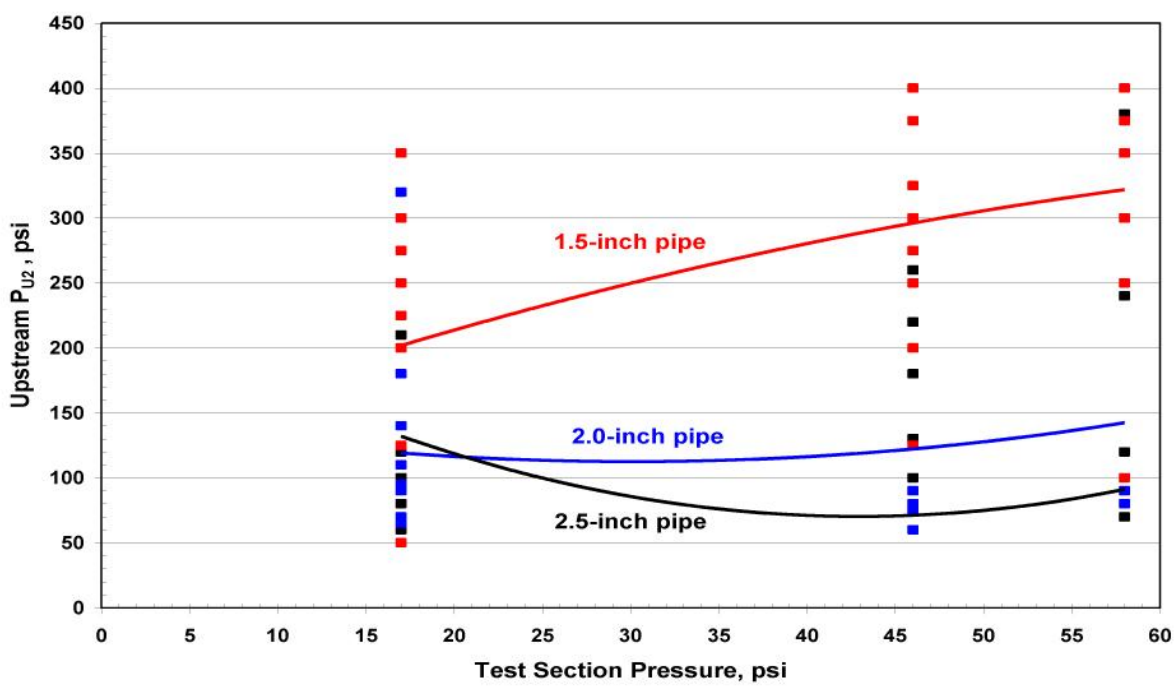

Graph 7 – Maximum downstream pressure transducer readings during bubble expansion in straight-tube tests.

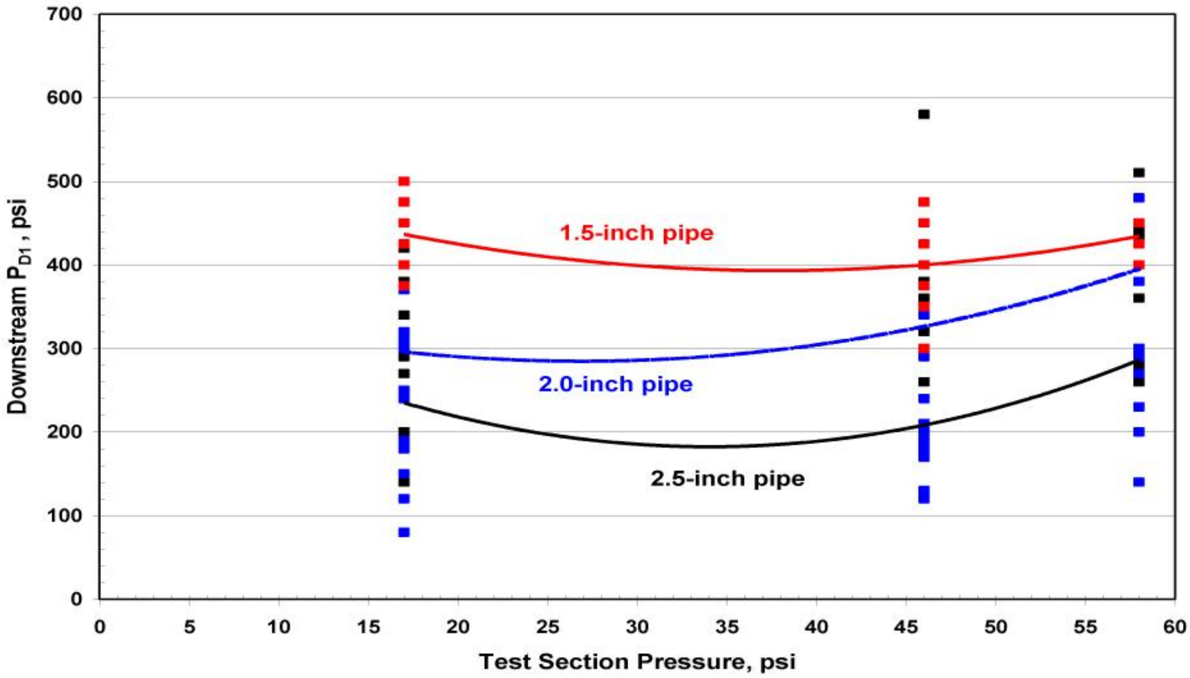

Graph 8 – Maximum downstream pressure transducer readings during bubble collapse in straight-tube tests.

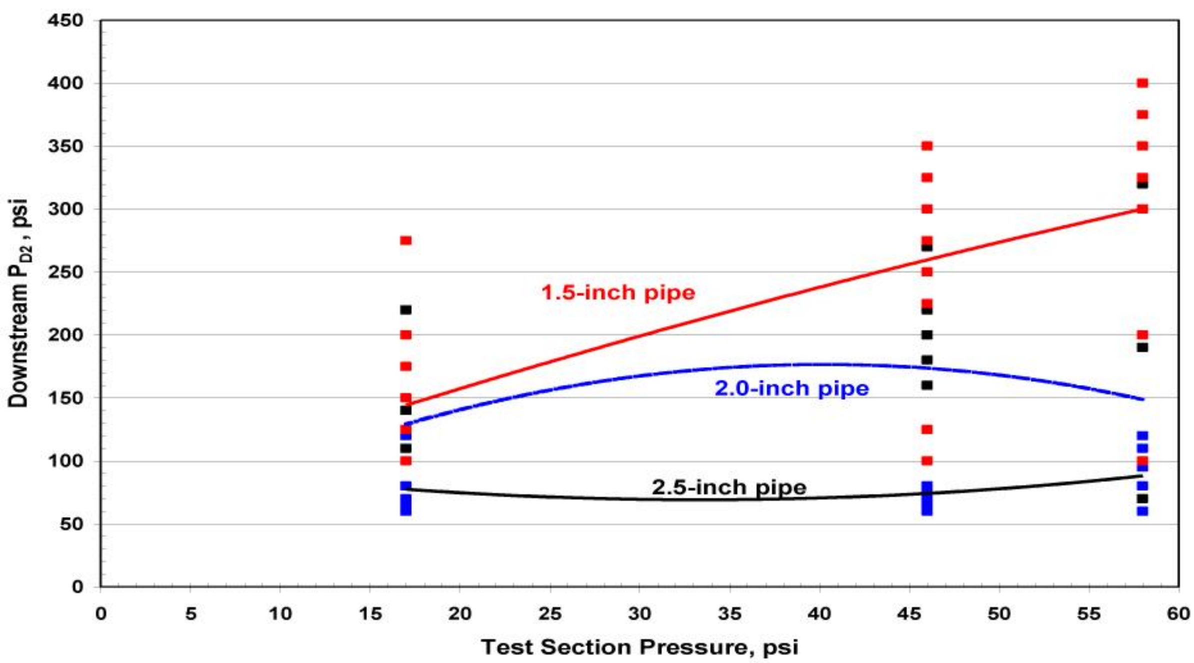

Graph 9 – Effects of fluid velocity on measured bubble lifetime in straight-tube tests.

(17 psi = squares and long lines; 46 psi=diamonds and medium lines; 58 psi=triangles and short lines)

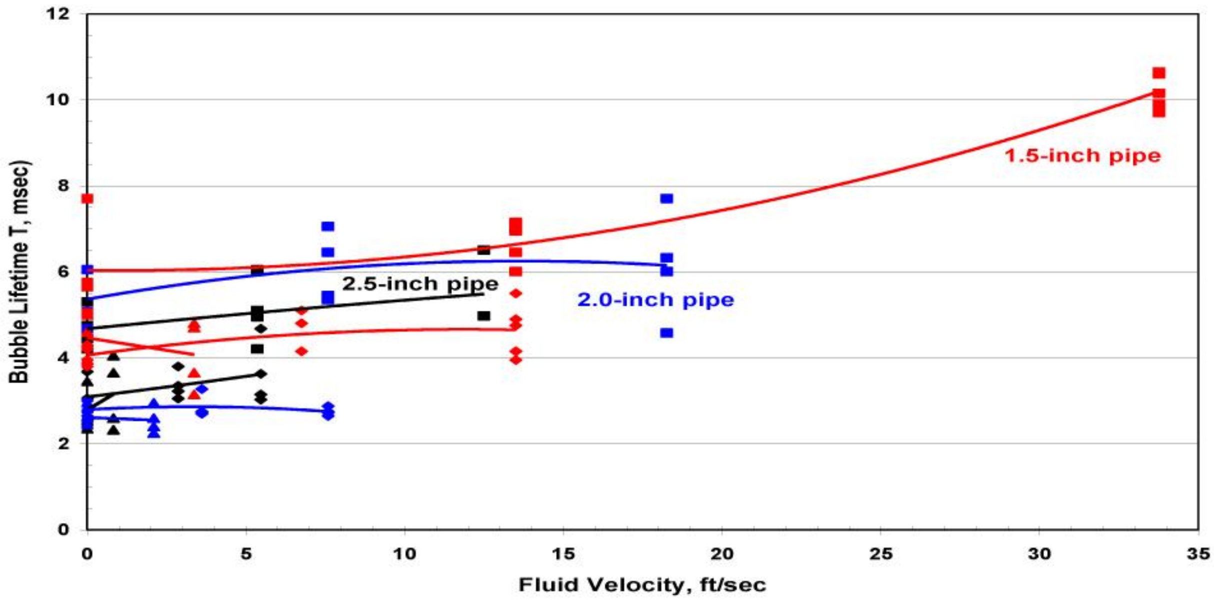

Graph 10 – Effects of fluid velocity on maximum upstream pressure during bubble expansion in straight-tube tests.

(17 psi =squares and long lines; 46 psi=diamonds and medium lines; 58 psi=triangles and short lines)

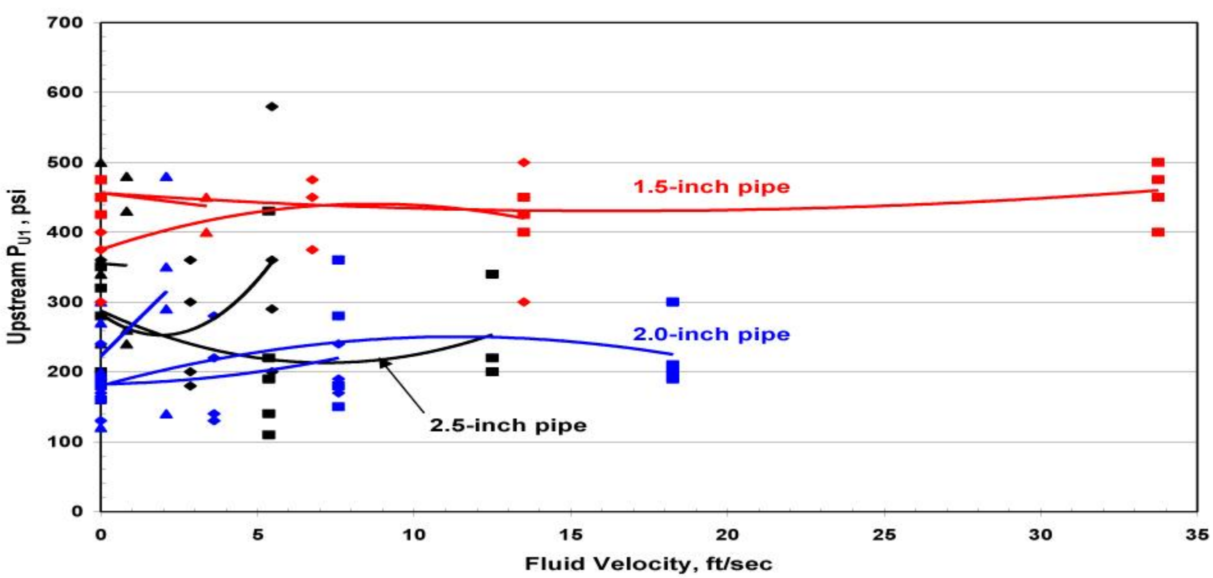

Graph 11 – Effects of fluid velocity on maximum upstream pressure during bubble collapse in straight-tube tests.

(17 psi =squares and long lines; 46 psi=diamonds and medium lines; 58 psi=triangles and short lines)

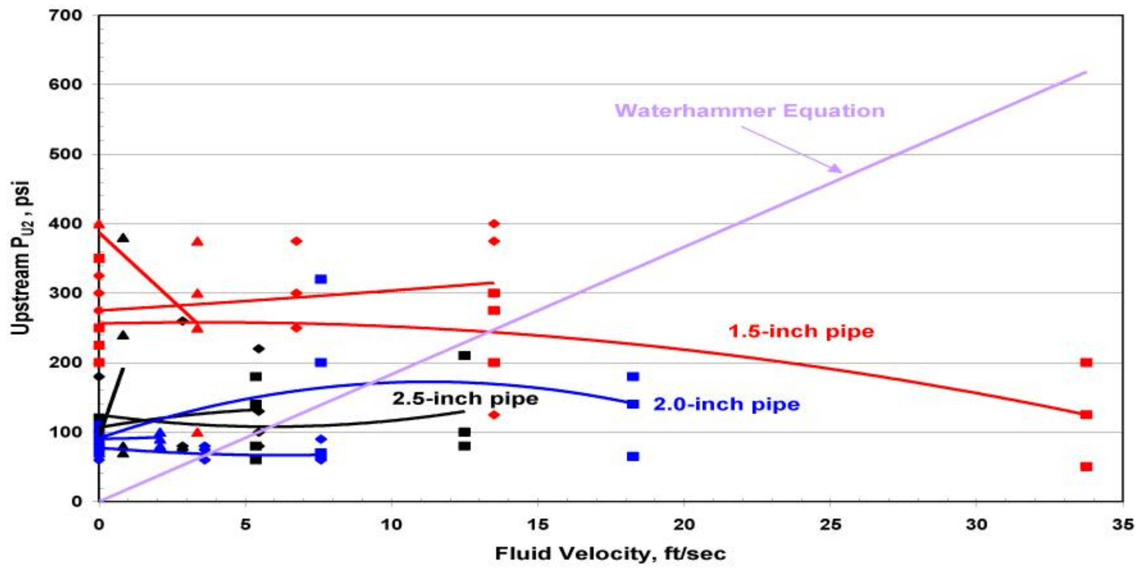

Graph 12 – Effects of fluid velocity on maximum downstream pressure during bubble expansion in straight-tube tests.

(17 psi =squares/long lines; 46 psi=diamonds/medium lines; 58 psi=triangles/short lines)

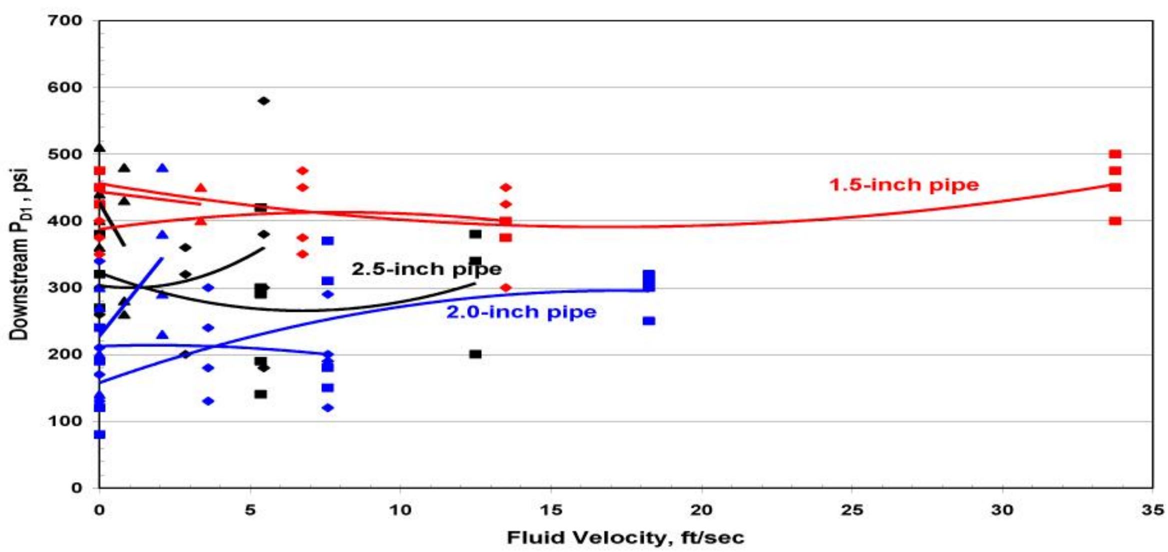

Graph 13 – Effects of fluid velocity on maximum downstream pressure during bubble collapse in straight-tube tests.

(17 psi =squares and long lines; 46 psi=diamonds and medium lines; 58 psi=triangles and short lines)

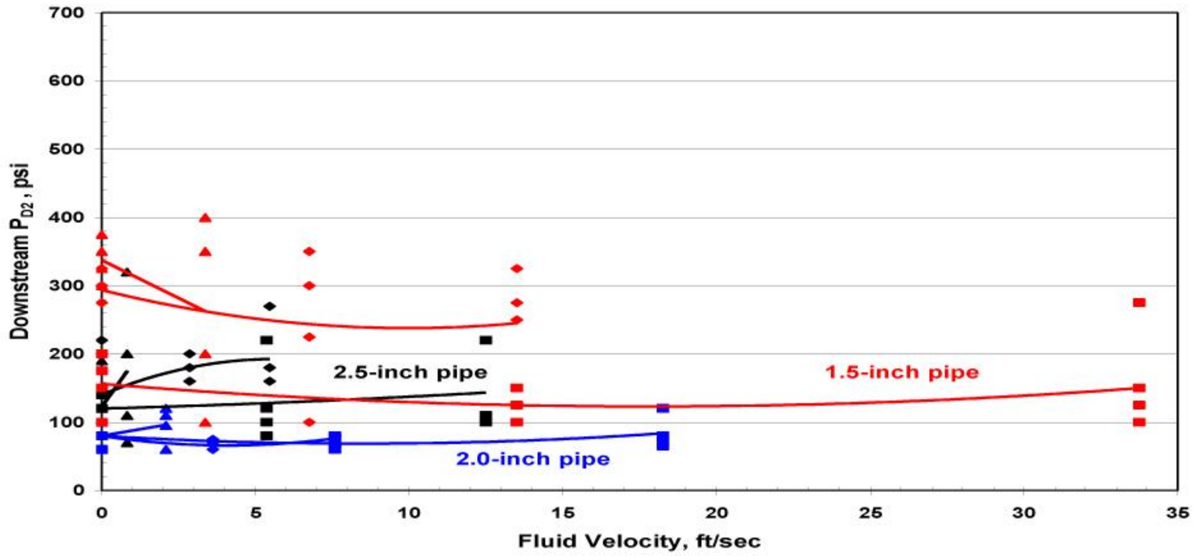

Graph 14 – Correlation of upstream bubble expansion pressure with bubble lifetime in straight-tube tests.

(17 psi=squares/lines on the right; 46 psi=diamonds/lines in the center; 58 psi=triangles/lines on the left)

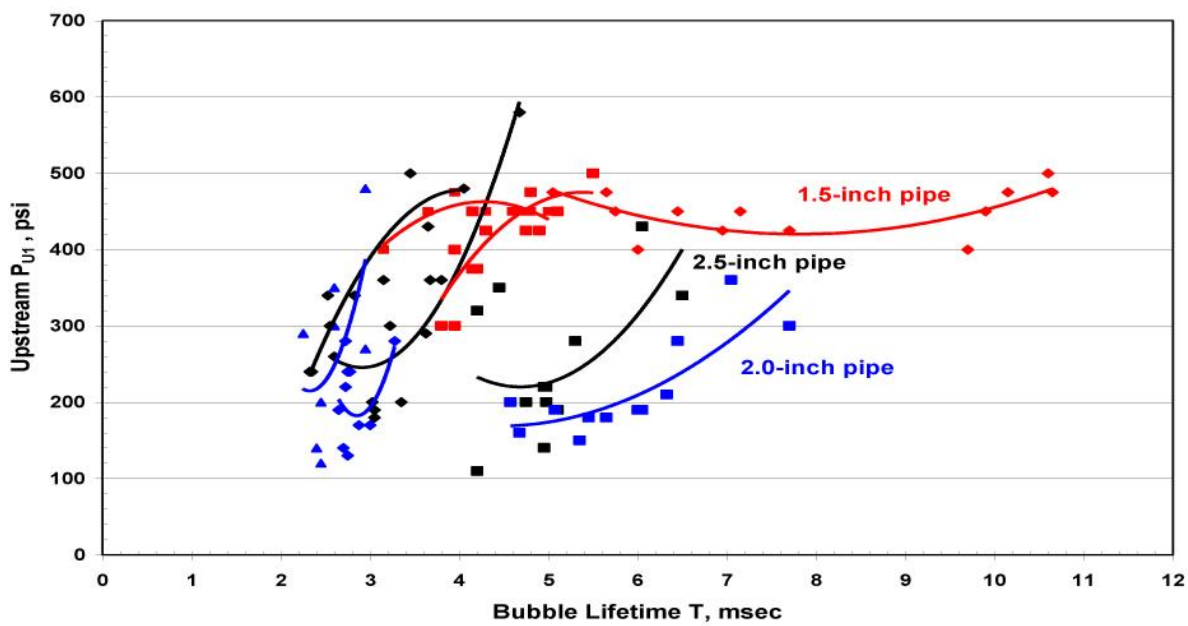

Graph 15 – Correlation of upstream bubble collapse pressure with bubble lifetime in straight-tube tests.

(17 psi=squares/lines on the right; 46 psi=diamonds/lines in the center; 58 psi=triangles/lines on the left)

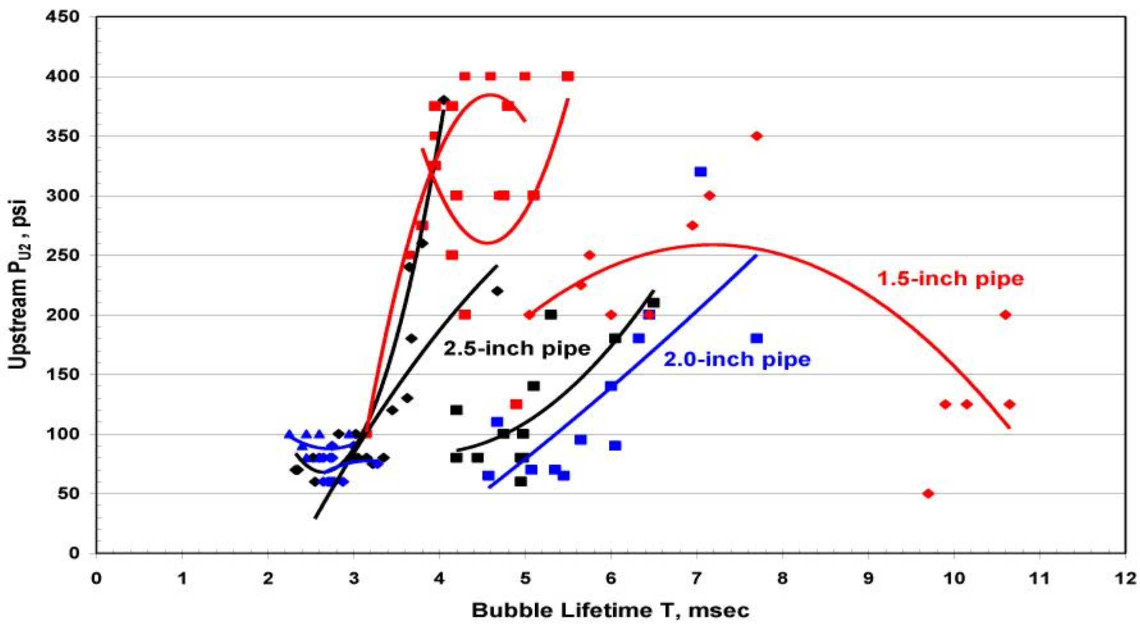

Graph 16 – Correlation of downstream bubble expansion pressure with bubble lifetime in straight-tube tests.

(17 psi=squares/lines on the right; 46 psi=diamonds/lines in the center; 58 psi=triangles/lines on the left)

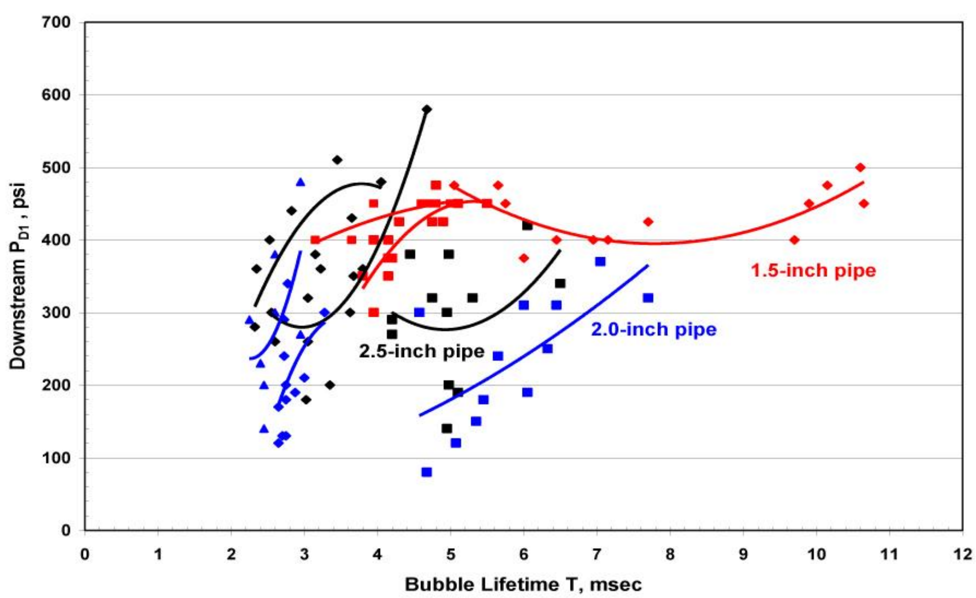

Graph 17 – Correlation of downstream bubble collapse pressure with bubble lifetime in straight-tube tests.

(17 psi =squares/lines on the right; 46 psi=diamonds/lines in the center; 58 psi=triangles/lines on the left)

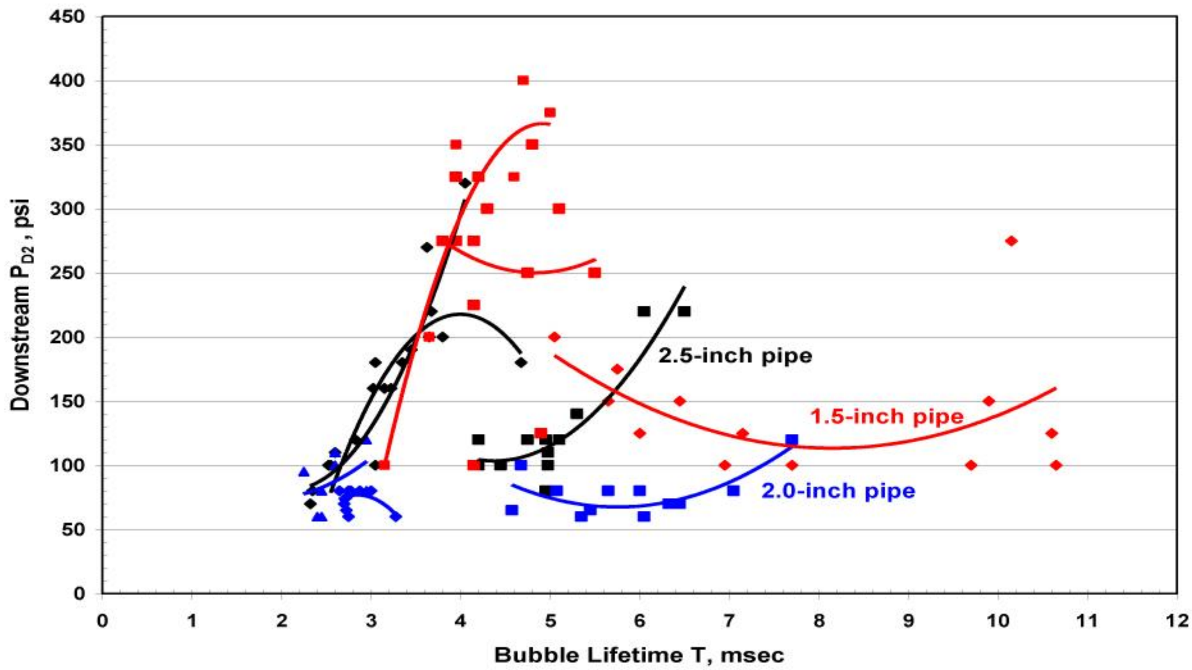

Graph 18 – Upstream pressure transducer readings for all nozzle/orifice tests. (t_U = black diamond's; P_{U2} = red triangles)

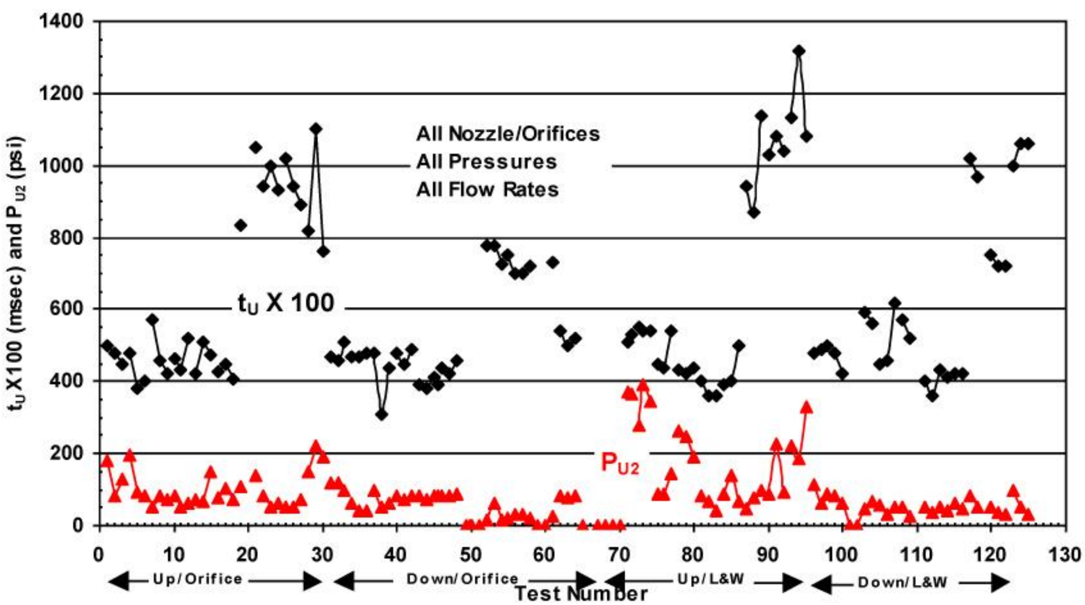

Graph 19 – Downstream pressure transducer readings for all nozzle/orifice tests. (t_D = black diamond's; P_{D2} = red triangles)

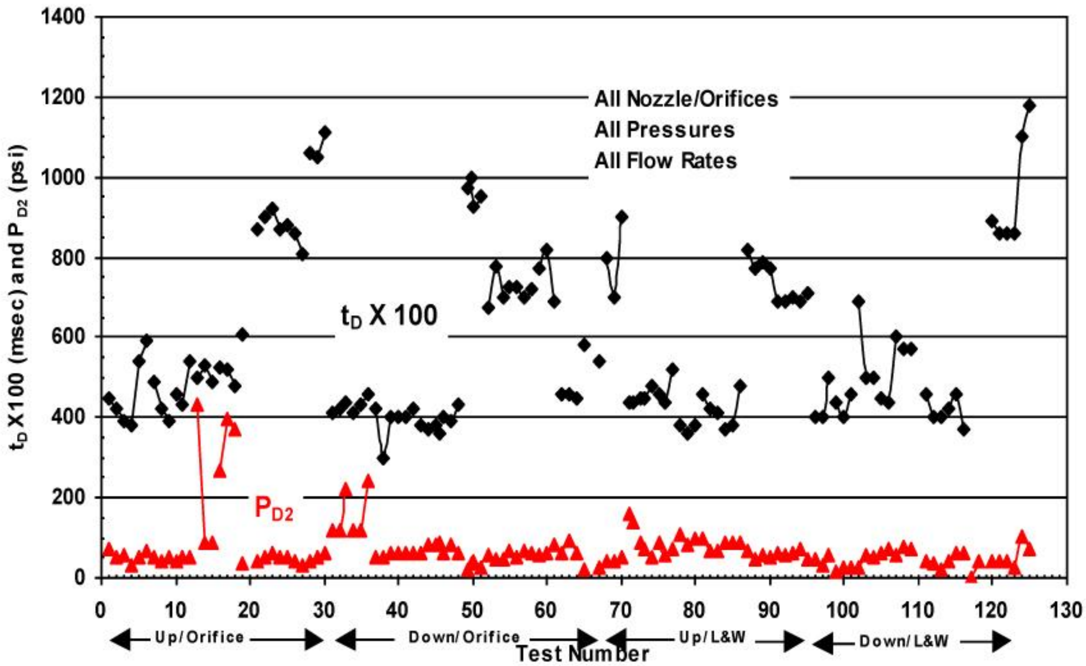

Graph 20 – Effects of test section pressure on bubble lifetime with sparker upstream of orifice

(gray data points and curve; all other data points and curves from straight-tube test sections, see Graph 4.)

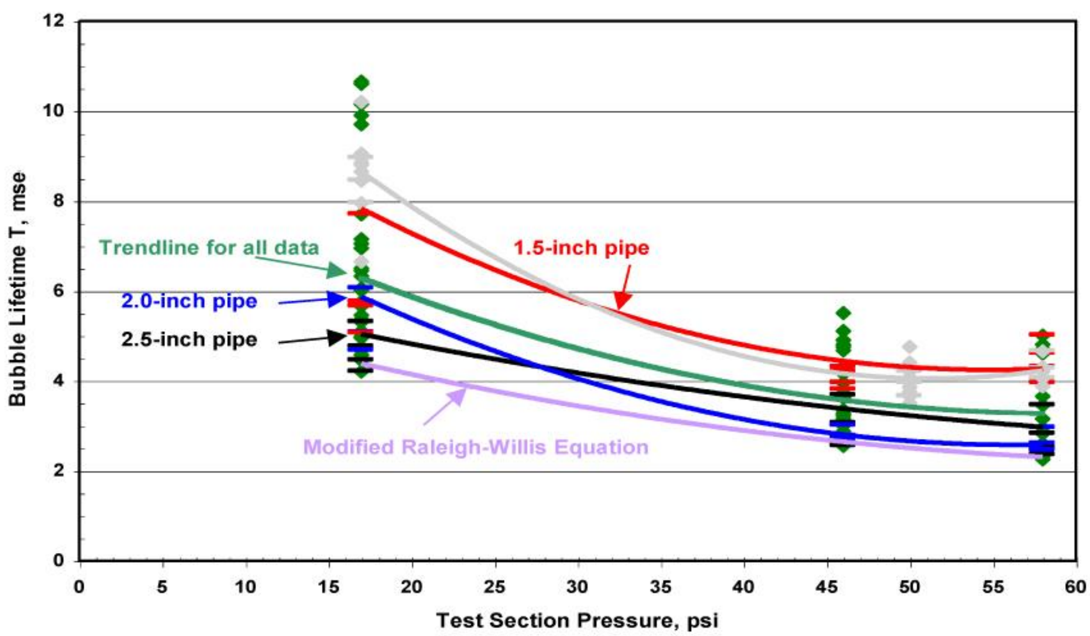

Graph 21 – Maximum upstream pressure transducer readings during bubble collapse with sparker upstream of orifice

(gray data points and curves; all other data points and curves from straight-tube test sections, see Graph 6.)

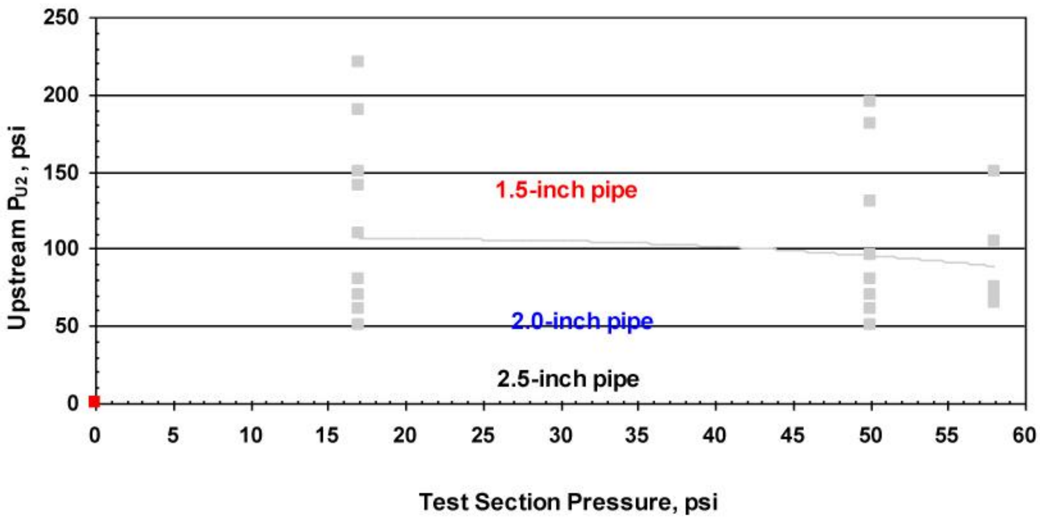

Graph 22 – Maximum downstream pressure transducer readings during bubble collapse with sparker upstream of orifice

(gray data points and curves; all other data points and curves from straight-tube test sections, see Graph 8.)

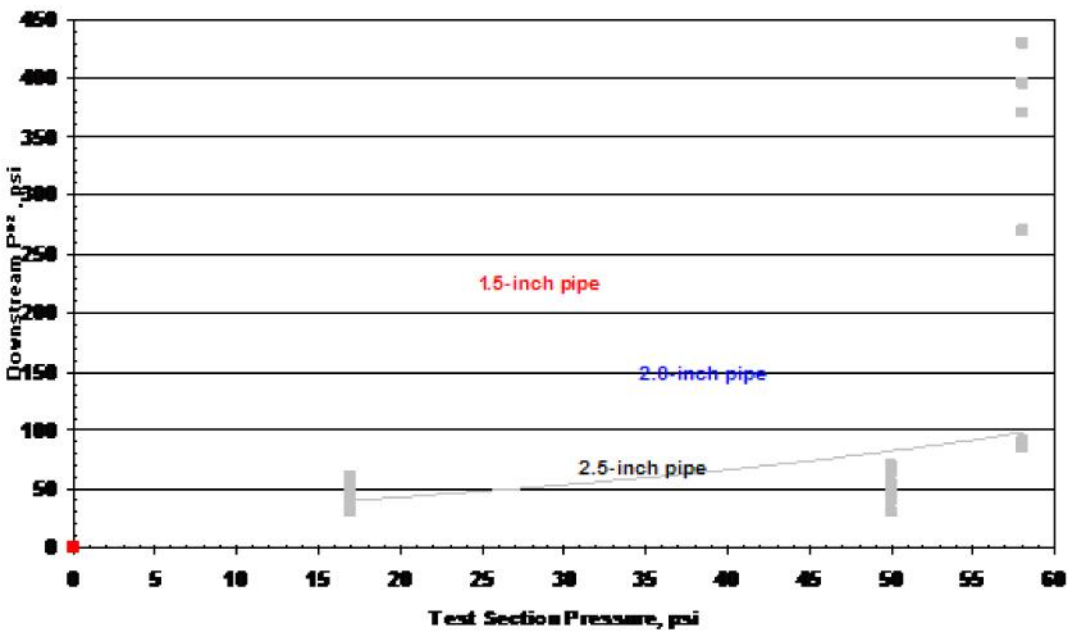

Graph 23 – Effects of fluid velocity on measured bubble lifetime with sparker upstream of orifice

[gray data points and curves. (17 psi =squares; 50 psi=diamonds; 58 psi=triangles); all other data points and curves from straight-tube test sections, see Graph 9.]

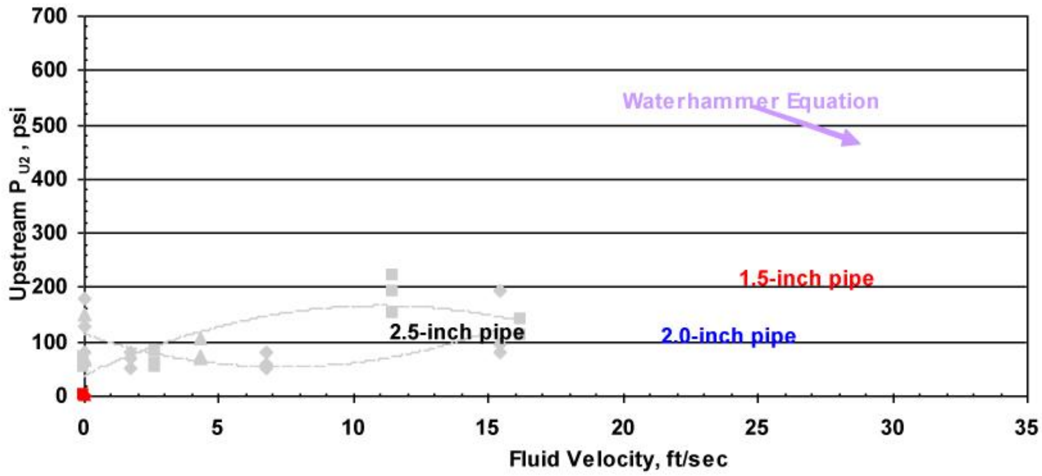

Graph 24 – Effects of fluid velocity on maximum <u>upstream</u> pressure during bubble <u>collapse</u> with sparker upstream of orifice

[gray data points and curves. (17 psi =squares; 50 psi=diamonds; 58 psi=triangles); all other data points and curves from straight-tube test sections, see Graph 11.]

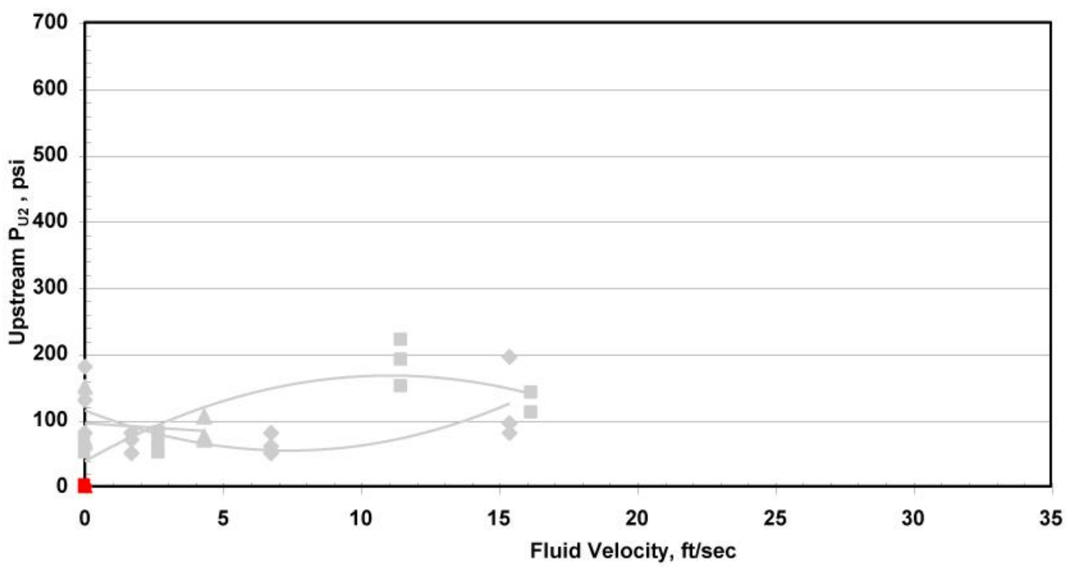

Graph 25 – Effects of fluid velocity on maximum <u>downstream</u> pressure during bubble <u>collapse</u> with sparker upstream of orifice

[gray data points and curves: (17 psi =squares; 50 psi=diamonds; 58 psi = triangles); all other data points and curves from straight-tube test sections, see Graph 13.]

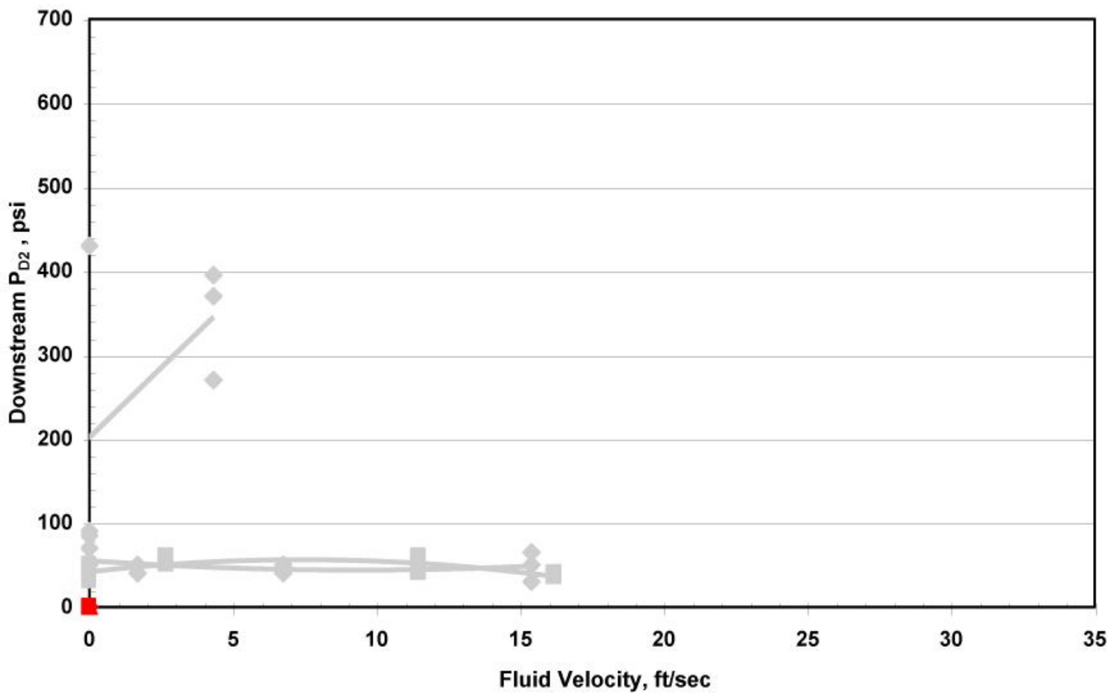

APPENDIX D – RMOTC DOWNHOLE SEISMICPULSER™ SOURCE TEST

Seismic While Drilling (SWD) Demonstration at the Rocky Mountain Oilfield Testing Center (RMOTC), Casper, Wyoming

Surface Seismic Data Recorded Using ION VectorSeis™ Receivers

Seismic Data Prepared by:
Ron Evans
ION Geophysical, Inc.

Text Contributor: Robert H. Stokes

Table of Contents

List of Figures

List of Tables

This page intentionally left blank

1.0 INTRODUCTION

An 8-in diameter x 26 ft long SeismicPULSER™ downhole tool was designed and built by Technology International, Inc. and tested at the Rocky Mountain Oilfield Test Center (RMOTC) near Casper, Wyoming as part of an advanced SWD Demonstration System. Typical sparkers used for seismic sources generate high frequency signals (1–10 kHz) that are depth dependent. These high frequencies severely limit the propagation range to shallow depth and short distances. The SeismicPULSER™ frequency is independent of depth and was generating a programmed to low frequency fundamental signal (two Hz) that will propagate to the surface from over 15,000 ft. The rationale for selecting two Hz for the SeismicPULSER™ during the RMOTC test was solely because it was assumed to be below the bandwidth range of the ambient noise generated in a drilling environment. The objective of this field test was to demonstrate that the low frequency two Hz signal was generated and would propagate to the surface from the maximum available well depth of 4,000 ft.

The SeismicPULSER™ downhole tool had a selectable horizontal or vertical sparker as shown in Figures 1 and 2 below.

Figure 1 – Horizontal Sparker

Figure 2 – Vertical Sparker

1.1 Down-hole Source

The firing mechanism for the SeismicPULSER™ down-hole system is controlled by the mudflow rate. This rate has to reach a minimum of 350 gpm before the firing mechanism will respond. Once firing commences, and the flow rate remains above 350 gpm, repeat firings take place every 20 seconds. The exact first fire time is not known and, therefore, cannot be flagged on the surface recording system. For these tests it was necessary to estimate this time by having the drilling rig contact the recording personnel

by radio when the correct flow rate had been achieved. Then the seismic crew would record a long period in order to pick up a repeated number of firing sequences. For the purpose of this test, 100 second recording periods were used at the surface recording stations. The SeismicPULSER™ directional source was preset to fire either horizontally or vertically, one test day was assigned for each mode.

The main objective of this test was to deploy, fire, and record the seismic energy generated by the down-hole source in a pseudo-operating well site environment. This environment will necessarily be active and contain many sources of background noise activity. In addition, the firing mechanism which requires that the mud pumps are running ensures that background noise levels are high.

1.2 Recording System

The ION Scorpion™ seismic recording system was used to monitor and record the seismic signal generated by the SeismicPULSER™, together with all other sources of background seismic energy in the vicinity of the well head area.

Other seismic "background" energy recorded during this test included, but not limited to:

- Rig generator and mud pumping equipment,
- Drill pipe deployment,
- Vehicles, and
- Effect of wind on surface deployed receivers and cables.

Two orthogonal receiver lines were laid out close to the well head location. Each of the two lines employed 48 receivers at 55 ft spacing. The lines crossed at approximately 400 ft W of the well-head location. The depth of well, 45-4-X-21, was at approximately 5,665 ft measured depth below the surface.

Each receiver was a 3C MEMS (Micro-Electro-Mechanical System) specifically chosen for this project in order to sample the full waveform seismic energy generated by the down-hole sparker and other forms of seismic energy.

2.0 ROCKY MOUNTAIN OILFIELD TEST CENTER (RMOTC)

2.1 Description of the RMOTC

RMOTC partners with service companies and equipment manufacturers to test new ideas and products leading to increased recovery or reduced operating costs. Independent oil producers leverage technologies tested at RMOTC by evaluating new recovery processes before application. Inventors test, evaluate, demonstrate, and transfer new technologies to the oil and gas industry. Environmental companies explore ways to prevent and manage environmental risks. National laboratories and government organizations field test theoretical laboratory assumptions in a real world setting. Universities teaching theory in the classroom demonstrate the real-life application in the field and conduct leading-edge research.

RMOTC provides the following:

- The link between development and getting technology to the industry.
- The opportunity to field test, document and demonstrate the benefits of technology.
- The opportunity to leverage industry resources with those of RMOTC via cost sharing.
- Acceptance of the risks of production loss in a producing well.
- A large geologic database, facilities, and support staff.
- Professional staff with operating expertise and equipment to tweak ideas on-site
    - during the test, in an actual situation, not a simulated laboratory test.
- Adaptability, simulate offshore operations or renewable energy sources, for
    - example.
- Neutrality, no vested interest in any specific technology, interested in supporting the energy industry by increasing production, decreasing production costs, or lessening the environmental footprint.

2.2 RMOTC Location

RMOTC is a 10,000-acre U.S. Department of Energy facility located within the Naval Petroleum Reserve No. 3 (NPR-3) also known as Teapot Dome Oil Field, about 35 miles north of Casper, Wyoming and shown in Figure 3.

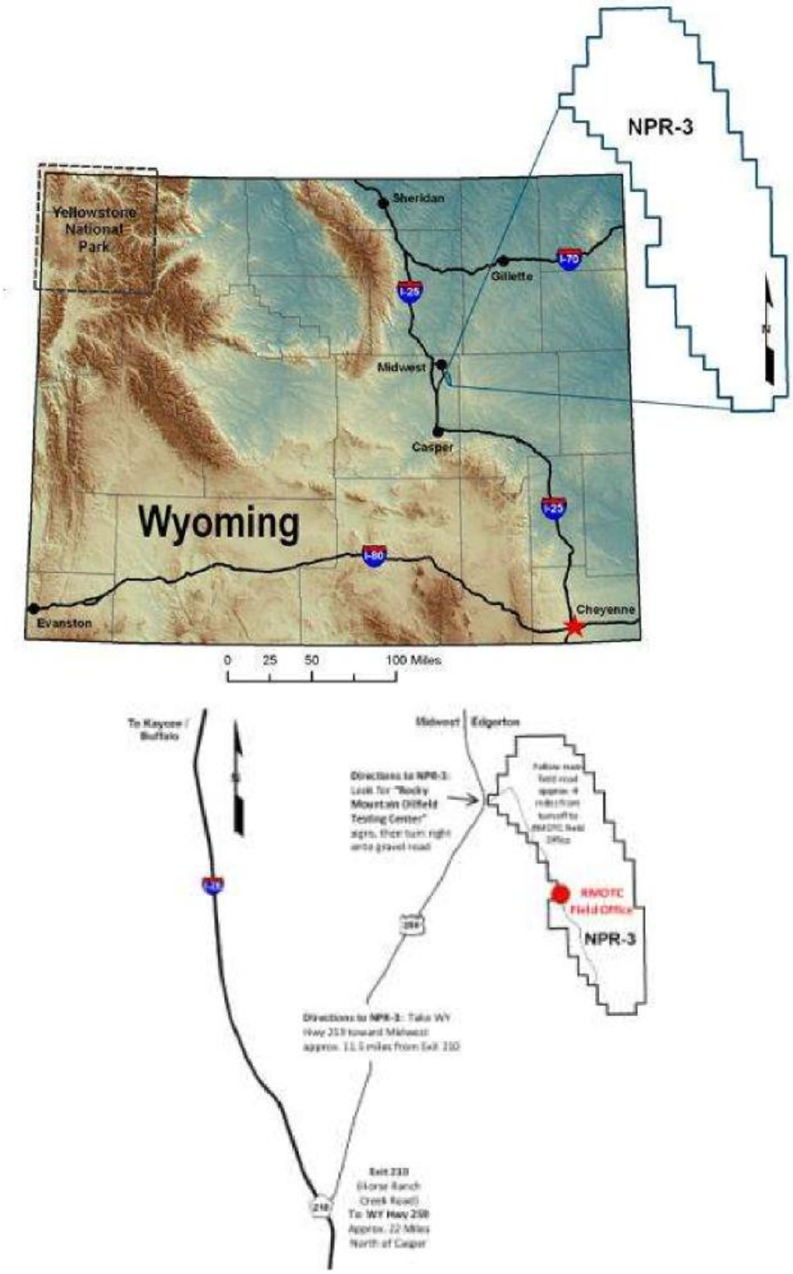

Figure 3 – RMOTC Location

3.0 SURVEY GEOMETRY

The two seismic receiver lines and the test well 45-4-X-21 geometry are shown in Figure 4 below.

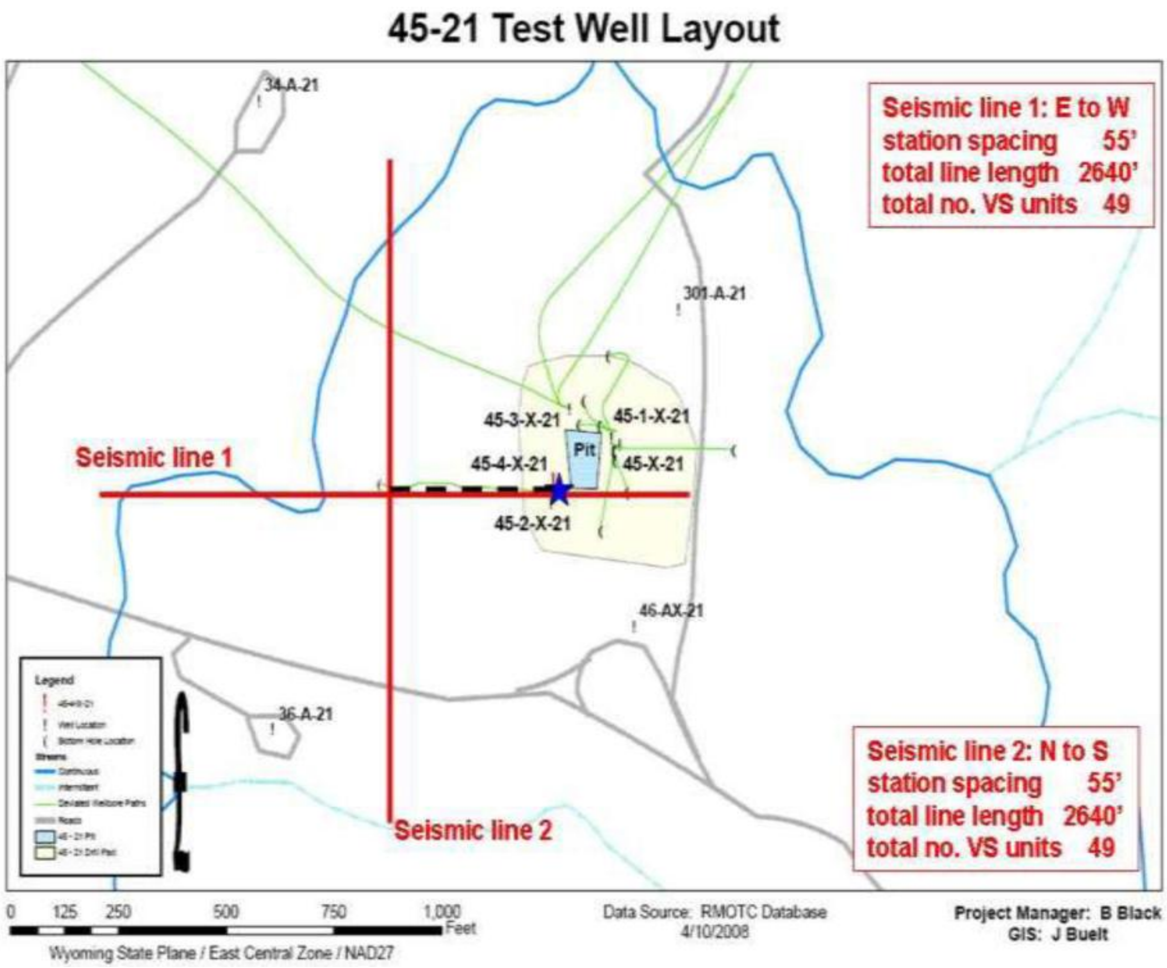

Figure 4 – 45-4-X-21 Test Well Layout

3.1 Borehole 45-4-X-21 Test Well Layout

The two seismic lines are approximately ½ mile in length, crossing at the center point of both lines. The crossing point is 403 feet to the W of the wellhead location. The borehole deviates almost directly W and the maximum inclination does not exceed 10°. The survey was designed such that surface receivers could be located directly above the well track. However, due to the infra-structure around the rig-site, the EW line had to be offset approximately 100 ft to the S of the wellhead.

3.2 GPS Measurements

GPS (global positioning system) coordinates were taken for all receivers on both seismic lines 1 and 2. The basis for calculation of GPS values is as follows:

- The data was collected using Zterm on a Trimble device
- Corpscon6 was used to convert the original logs from WGS-84 latitude-longitude to NAD27 using the following parameters

- Geographic, NAD83 ====>> State Plane NAD27 4902, Wyoming ll, U.S. feet x Where possible DGPS data with more than 6 satellites is represented x Rogue values were manually deleted
- Also shown are the mean for each cluster, standard deviation and height in feet

The results from the GPS measurements are shown Figures 5 and 6.

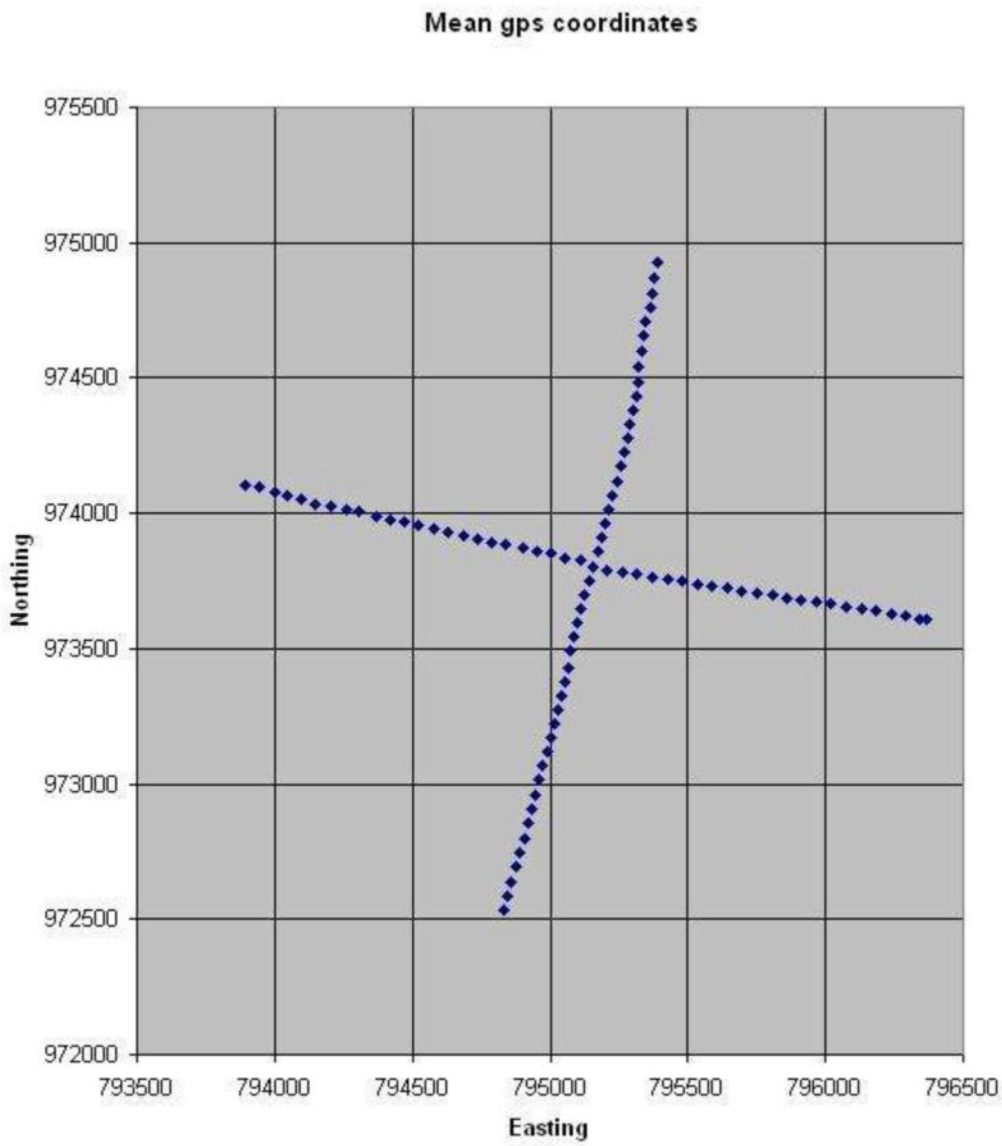

Figure 5 – Sensor Locations

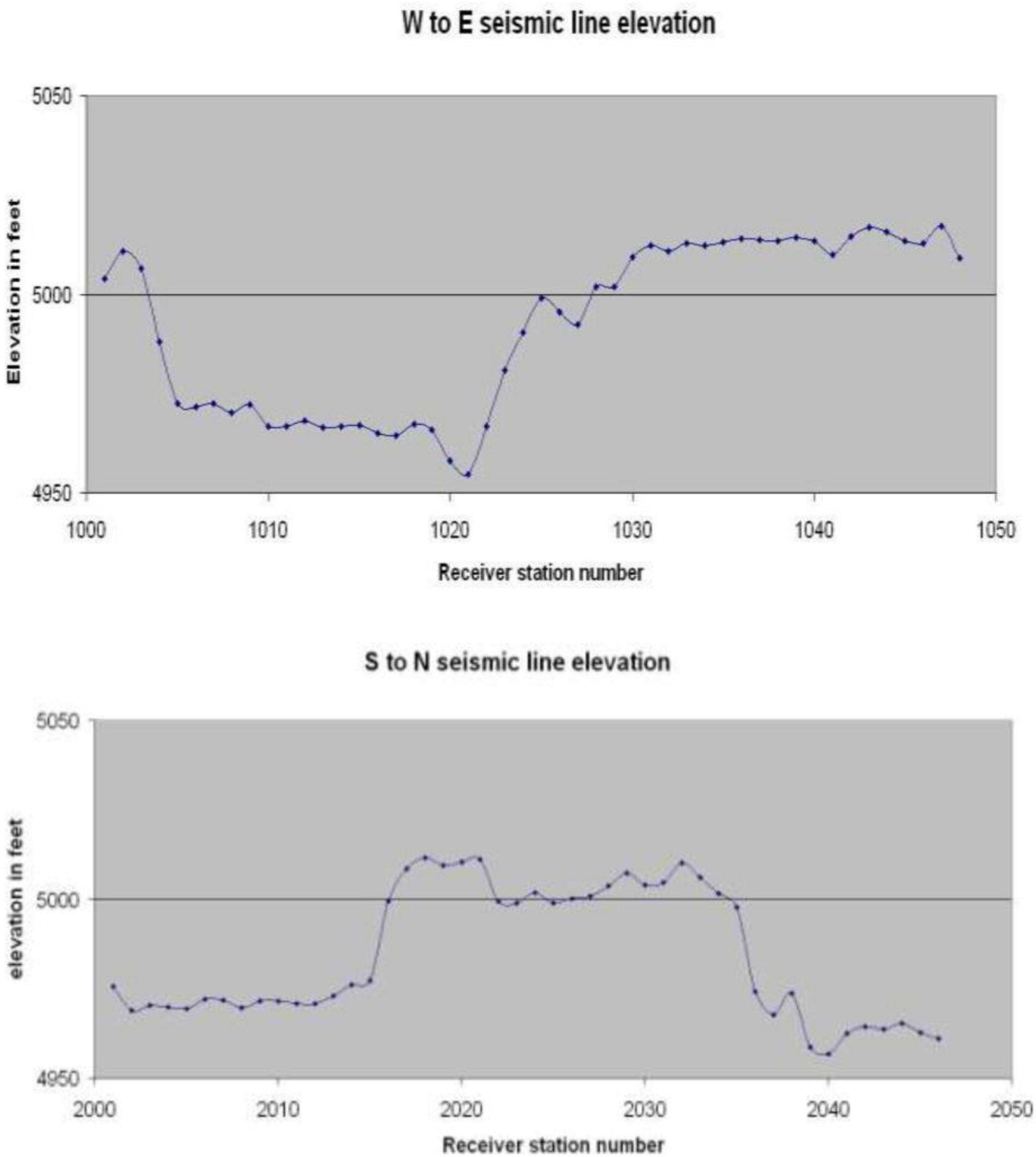

Figure 6 – Sensor Elevations

4.0 GEOLOGIC COLUMN FOR TEST WELLS

The geologic section breached by the RMOTC test site well 45-4-X-21, is shown in Figure 7. The well is cased down to approximately 650 ft depth. Directly below the casing lies the Steele Shale formation, containing a number of thin sandstone channels, the Sussex and Shannon sands. Parts of this Shale section had stability problems, witnessed by the bore-hole wall collapse during well cleaning operations. The bore-hole wall integrity may also have been affected during horizontal sparker operations. The deeper sandstone formations, first, second, and third Wall Creek, the Dakota and the Lakota offer solid well-bore conditions and are considered ideal for transmission of the sparker energy into the rock. The deeper Alcova Limestone formation should provide good reflections.

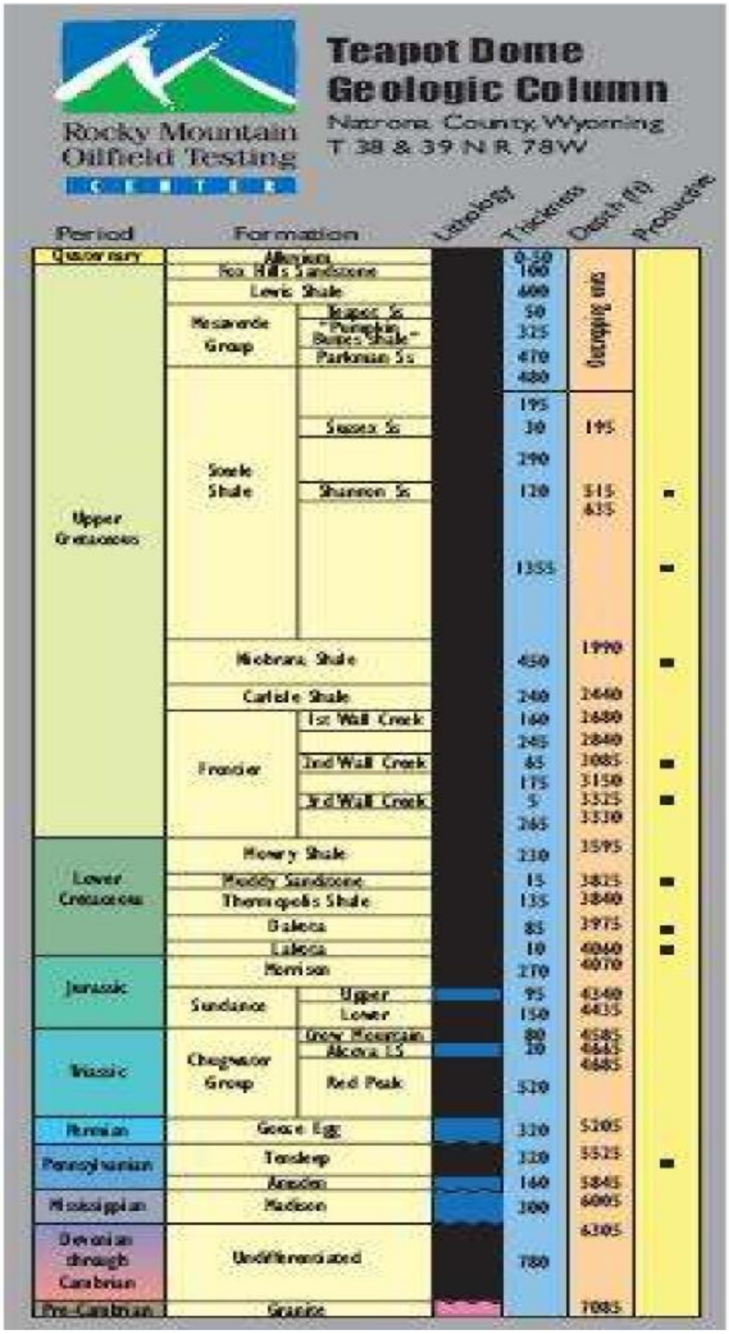

Figure 7 – Formations and Rock Types at RMOTC

5.0 SEQUENCE FOR THE SHOOTING PROGRAM

The original shooting program for the first day of testing is shown in Table 1 with the sparker in the horizontal position. The original program for the second day of shooting was a replica with the sparker set to the vertical mode position.

Table 1 – Shooting Sequence

PHASE I - HORIZONTAL SPARKER						DATA TO BE RECORDED		
No.	Target Depth (feet)	Measured Depth (feet)	Tripping Flow Rate (GPM)	Testing Flow Rate (GPM)	Flow Duration	Direction Analysis	Energy Analysis	Velocity Analysis
1	210		<200	350-400	2-3 min.			
2	390		<200	350-400	2-3 min.			
3	570		<200	350-400	2-3 min.			
4	750		<200	350-400	2-3 min.			
5	930		<200	350-400	2-3 min.			
6	1110		<200	350-400	2-3 min.			
7	1290		<200	350-400	2-3 min.			
8	1470		<200	350-400	2-3 min.			
9	1650		<200	350-400	2-3 min.			
10	1830		<200	350-400	2-3 min.			
11	2010		<200	350-400	2-3 min.			
12	2190		<200	350-400	2-3 min.			
13	2370		<200	350-400	2-3 min.			
14	2550		<200	350-400	2-3 min.			
15	2730		<200	350-400	2-3 min.			
16	2910		<200	350-400	2-3 min.			
17	3090		<200	350-400	2-3 min.			
18	3270		<200	350-400	2-3 min.			
19	3250		<200	350-400	2-3 min.			
20	3630		<200	350-400	2-3 min.			
21	3810		<200	350-400	2-3 min.			
22	3990		<200	350-400	2-3 min.			
23	4170		<200	350-400	2-3 min.			
24	4350		<200	350-400	2-3 min.			
25	4530		<200	350-400	2-3 min.			
26	4710		<200	350-400	2-3 min.			
27	4890		<200	350-400	2-3 min.			
28	5070		<200	350-400	2-3 min.			
POH								

1) Trip into well stopping after every ~~2~~ stands (180 feet) to test.
2) For each test flow 350 to 400 GPM for 2-3 minutes.
3) POH after Test No. 28, repeating tests at selected depths.

However, as the testing program progressed two problems dictated that this sequence would have to be abandoned. 1) The signal-to-noise ratio was extremely low due mainly to the high ambient noise of the rig site environment. The situation was re-assessed, and many test shots were recorded just to get a handle on the seismic character of the background noise. 2) The borehole had severe stability problems and much time was lost trying to stabilize the hole. These stability problems prevented any operations greater than 3,883 ft depth. The actual shooting sequence is shown in Table 2 and Table 3.

Table 2 – Day 1 Summary of Seismic Data – Part 1

Record No.	Sparker Position	Tool Depth	Mudflow Rate	Comments
1 9a	Horizontal	778 ft	100 gpm	Background noise test, three components, Z, HX, HY
1 9b	“	778 ft	100 gpm	Background noise test, Hx component and freq spectrum
20	“	778 ft	200 gpm	Background noise test, HX component and freq spectrum
12	“	778 ft	100 gpm	Hammer Test, pulses at approx 10 sec, HX component and freq spectrum
7	“	778 ft	380 gpm*	Pulse test, HX component and freq spectrum
11	“	778 ft	380 gpm*	Pulse test, rotate 45 deg from No. 7, HX component and freq spectrum
21	“	3,883 ft	350 gpm*	Pulse test, HX component and freq spectrum
23	“	3,883 ft	350 gpm*	Pulse test, rotate 45 deg, HX component and Freq spectrum
24	“	3,883 ft	350 gpm*	Pulse test, rotate 45 deg, HX component and freq spectrum

* Sparker Operating

Table 3 – Day 2 Summary of Seismic Data – Part 1

Record No.	Sparker Position	Tool Depth	Mudflow Rate	Comments
26	Vertical	775 ft	0 gpm	Tap Test, three components, Z, HX, HY and freq spectrum
28	“	775 ft	0 gpm	Hammer Test, pulses approx 10 sec, 2 comp. Z & HY
29	“	775 ft	100 gpm	Background noise test
30	“	775 ft	207 gpm	Background noise test
31	“	775 ft	365 gpm*	Pulse test
40	“	2,950 ft	358 gpm*	Pulse test, sparker operating
41	“	2,950 ft	365 gpm	Background noise test, no sparker

* Sparker Operating

6.0 SEISMIC DATA ACQUISITION AND ANALYSIS OF RMOTC TESTS

The seismic data processing sequence applied to this data is very limited. No advanced processing techniques were considered for this report. The seismic data were recorded in SEG-Y (Society of Exploration Geophysicists Y) format, but were re-formatted for use of the Seismic Processing Workshop (SPW) software package (Copyright 2005 Parallel Geoscience Corporation).

Processing sequence:

- Re-format from SEG-Y to SPW format;
- Trace selection based on field file and component number;
- Re-sample from 2ms to 8ms;
- Sorting the data to Vertical, in-line HX and cross-line HY components;
- Bandpass filters used were 0–1.5, 7.5–9.0 Hz;
- Noisy trace elimination; and
- Amplitude gain selection to enhance trace display.

It should be noted that the gain is applied to the field file data selected for display, and does not vary from trace to trace for the subsets of the seismic data shown.

A summary of the presented data is summarized in Table 4 and 5. Table 4 shows the Figure number and the record number of each the seismic recordings and comments on the data on Day 1.

Table 4 – Day 1 Summary of Seismic Data – Part 2

Figure No.	Record No.	Sparker Position	Tool Depth	Mud Flow	Comments
8	1 9a	Horizontal	778 ft	100 gpm	Noise only no freq spectrum, Z, HX. HY
12	19b	“	778 ft	100 gpm	Noise Test, no freq below 3 Hz, Freq at 5.7 Hz. probably 5th harmonic of 1.03 fundamental
10	20	“	778 ft	200 gpm	Noise test, no freq below 3 Hz, freq at 5.6, probably 3rd harmonic 1.87 fundamental
17	12	“	778 ft	100 gpm	Hammer Test, pulses at 10 sec, Freq at 3.3, 3.7, 5.1, 5.4, 5.7, 6.6, and 7.3 Hz
19	7	“	778 ft	380 gpm*	Freq at 3.4, 5.4, 5.6, and 6.9 Hz
20	11	“	778 ft	380 gpm*	Freq at 3.35, 5.35, 6.7 Hz
21	21	“	3,883 ft	350 gpm*	Freq at 3.25, 5.25, 6.5 Hz
22	23	“	3,883 ft	350 gpm*	Freq at 3.3, 5.3, 5.7, 6.6 Hz
23	24	“	3,883 ft	350 gpm*	Freq at 3.3, 5.3, 5.8, 6.6 Hz

* Sparker Operating

Table 5 shows the Figure number and the record number of each the seismic recordings and comments on the data on Day 2.

Table 5 – Day 2 Summary of Seismic Data – Part 2

Figure No.	Record No.	Sparker Position	Tool Depth	Mud Flow	Comments
9	26	Vertical	775 ft	0 gpm	Tap Test, 3 components
18	28	"	775 ft	0 gpm	Hammer Test, 2 comp. Z & HY
13	29	"	775 ft	100 gpm	Noise Test, fo=1 .03 Hz
11	30	"	775 ft	207 gpm	Noise Test
24	31	"	775 ft	365 gpm*	Small 5.3 Hz signal present
14a, 15,25,27	40	"	2,950 ft	358 gpm*	5.3 Hz signal present
14b, 16,26	41	"	2,950 ft	365 gpm	No Sparker

* Sparker Operating

6.1 Preliminary Seismic Data Analysis

All seismic data was received and recorded by the ION VectorSeis Receiver. The vertical, VZ component of the ION three component sensor had a malfunction; therefore, is not included in most of the presented data. The other two horizontal components, HX and HY were operational and the recoded data was essentially the same for both. Only the HX data will normally be presented.

Figure 8 shows the seismic data recorded for both sensor lines and each of the three components VZ, HX and HY. Sensor Line 1 (EW) is represented by traces 1–47, and Sensor Line 2 (NS) by traces 48–97 are numbered across the top. The vertical axis displays the 100 sec of recorded time from 0–100,000 in msec. It is obvious from Figure 8 that this was not a quite environment.

The seismic data presented on the left is from the W to E sensor array and the data on the right is from the S to N sensor array.

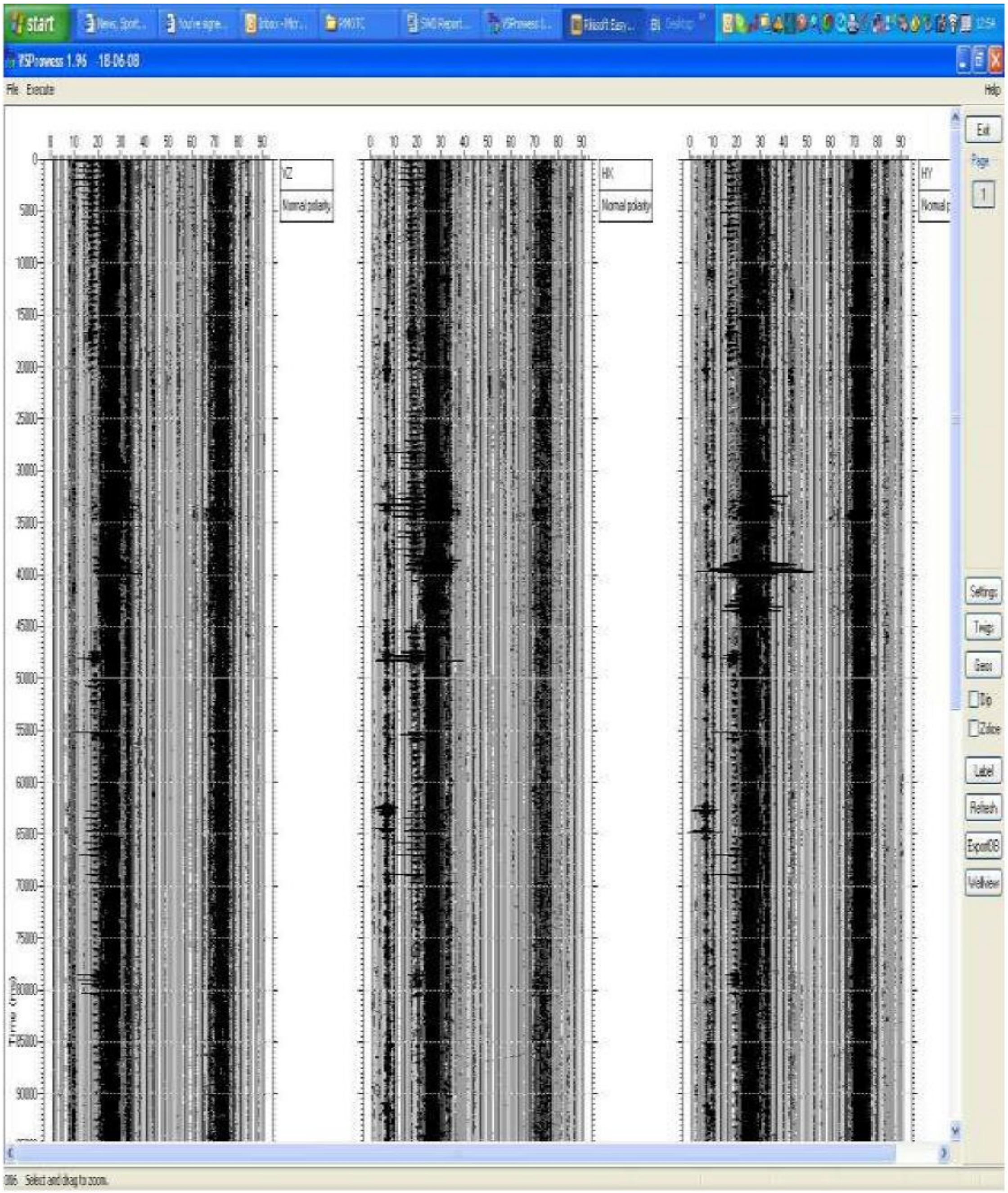

Figure 8 – Background Noise Test

Note: Analysis of the recorded seismic data is as follows:

A number of seismic records have been analyzed for sparker seismic energy patterns. The main energy package will naturally be contained in the low frequency bandwidth (<7 Hz). Consequently, the seismic has been displayed after application of a low-pass filter (1.5–3.0, 6.0–9.0 Hz). The seismic record is 100 sec long, which means that several 20 sec interval pulses are captured. The two Hz pulses have only 1 sec duration so it is difficult to see a 1 sec pulse imbedded in the 100 sec seismic record.

In all of the data, Figures 9–21 the 100 sec of seismic data is presented at the top of page. The seismic data presented on the left is from the W to E sensor array and the data on the right is from the S to N sensor array. The spectral content of this 100 sec data is presented at the bottom of the page. The vertical axis on the seismic data covers a time of 100 sec and is labeled in msec x 10^6. The main grid lines each represent 20 sec.

The spectral plots have been calculated from the unfiltered seismic data. Each spectral plot has been calculated from the full 100 sec of data. The information shown is the summation all traces included in the spectral analysis window. This is true for all displays relating to both the horizontal and vertical sparker.

6.2 Coherent Seismic Events

Most energy is generated at or close to the well site area. The hyperbolic character of the seismic events indicates this, and also, the true amplitude seismic trace displays show that most of the energy is contained in the near-offset traces. This is true for all background noise records, hammer-on-casing records, and for seismic records where the down-hole source is firing. Therefore, when the down-hole source is firing, the energy generated by the sparker has to compete with all the other coherent noise energy. Furthermore, the sparker firing mechanism (mudflow at 350 gpm) will inherently generate a coherent noise background.

6.3 Incoherent Background Seismic Noise

The level of pure random noise can be assessed by the spectral plots shown in this report. At very low frequencies (<3 Hz) all the seismic records show no response. The only exception to this rule is the sensor "tap test" conducted during the survey when a member of the seismic crew manually tapped the sensor with his finger and the response is shown in Figure 9. The results observed from this tap test could be interpreted as proof that the three component digital sensors are operating correctly, and can record frequencies down to 1 Hz. However, all other seismic records analyzed for this report indicate that there is no response below 3 Hz. The most probable explanation for the low frequency response from the tap test is that the vibration of the sensor from tapping is much larger than any signal produced by the SeismicPULSER™ or most other recorded seismic signals. The tap test may be an adequate "go" or "no-go" test, but not a valid test to determine frequency response.

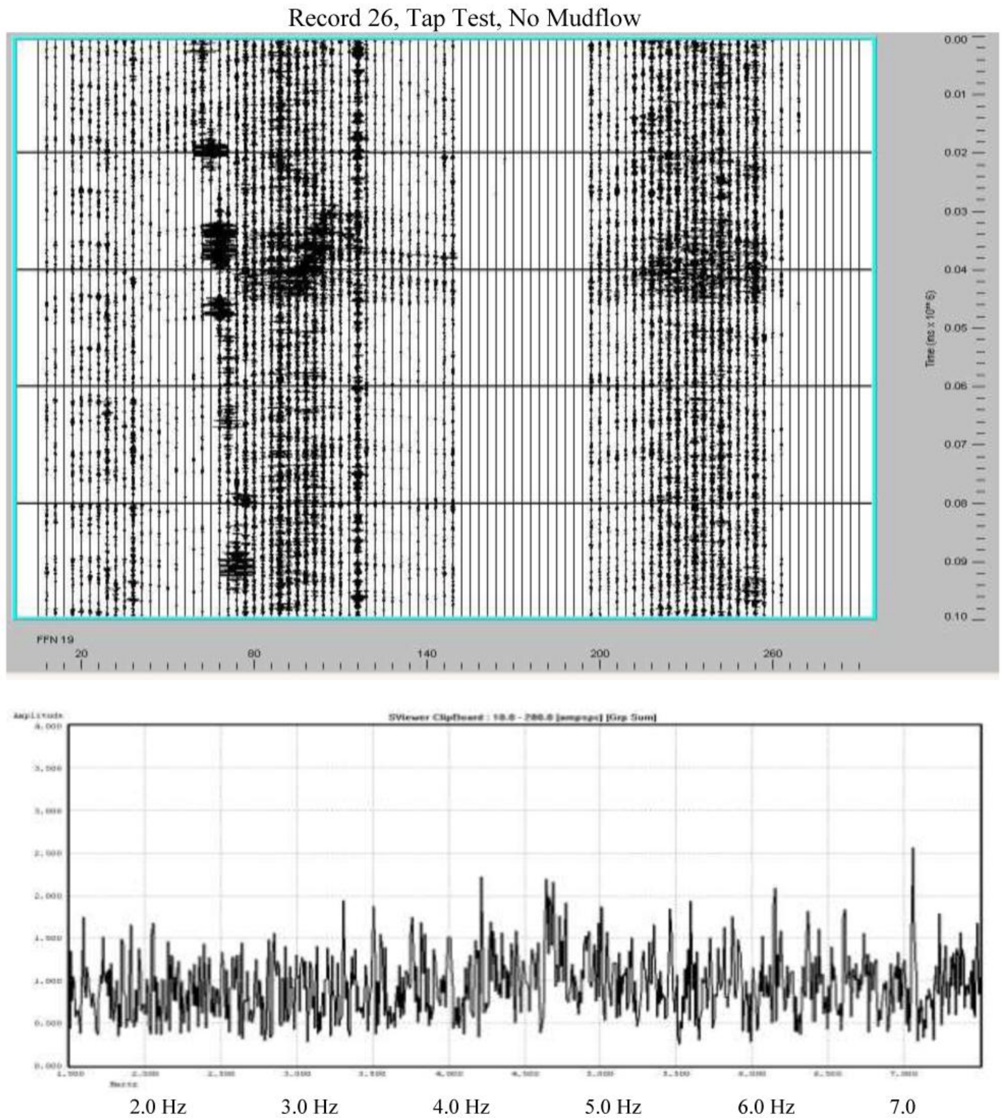

Figure 9 – Tap Test

Note that the VectorSeis™ data sheet (Appendix Db) states that the digital low-cut filter is preset at three Hz. with a 12 dB/octave roll-off. According to the Scorpion system engineers on-site during this survey, the system digital low-cut filter was turned off during the two days of recording. Even though the filter was supposedly turned off, the evidence shows that no data was recorded below three Hz, so there seems to be a frequency limitation to the sensor other than the filter. It should also be reported that high background noise levels were caused by strong winds during the two days of testing. The recording crew made the comment on a number of occasions that conventional seismic acquisition would, generally, have been discontinued under these conditions. This option, however, was not available for this survey. Even this high wind induced noise did not produce any signals below three Hz, giving credence to the conclusion that the sensors did not respond to frequencies below three Hz.

6.4 Coherent Background Seismic Noise Generated by the Mudflow Mechanism

During rotary drilling operations it is necessary to pump mud down through the drill pipe and up through the borehole itself. The mud is generally used to remove debris, such as rock cuttings, maintain borehole stability, seal off porous zones and isolate formation fluids. During this trial, the mud pump was used to maintain the stability of the borehole wall, which was particularly unstable in the upper part of the well.

The mudflow is an essential factor in the SeismicPULSER™ firing mechanism. The SeismicPULSER™ was powered by a downhole turbine that would turn on when the mudflow reached a magnitude of 350 gpm. Below this flow rate the SeismicPULSER™ would not fire. Whenever the flow was 350 gpm or higher, the SeismicPULSER™ was set to fire automatically every 20 seconds.

Analysis of the coherent noise produced by mud pump operations is pivotal to the interpretation of the low frequency seismic data recorded at the surface receivers. When the mudflow is at 350 gpm, the mud pump is operating at 197 surges per minute (spm). This generates a fundamental frequency of 197 / 60 = 3.3 Hz. In all cases where the mudflow is 350 gpm there is a strong signal at approximately 3.3 Hz as well as the second harmonic of 6.6 Hz. Non-linear acoustic studies, Urick[1], have shown that when operating at high acoustic source level the fundamental frequency reaches a saturation level and the rest of the energy goes into harmonics of that frequency. That explains why the harmonics of the fundamental frequency are so high in amplitude and do not roll off as might be expected.

When the mudflow is at 200 gpm (112 spm), it generates a fundamental frequency of 1.87 Hz. None of the recorded spectrums at 200 gpm show a signal at 1.87 Hz. The 200 gpm mudflow should produce a signal similar in amplitude as the 350 gpm flow, but there is no evidence of a 1.87 Hz signal in any of the data. (See Figure 10 and 11). This is another indication that the VectorSeis™ recording system is not displaying any signal below 3 Hz. One might expect that the application of a roll-off filter would reduce the energy at 1.87 Hz by a few dB, but should still be spectrally visible. However, there is absolutely no evidence of residual 1.87 Hz energy in the seismic data analyzed. The 3rd harmonic of 1.87 Hz is probably the strong signal seen at 5.6 Hz in Figure 10 and 11.

Record 20, Mudflow @ 200 gpm

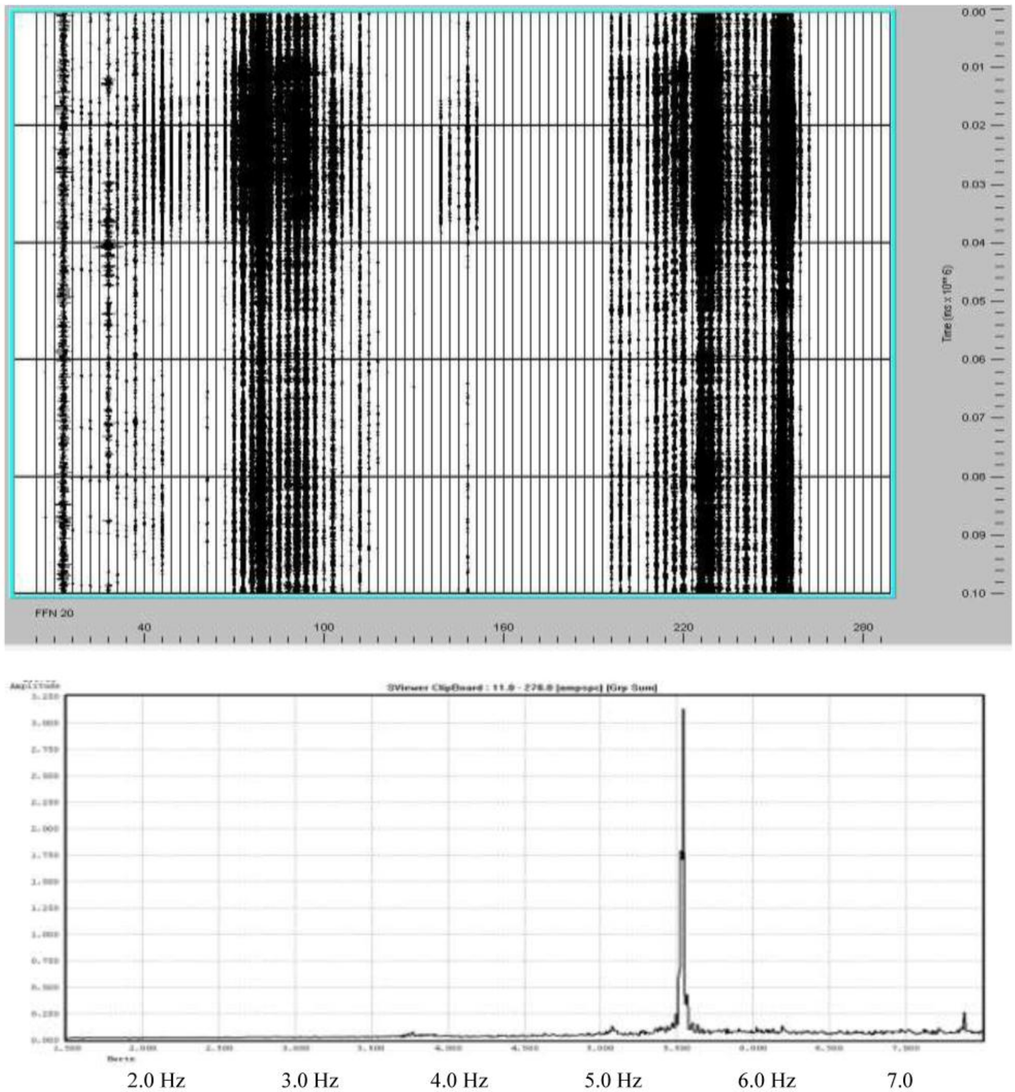

Figure 10 – 200 gpm Flow Noise Test No. 1

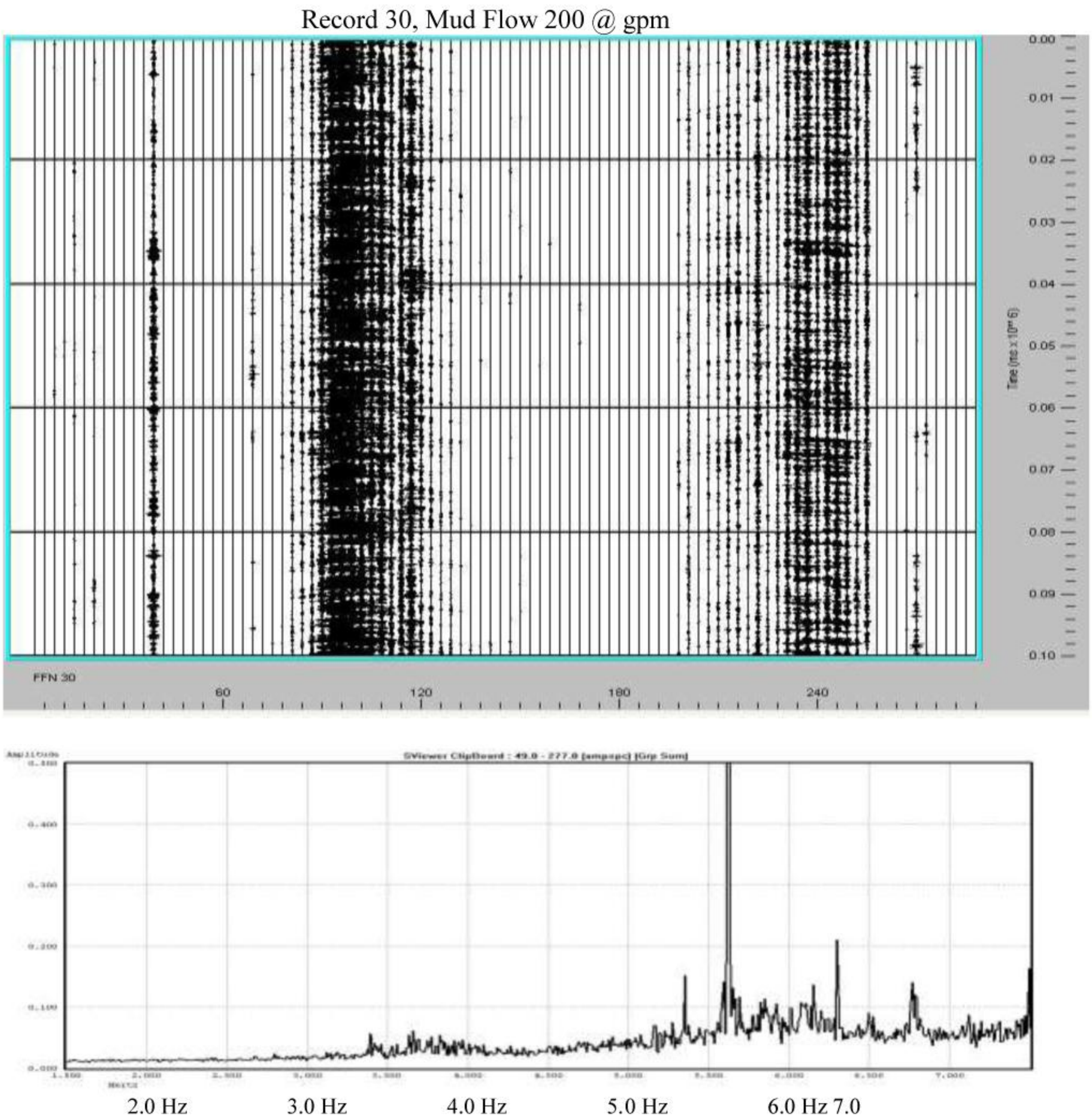

Figure 11 – 200 gpm Flow Noise Test No. 2

The 100 gpm flow rate was produced with the mud pump running at 62.2 strokes per minute (spm) producing a fundamental frequency of 1.03 Hz. Again there is no evidence of signal at 1.03 Hz seen in Figure 12 and 13. In Figure 12, there is a strong signal of unknown origin at 5.7 Hz. In Figure 13 there are many signals of unknown origin. There is a signal at 3.1 Hz which is possibly the 3rd harmonic of the 1.03 Hz fundamental frequency. It is expected that the noise produced by the 100 gpm mudflow would be less than the noise produced by the 200 gpm mudflow. Comparison of the two sets of data might lead one to believe that the 100 gpm was higher than the 200 gpm, but the two amplitudes scales are not the same. A true comparison of the recorded seismic data requires that all data be displayed at true amplitudes, and this can be difficult given the varying background noise levels and the directionality of the source. For each individual seismic data displayed, all three components from the same record have been displayed using similar amplitude parameters. For comparison between records, however, amplitudes will vary considerably and consequently, comparisons between shots are hard to make.

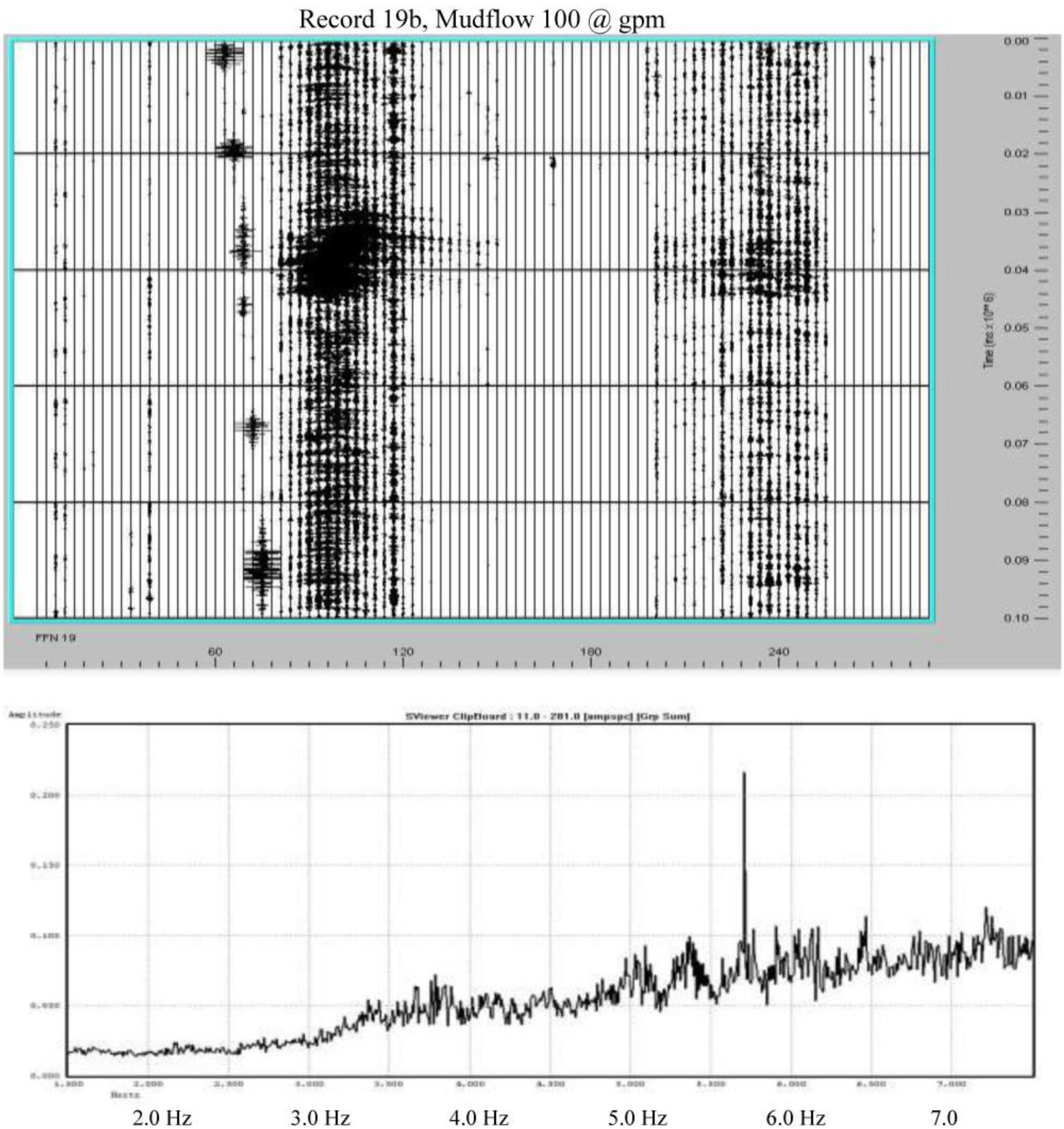

Figure 12 – 100 gpm Flow Noise Test No. 1

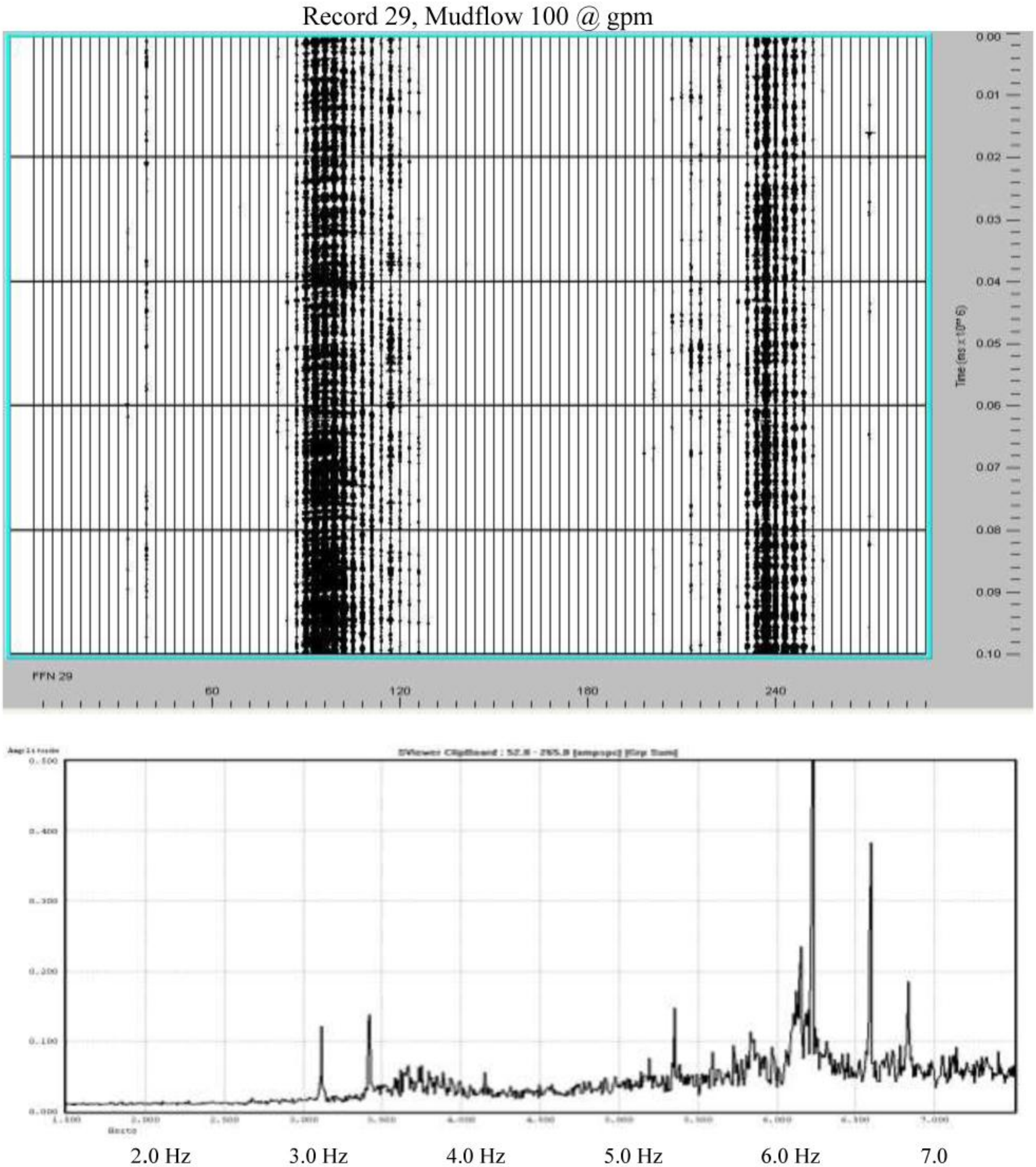

Figure 13 – 100 gpm Flow Noise Test No. 2

6.5 Modulating Low Frequency Signal

"The process by which some characteristic of one signal is varied in accordance with another signal." Encyclopedic Dictionary of Applied Geophysics, 1991, Robert E Sheriff.

Water to some extent is a nonlinear medium and the change in density caused by a change in pressure of a sound wave is not linearly proportional to the change in pressure. In any nonlinear system, frequencies different from the input frequency occur at the output. The theory of nonlinear interaction of two parallel sound waves was originally worked out by Westerfelt[2] and was experimentally verified by Bellin and Byer[3].

When two sound waves of differing frequencies (F1 and F2) propagate in the same direction through water, they interact with each other to form the sum (F1 + F2) and difference frequencies (F1 – F2) of the original frequencies. The sum frequency (F1 + F2) is of particular interest for these tests because the low frequencies, <3 Hz, are obviously being suppressed by the receiving electronics.

Previous-in-house tests by Glowka, et al. [4], conducted with a sparker showed that the pressure of water flow in a pipe was modulated by the sparker. This confirmed that when the SeismicPULSER™ is operating, it can modulate the 350 gpm mudflow signal of 3.3 Hz to produce a 5.3 Hz signal which equates to F1 + F2 or 3.3 Hz + 2.0 Hz = 5.3 Hz.

The rig environment, of course, contained many sources of background noise but the largest is from the mud pumps with a 3.3 Hz and 6.6 Hz frequency as a function of the 350 gpm pumping rate, as shown in Figure 14a. The original rationale was to program the SeismicPULSER™ at a low operating frequency of two Hz, since it was assumed to be below the bandwidth range of the background rig noise. Seismic records show that the sensors recorded no coherent energy below 3 Hz. With the receiving sensors and recording system not recording signals below 3 Hz, it was not possible to see the 2 Hz sparker signal. However, it was discovered that the two Hz signal apparently modulated with the 3.3 Hz mudflow signal, creating the combined signal of 5.3 Hz, as shown in Figure 14b.

Figure 14a below shows the recorded frequency spectrum of background noise with mudflow at 350 gpm with the SeismicPULSER™ operating and Figure 14b shows the recorded frequency spectrum background noise several minutes later without the SeismicPULSER™ operating. It is obvious comparing these two figures that a 5.3 Hz signal is present when the sparker is operating and not present when the sparker is not operating. This 3.3 Hz, 5.3 Hz and 6.6 Hz signal pattern can be seen on almost all of the seismic data recorded when the SeismicPULSER™ was firing.

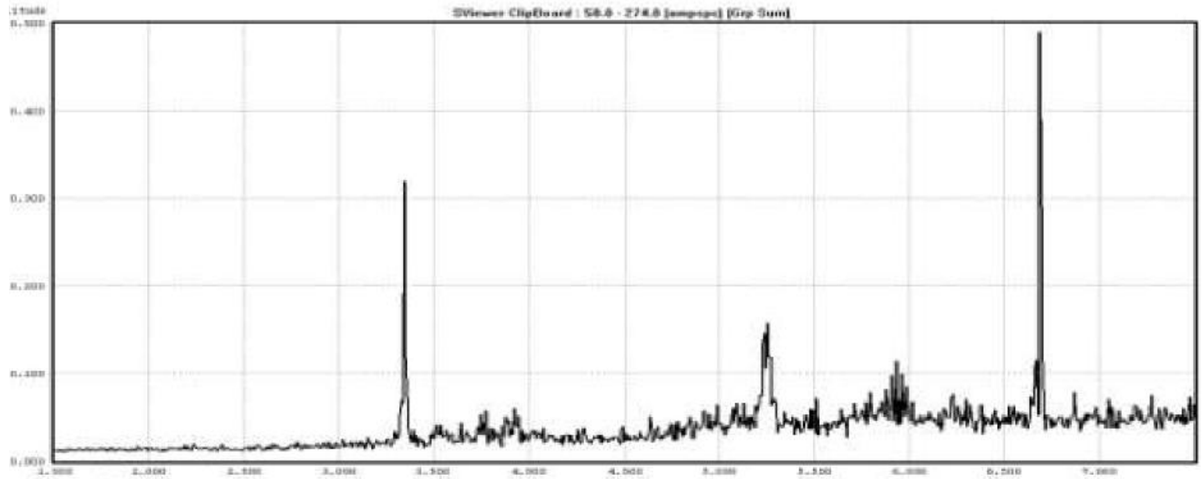

2.(2.0 Hz 3.0 Hz 4.0 Hz 5.0 Hz 6.0 Hz 7.0

Figure 14a – Sparker Operating With Mudflow @ 350 gpm

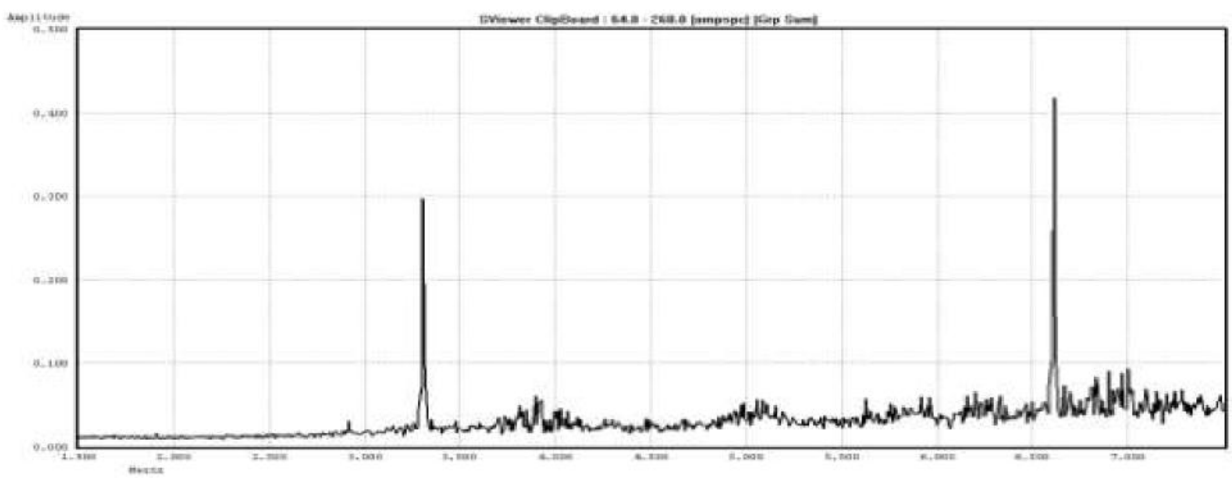

2.0 Hz 3.0 Hz 4.0 Hz 5.0 Hz 6.0 Hz 7.0

Figure 14b – Flow Noise With Mudflow @ 350 gpm, No Sparker, Test No.1

The spectral data presented in Figure 14a and 14b was taken from Record 40 and 41 respectively. The seismic data presented in Figure 15 is the recorded seismic data with 350 gpm mudflow without the SeismicPULSER™ operating. Figure 16 is the recorded seismic data with the SeismicPULSER™ operating.

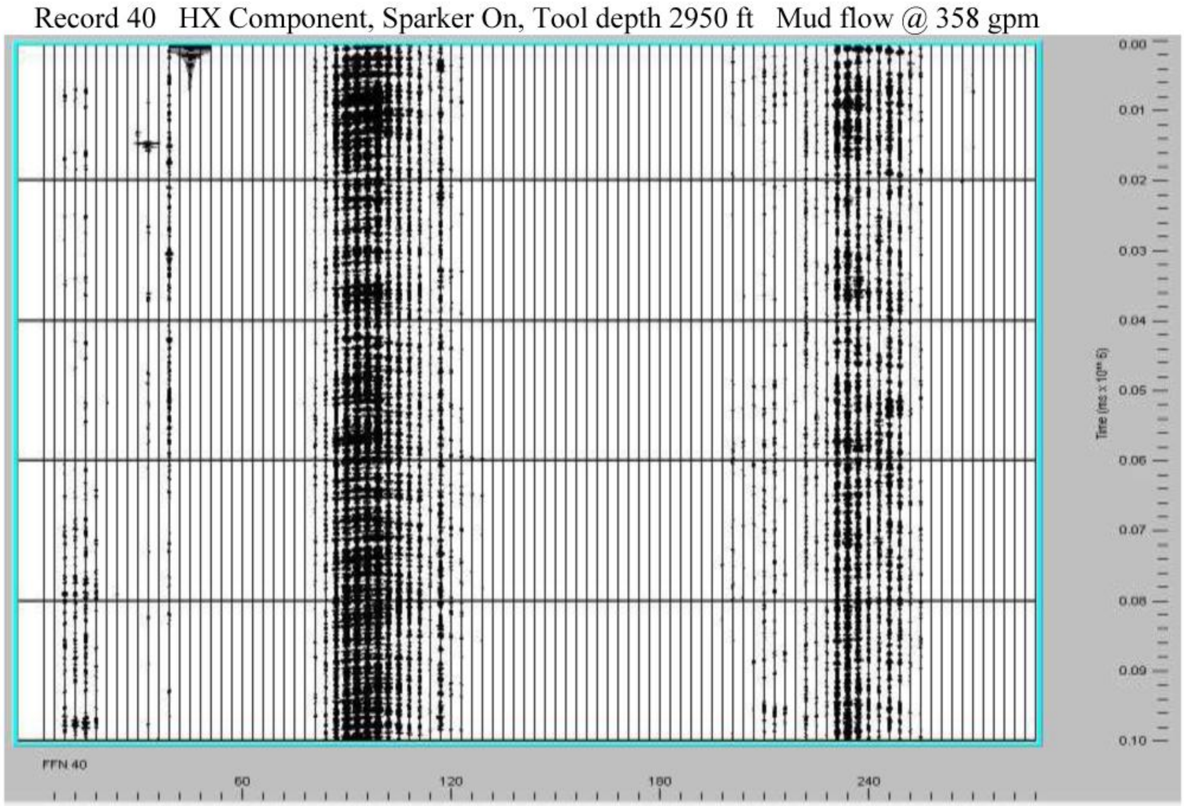

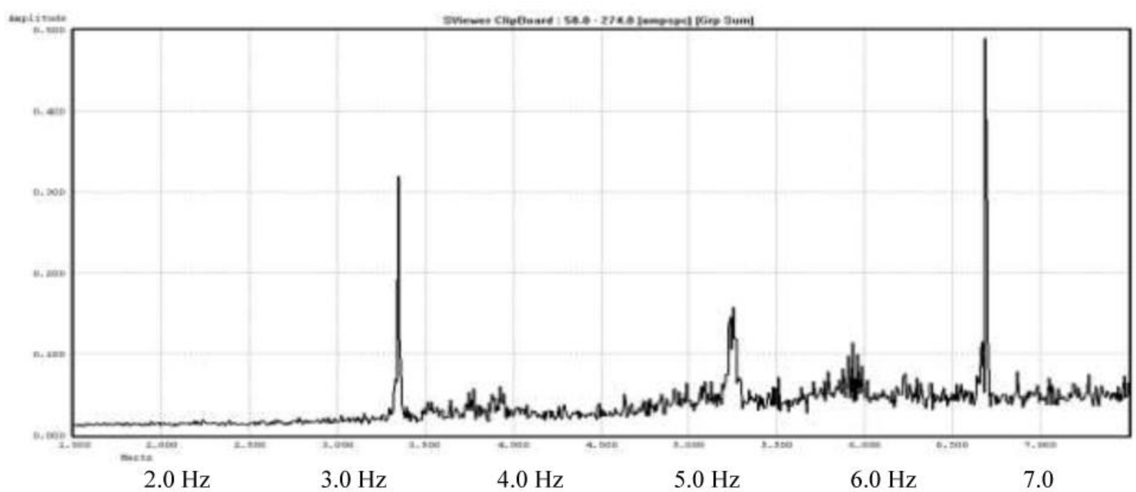

Figure 15 – Sparker Operating With Mudflow @ 350 gpm

Record 41   HX Component, No Sparker, Tool depth 2950 ft   Mudflow @ 358 gpm

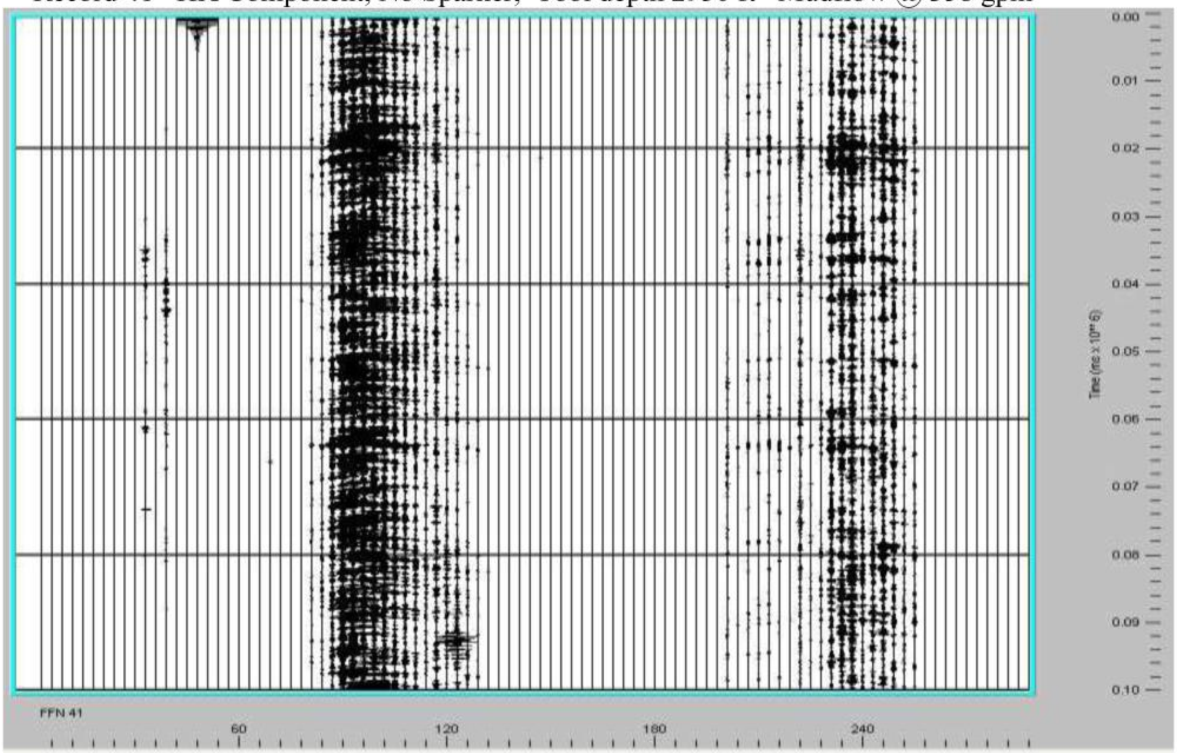

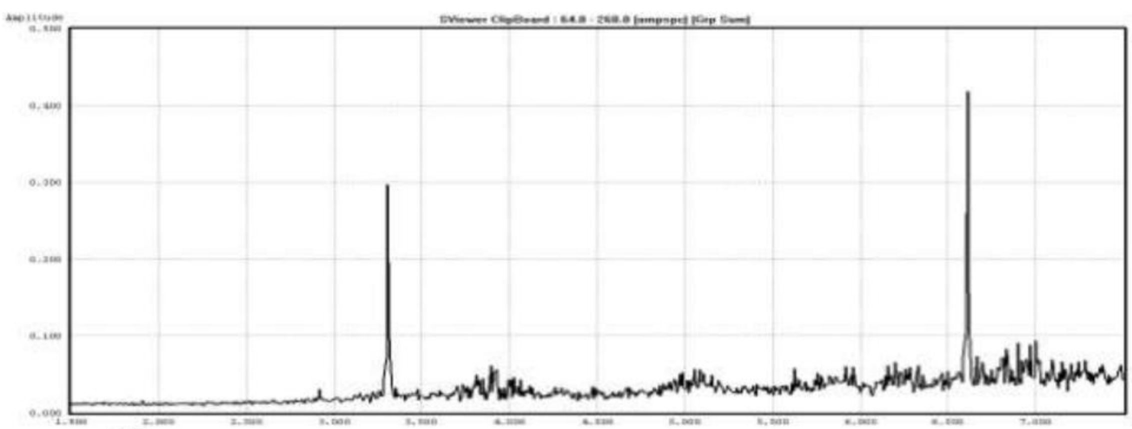

2.0 Hz   3.0 Hz   4.0 Hz   5.0 Hz   6.0 Hz   7.0

Figure 16 – Flow Noise With Mudflow @ 350 gpm, No Sparker, Test No. 2

Both hammer tests, seismic records Figure 17 and 18 below, show seismic activity at 5.3 Hz. There is, obviously, no modulation occurring with the sparker on these records as both records were recorded without the sparker firing. The hammer test generated signals across the entire frequency band and the 5.3 Hz signal is not from modulation.

Record 12, Hammer Test, Mudflow @ 200 gpm

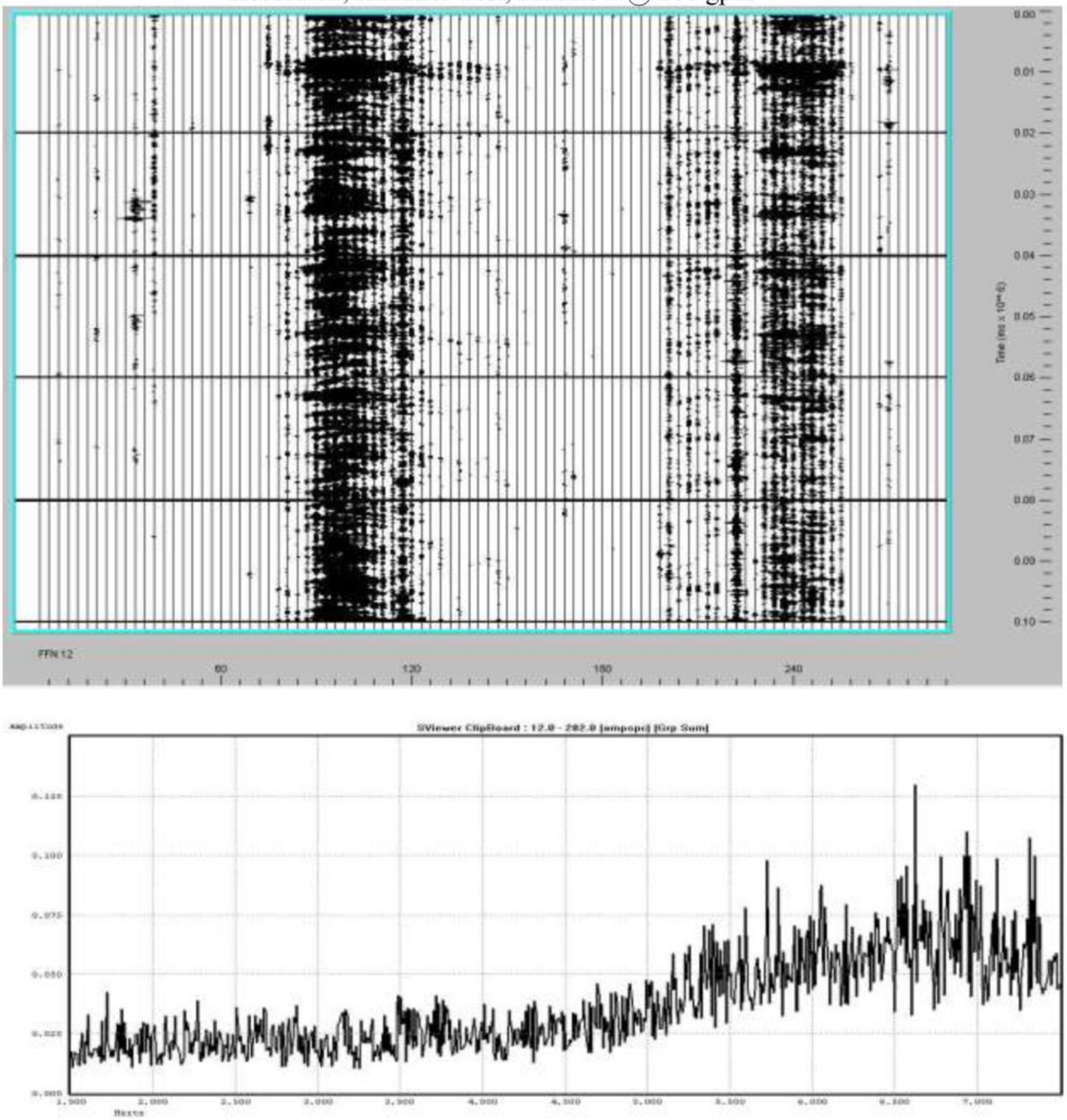

2.0 Hz 3.0 Hz 4.0 Hz 5.0 Hz 6.0 Hz 7.0

Figure 17 – Hammer Test No.1

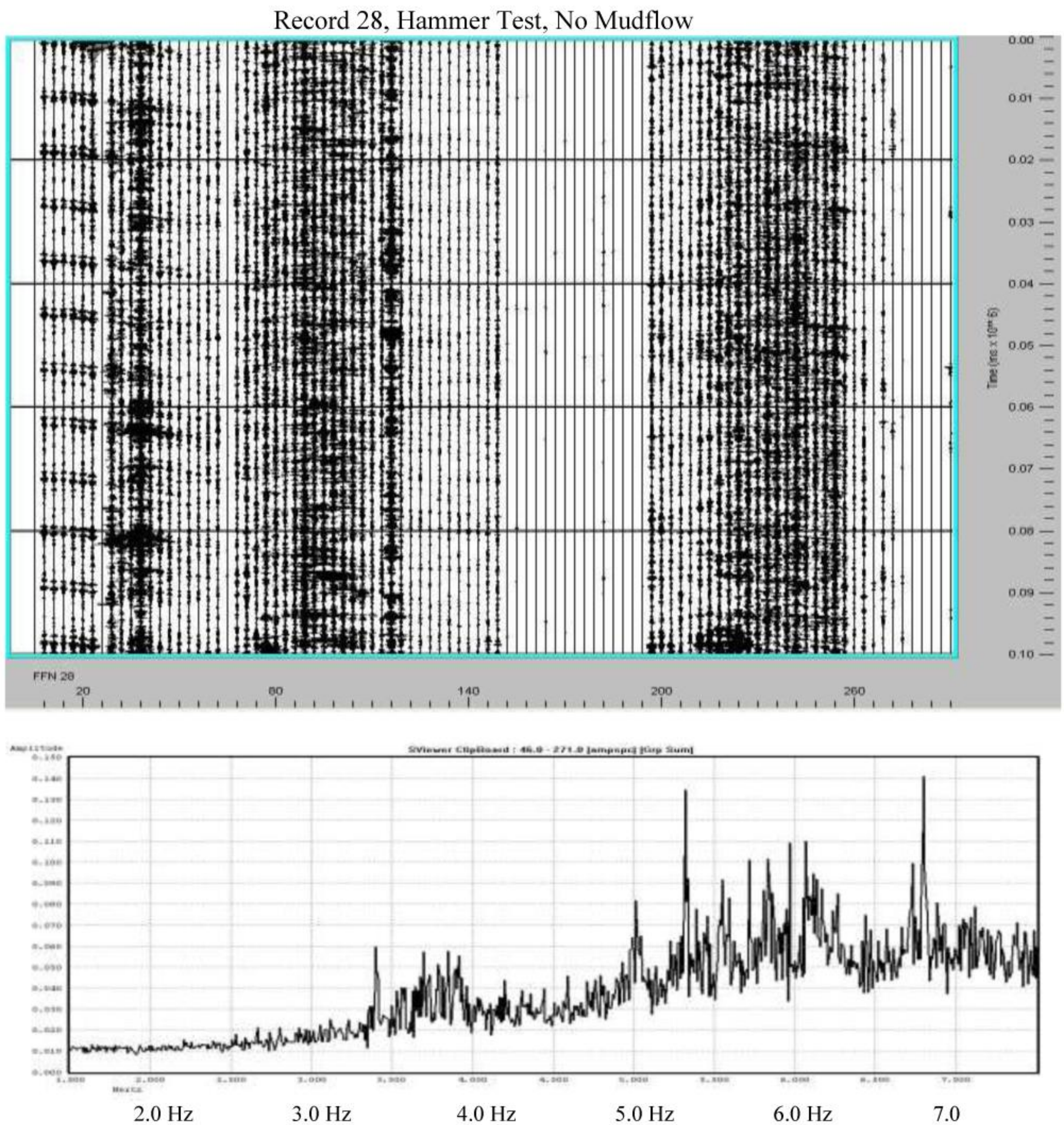

Figure 18 – Hammer Test No. 2

Overall, most of the shots with the sparker firing, show the presence of the 5.3 Hz modulated signal, but there are some records where it is small. Some noise records also show a 5.3 Hz signal.

The spectral analysis was performed on the seismic data integrated for the entire 100 sec period. The 2 Hz signal produced by the sparker only has a duration of 1 sec every 20 sec. The recorded seismic record integrates over a time span of 100 sec, so there is only a maximum probability of integrating the energy from 5 sec of the 5.3 Hz modulated signal in the 100 sec recording. The mud pump noise is continuous over the entire 100 sec. Therefore, the energy in the 5.3 Hz signal is only 5 sec/100 sec or 0.005 of the energy of mudflow noise and consequently will always be much lower.

6.6 Horizontal Directivity

Some runs were made to determine if any horizontal directivity could be determined. Figure 19 was made at 778 ft depth with the horizontal sparker pulsing. The drill pipe was then rotated 45° and Figure 20 was recorded. The 3.3 Hz, 5.3 Hz and 6.6 Hz signals are approximately the same but there are notable differences in the spectrum around 3.6 Hz. Figure 21 was recorded at 3,883 ft depth with the horizontal sparker. The drill pipe was then rotated 45° and Figure 22 was recorded. The drill pipe was then rotated another 45_0 and Figure 23 was recorded. There are some small changes in the spectral record but the most notable is the increased 5.3 Hz signal in Figure 23 after the drill pipe had been rotated 90°. It is assumed that in Figure 21 the horizontal sparker was facing away from the crossed array and in Figure 23, after rotating 90°, the sparker is facing toward the array. Because of the close proximity of the vertical sparker to the mud flow vents it is logical to assume that the vertical sparker will have greater opportunity to modulate the mudflow than the horizontal sparker, but the 5.3 Hz modulation signal is seen with the horizontal sparker as well.

Record 7, Horizontal Pulse, 775 ft Depth, Mudflow @ 350 gpm

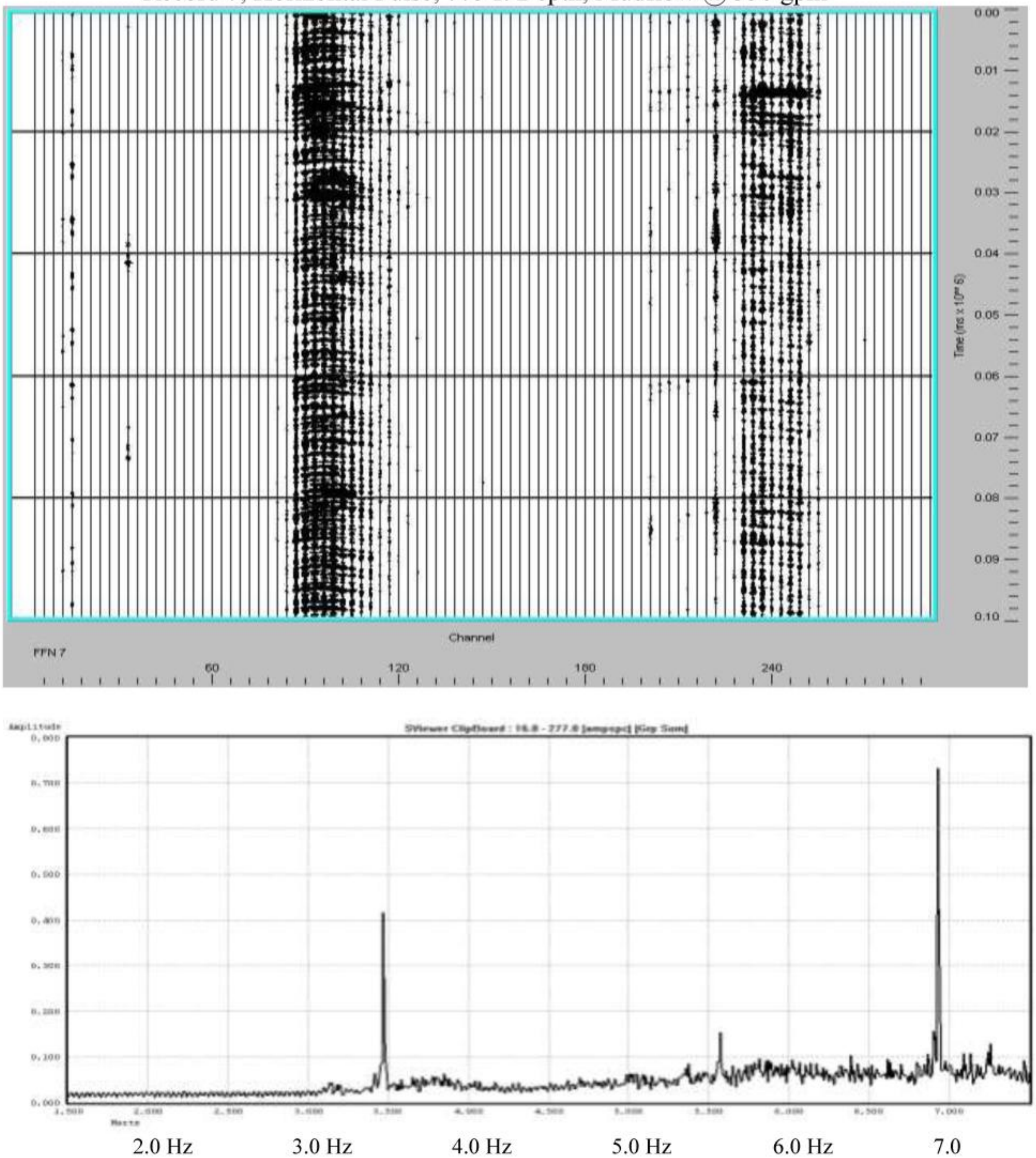

Figure 19 – Horizontal Pulse at 778 Feet

Record 11, Rotate 45^0, 778 ft depth, Mudflow @ 350 gpm

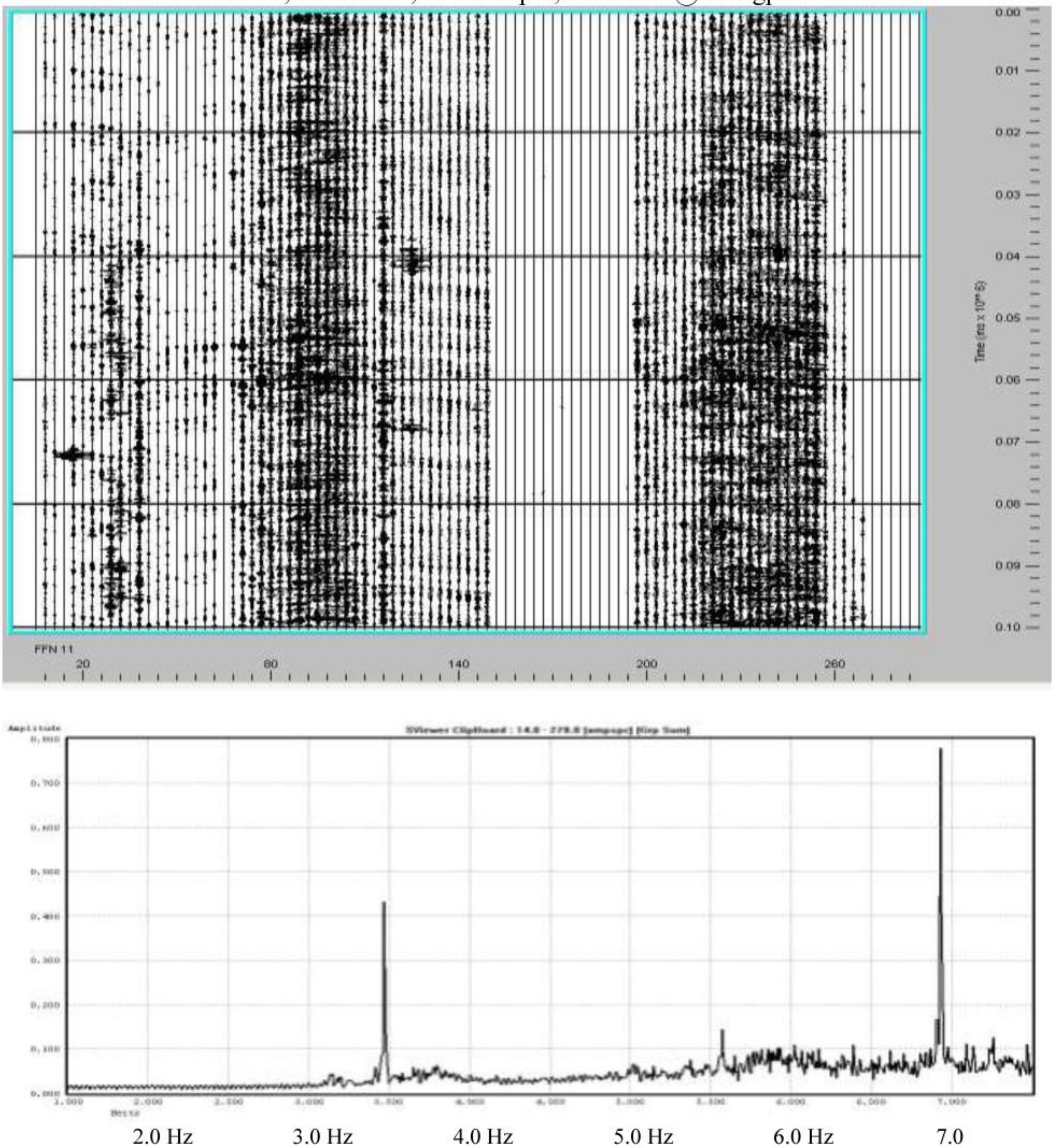

Figure 20 – Horizontal Pulse Rotate 45°

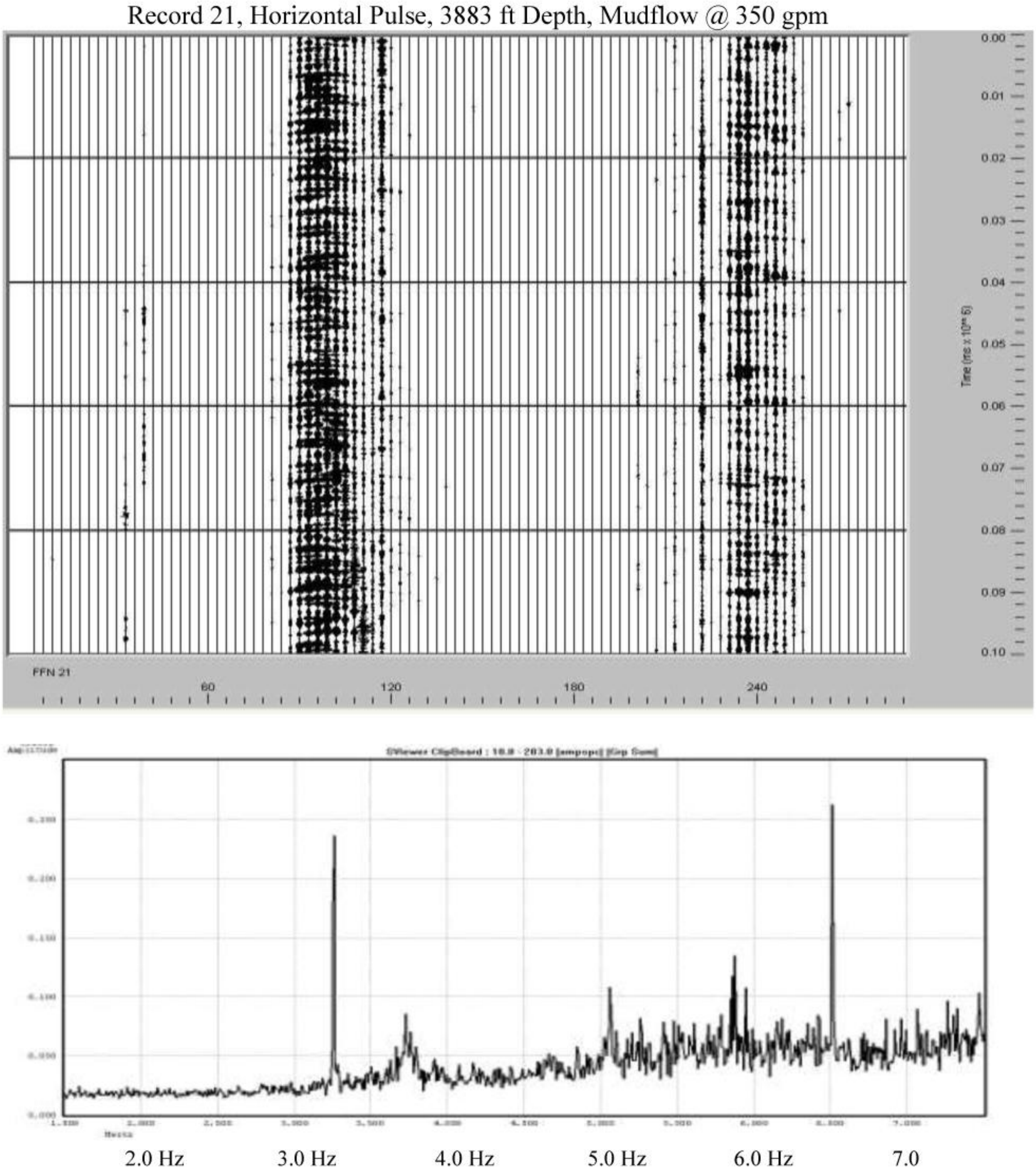

Figure 21 – Horizontal Pulse at 1338 ft Depth

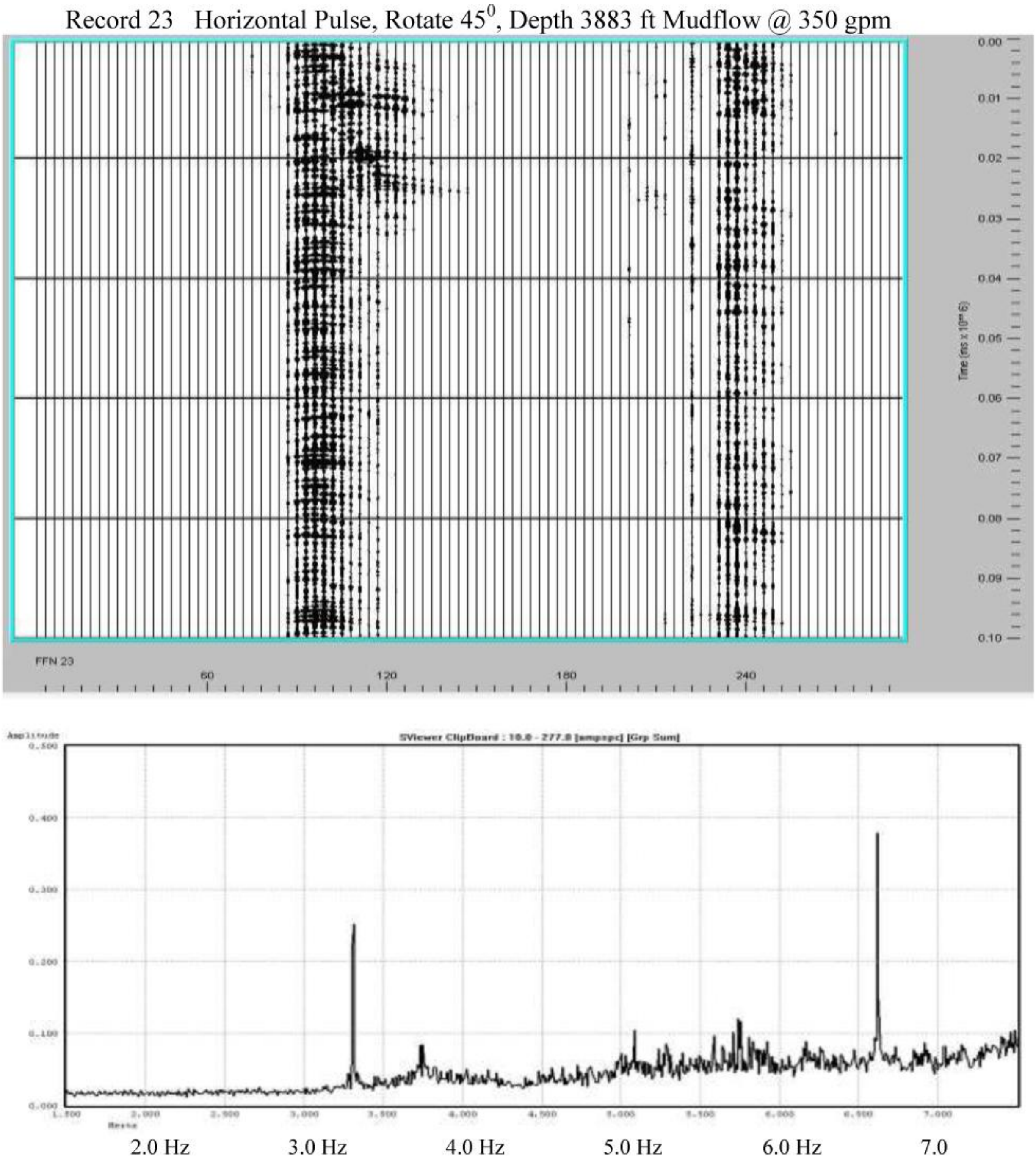

Figure 22 – Horizontal Pulse Rotate 45°

Record 24, Horizontal Pulse, Rotate Additional 45^0, Depth 3883 ft, Mudflow @ 350 gpm

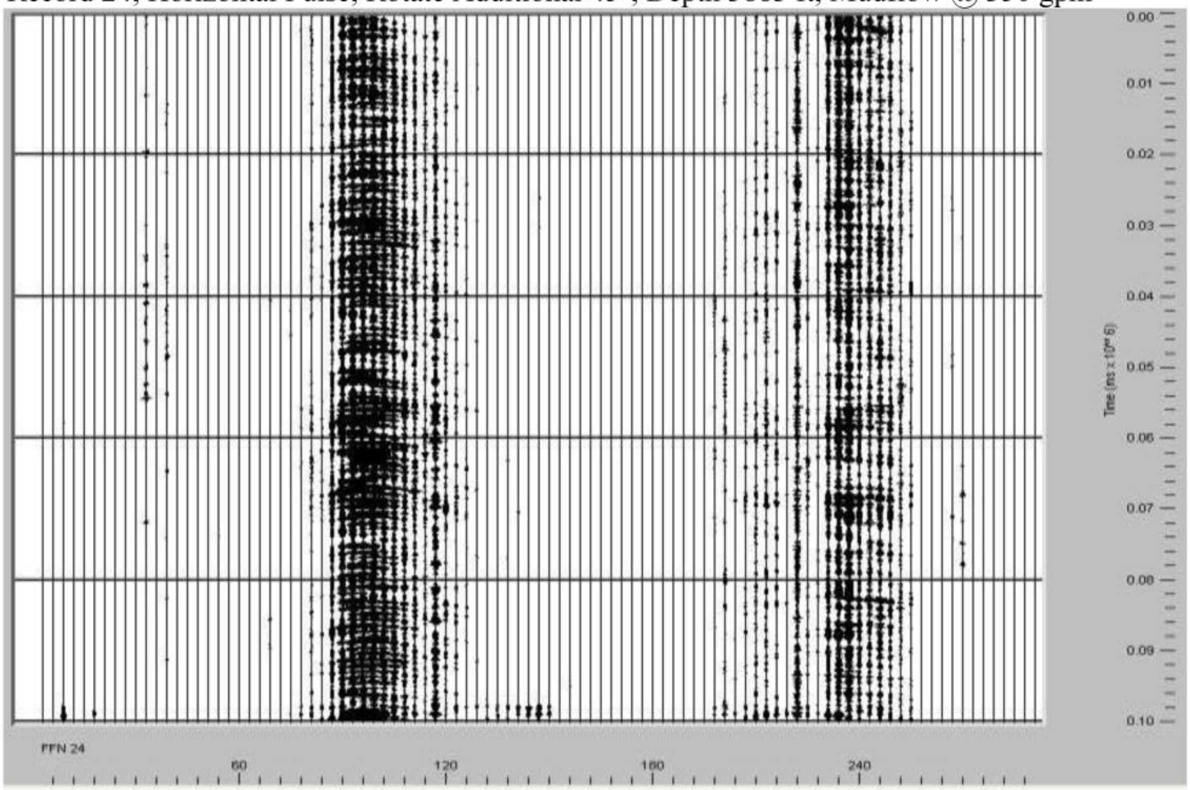

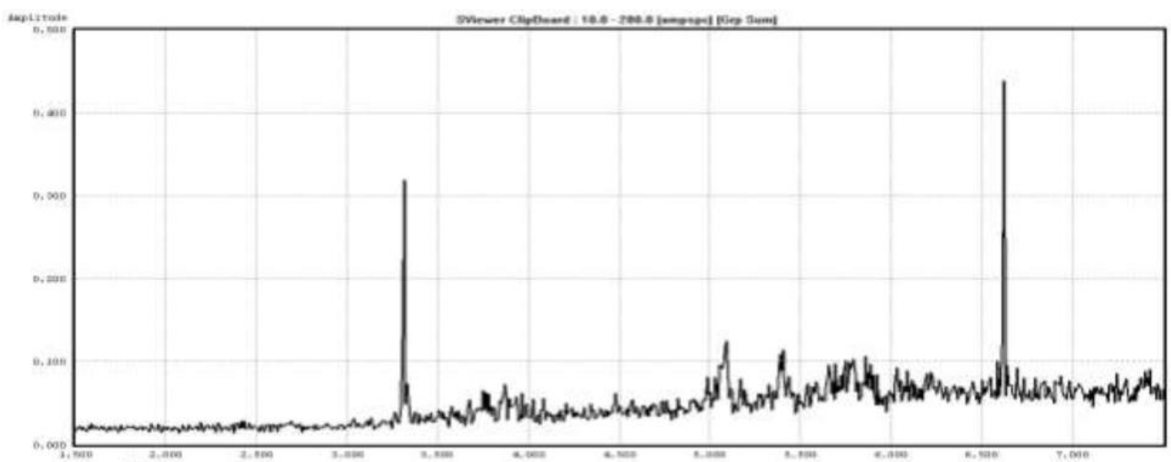

2.0 Hz 3.0 Hz 4.0 Hz 5.0 Hz 6.0 Hz 7.0

Figure 23 –Horizontal Pulse Rotate 45°

6.7 Comparison of Different Records and Different Components

A true comparison of the recorded seismic data requires all data to be displayed at true amplitudes, and this can be difficult given the varying background noise levels and the directionality of the source. For each individual seismic data displayed, all three components from the same record have been displayed using similar amplitude parameters. For comparison between records, however, amplitudes will vary considerably and consequently, comparisons between shots are hard to make.

6.8 Background Noise Prediction

Pre-analysis of the data might imply that the coherent noise background is controlled very much by the rig site operations, and is therefore predictable. One example would be to compare records for Figure 14a and 14b, recorded on day two of the test. For both records the mud pump equipment is running at approximately 350 gpm. The background noise levels, including mudflow fundamental and harmonic frequencies, are similar. However, this is not always true. Figures 12 and 13 compare two background noise seismic records taken on different days with the mudflow at 100 gpm, and they show different harmonic peak frequencies. Similarly, Figures 10 and 11, with the mud flow at 200 gpm, the harmonic peak frequencies are similar, but the average amplitudes of the two records are different. As stated earlier, amplitude comparisons between shots are not consistent.

Examples can be found where general background noise increases with mud flow, but this is not always the case. In conclusion, techniques designed to predict and subtract background seismic noise mechanisms should be used carefully.

6.9 Seismic Pulse Energy Every 20 Seconds

Visual inspection of the seismic records indicates that most records show seismic event periodicity, which is not surprising given that the main background noise originates from the rig-site mud pumps. Some of the sparker records appear to show a pattern of 20 sec periodicity, Figure 24 of Record 31 is a good example. Using a pair of dividers set to for 20 sec, repetitive pulses can be seen at 18, 36, 56, 76, and 96 sec. This evidence, supporting a 20 sec periodic energy pulse, is not overwhelming, but it does appear. As stated earlier, the two Hz signal produced by the sparker only has a duration of one sec every 20 sec. The recorded seismic record covers a time span of 100 sec so there is only a maximum probability of seeing five sec of the two Hz signal in the 100 sec recording resulting in a very low probability. An autocorrelation function calculated for these seismic records does show a slight increase in amplitude at 20 sec lag time and is presented in section 7.0.

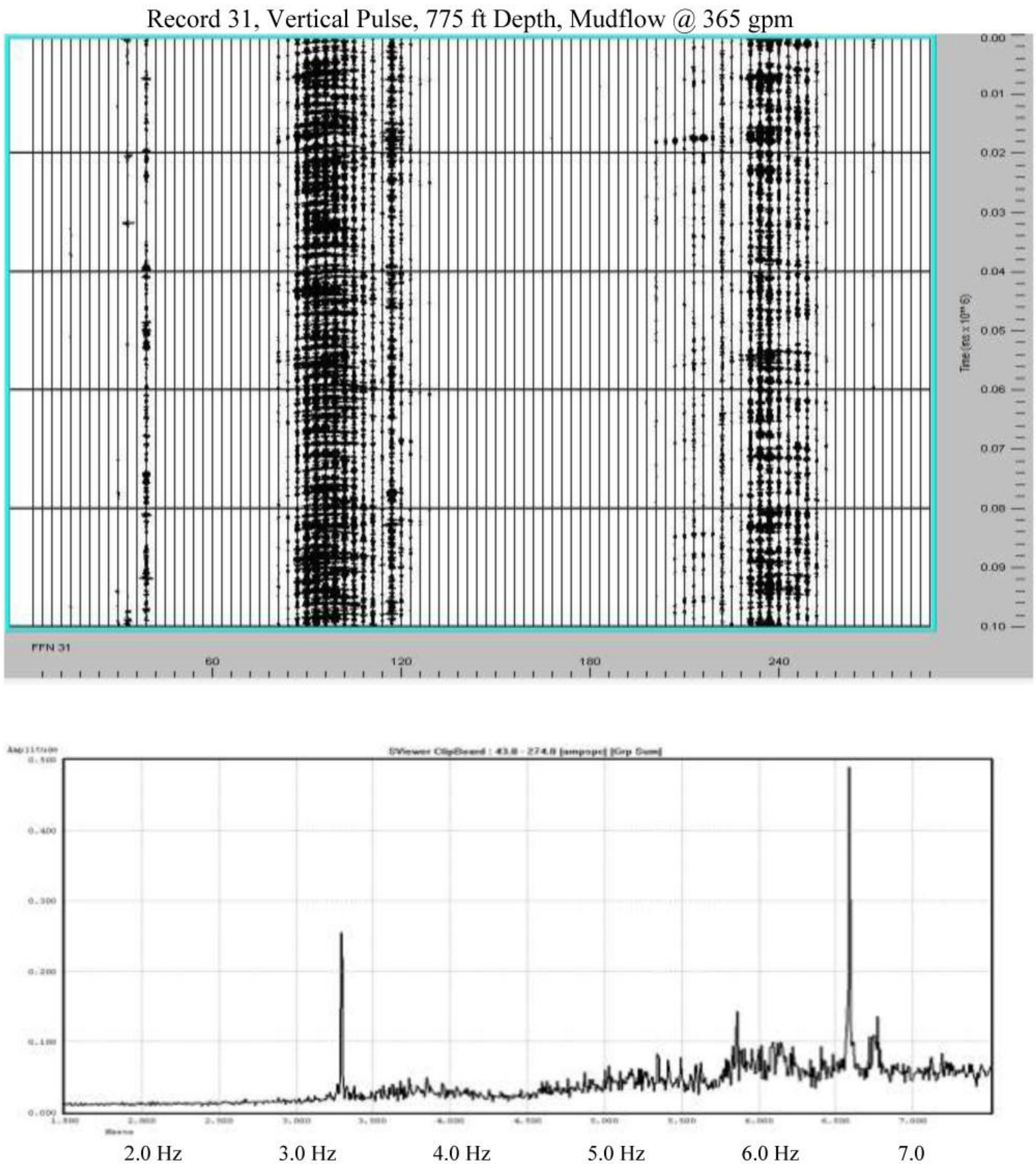

Figure 24 – 20 Second Periodicity

7.0 AUTOCORRELATION ANALYSIS

Autocorrelation was performed on selected sets of data to see if any 20 sec periodicity was apparent. Records 40 and 41 were chosen because that was the only set of data that had flow noise for mudflow at 350 gpm with and without the sparker firing. Autocorrelation (windowed region shown) of the flow noise and the sparker firing at 20 sec intervals, shown in Figure 25 and 26. Figure 25 does show some small autocorrelation. An expanded autocorrelation of Records 40 and 41 are shown in Figure 27.

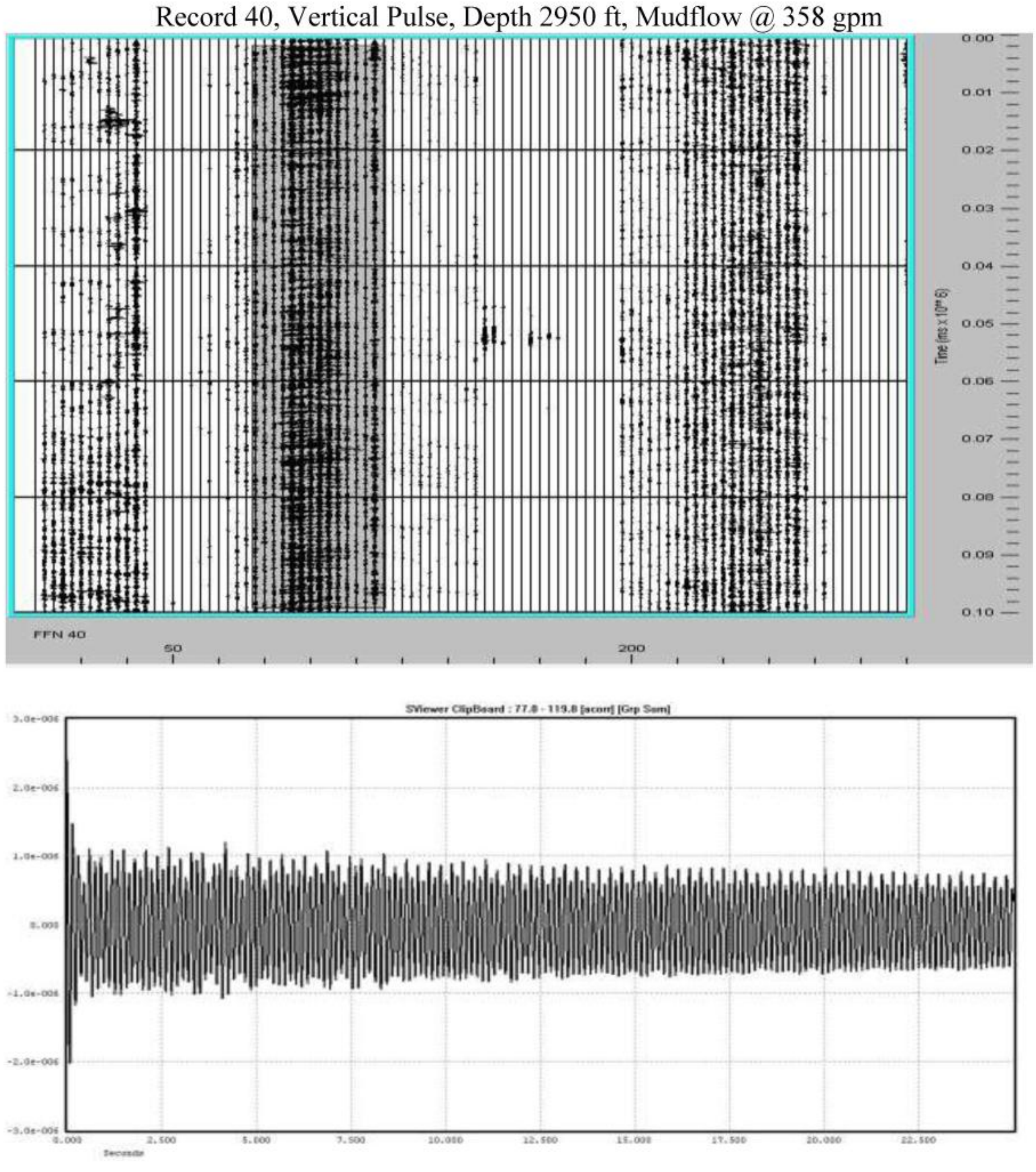

Figure 25 – Autocorrelation of Vertical Pulse

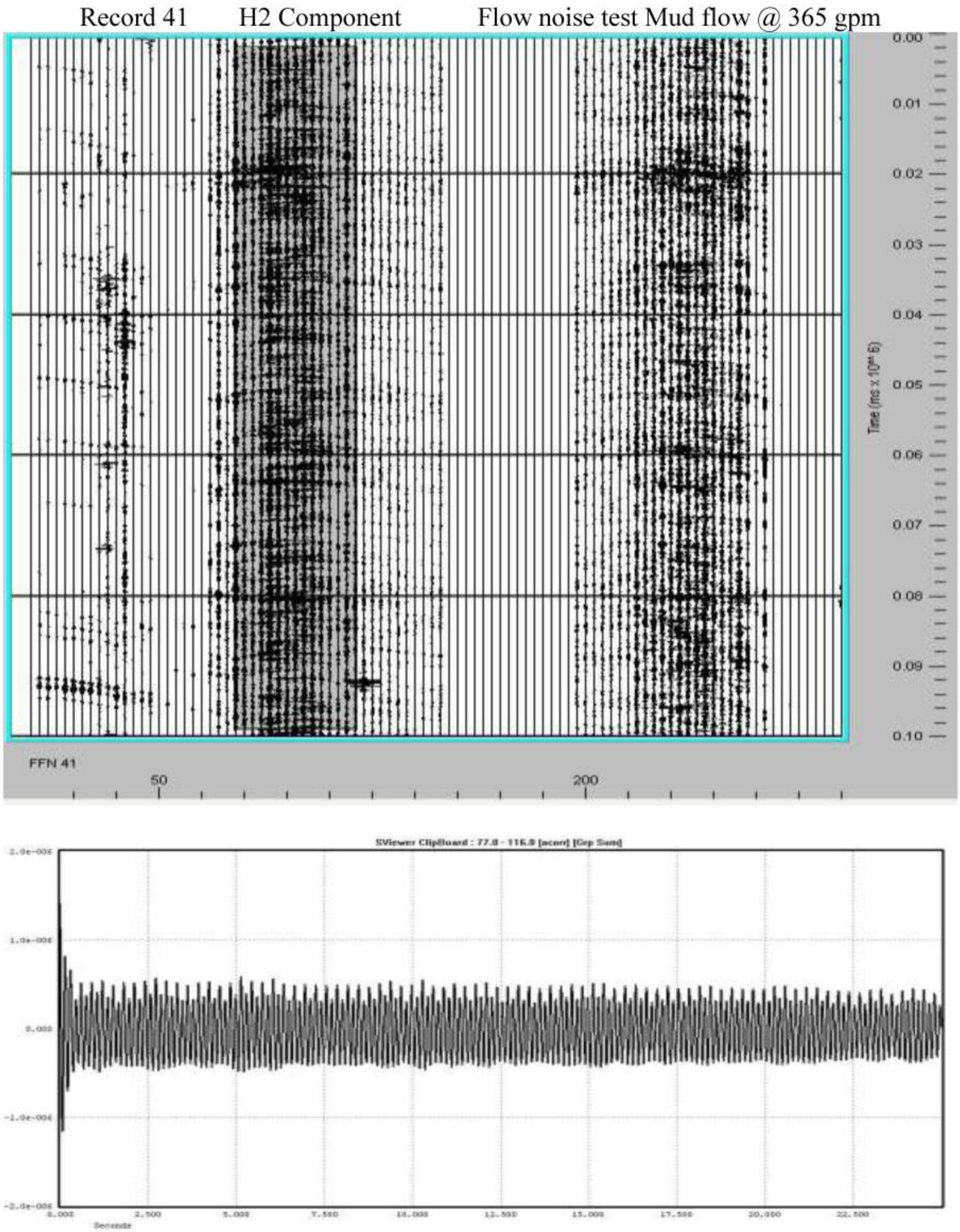

Figure 26 – Autocorrelation of Mudflow Only @ 350 gpm

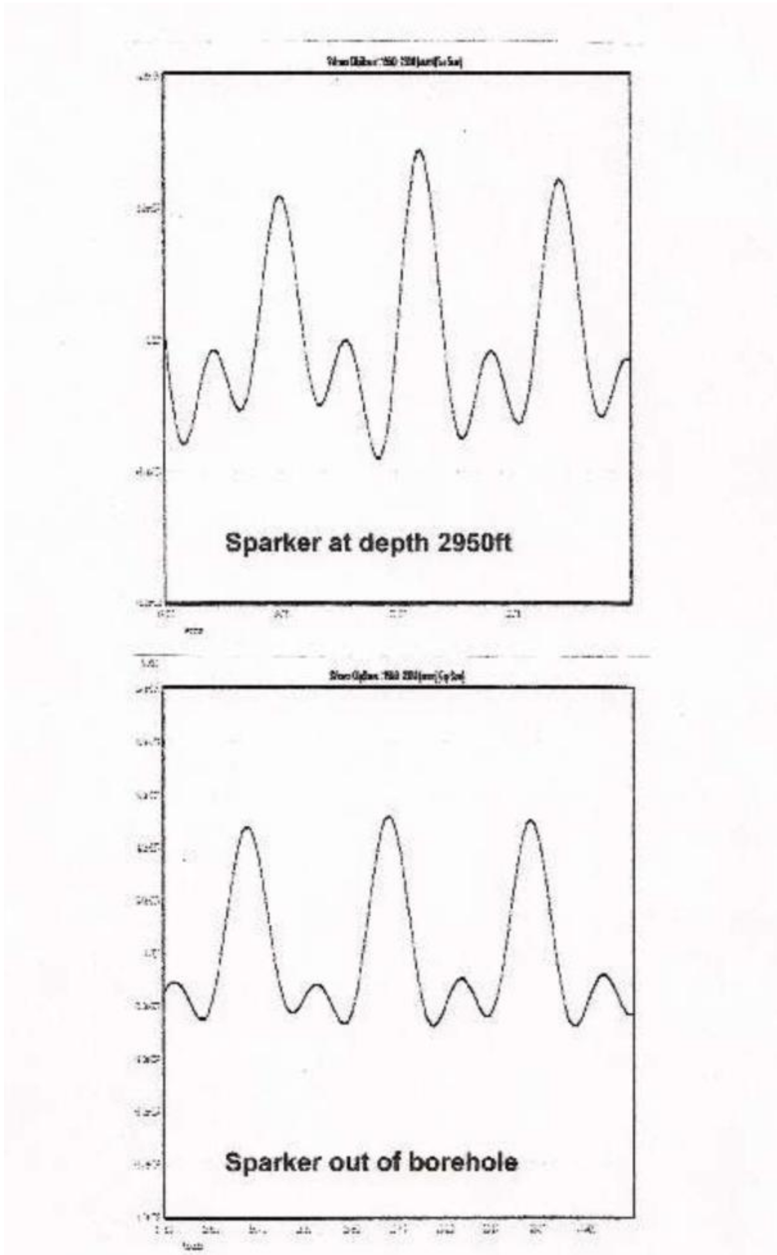

Figure 27 – Comparison of Autocorrelation With Sparker In and Out of Hole

8.0 CONCLUSIONS AND RECOMMENDATIONS

8.1 Conclusions

1. Even though the two Hz generated by the SeismicPULSER™ tool was not recorded due to surface receiver limitations, a 5.3 Hz modulation signal was detectable.
2. There is a 20.0 sec periodicity in the data, which corresponds to the time between sparker pulse sequences.

3. As the drill string was rotated 90° between sparker firings, the changing amplitude in the survey recordings showed that the 5.3 Hz modulated signal from the horizontal sparker had directional characteristics.
4. Increased power, and thus a greater signal to noise ratio, is desirable when operating when the pumps are running (see recommendation below for operating when the mud pumps are turned-off).
5. Determining the first arrival time by noting when the mud flow reached 350 gpm, thus activating the sparker firing sequence, is not an accurate method.
6. The field tests at RMOTC demonstrated that low frequencies can be generated and transmitted from 4,000 ft to the surface by an otherwise high frequency sparker.

8.2 Recommendations

1. The addition of a downhole clock that is synchronized with the surface recordings is required to perform commercial Drill Bit SWD services.
2. Design the SeismicPULSER^{TM} control system to have a selectable frequency tuned to operate in the quite zone of the ambient noise environment created by the rig and surrounding noise sources.
3. Commercial Drill Bit Seismic While Drilling services should be performed when the mud pumps are turned-off.

8.3 References

1. Urick, Robert J., Principles of Underwater Sound, 2nd Edition, 1975, page 75, McGraw-Hill, New York.
2. Westerfelt, P. J., Scattering of Sound by Sound, Journal Acoustic Society of America, 39:924, (1957)
3. Bellin, J. L. S, and Beyer, R. T., Experimental Investigation of an End-Fire Array.
4. Journal Acoustic Society of America, 34:105 1 (1962)
5. Glowka, David A., Advanced Seismic While Drilling System, Appendix C, Effects of Low-Pressure Flow on Spark-Generated Bubbles, (2008).

APPENDIX Da – ALL RECORDED SEISMIC DATA

Selected records from this data set were used in the report. Each Record shows 100 sec of recorded seismic data and a 20 sec expanded window. At the bottom of each record is the spectrum of the 100 sec recorded seismic signal.

Record 19a   All 3 Components   Background noise test   Mud flow @ 100 gpm

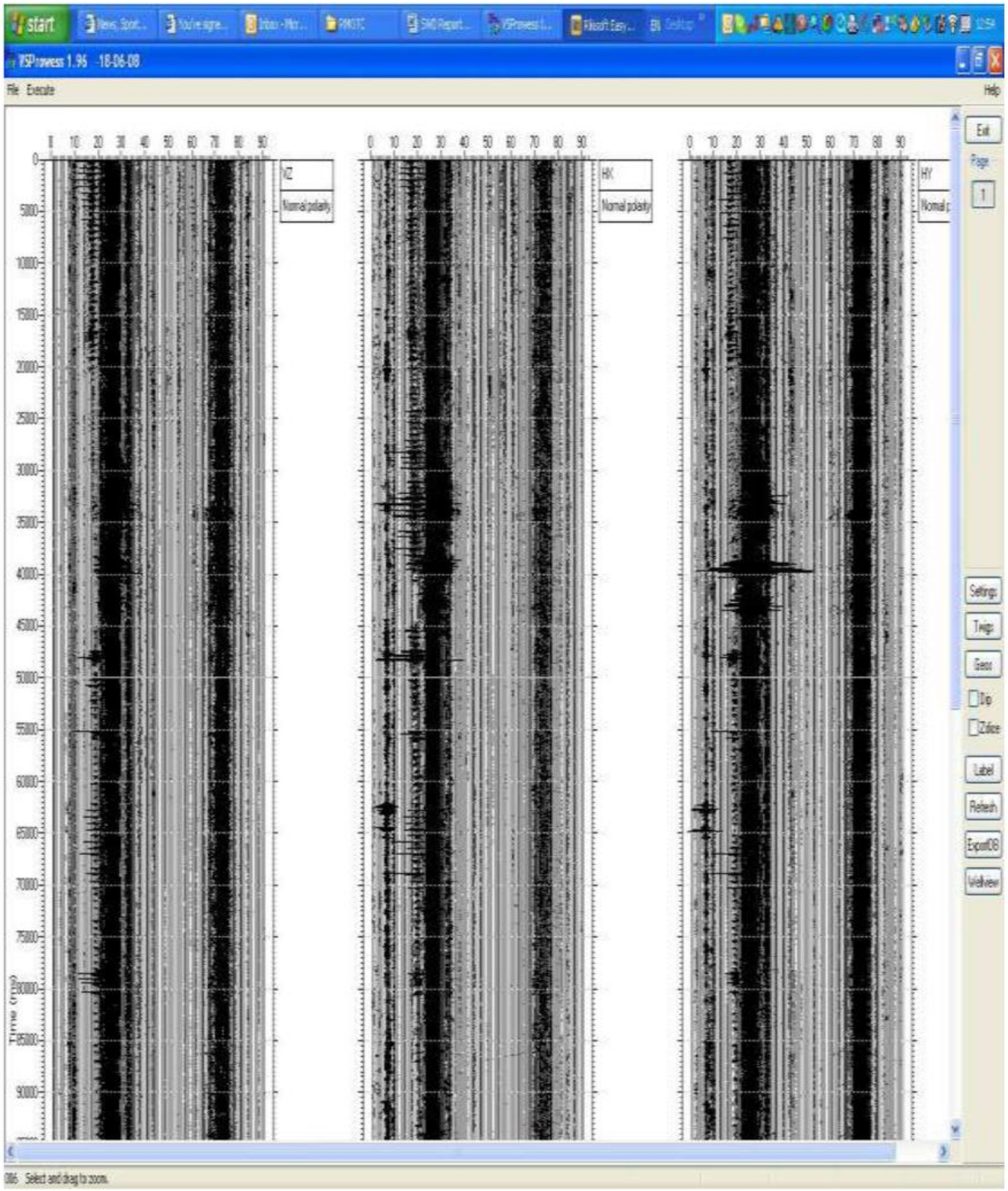

Record 19b, Z component, Background Noise Test, Mudflow @ 100 gpm

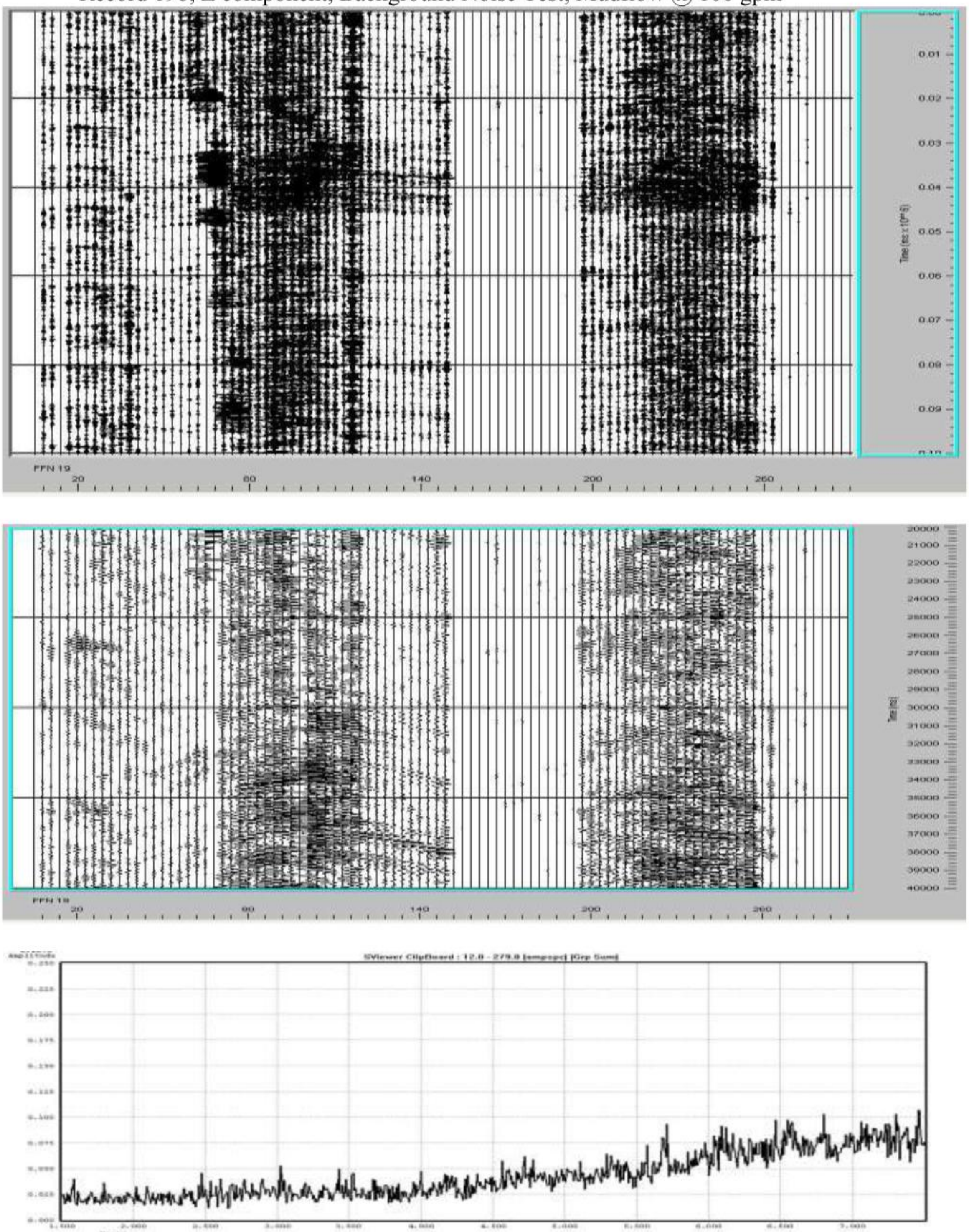

Record 19 HX component Background noise test Mud flow @ 100 gpm

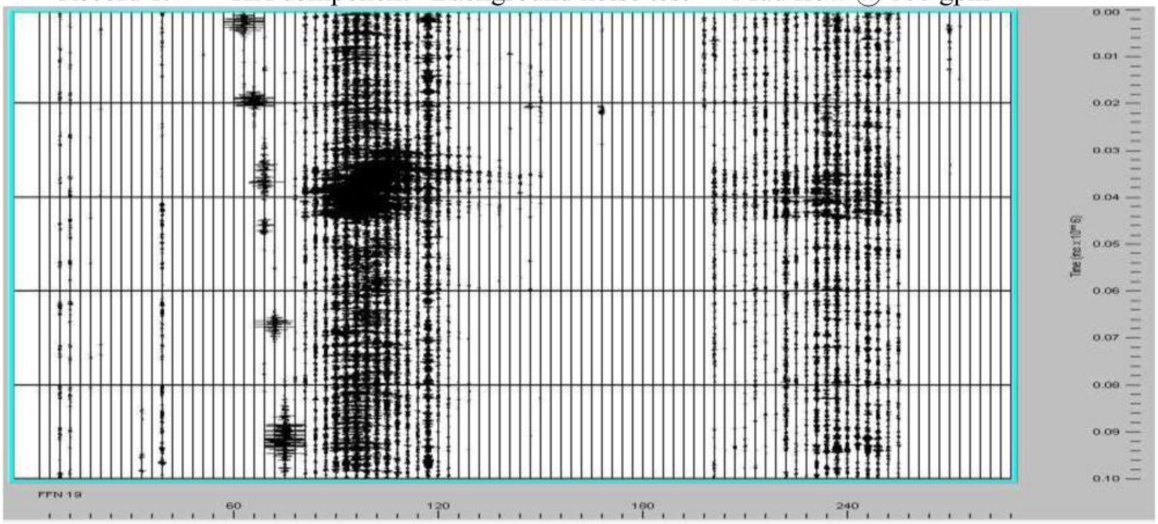

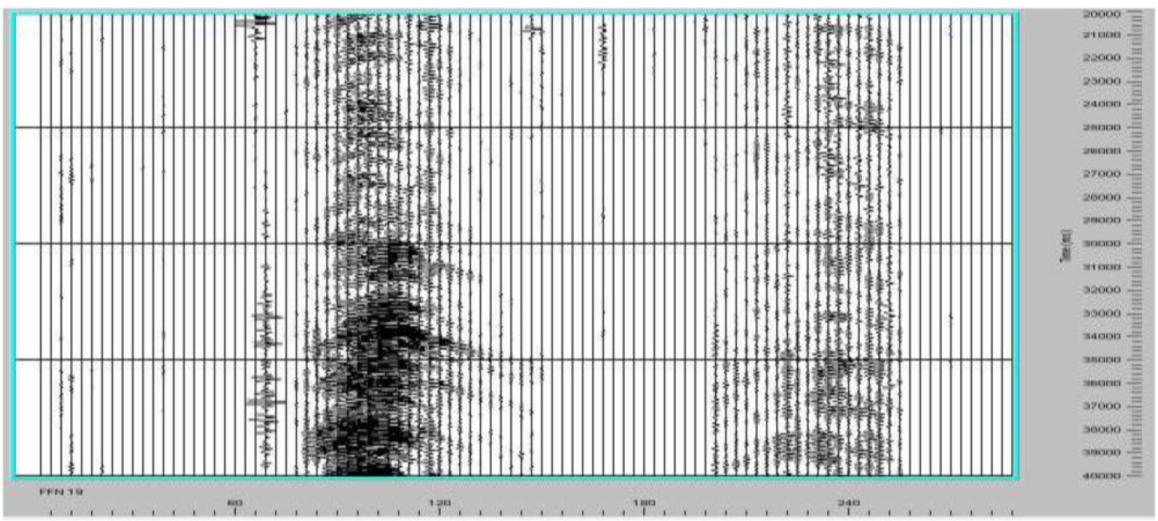

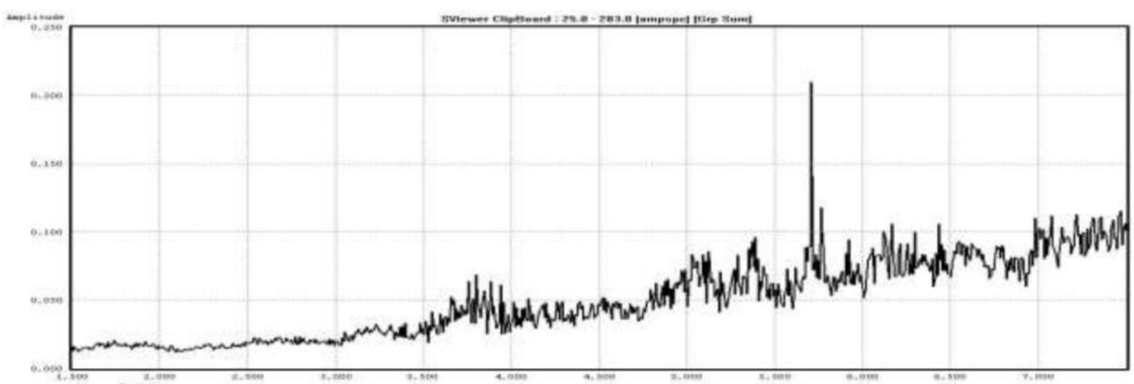

Record 19 HY component Background noise test Mud flow @ 100 gpm

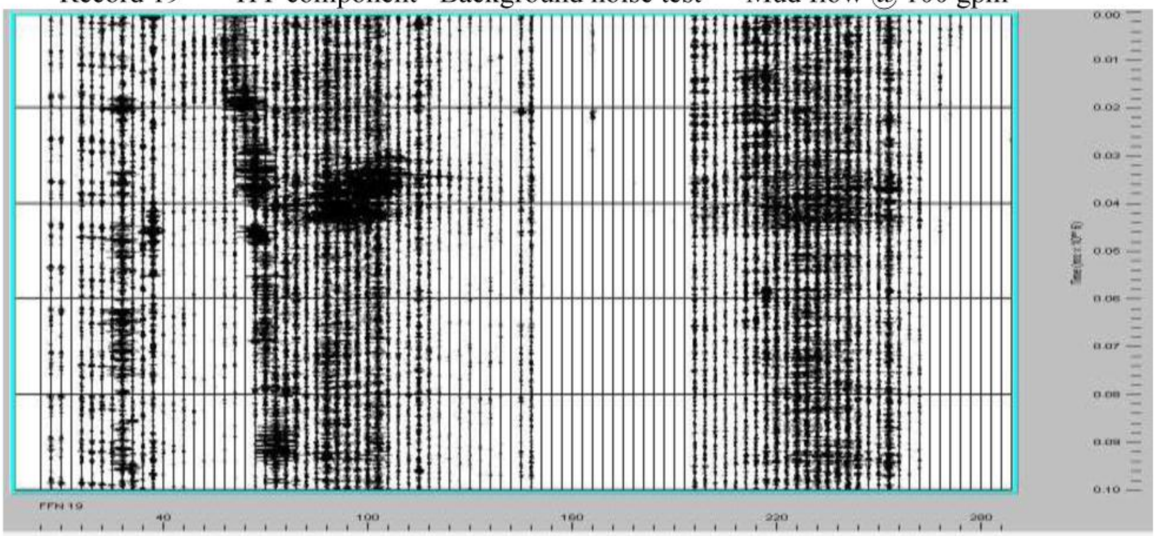

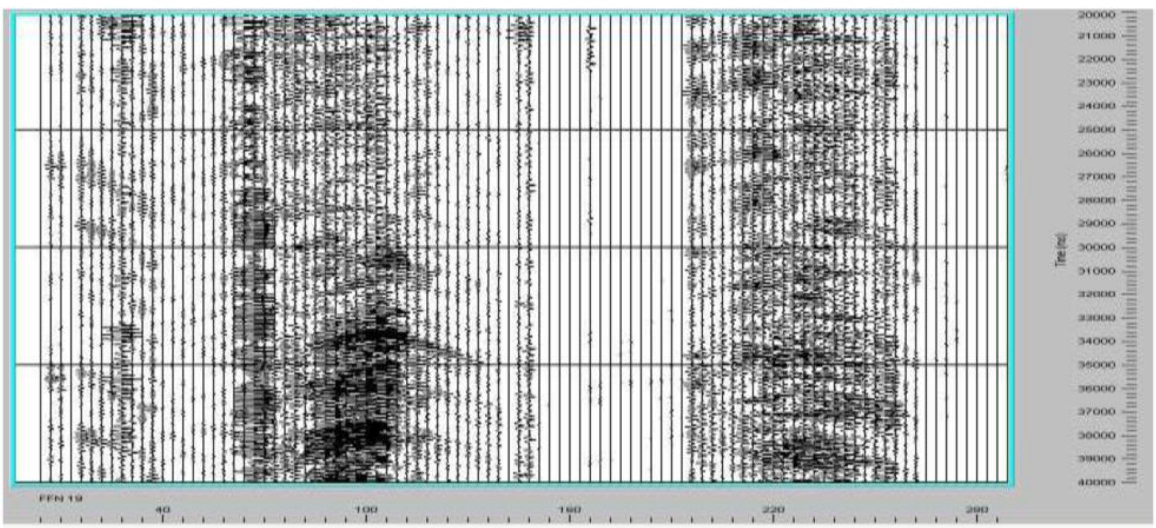

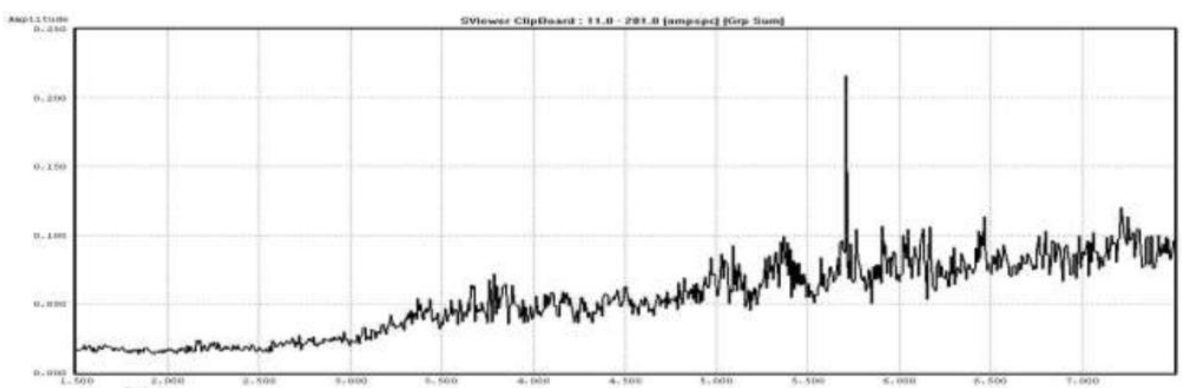

Record 20 Z Component Background noise test Mud flow @ 200 gpm

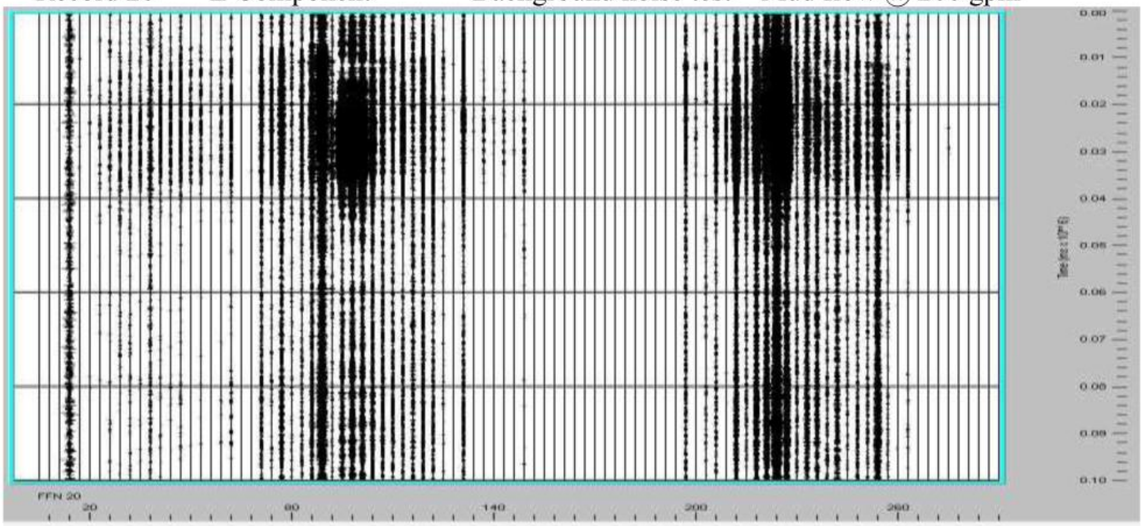

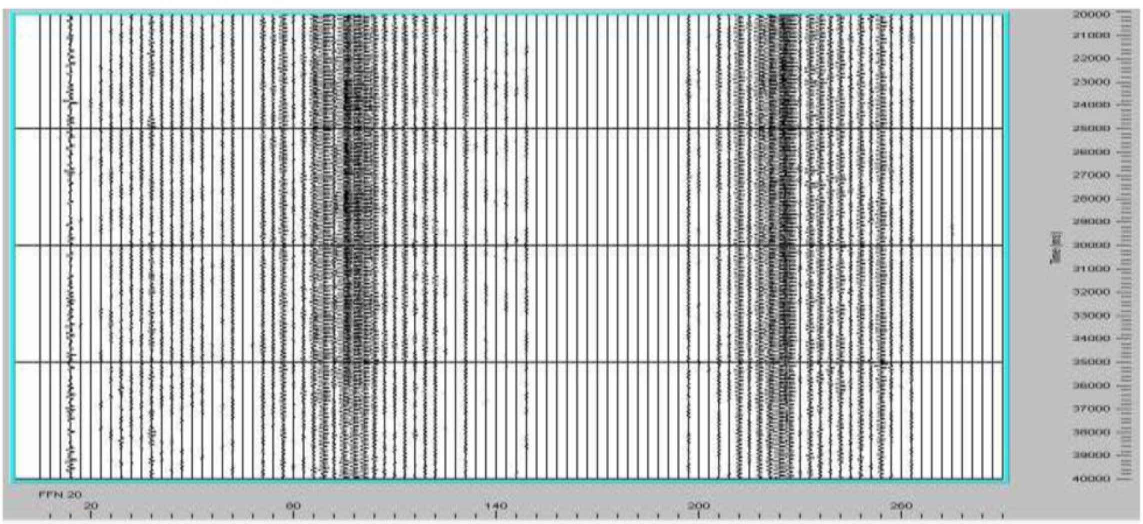

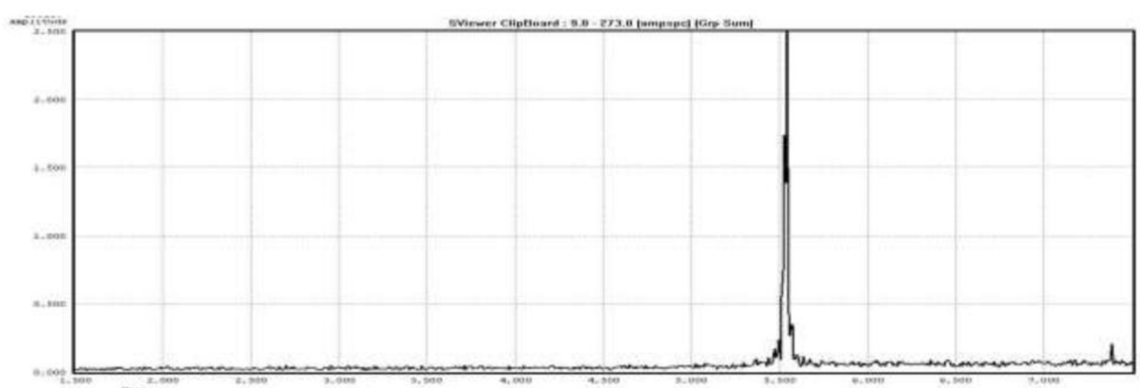

Record 20 HX component Background noise test Mud flow @ 200 gpm

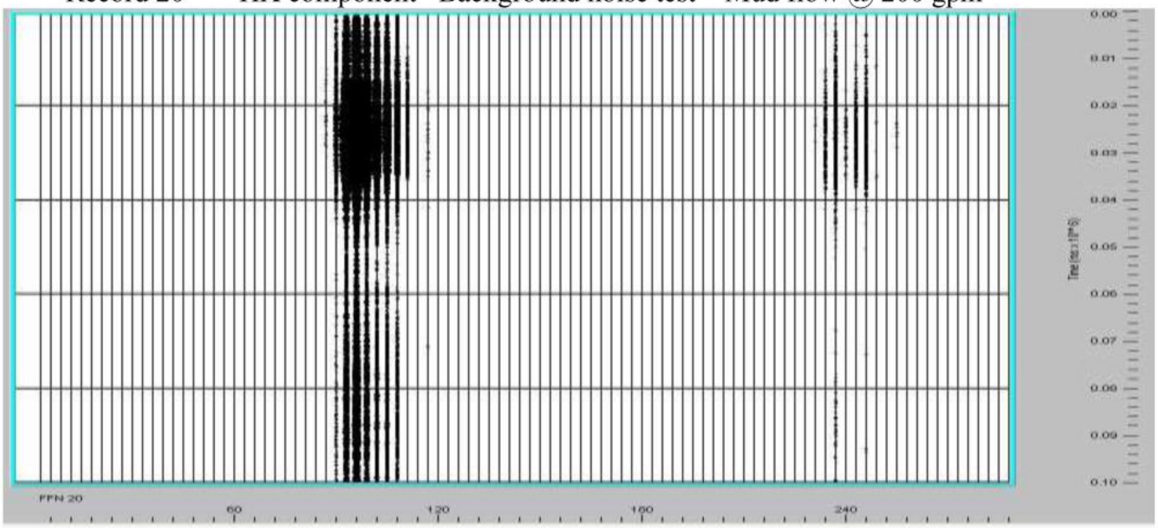

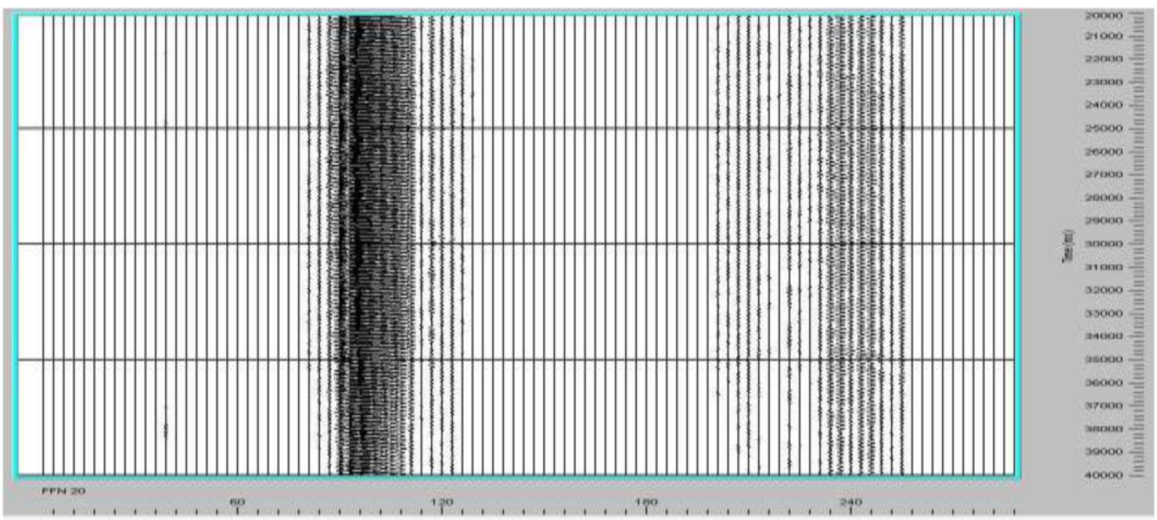

Record 20 HY component Background noise test Mud flow @ 200 gpm

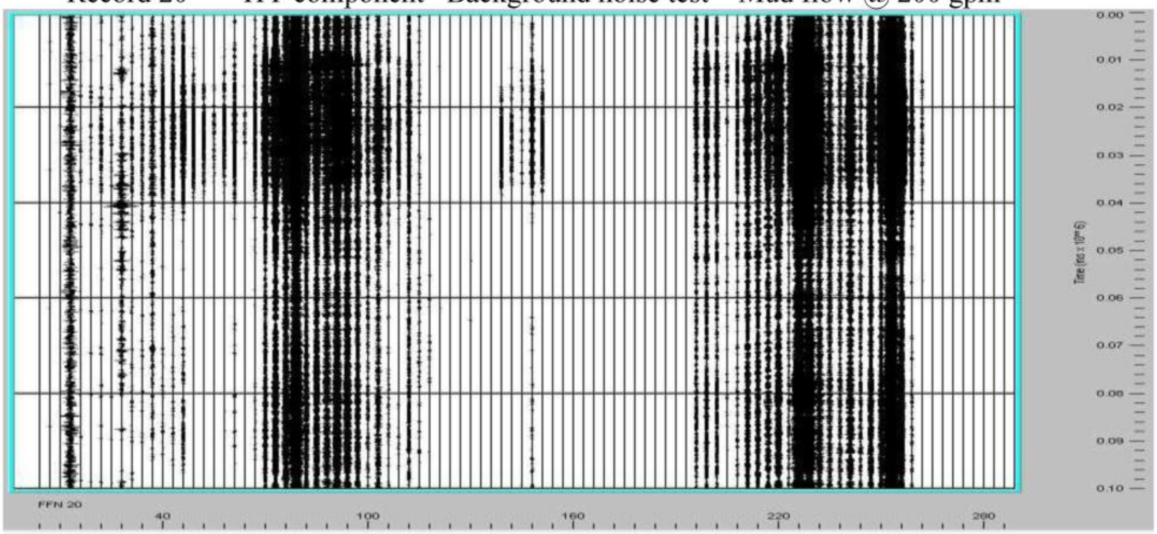

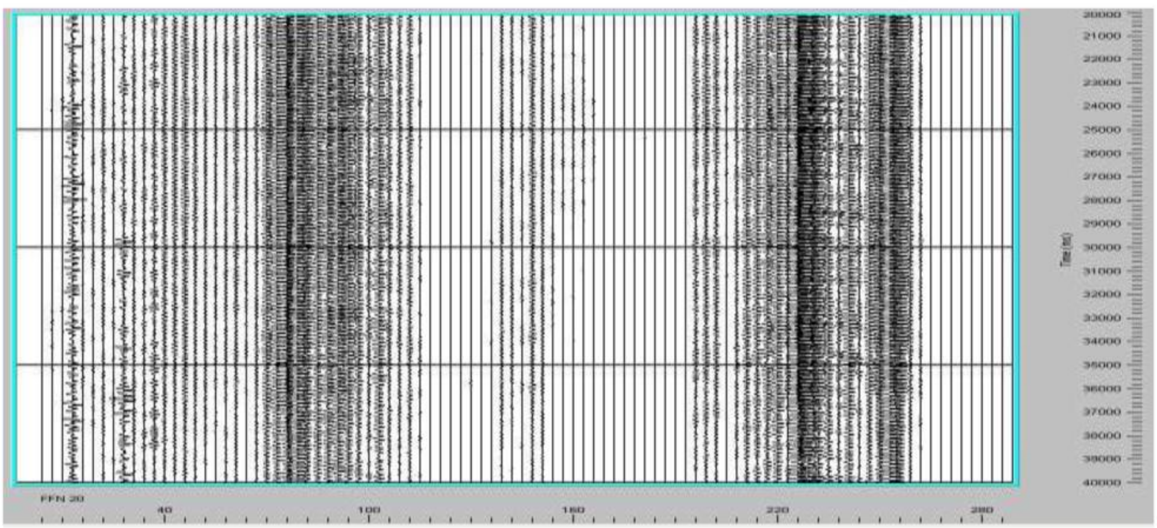

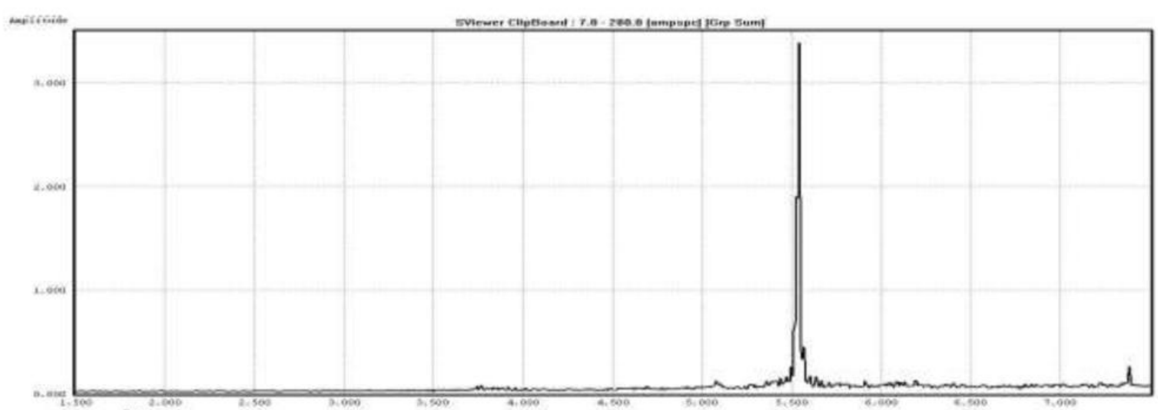

Record 12 Z Component, Hammer Test, Mud flow @ 200 gpm

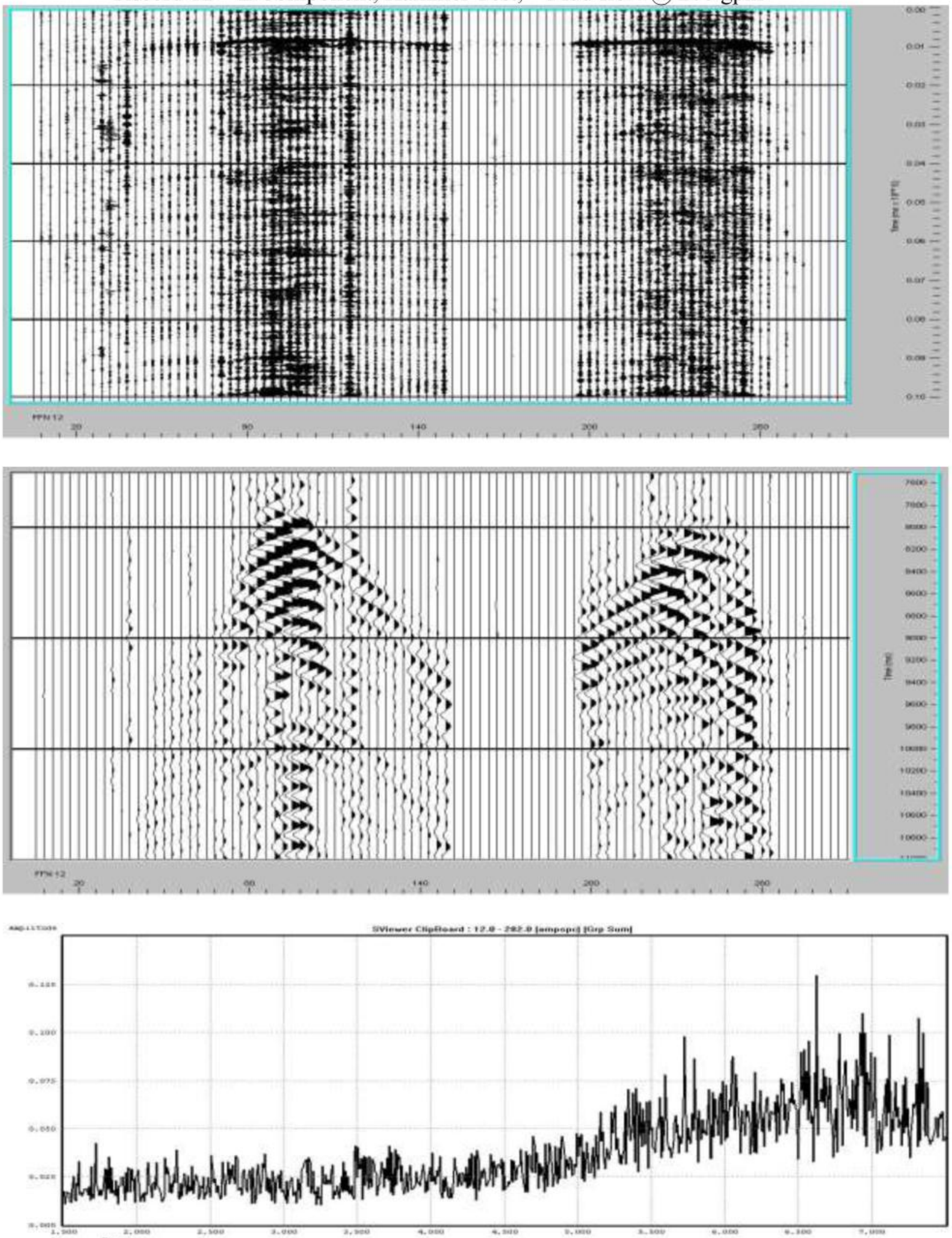

Record 12 HX Component Hammer Test Mud flow @ 200 gpm

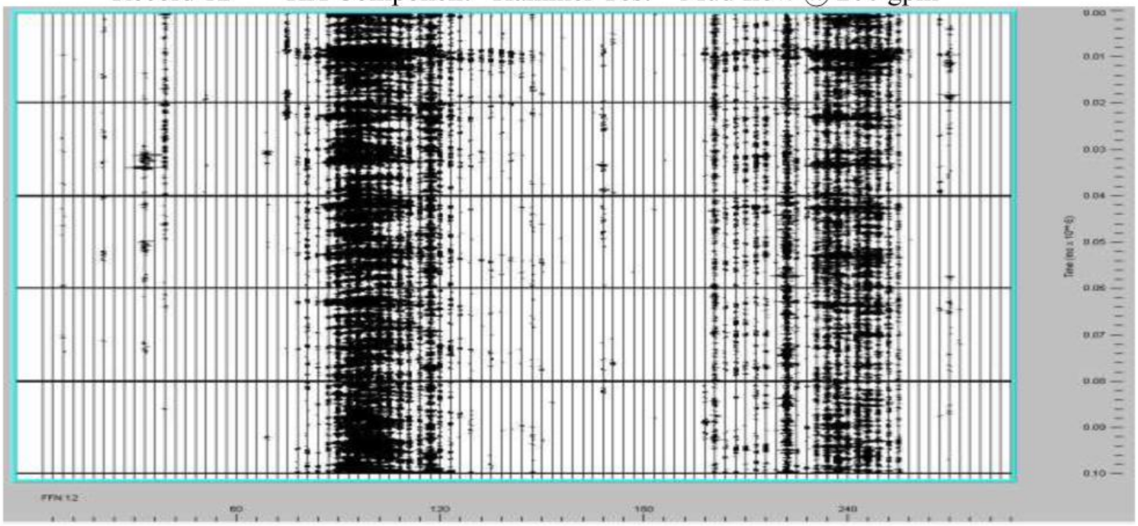

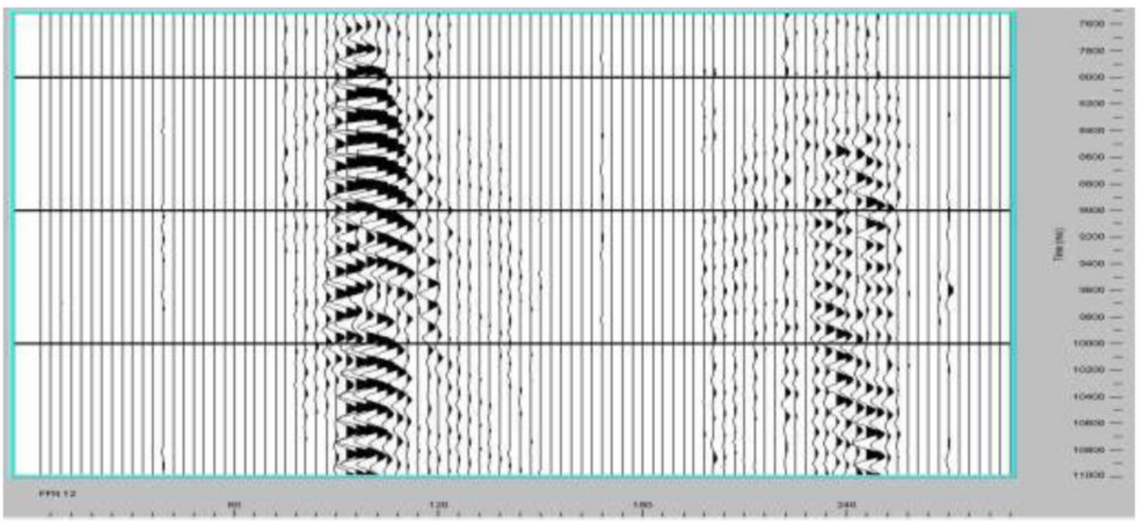

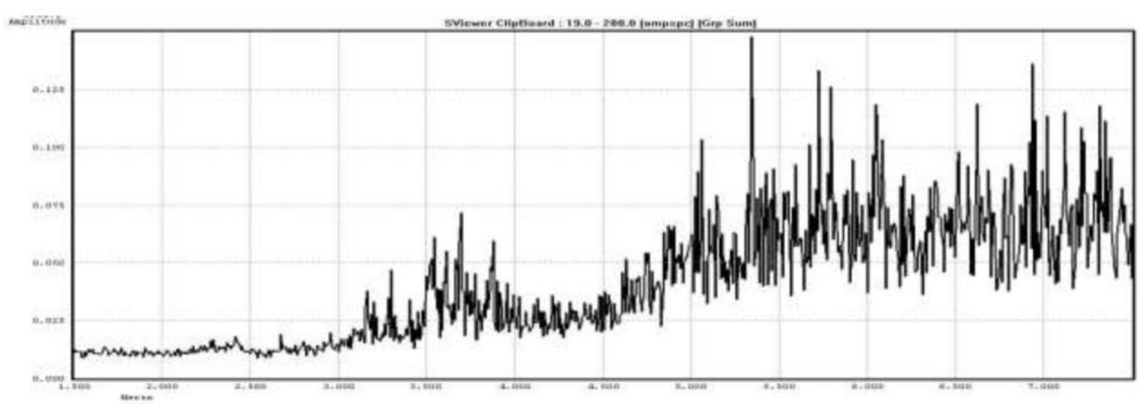

Record 20 HY component Background noise test Mud flow @ 200 gpm

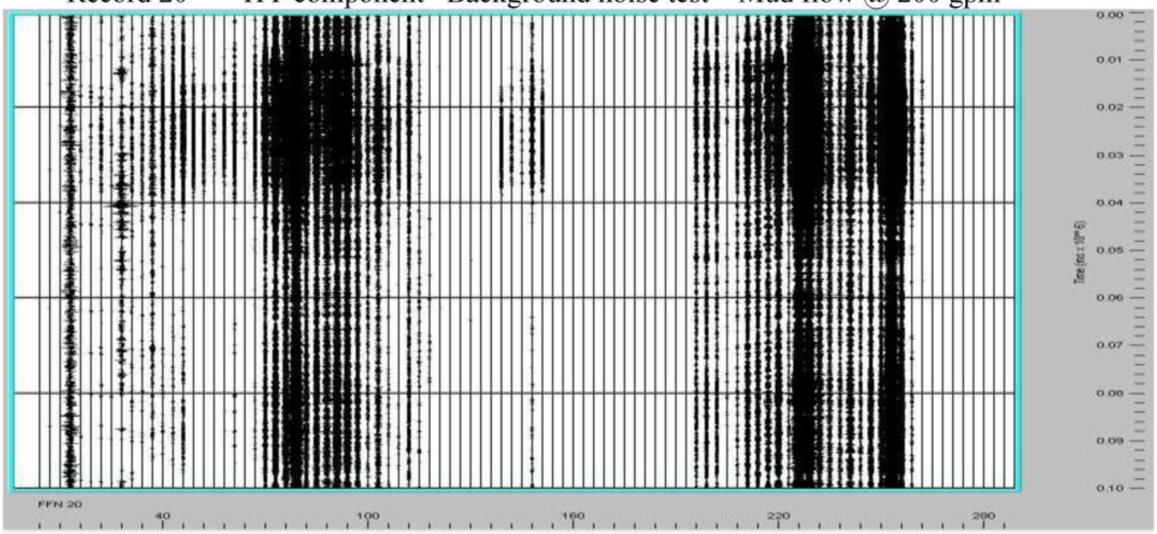

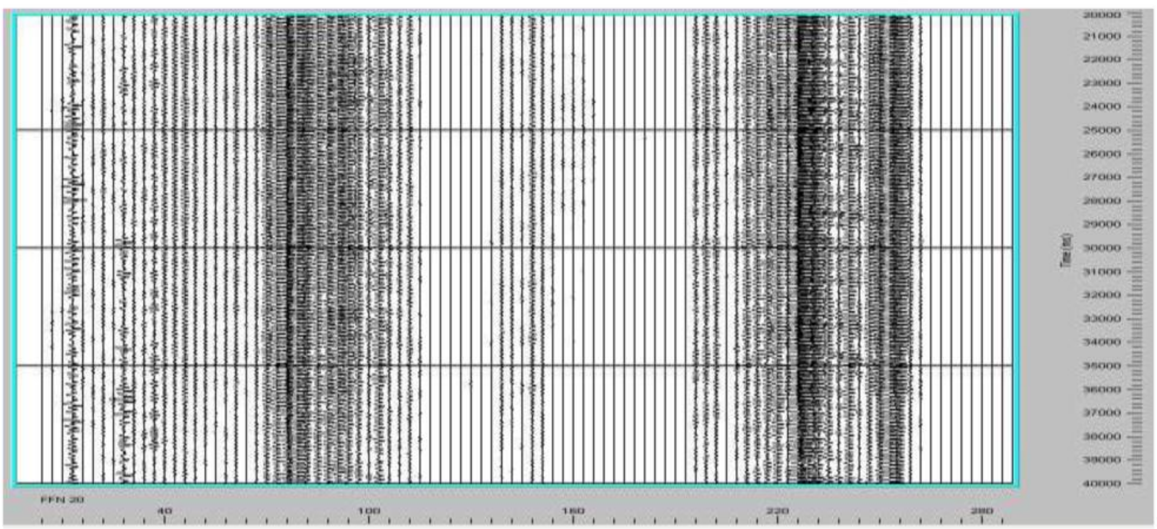

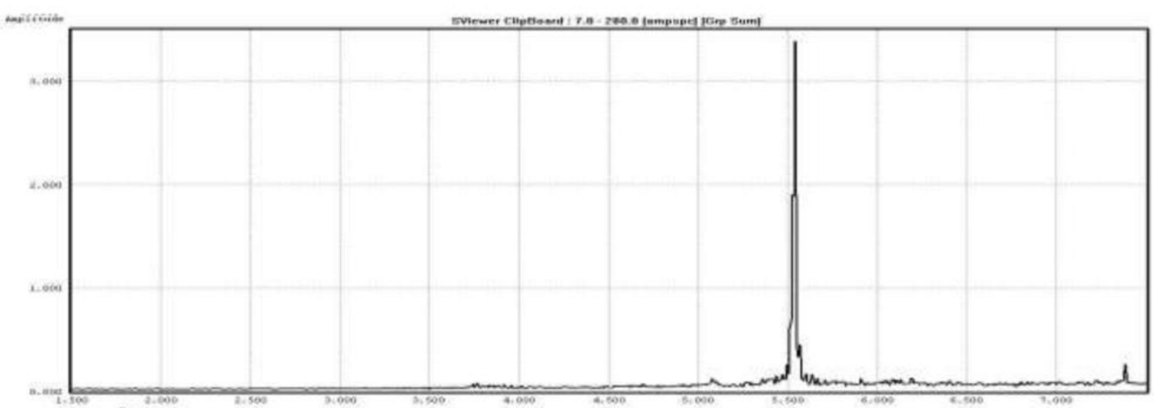

Record 12   Z Component, Hammer Test,   Mud flow @ 200 gpm

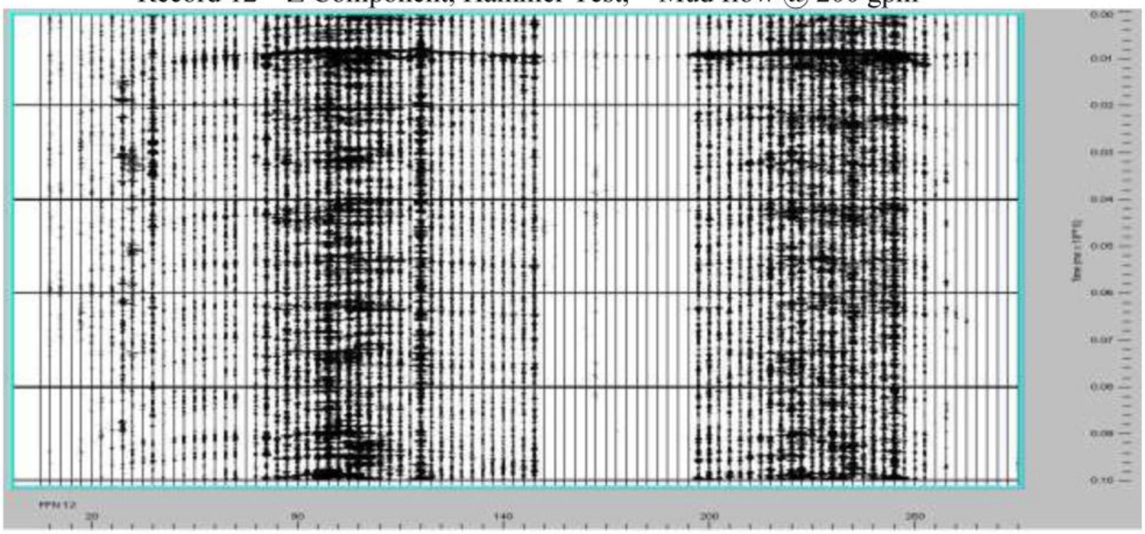

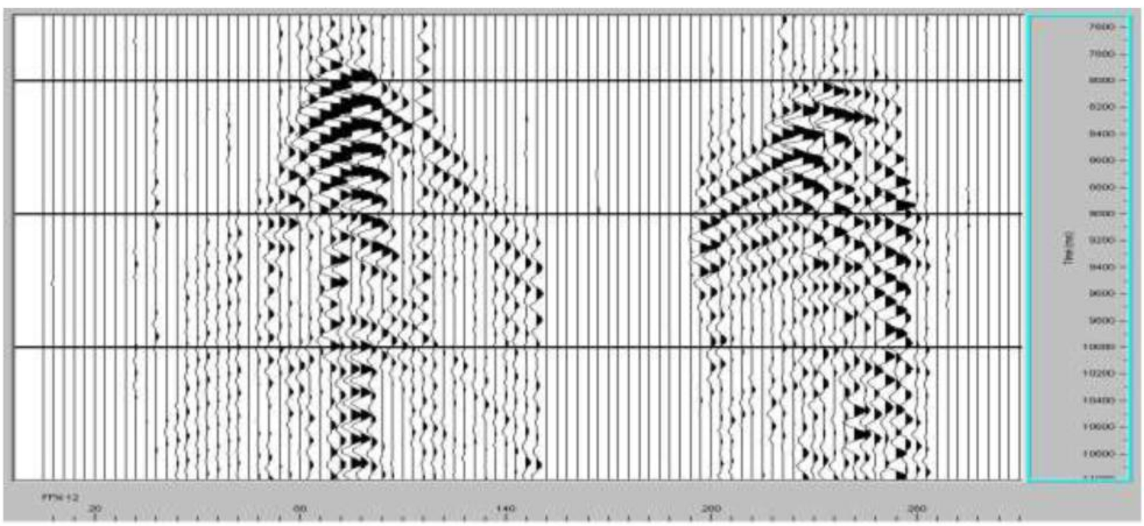

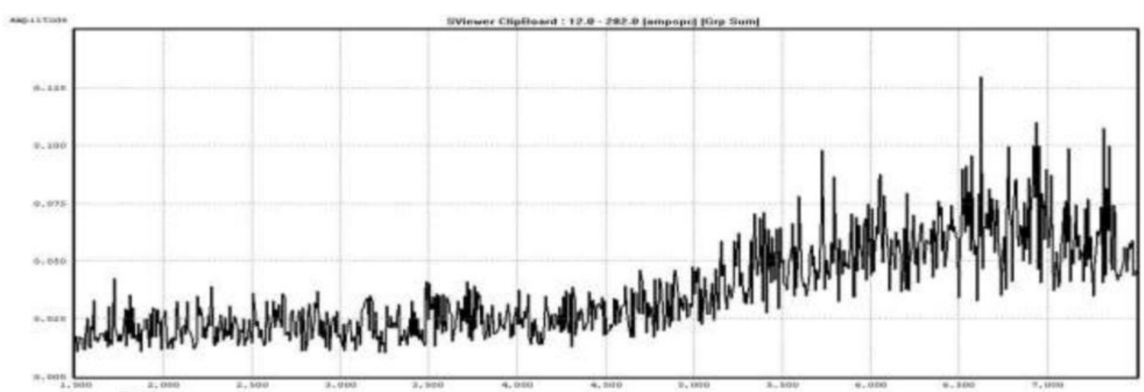

Record 12 HX Component Hammer Test Mud flow @ 200 gpm

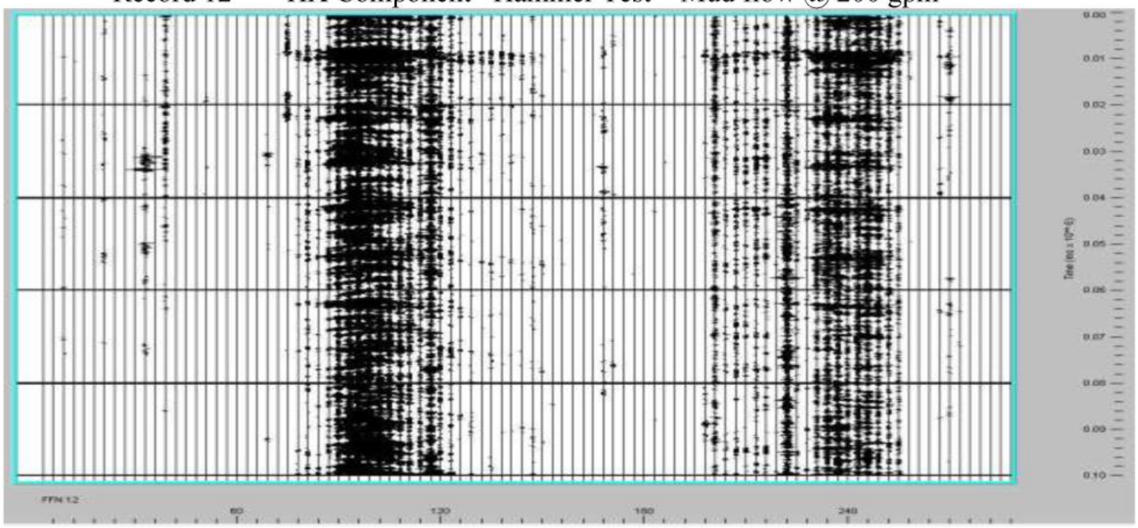

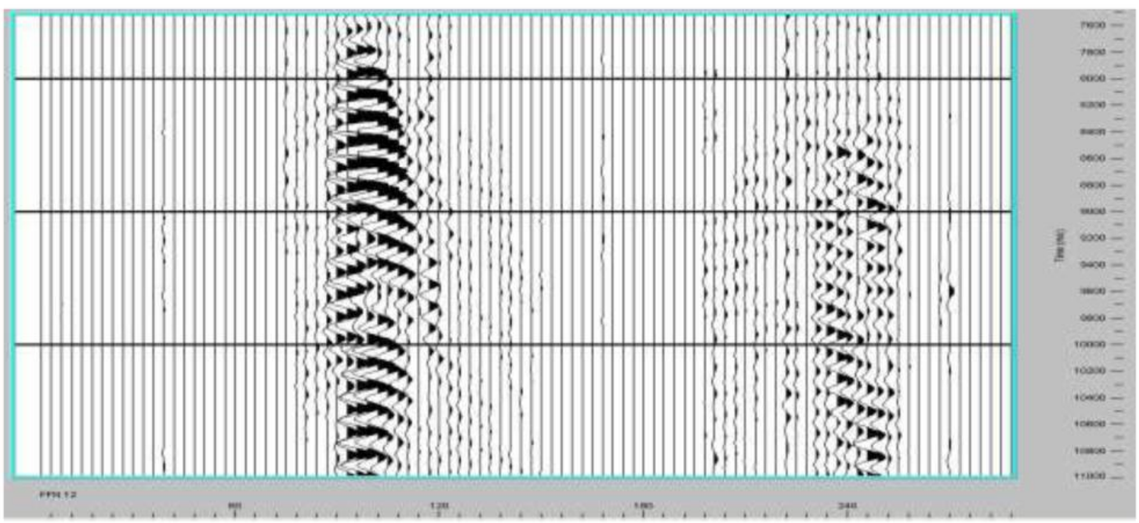

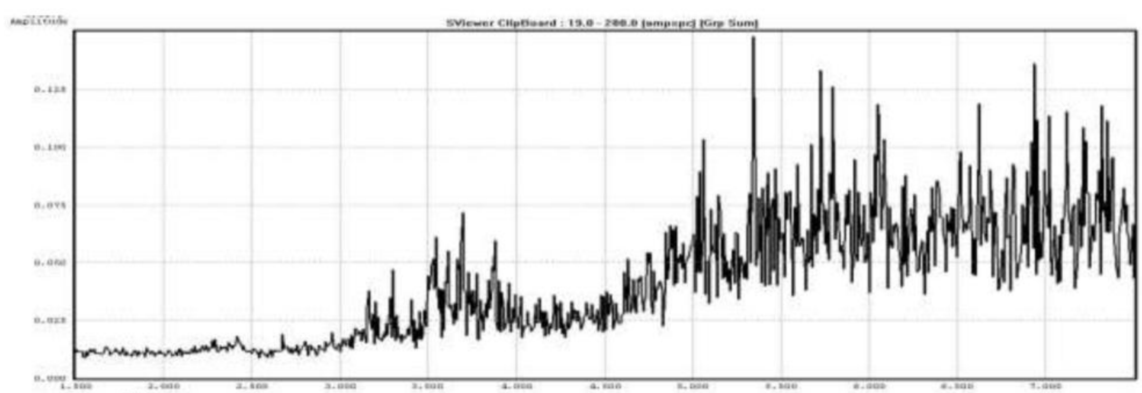

Record 12 HY Component Hammer Test Mud flow @ 200 gp**m**

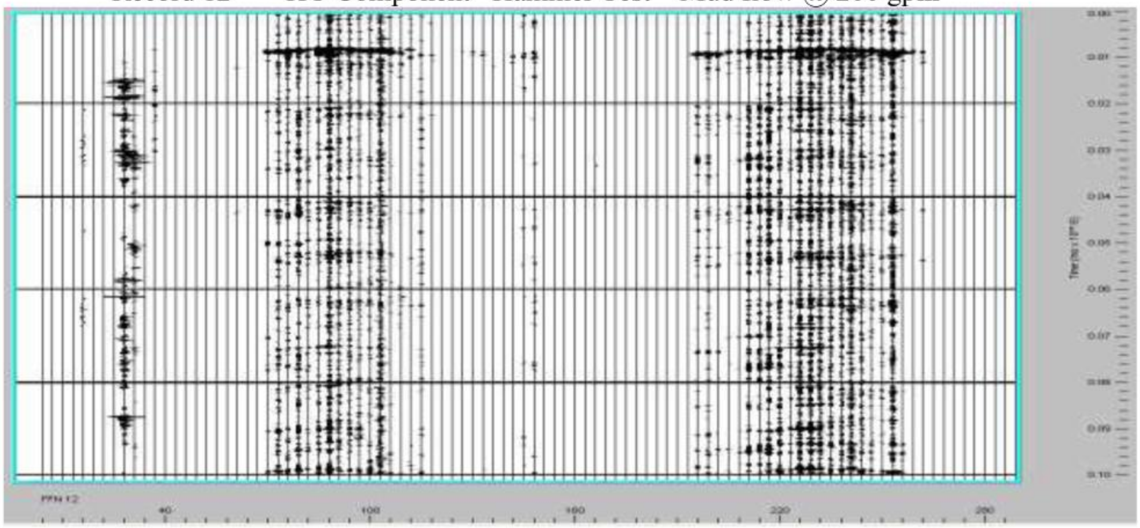

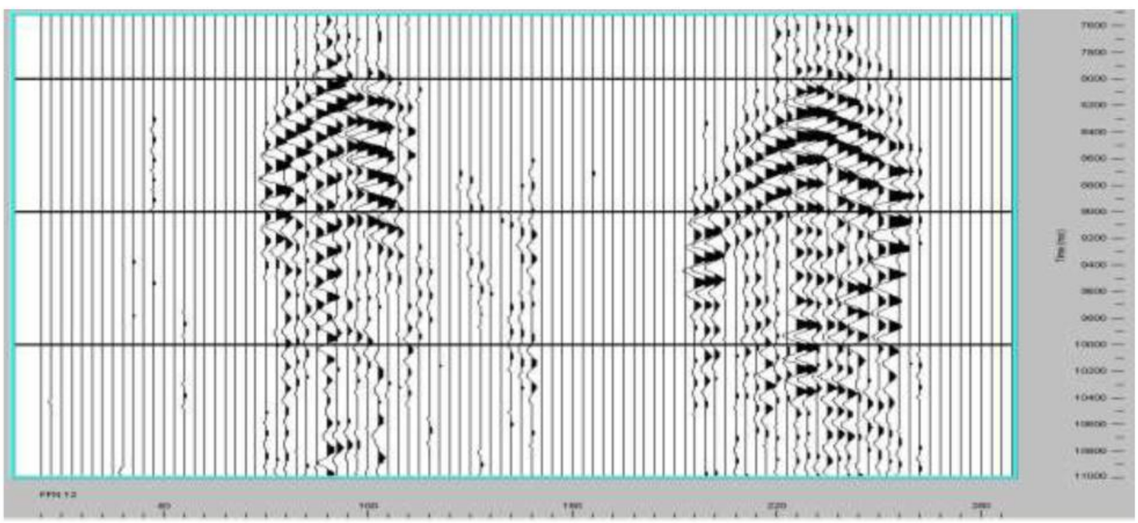

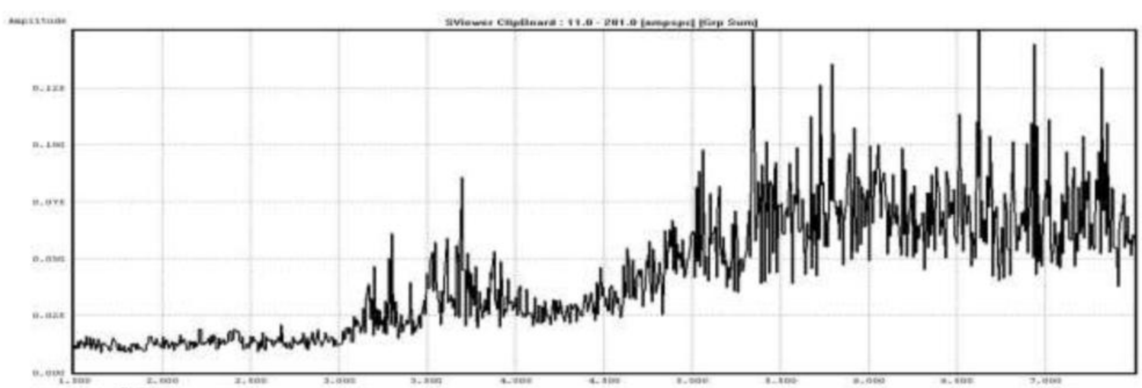

Record 7 Z Component Pulse Test Depth 778 ft Mud flow @ 380 gpm

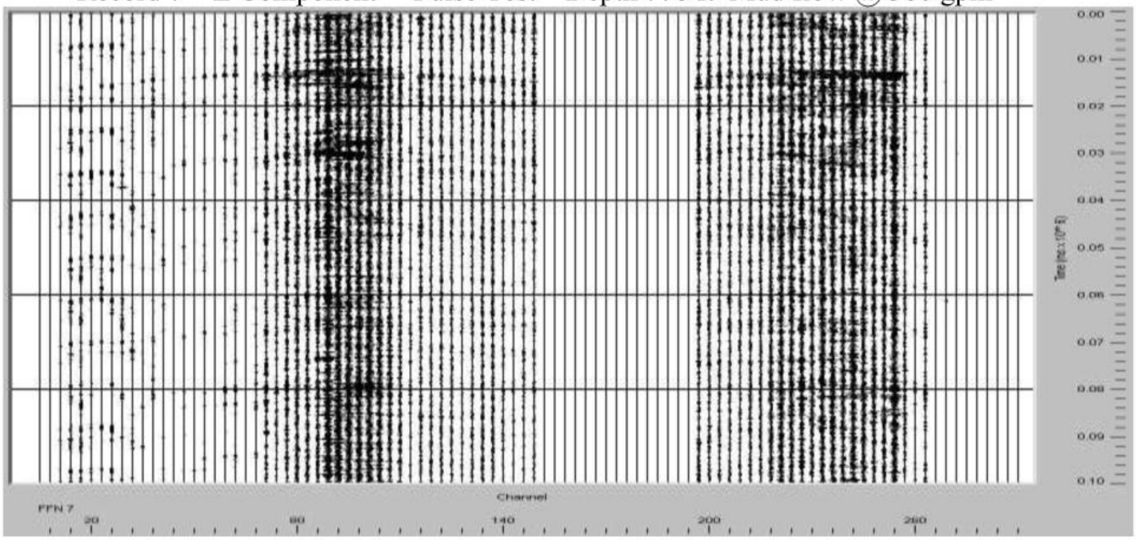

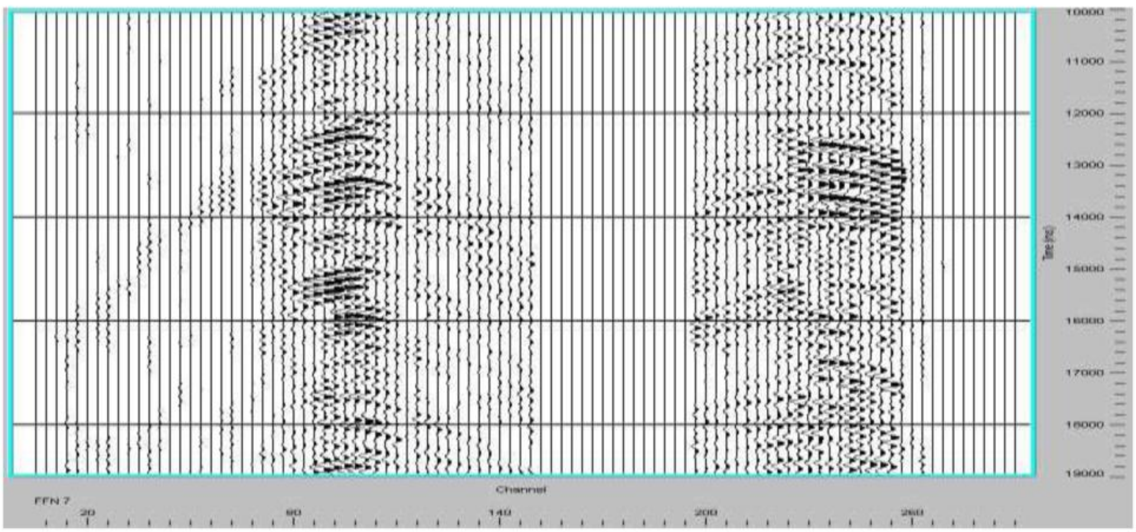

Record 7 HX Component Pulse Test Depth 778 ft Mud flow @ 380 gpm

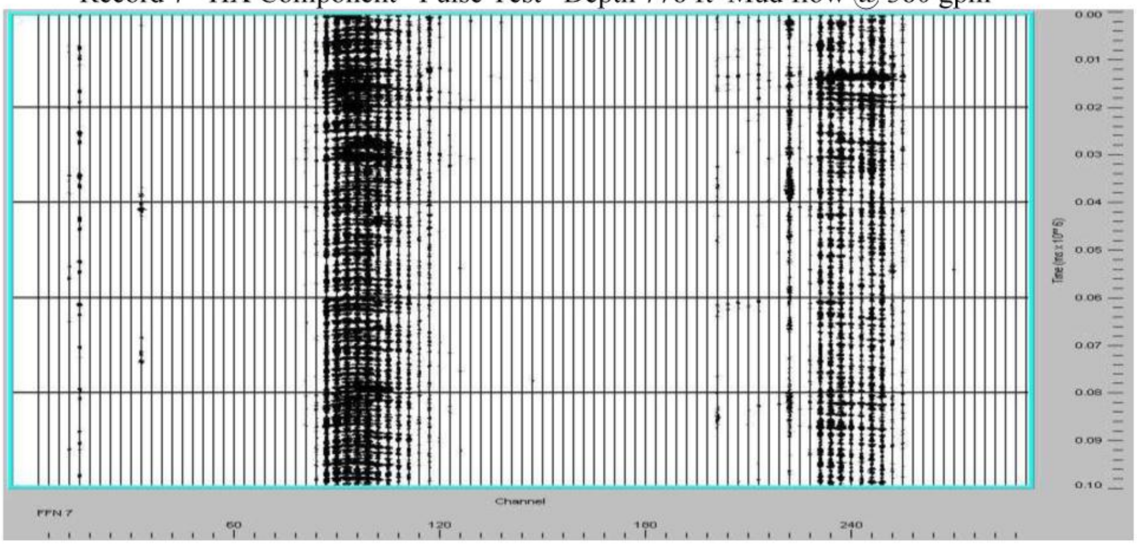

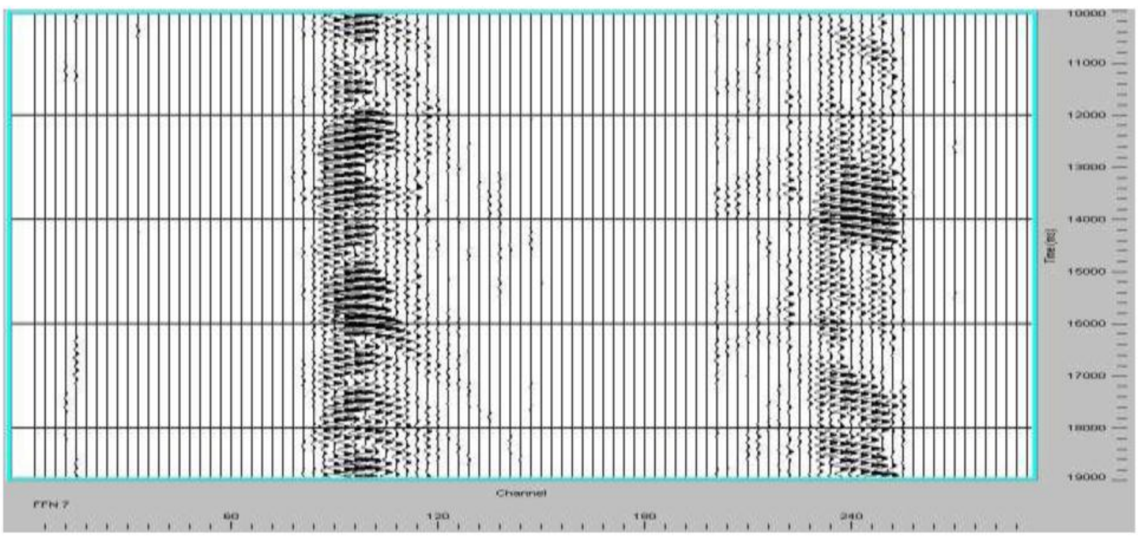

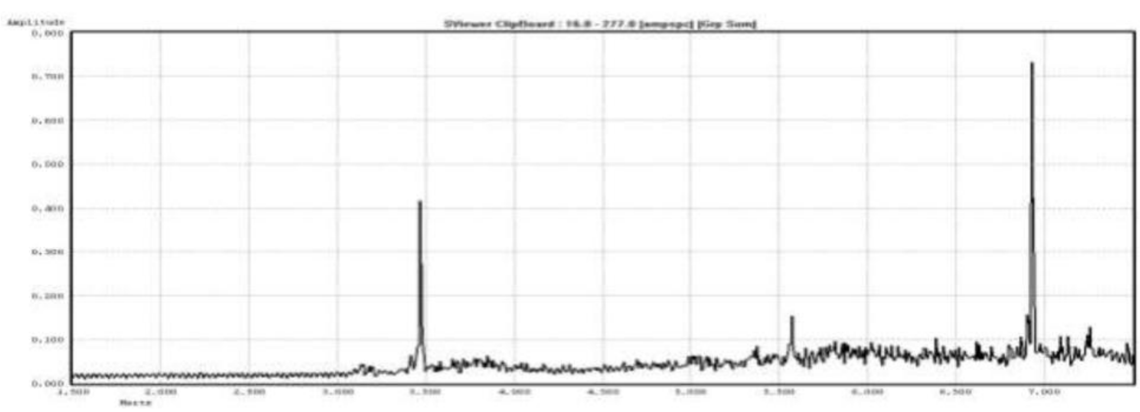

Record 7   HY Component   Pulse Test   Depth 778 ft Mud flow @ 380 gpm

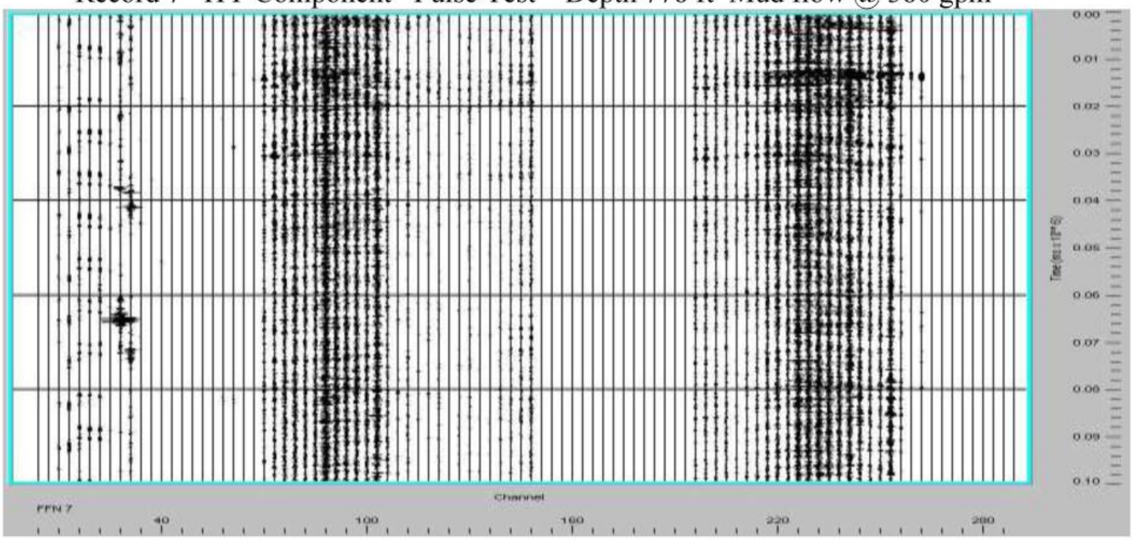

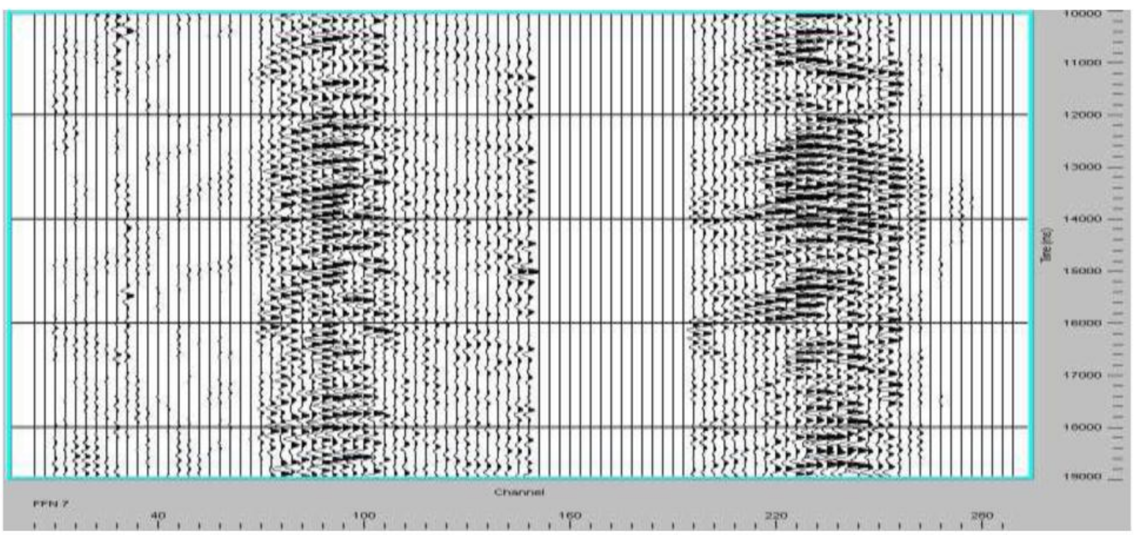

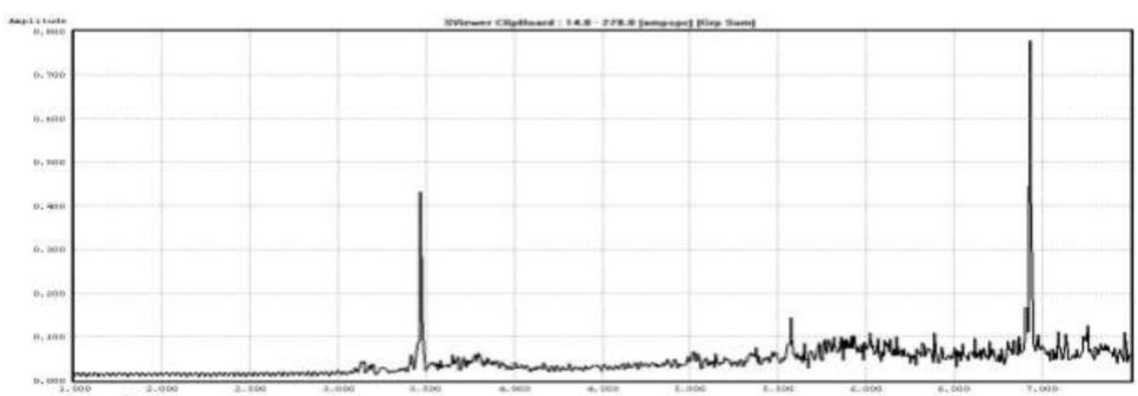

Record 11 Z Component Pulse Test (rot. 45^0) Depth 778 ft Mud flow @ 380 gpm

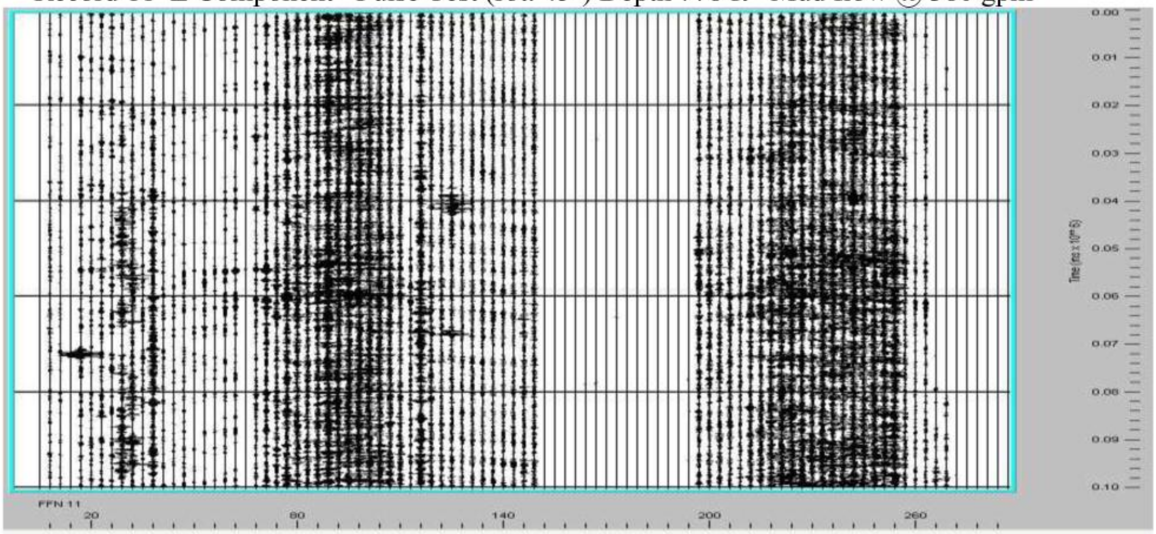

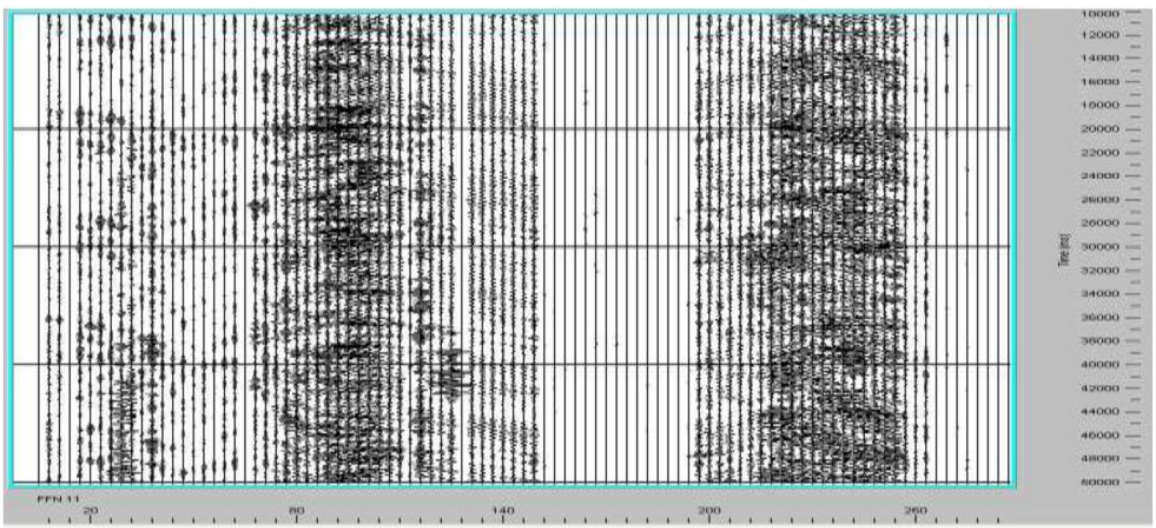

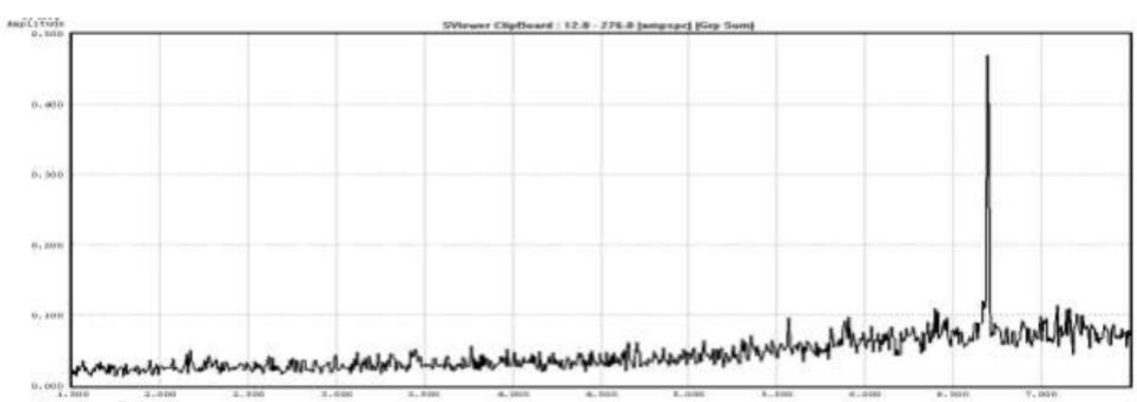

Record 11 -HX Component   Background Noise Test   Mudflow @ 100 gpm

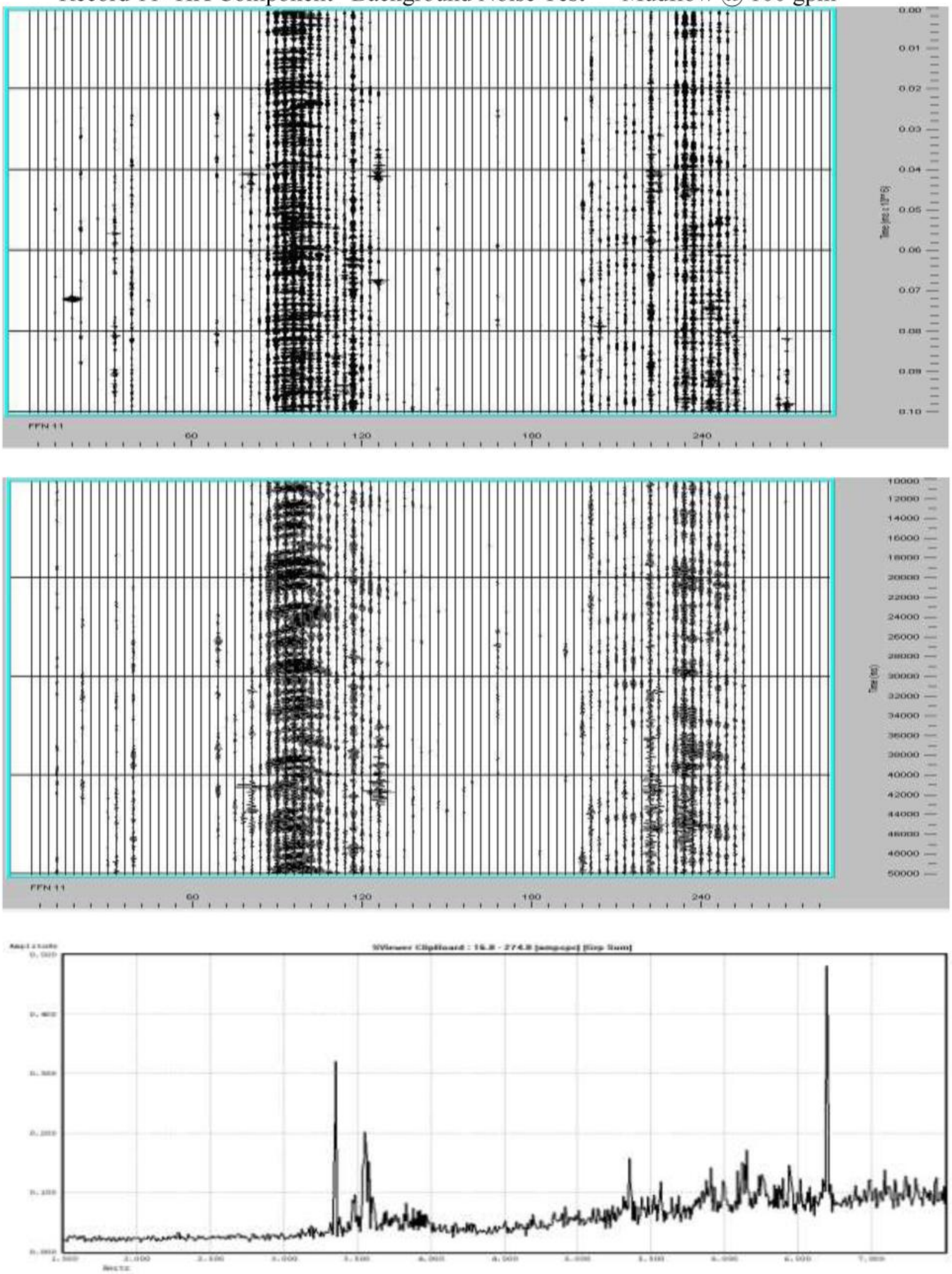

Record 11 HY Component Pulse Test (rot. 45^0) Depth 778 ft Mud flow @ 380 gpm

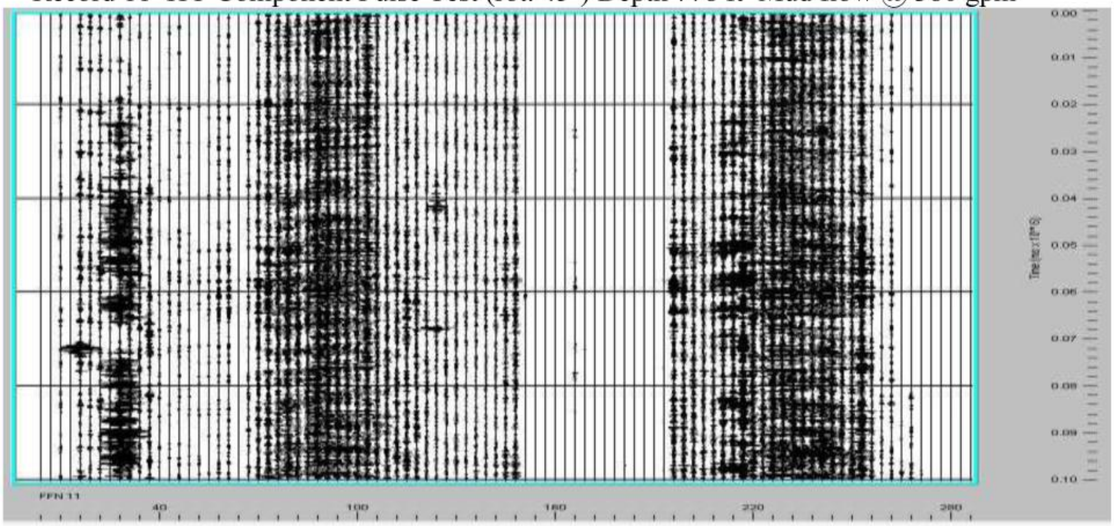

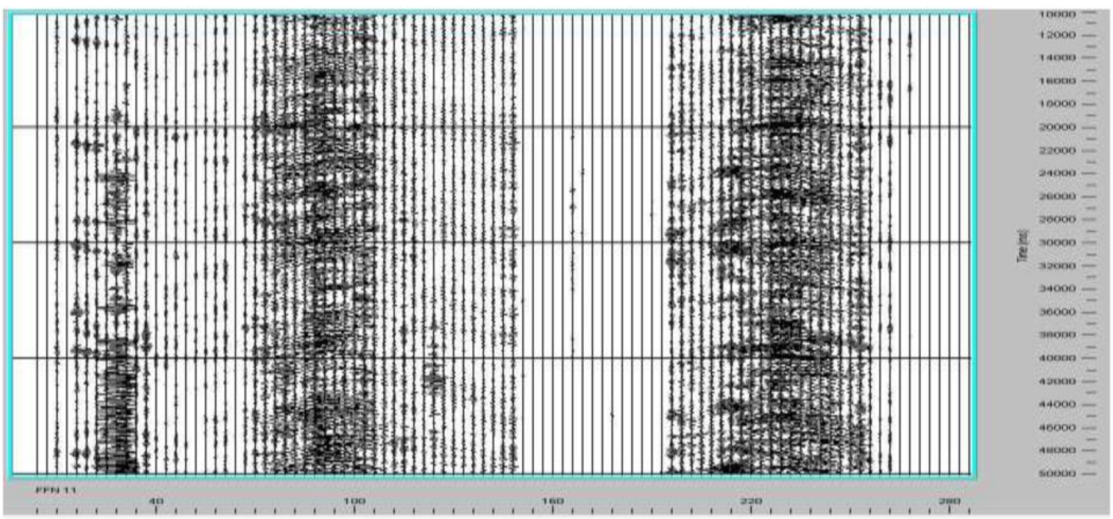

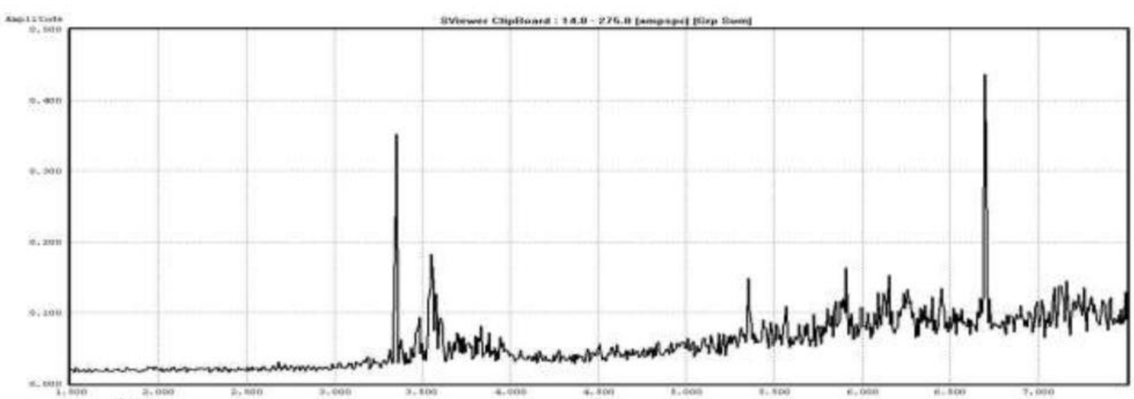

Record 21   Z Component   Pulse Test   Depth 3883 ft Mud flow @ 350 gpm

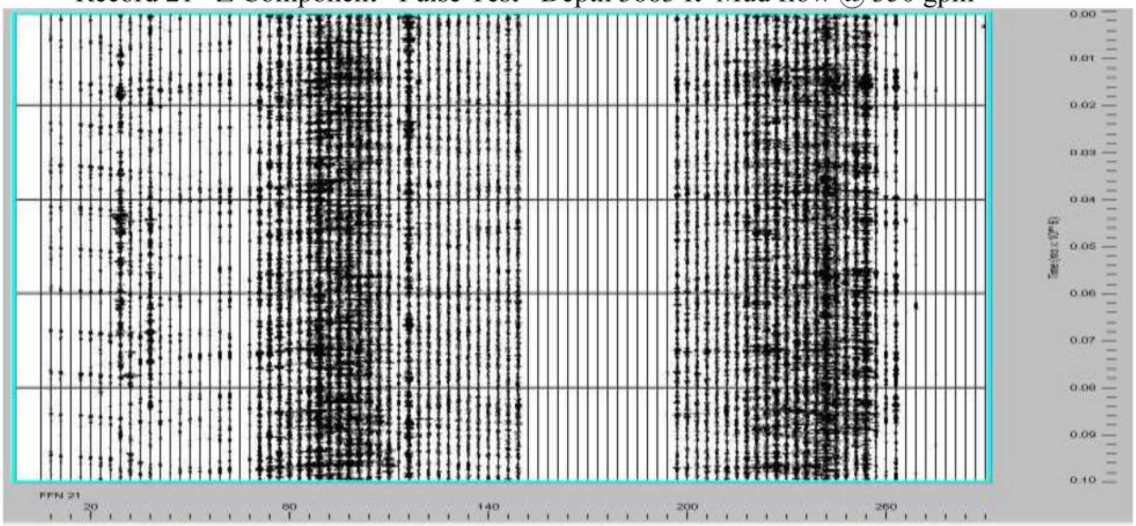

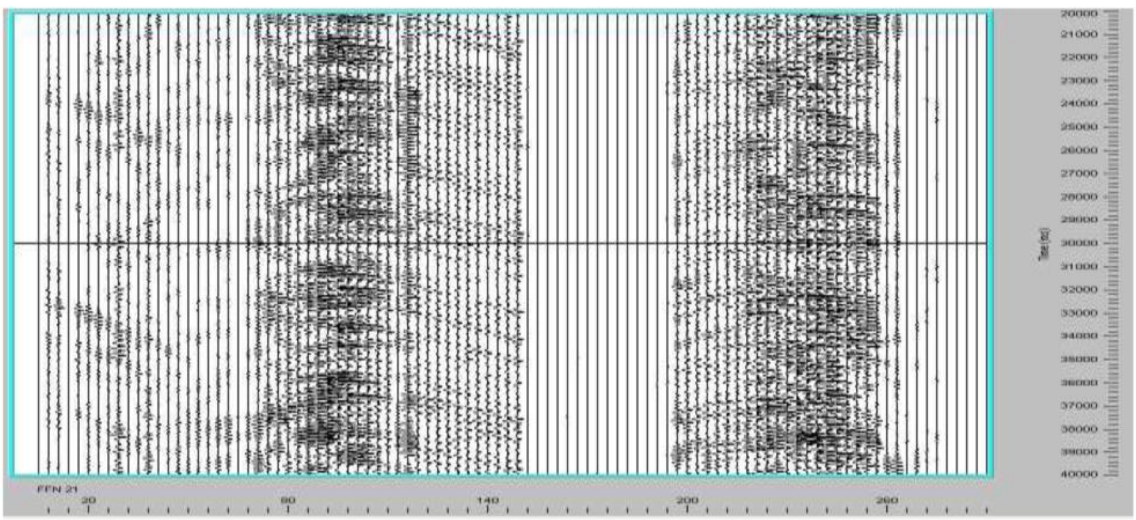

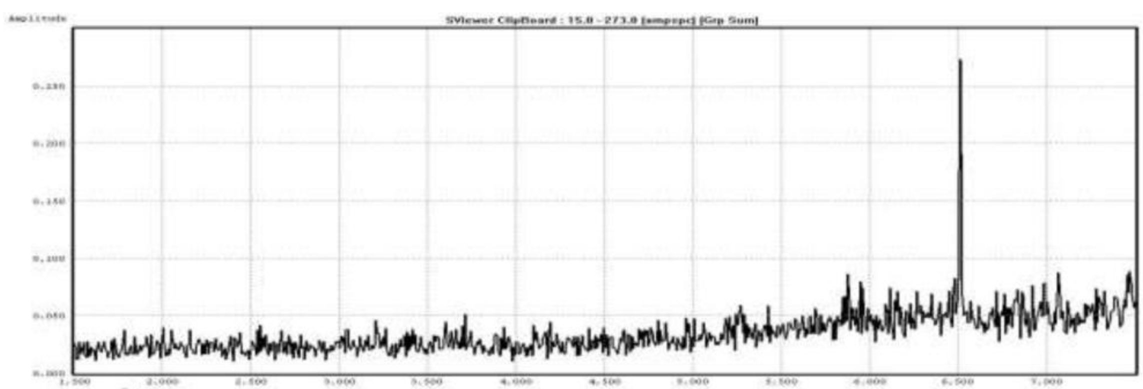

Record 21 HX Component Pulse Test Depth 3883 ft Mud flow @ 350 gpm

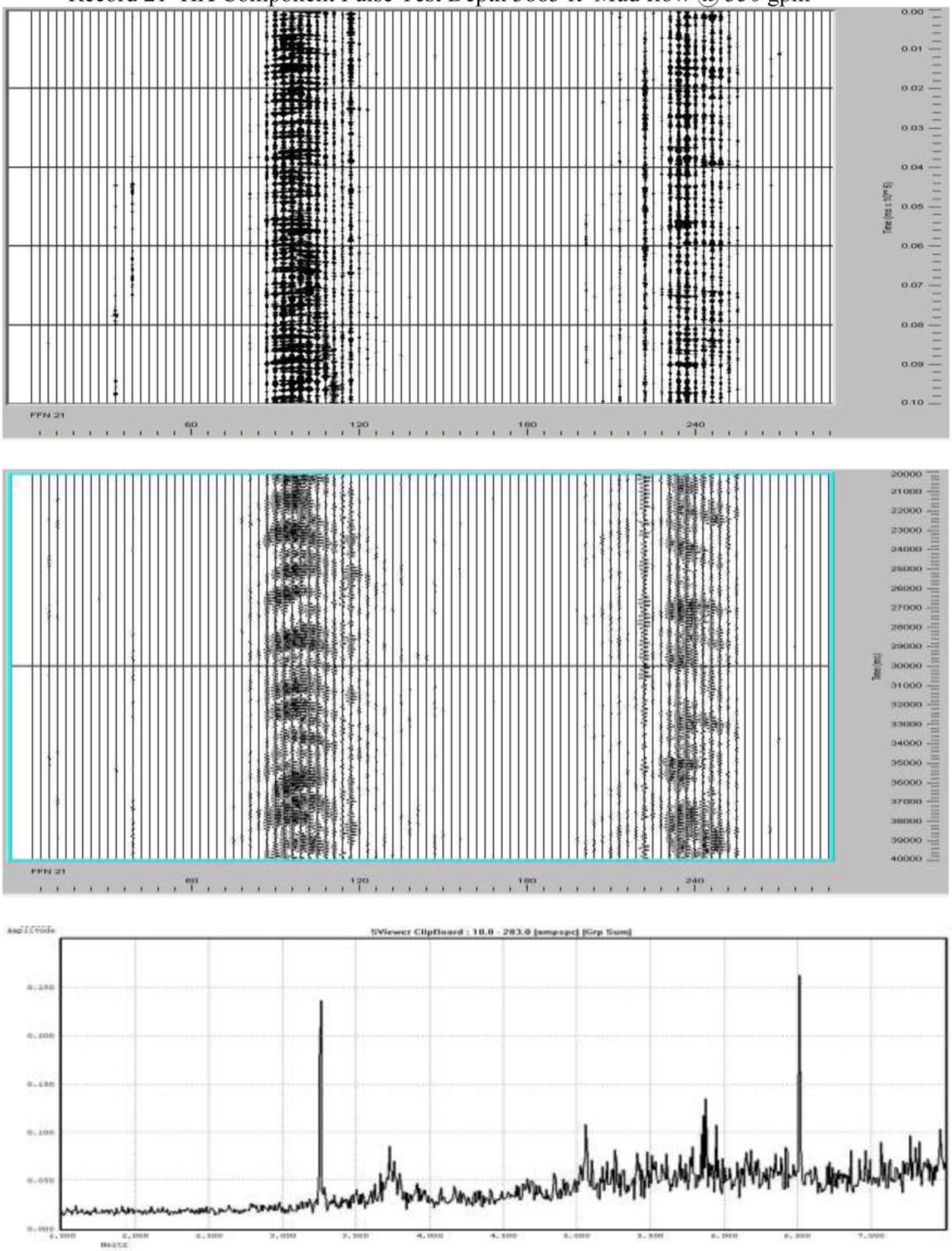

Record 21 HY Component Pulse Test Depth 3883 ft Mud flow @ 350 gpm

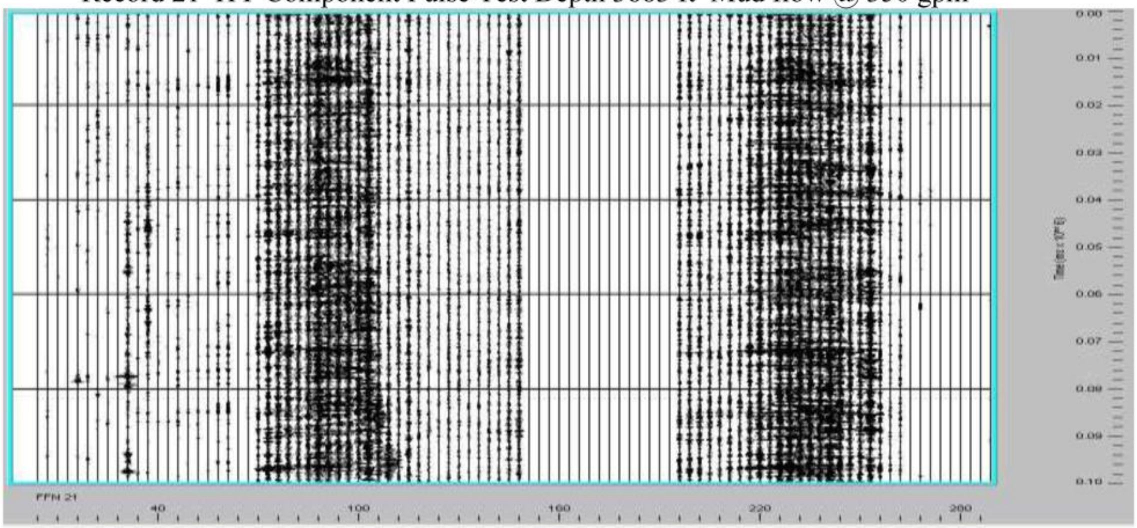

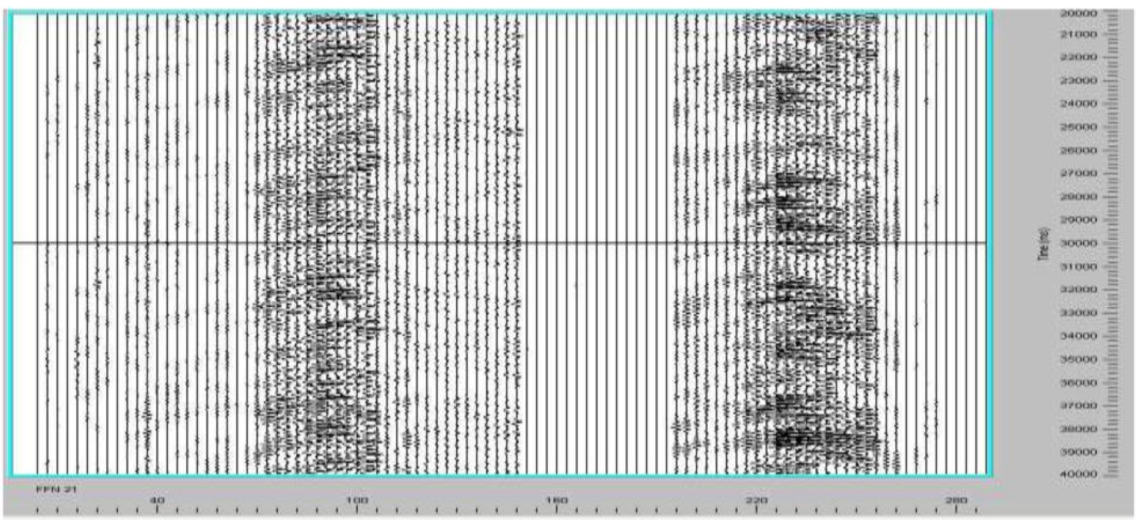

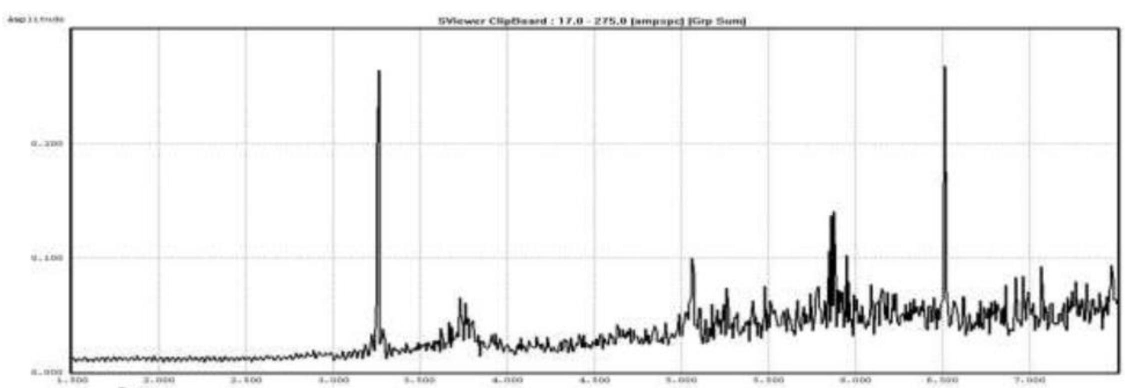

Record 23 Z Component Rotate 45^0 Pulse Test Depth 3883 ft Mudflow @ 350 gpm

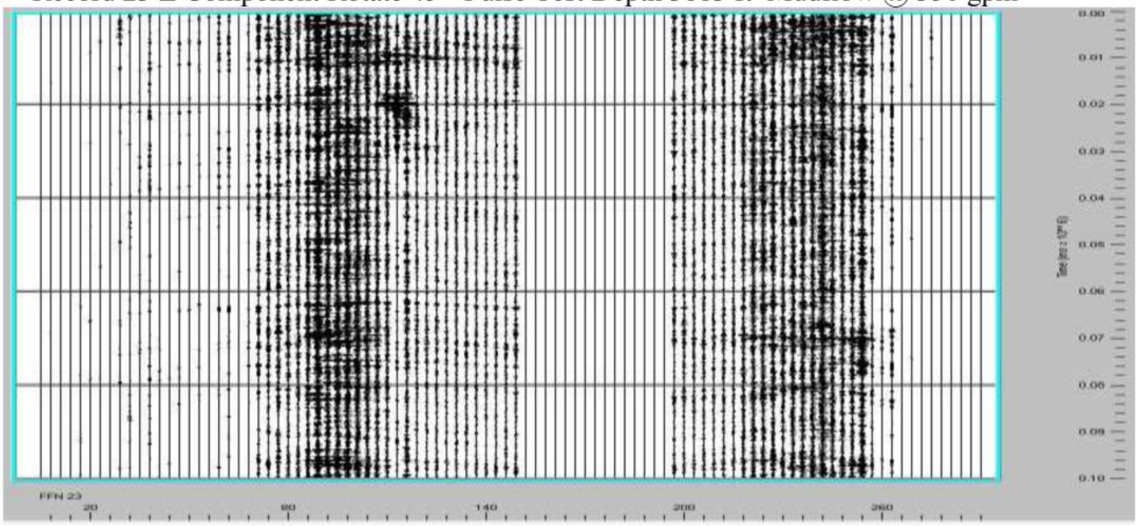

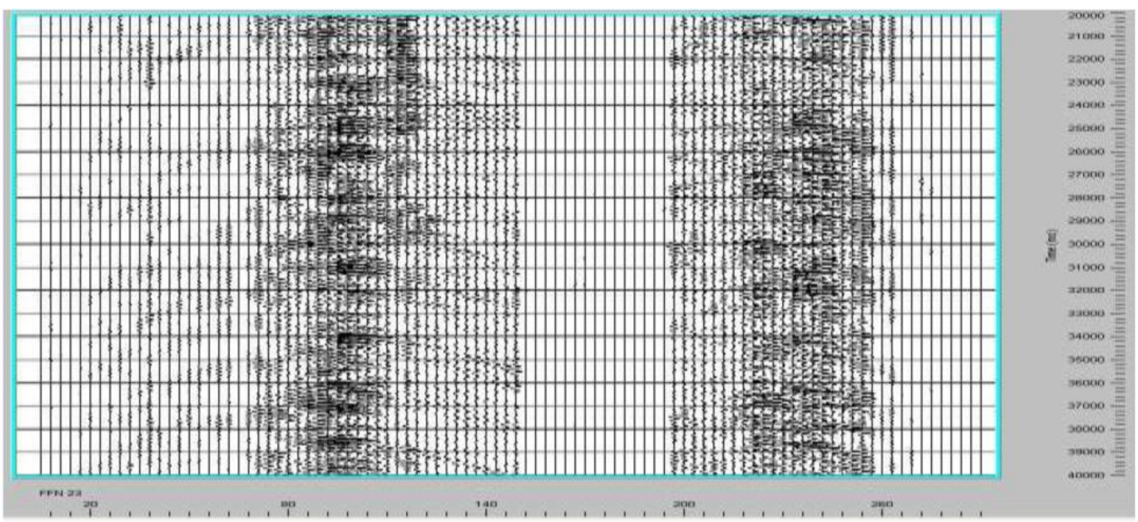

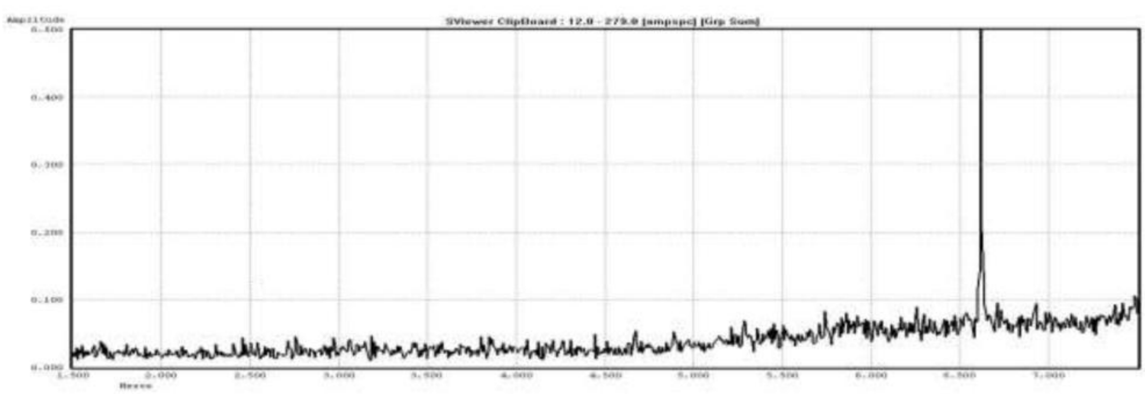

1

Record 23, HX Component, Rotate 45^0 Pulse Test Depth 3883 ft, Mudflow @ 350 gpm

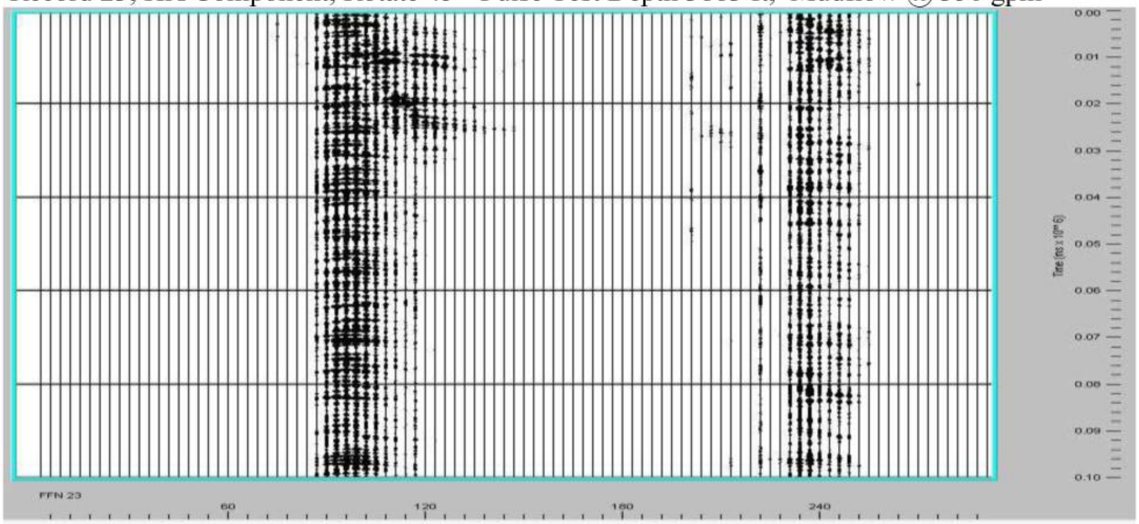

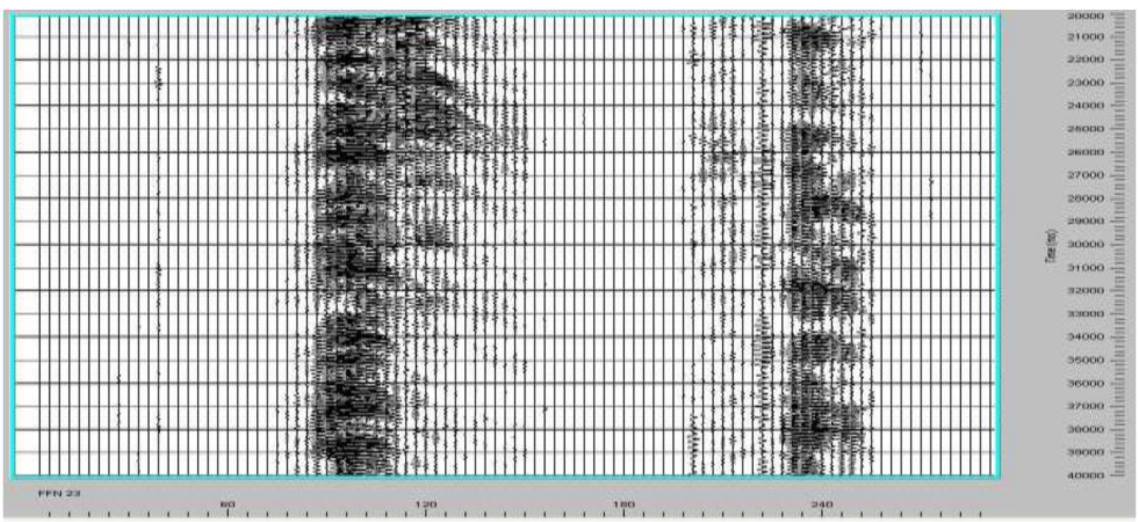

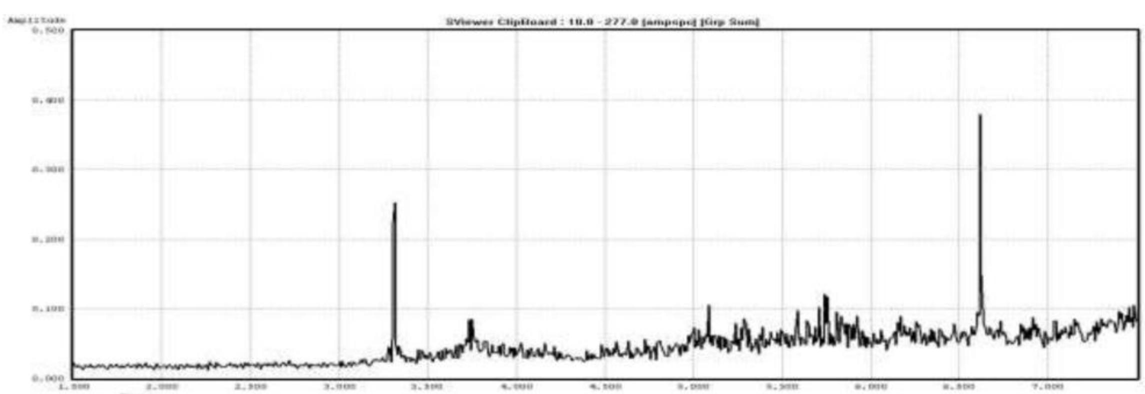

Record 23, HY Component, Rotate 45^0 Pulse Test, Depth 3883 ft, Mudflow @ 350 gpm

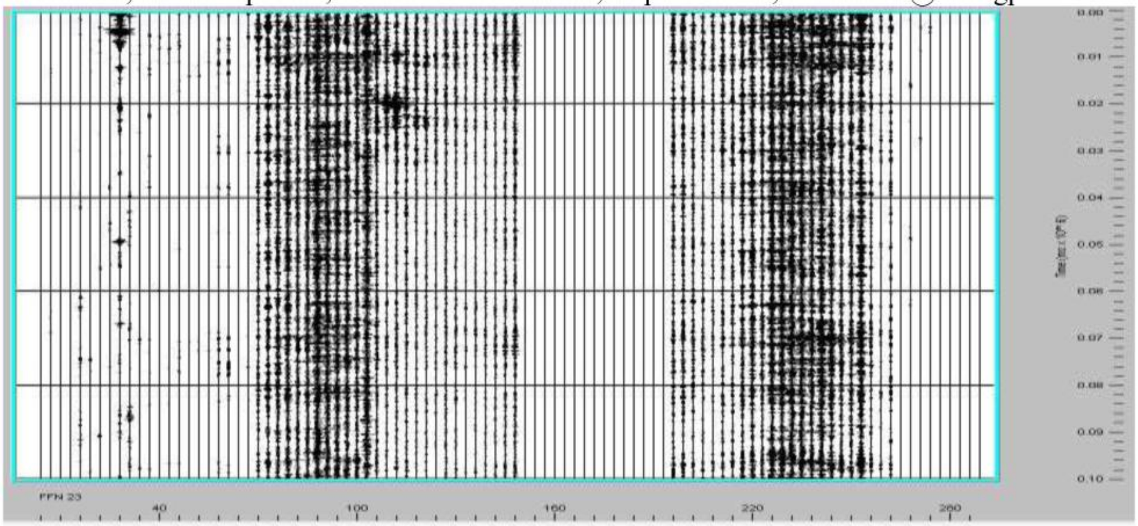

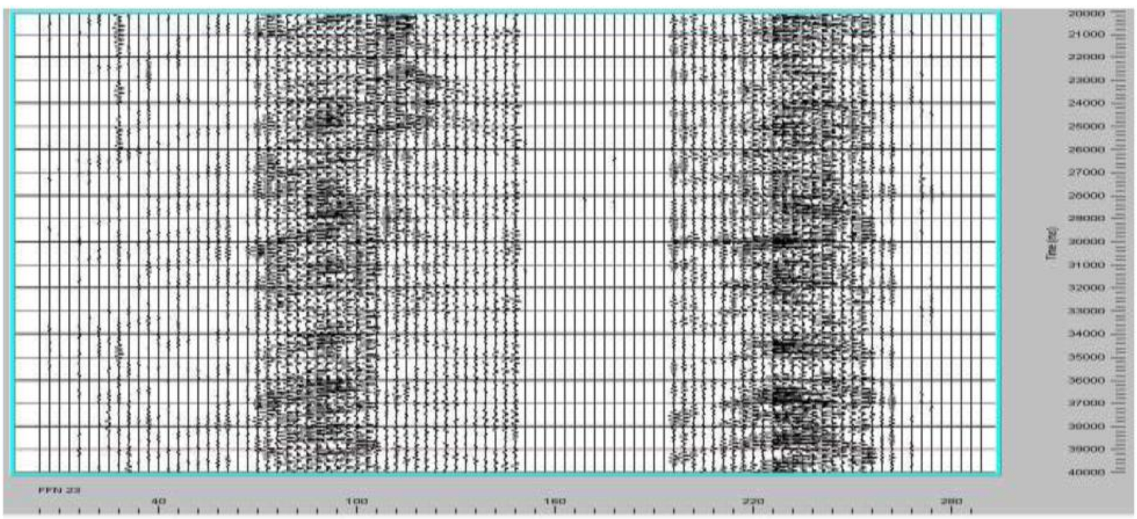

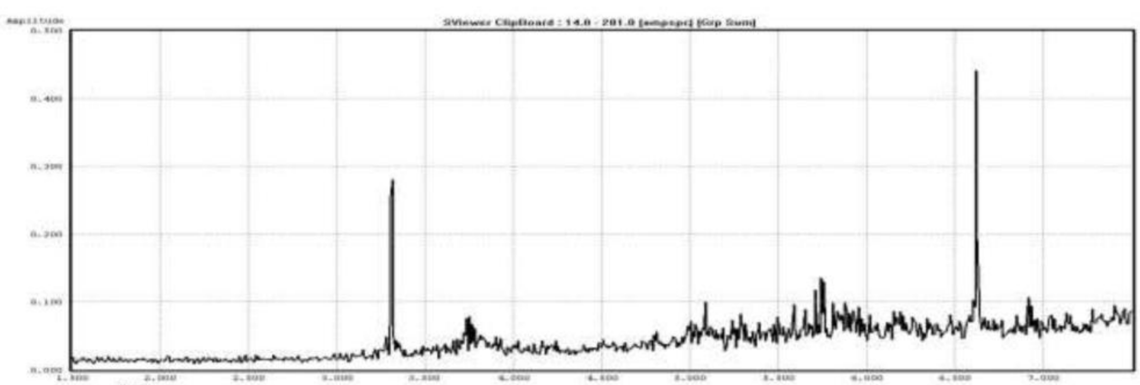

Record 24 Z Component Pulsing (rot. 45^0) Depth 3883 feet Mud flow @ 350 gpm

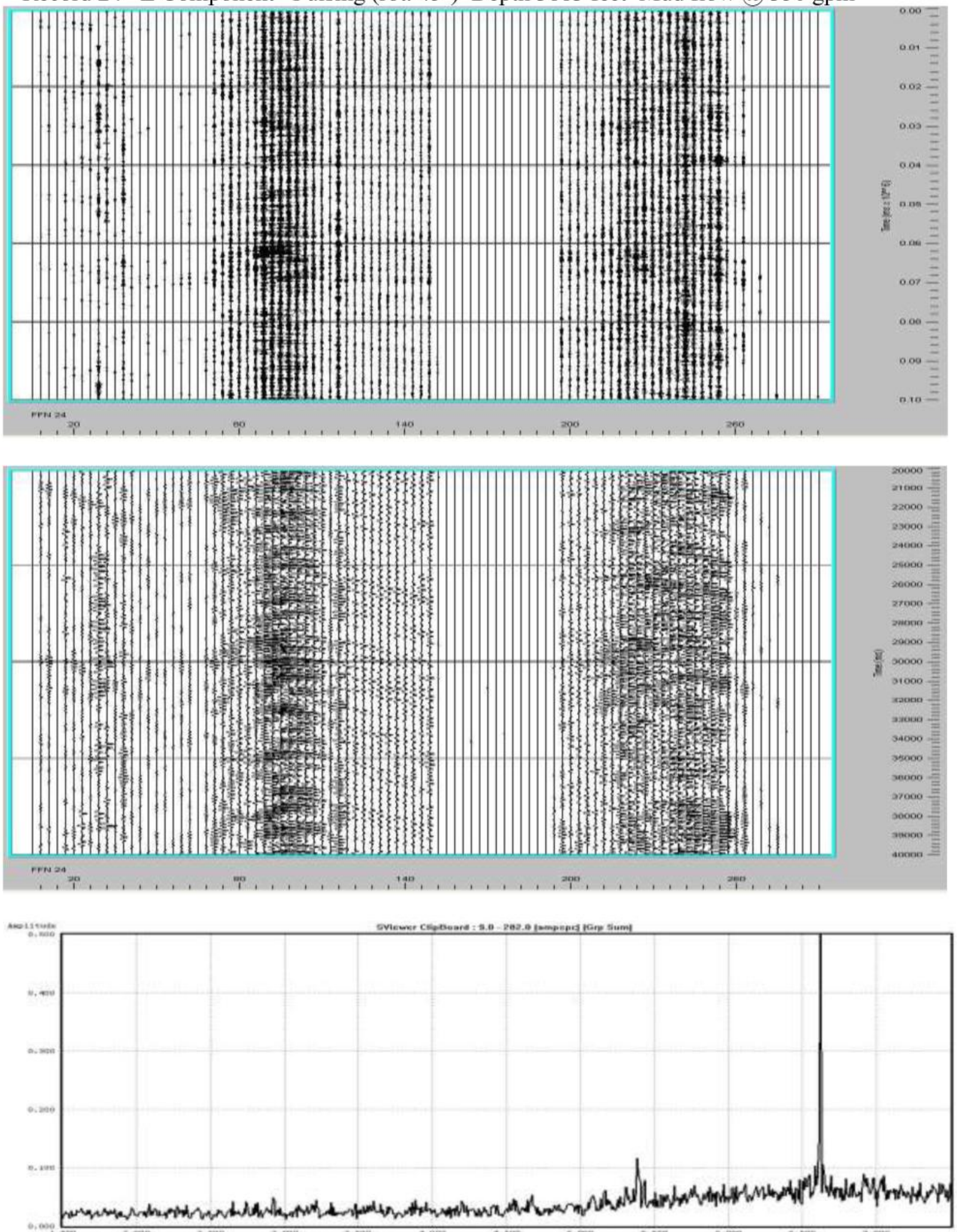

Record 24 HX Component Pulsing (rot. 45^0) Depth 3883 feet Mud flow @ 350 gpm

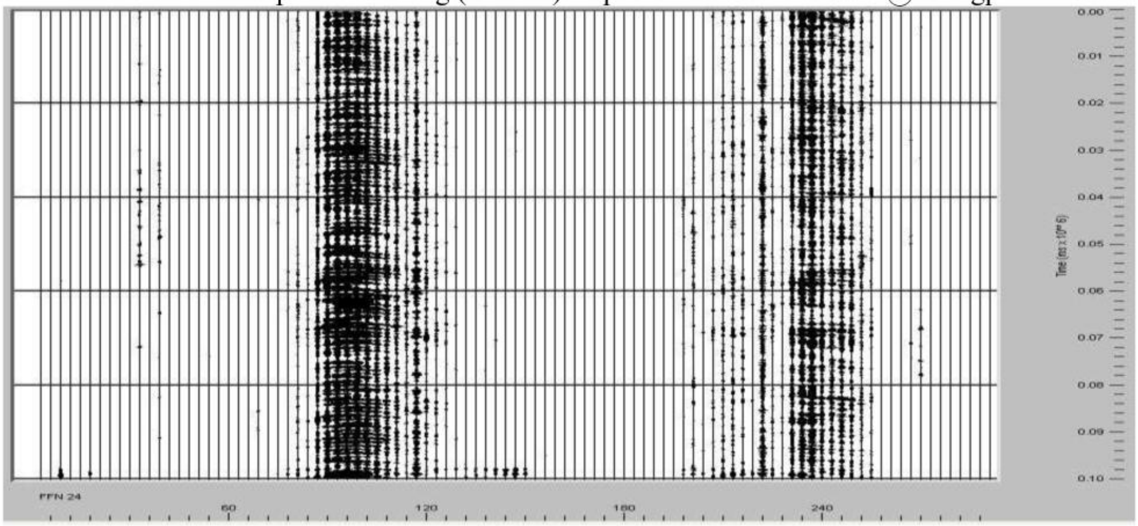

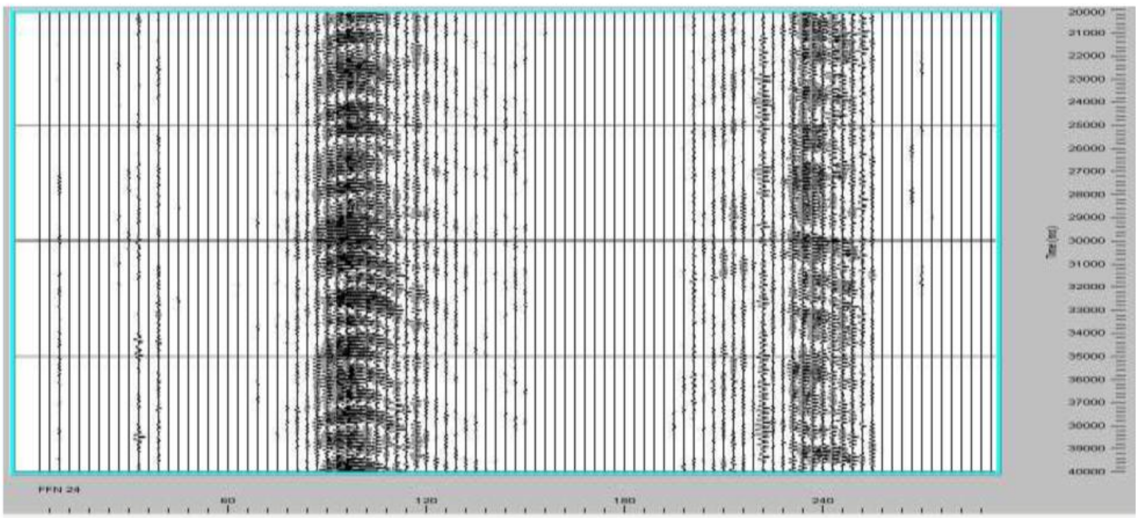

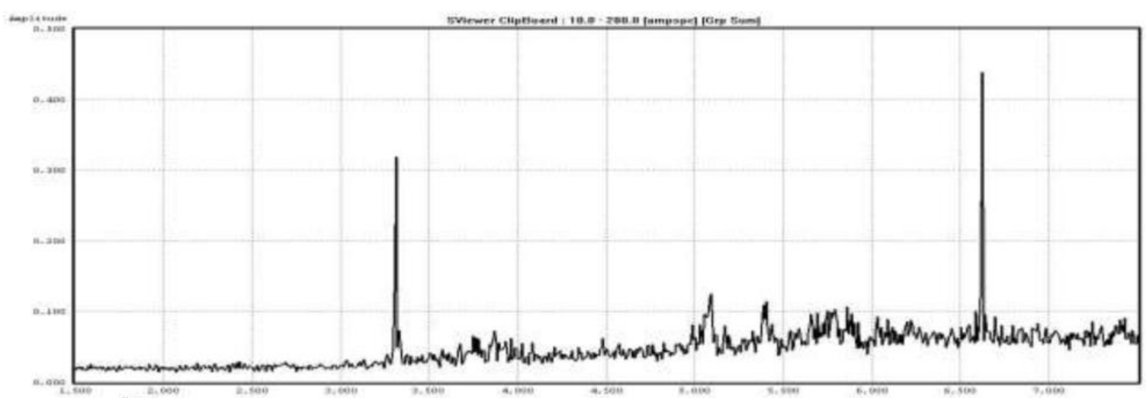

Record 24 HY Component Pulsing (rot. 45^0) Depth 3883 feet Mud flow @ 350 gpm

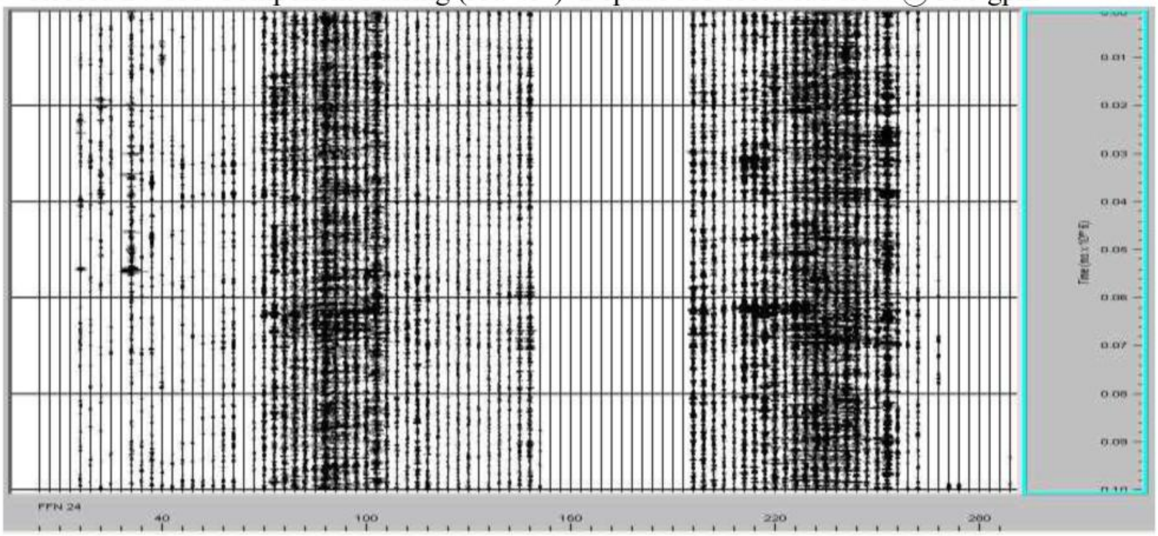

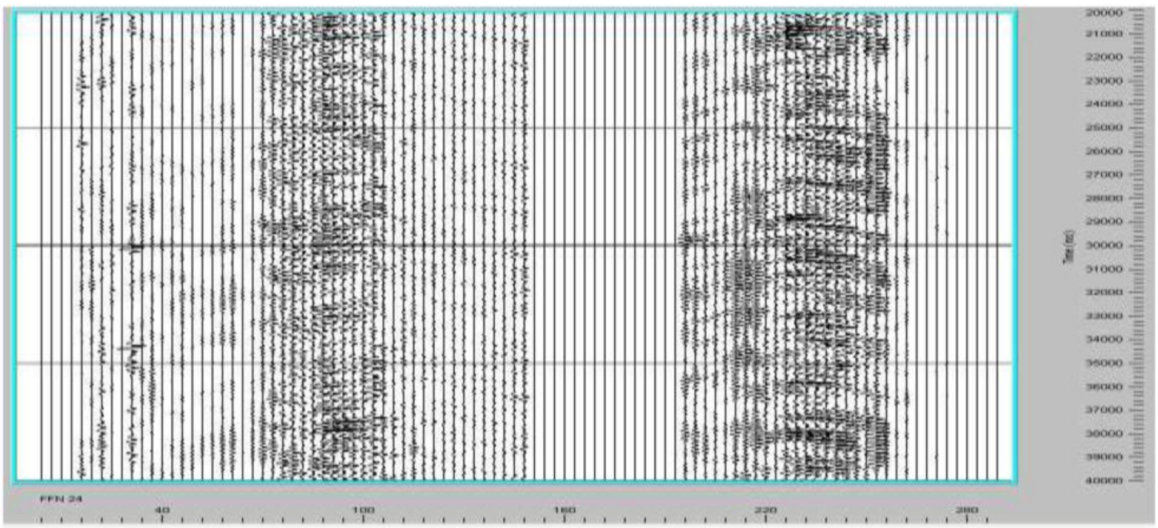

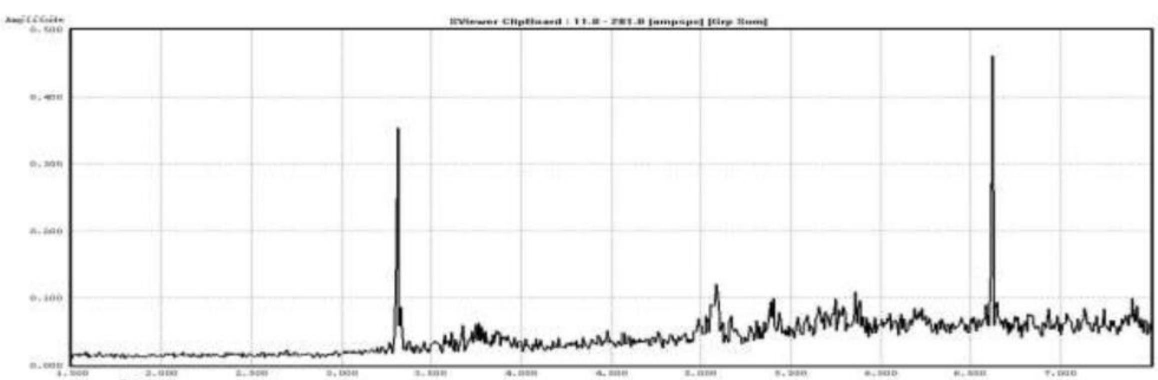

Record 26 Z Component SVSM tap test No mud flow

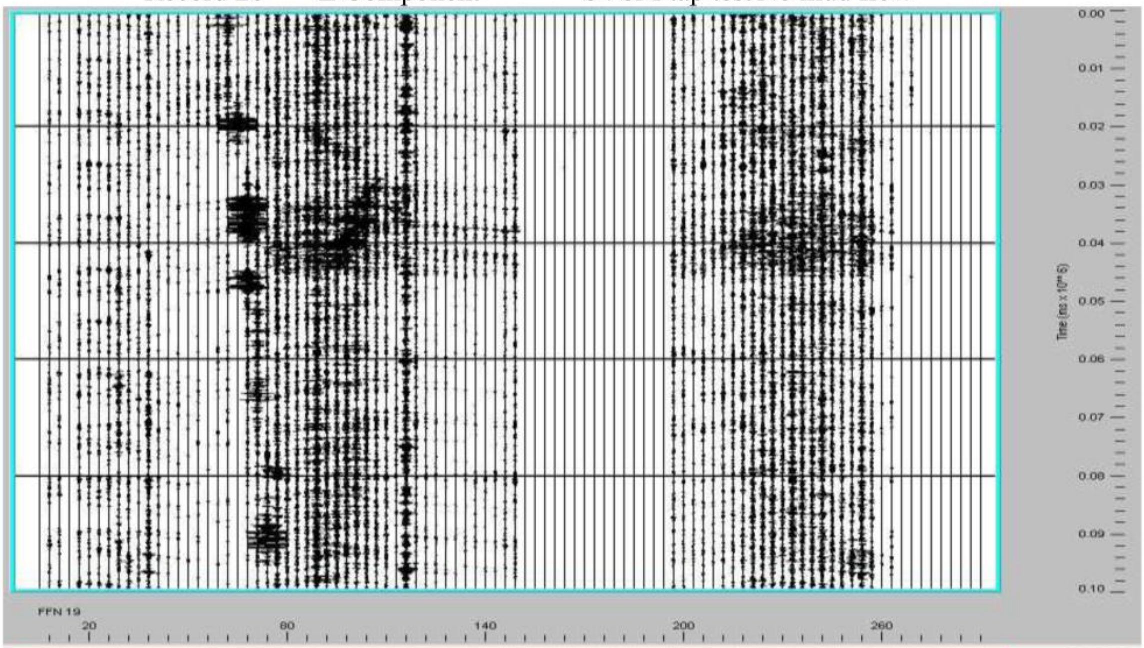

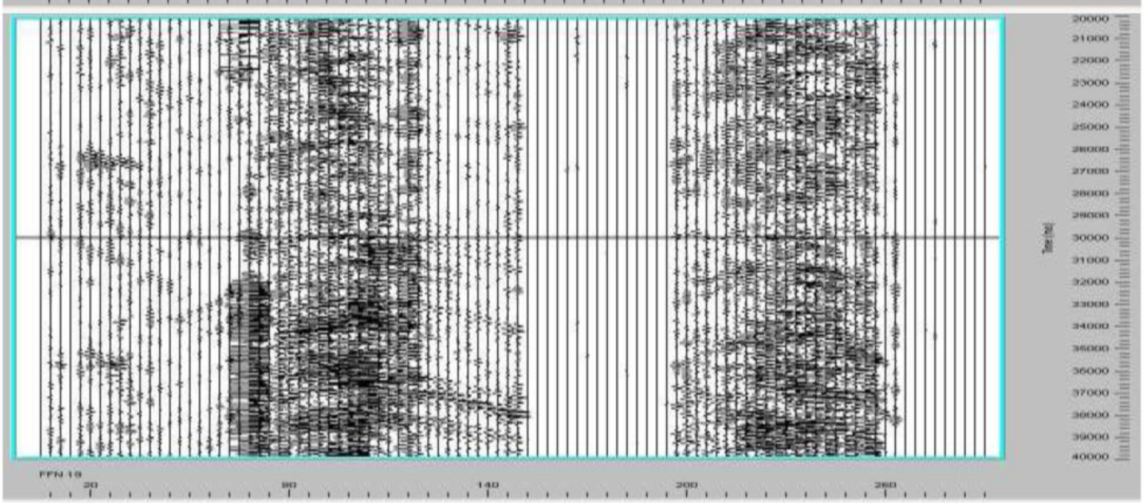

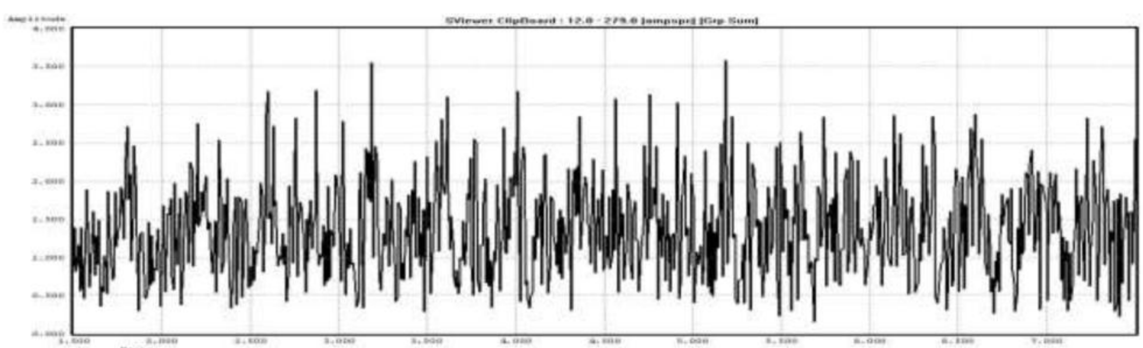

Record 26 HX Component SVSM tap test No mud flow

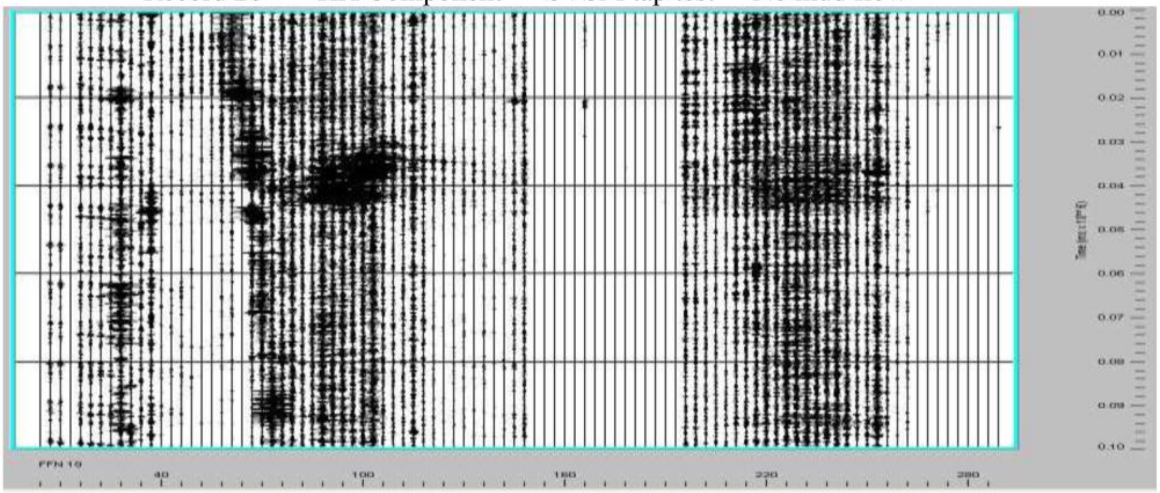

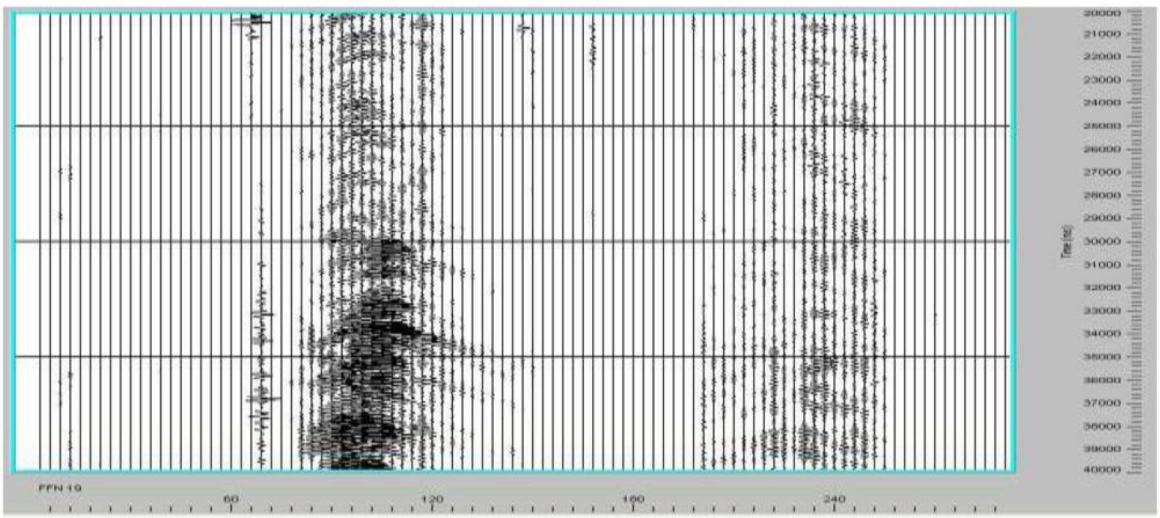

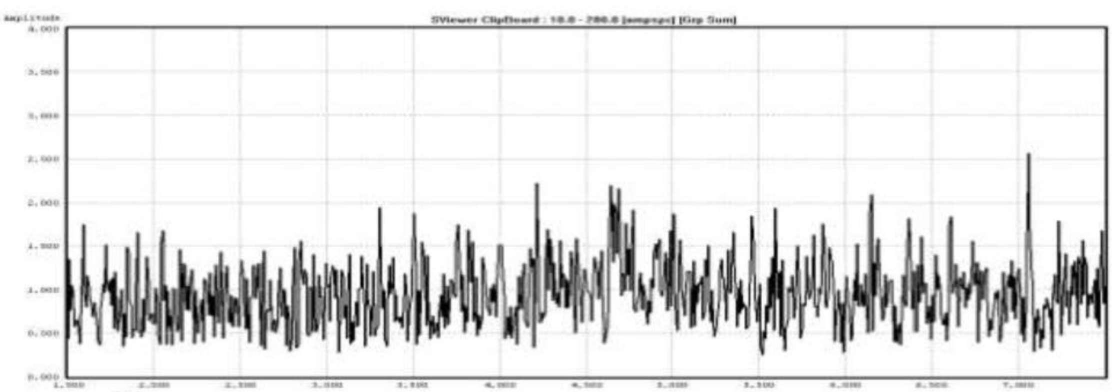

Record 26 HY Component SVSM tap test No mud flow

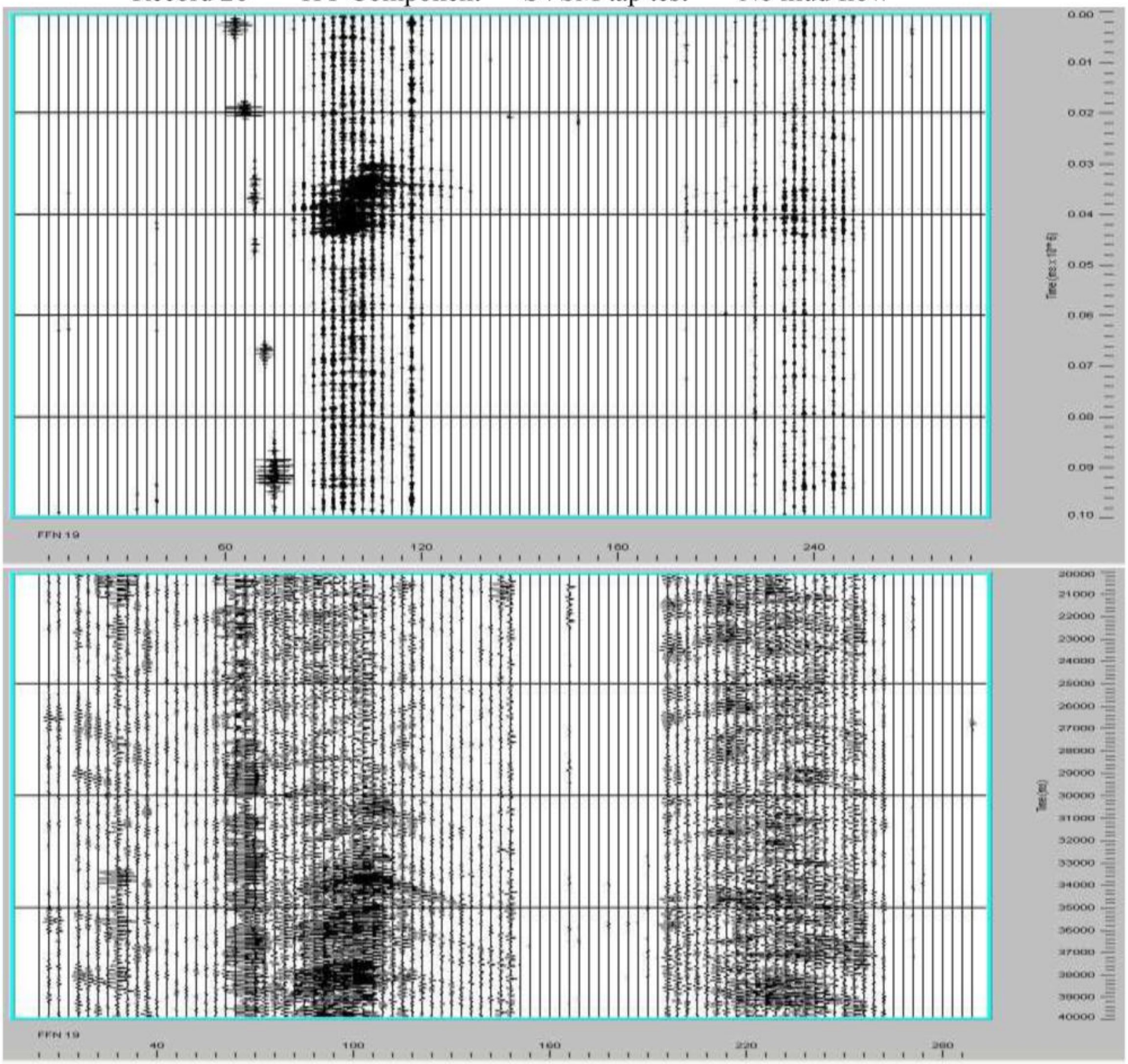

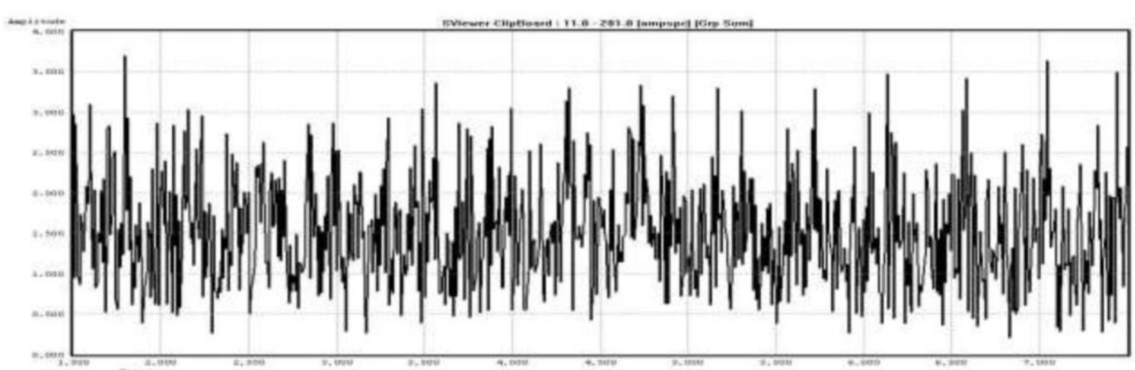

Record 28 Z Component Hammer test (10s interval)No mud flow

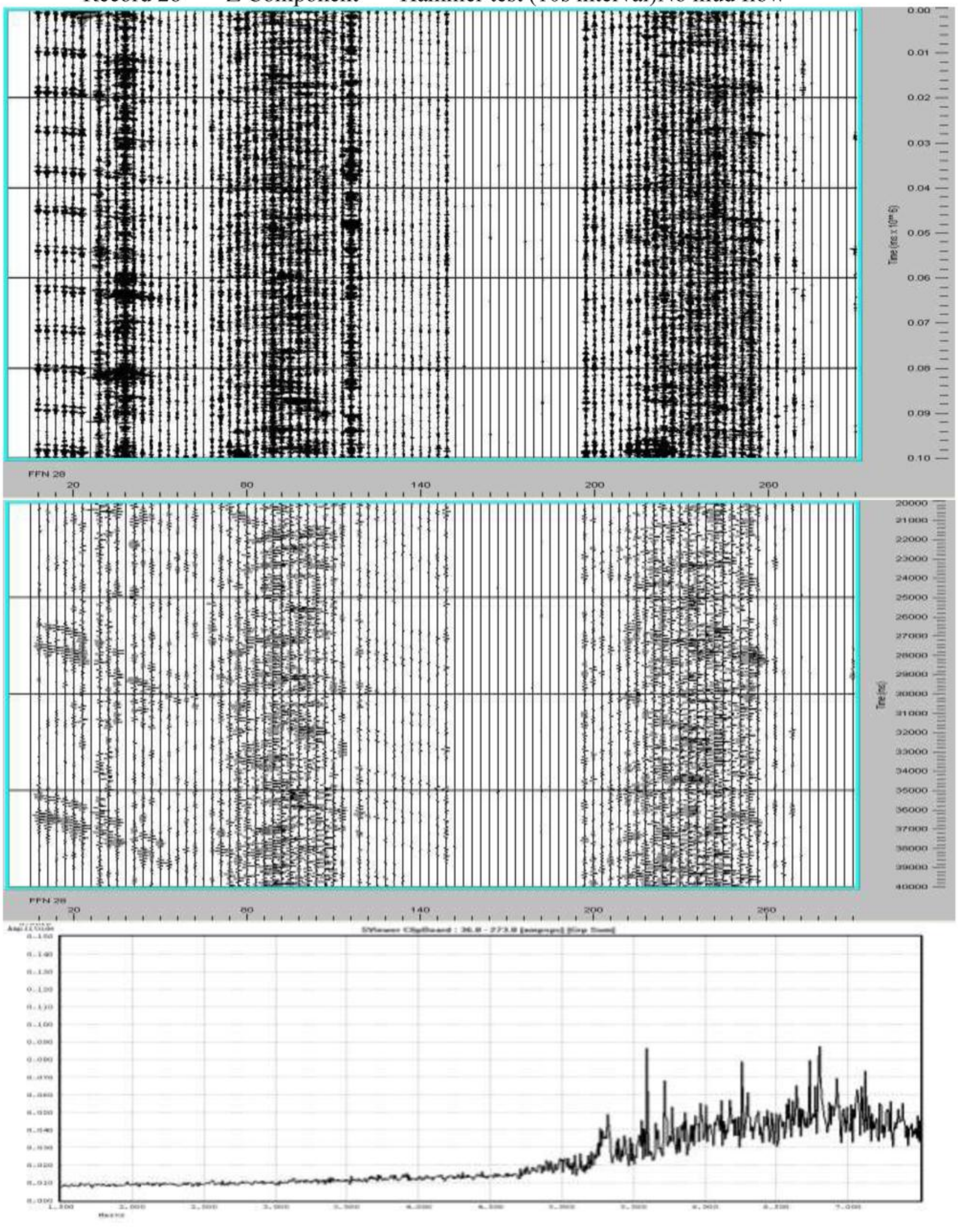

Record 28 HY Component Hammer test (10s interval) No mud flow

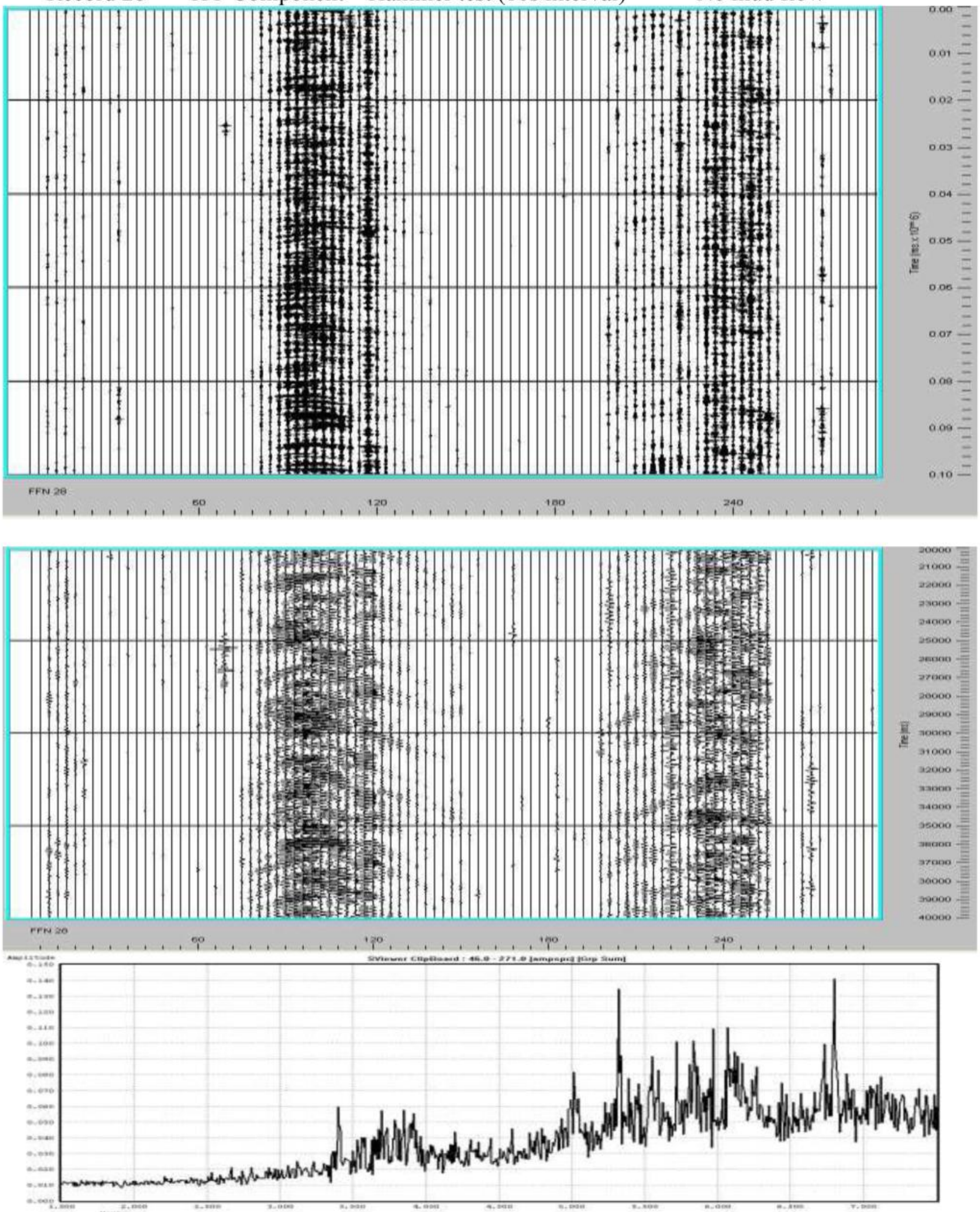

Record 28 HY Component Hammer test (10s interval) No mud flow

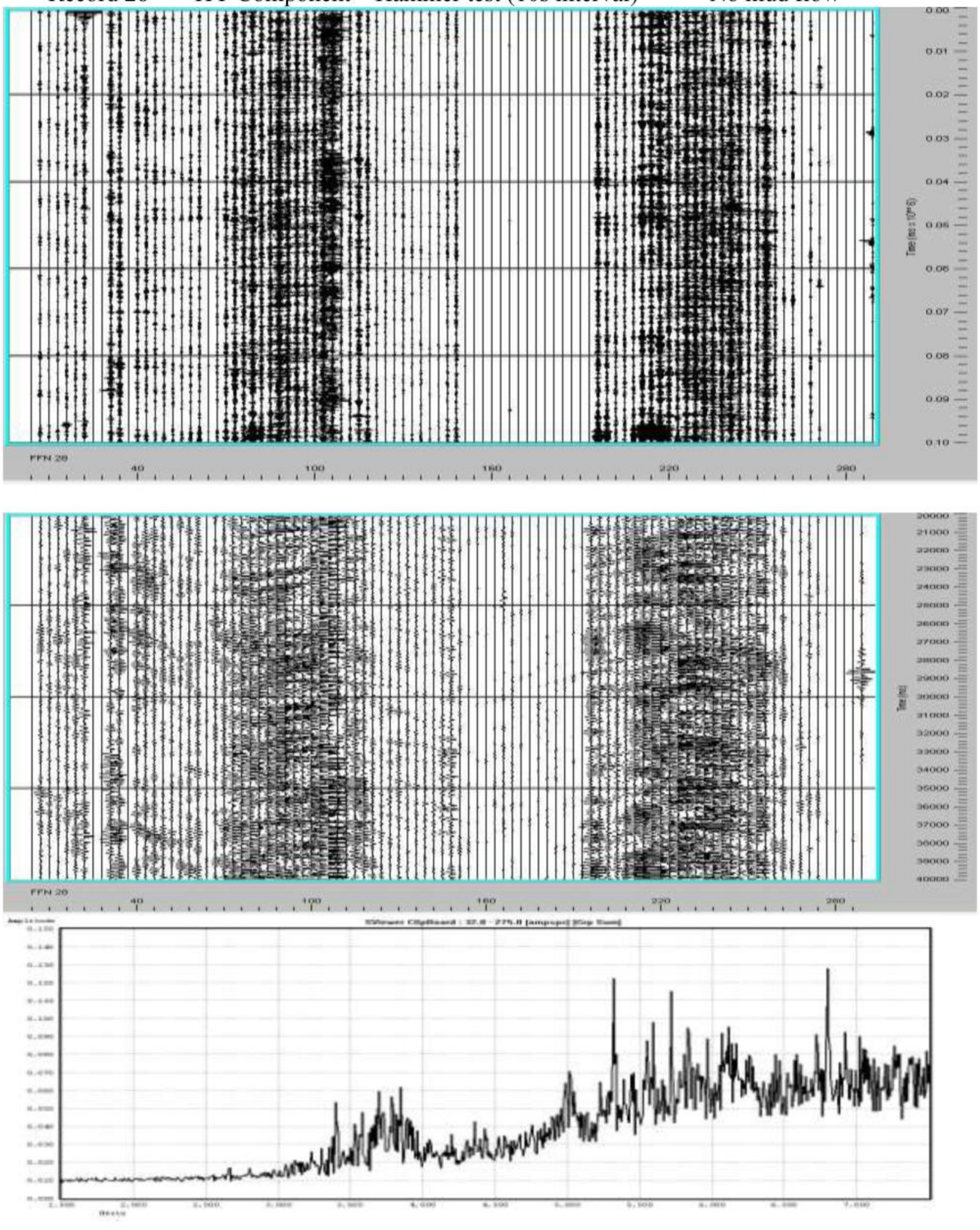

Record 29 Z Component Tool depth 775 ft Noise test Mud flow @ 100 gpm

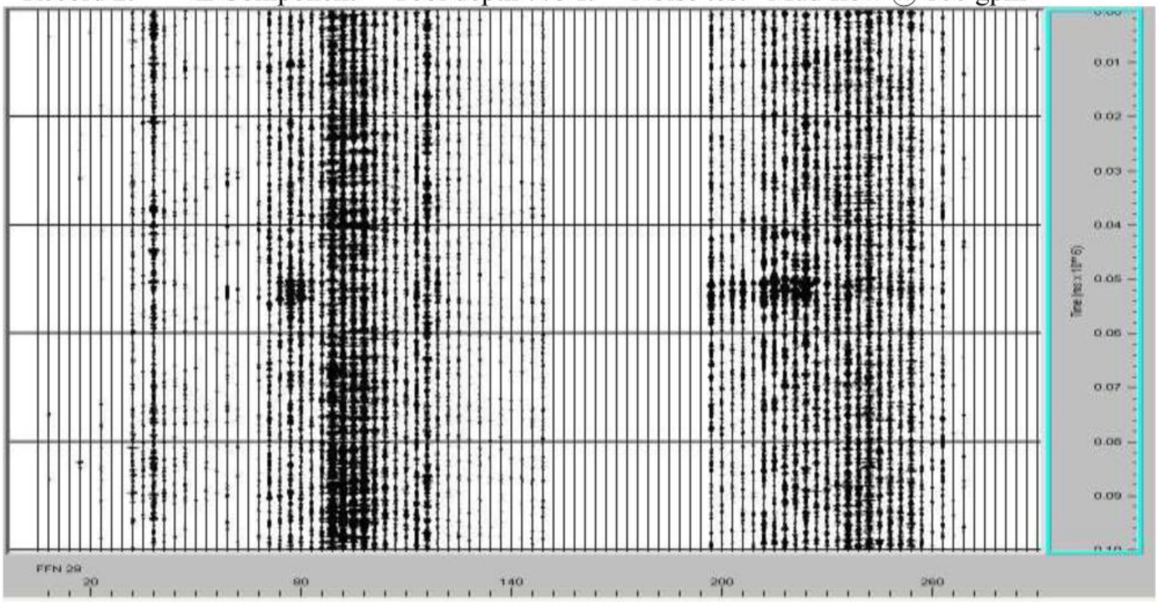

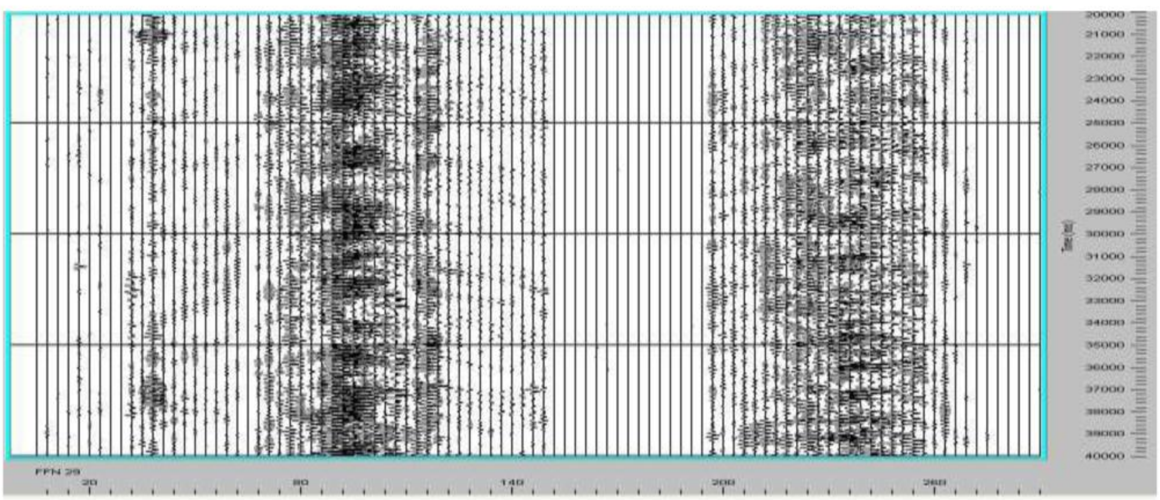

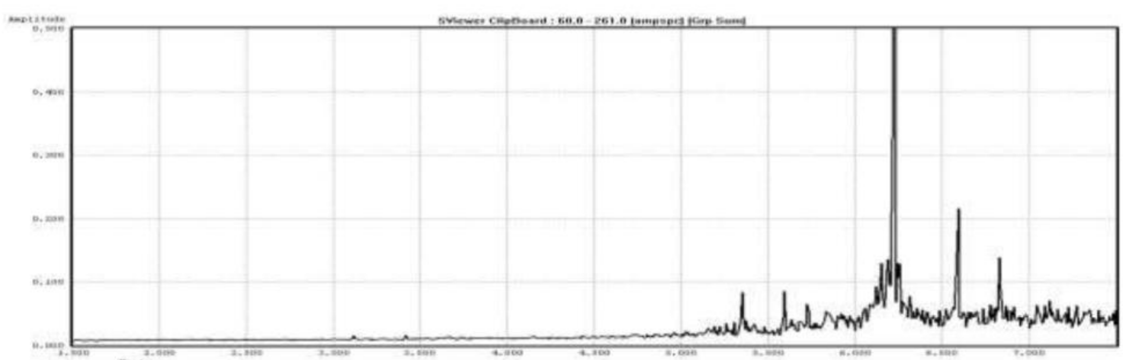

Record 29 HX Component Tool depth 775 ft Noise test Mud flow @ 100 gpm

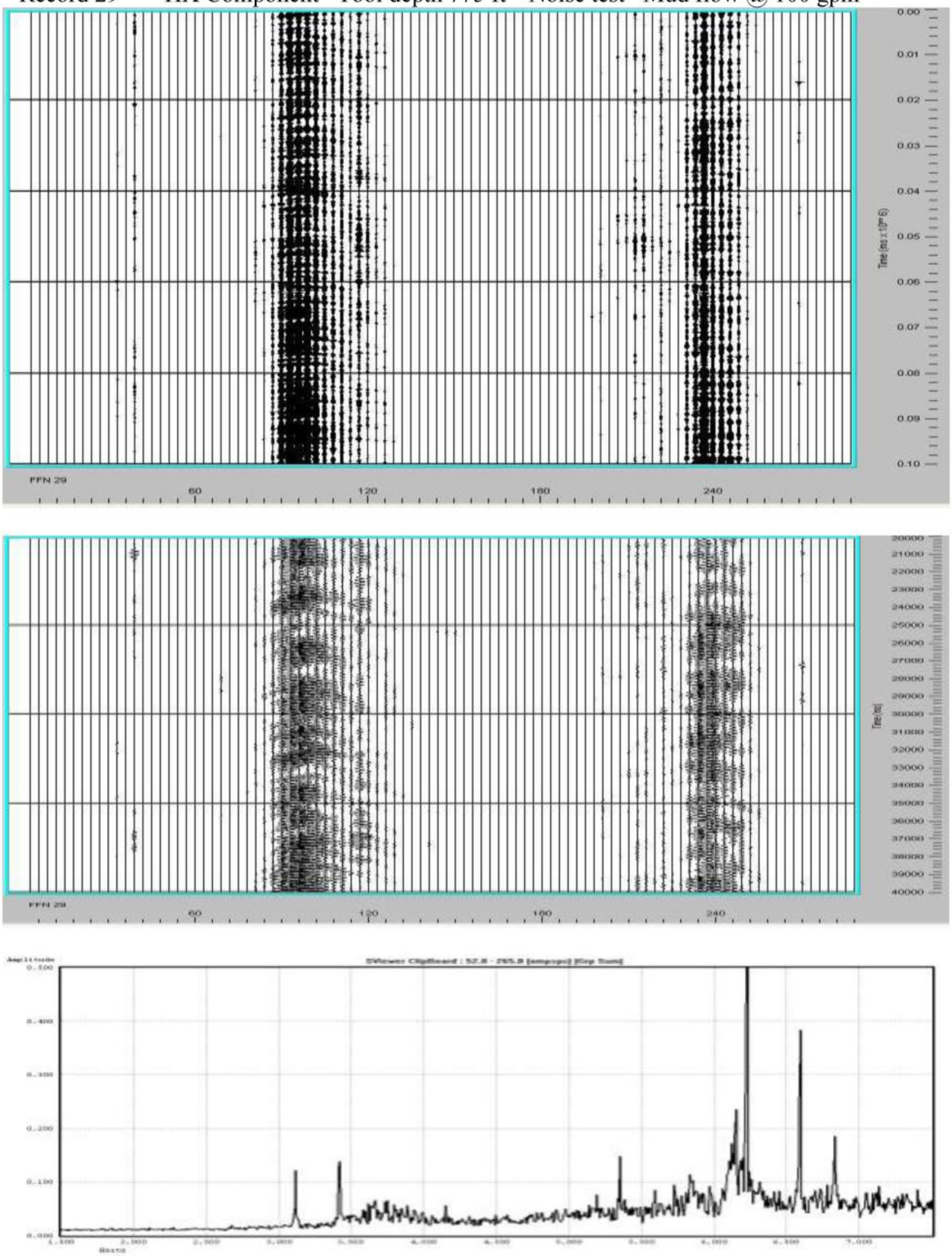

Record 29 HY Component Tool depth 775 ft Noise test Mud flow @ 100 gpm

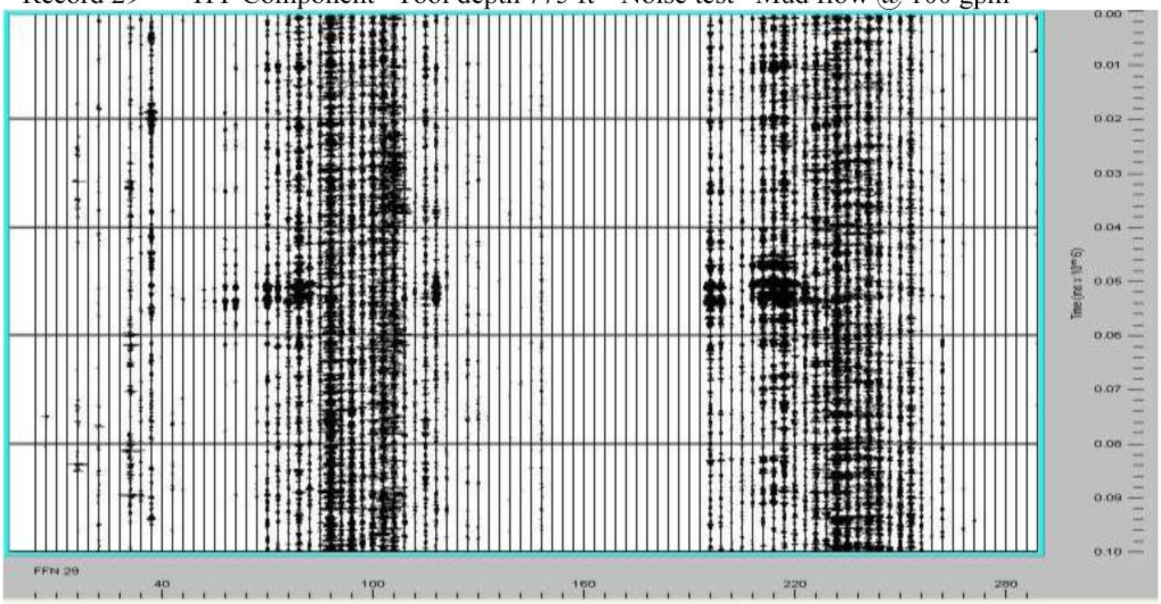

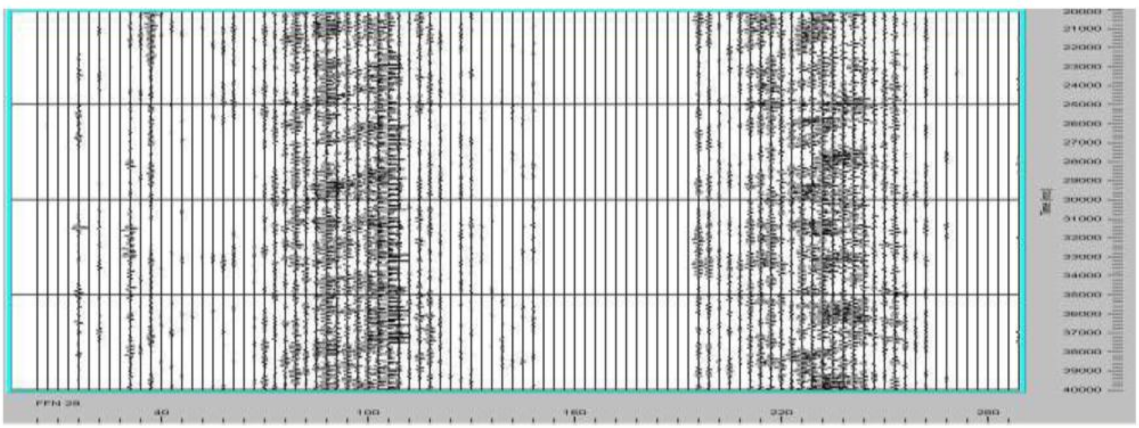

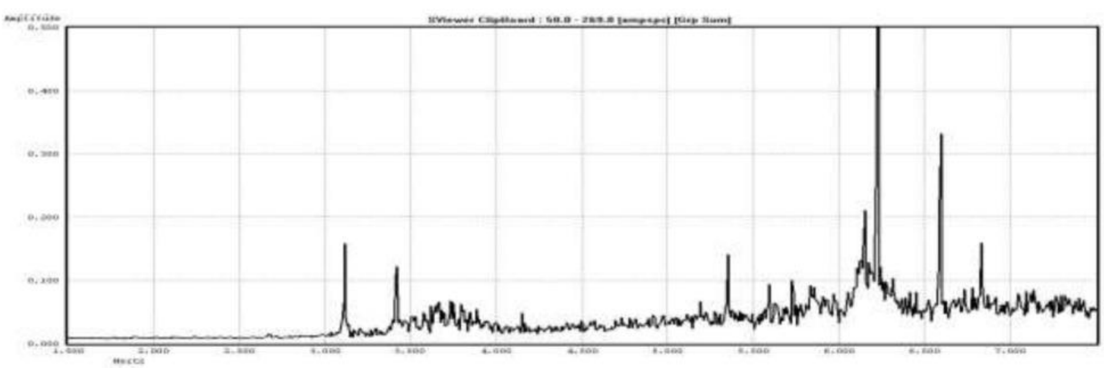

Record 30 Z Component Tool depth 775 ft Noise test Mud flow @ 207 gpm

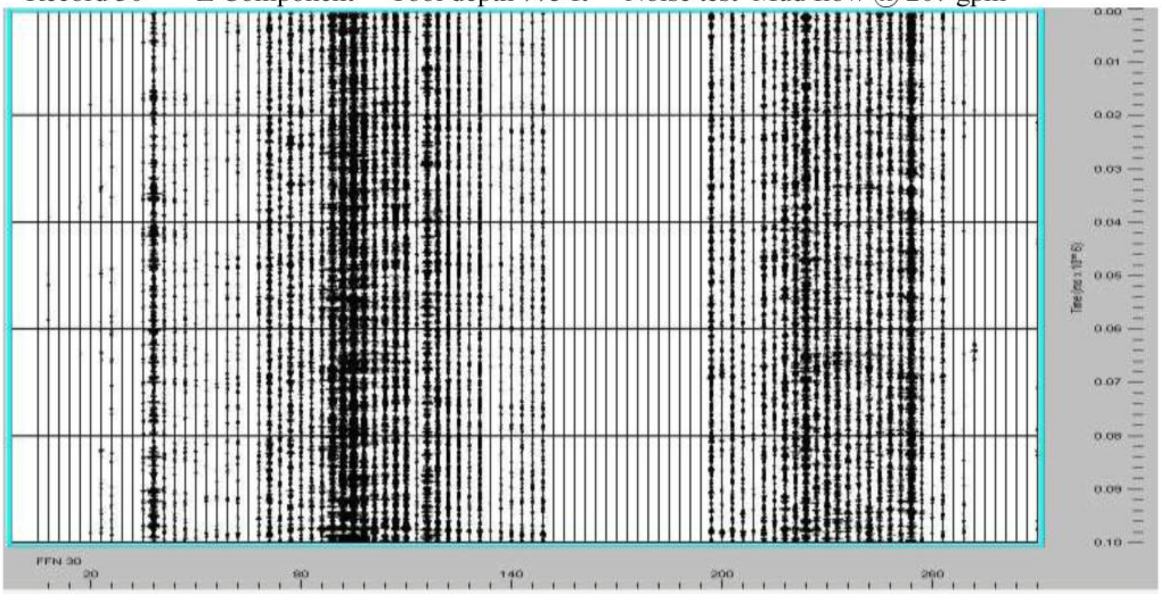

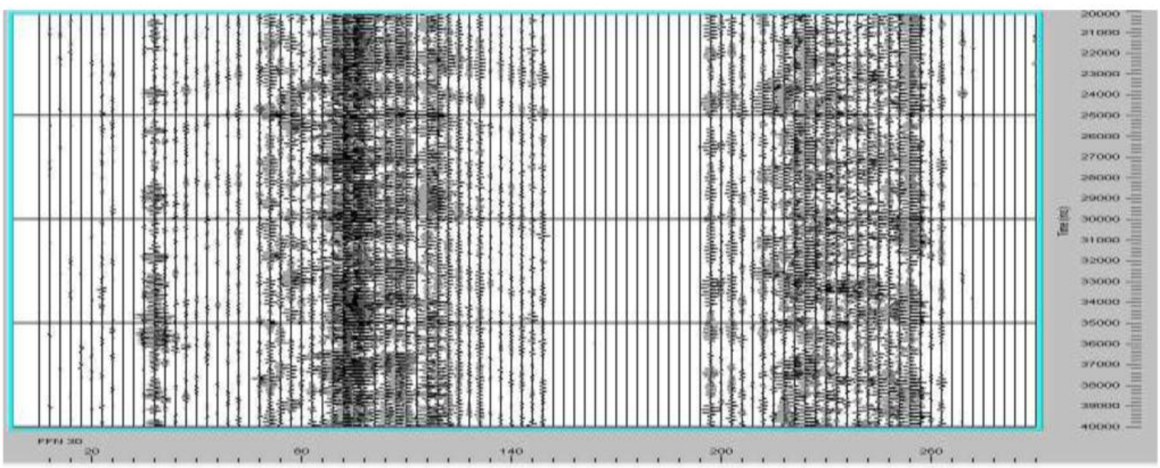

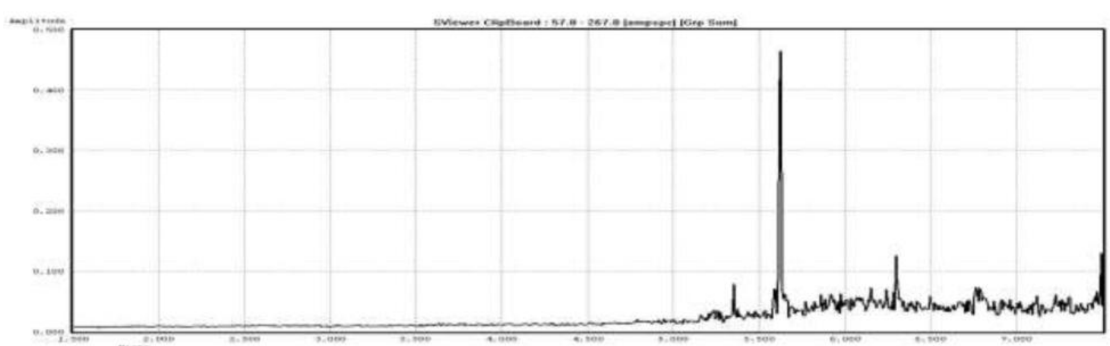

Record 30 HX Component Tool depth 775 ft Noise test Mud flow @ 207 gpm

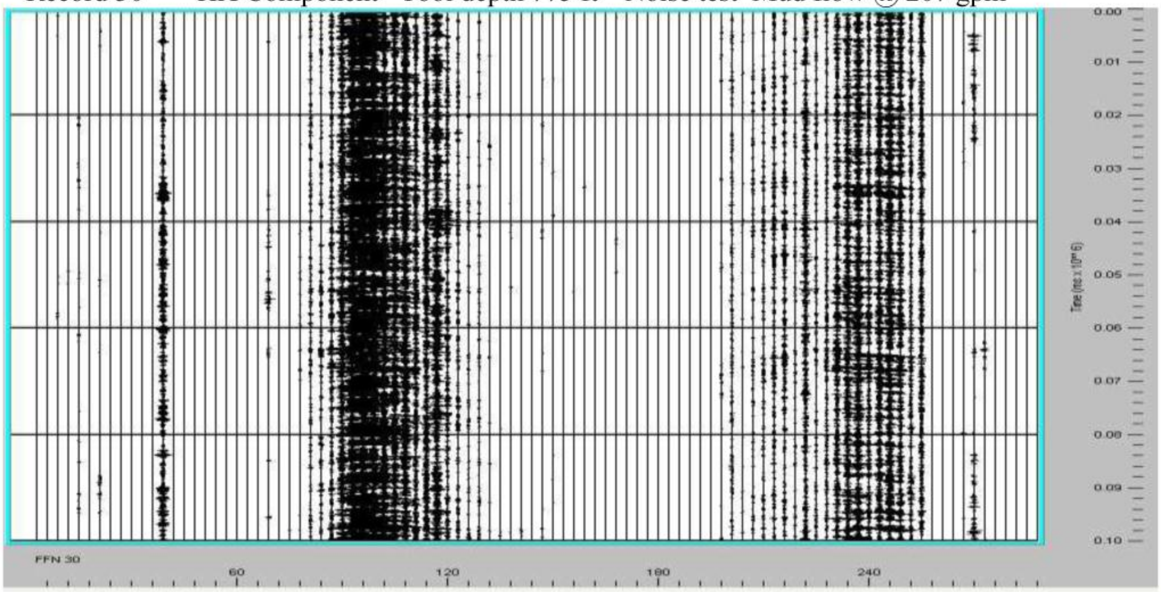

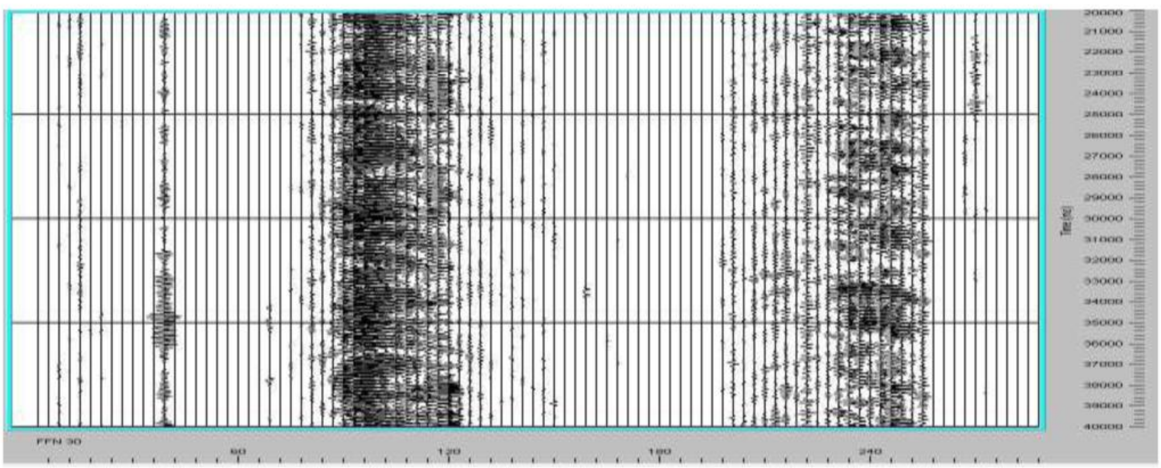

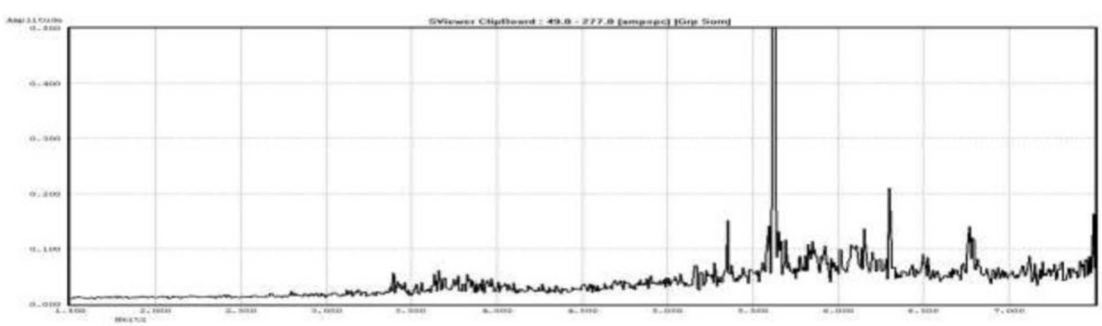

Record 30 HY Component Tool depth 775 ft Noise test Mud flow @ 207 gpm

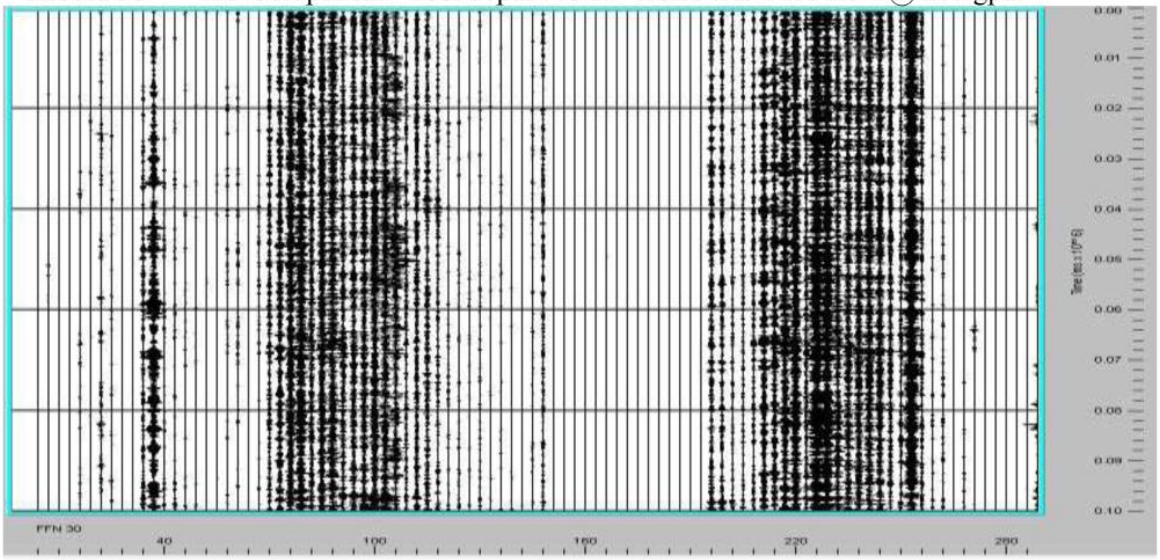

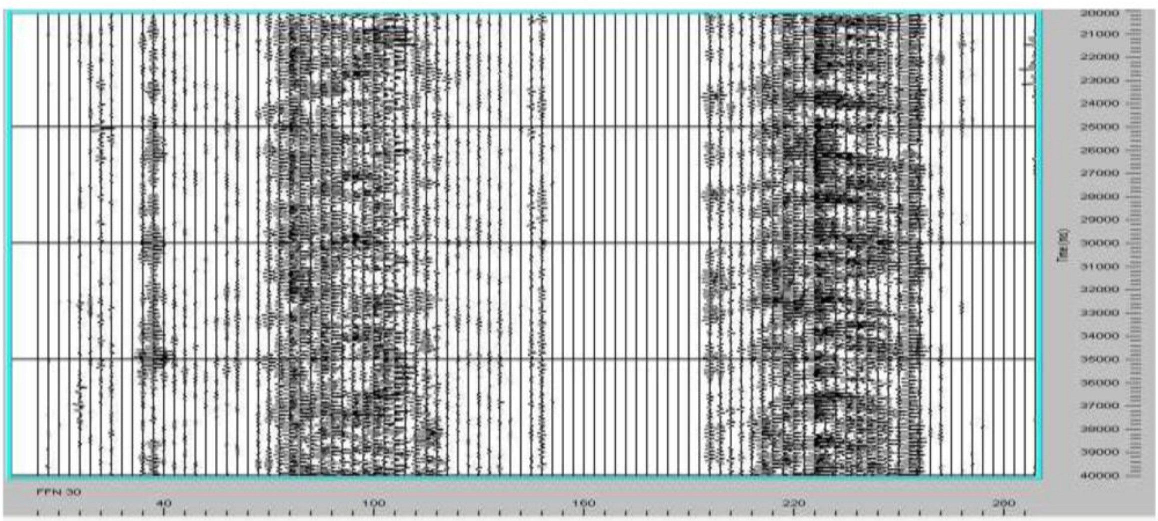

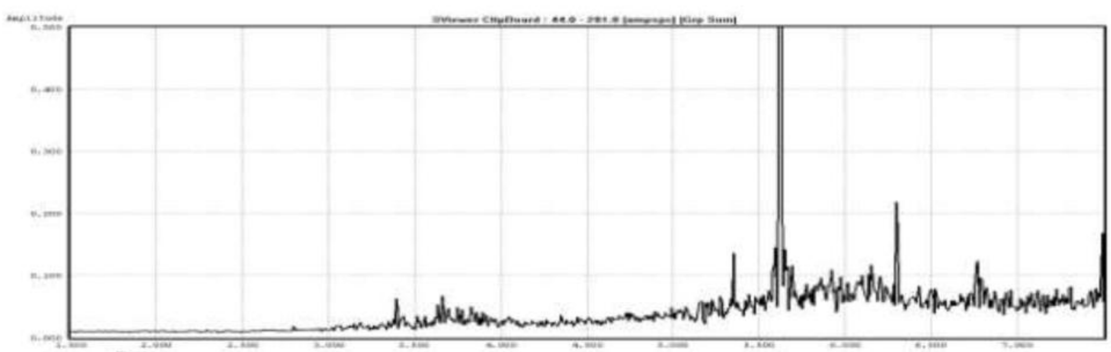

Record 31 Z Component Pulse test Tool depth 775 ft Mud flow @ 365 gpm

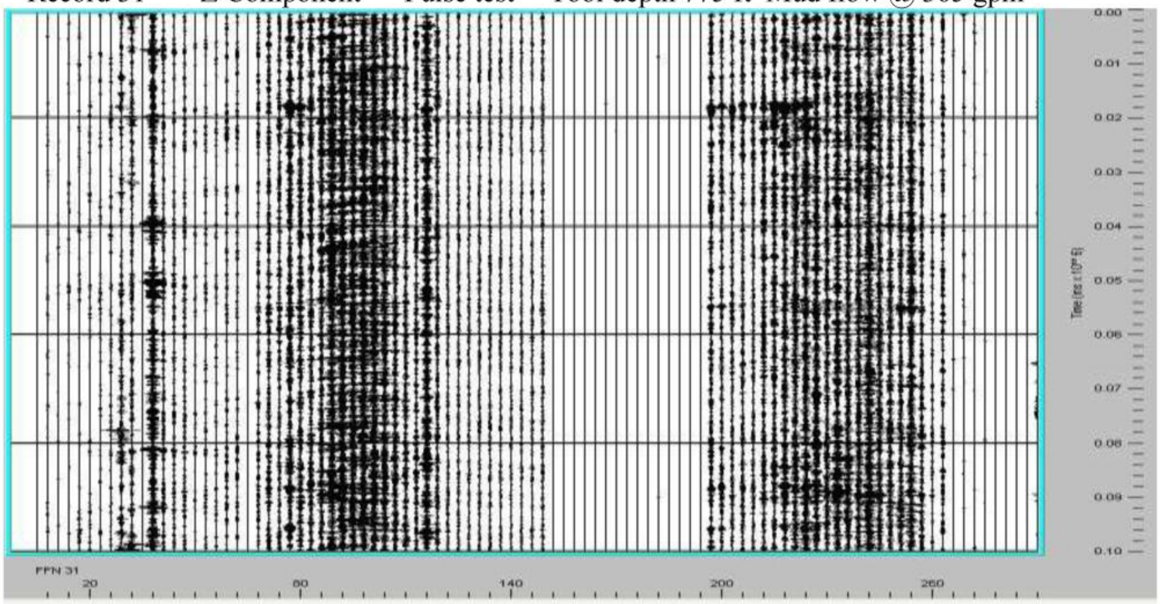

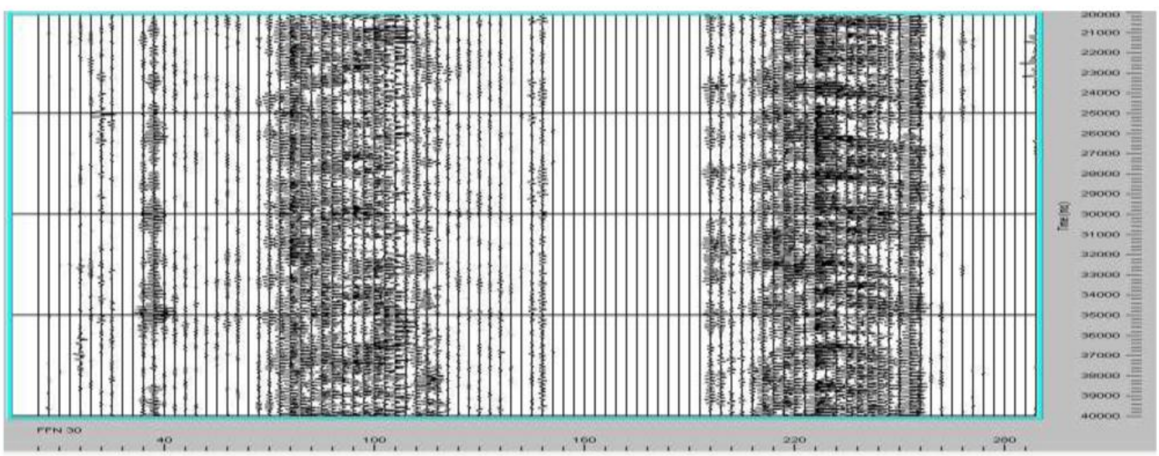

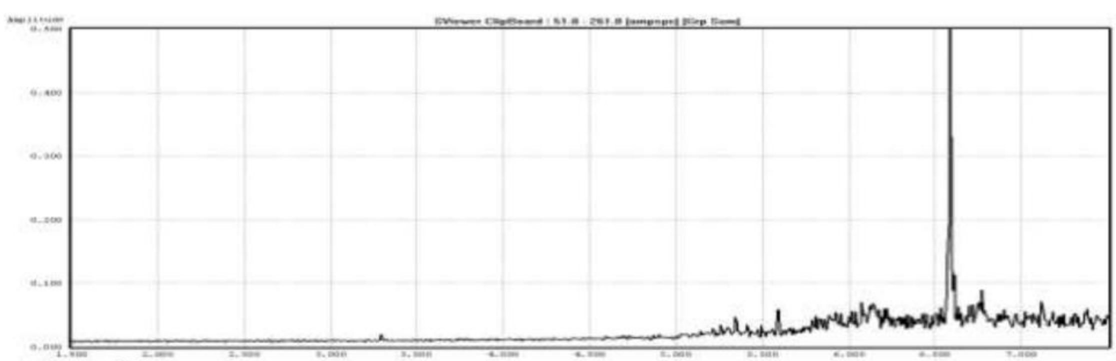

Record 31 HX Component Pulse test Tool depth 775 ft Mud flow @ 365 gpm

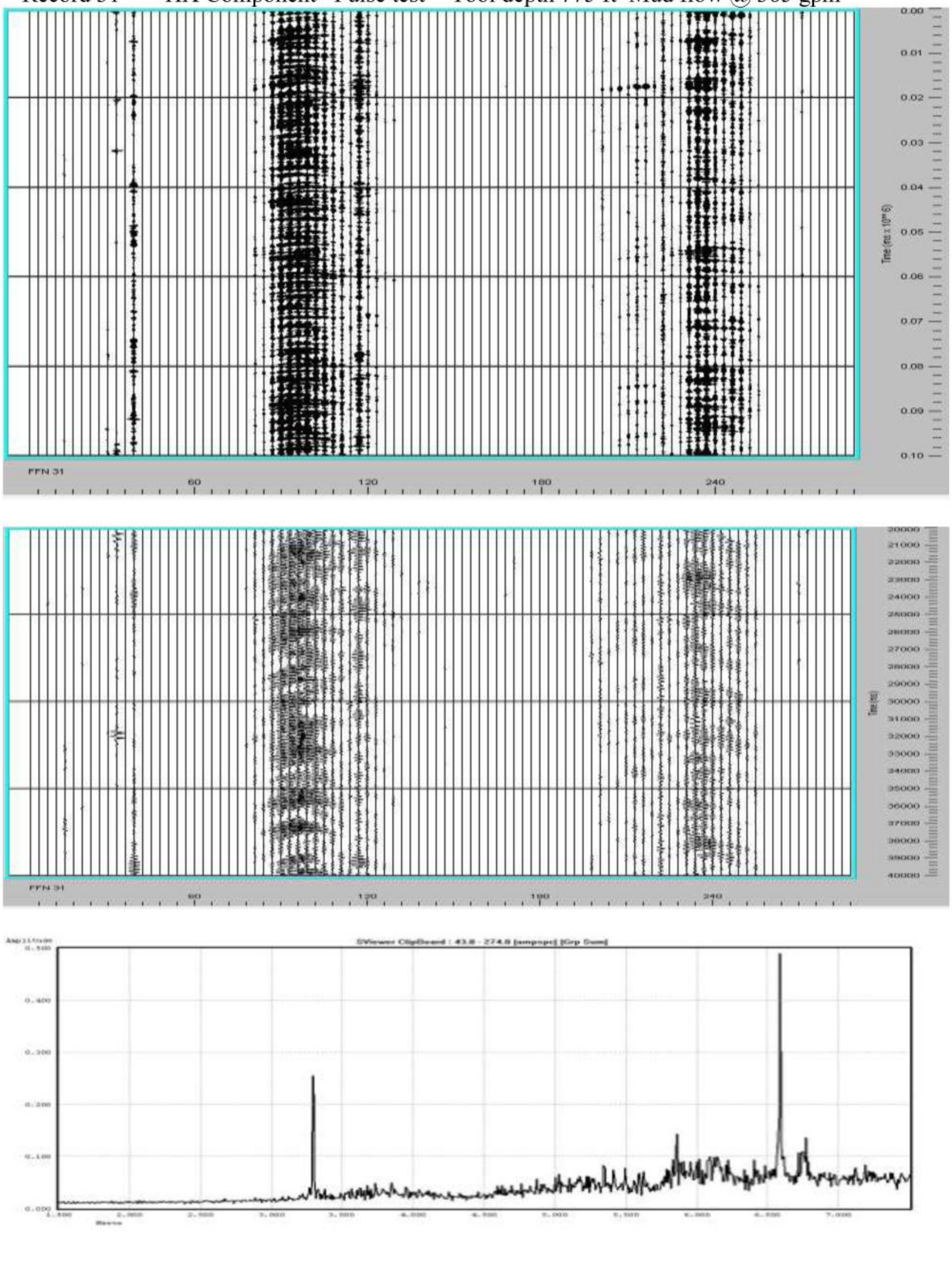

Record 31 HY Component Pulse test Tool depth 775 ft Mud flow @ 365 gpm

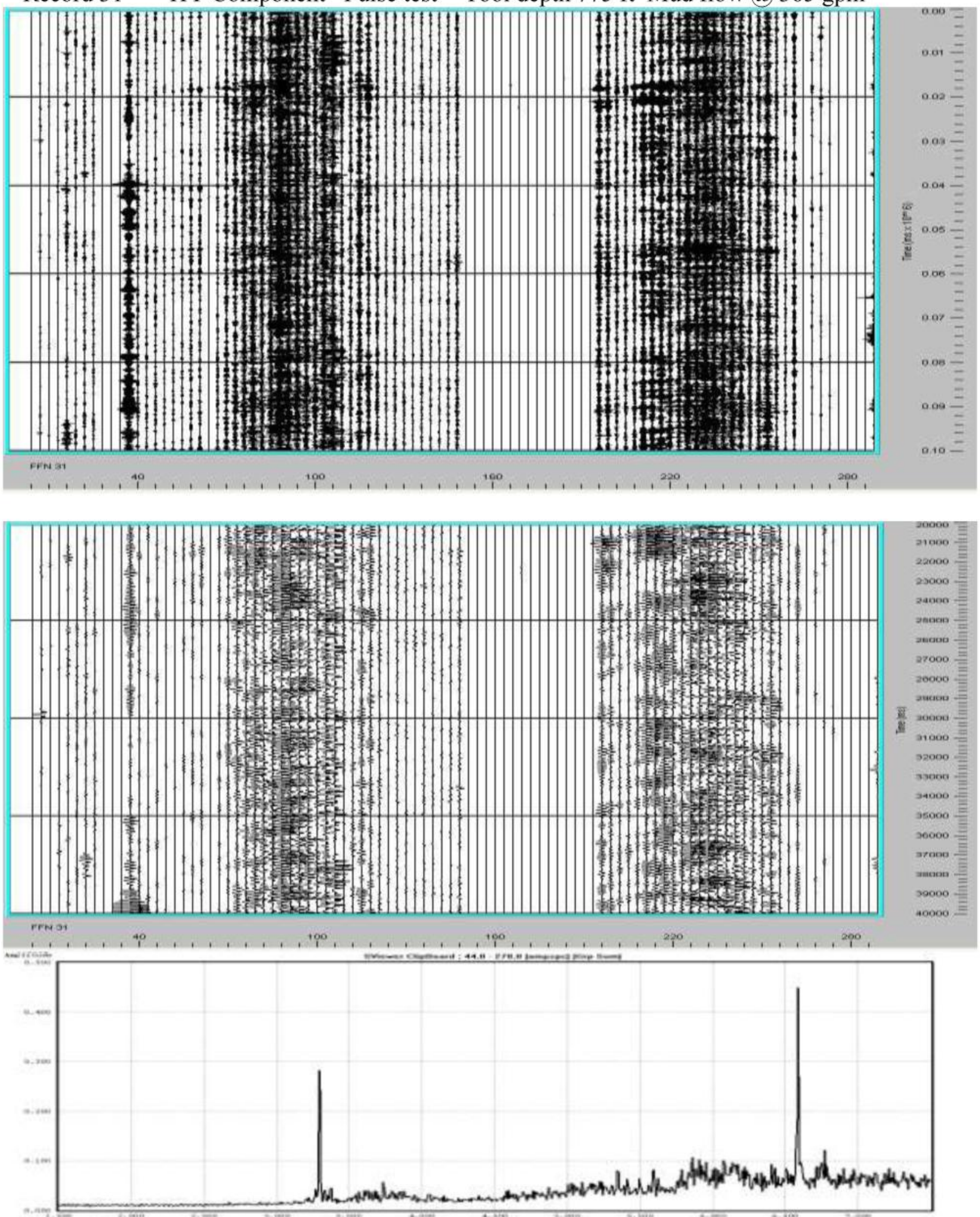

Record 40 Z Component Pulse test Tool depth 2950 ft Mud flow @ 358 gpm

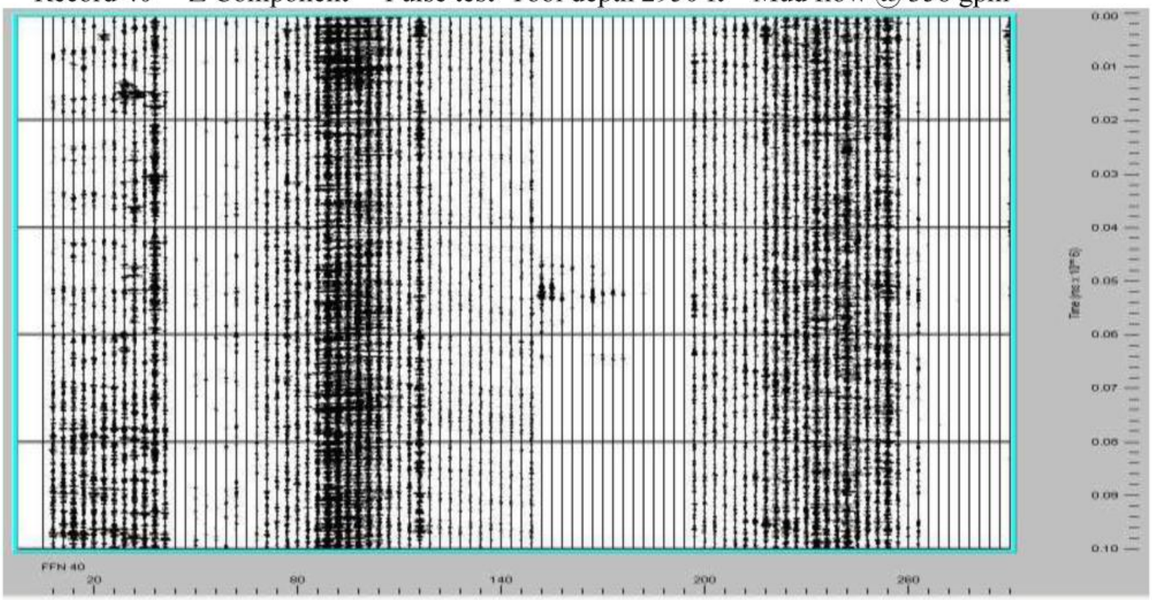

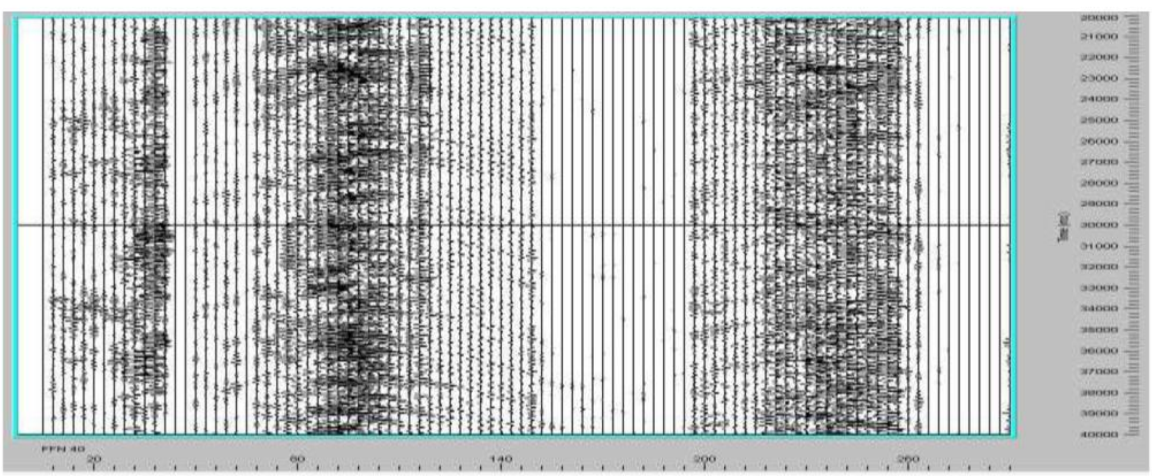

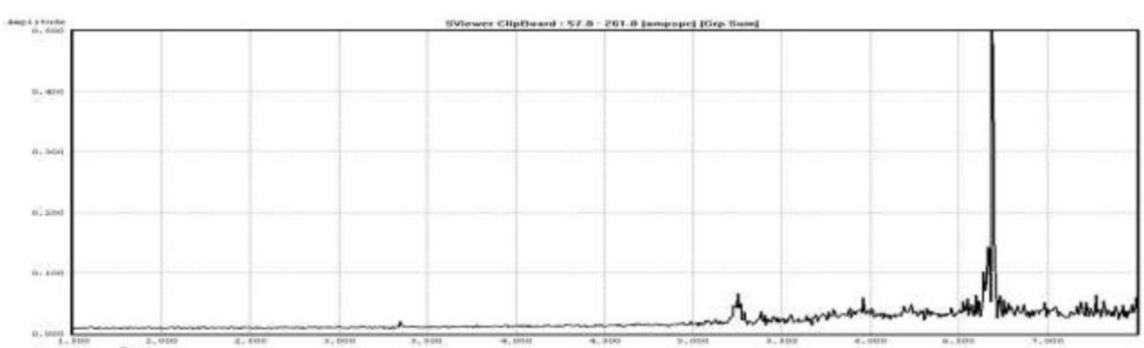

Record 40 HX Component Pulse test Tool depth 2950 ft Mud flow @ 358 gpm

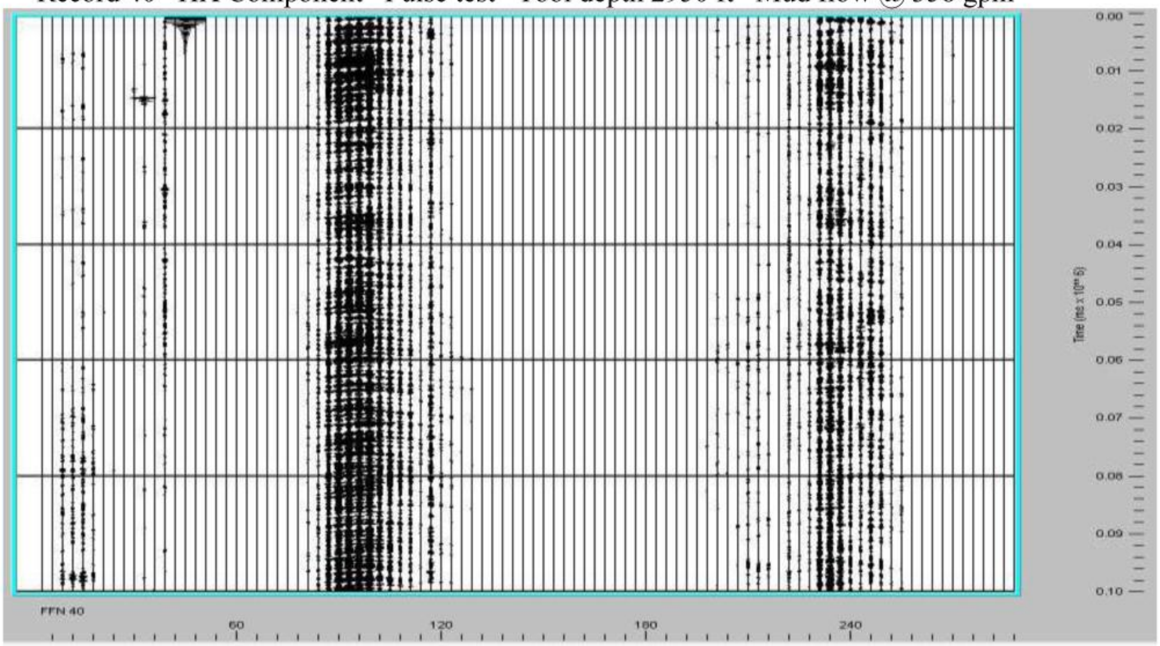

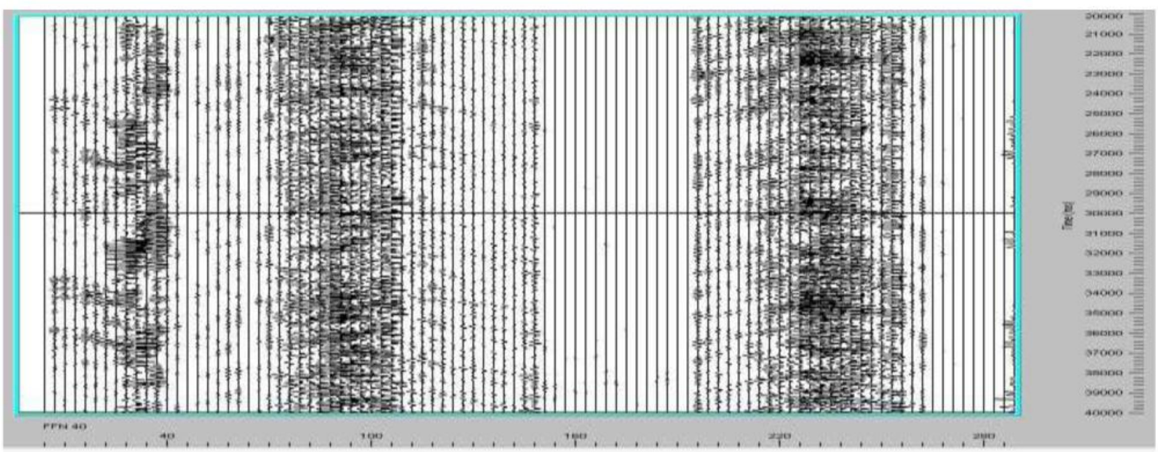

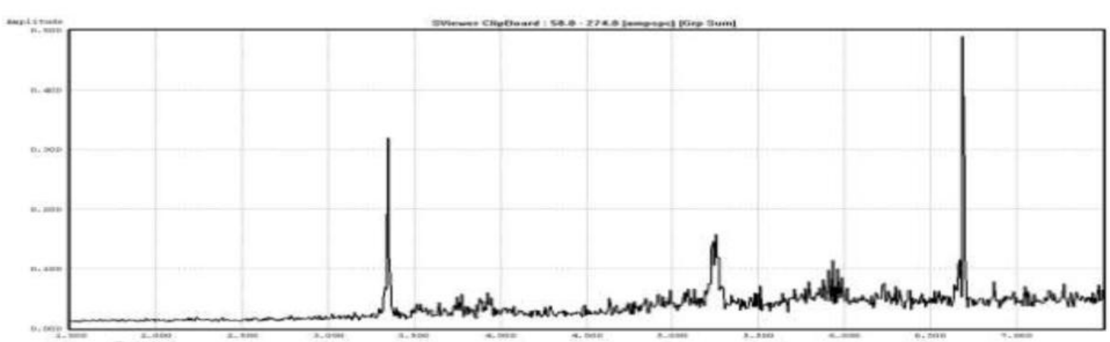

Record 40 HY Component Pulse test Tool depth 2950 ft Mud flow @ 358 gpm

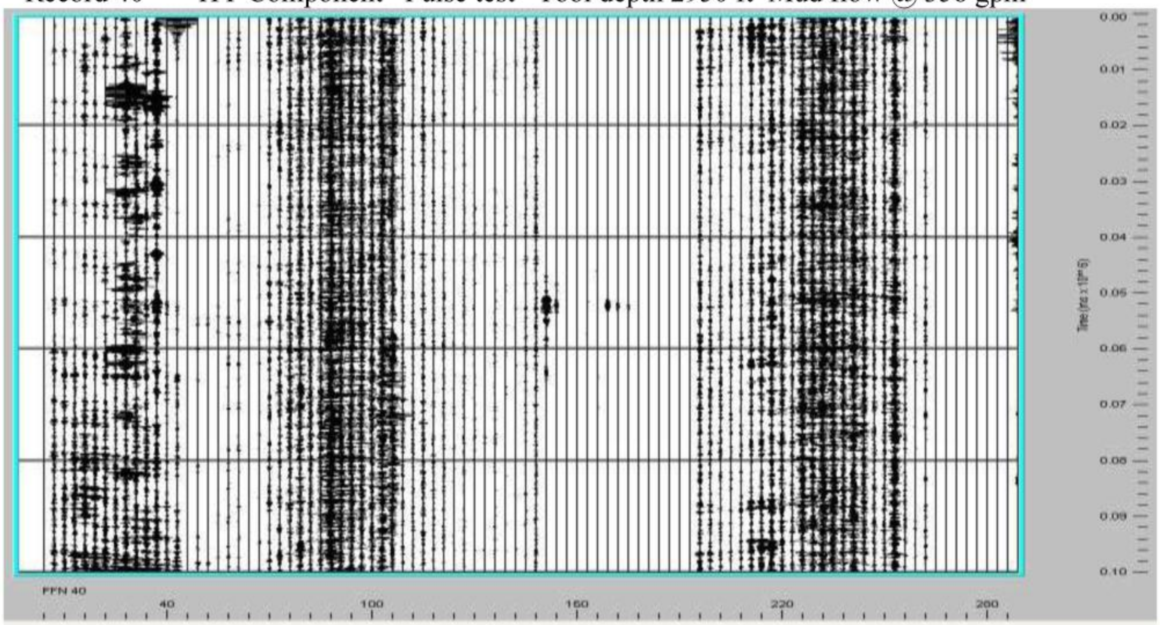

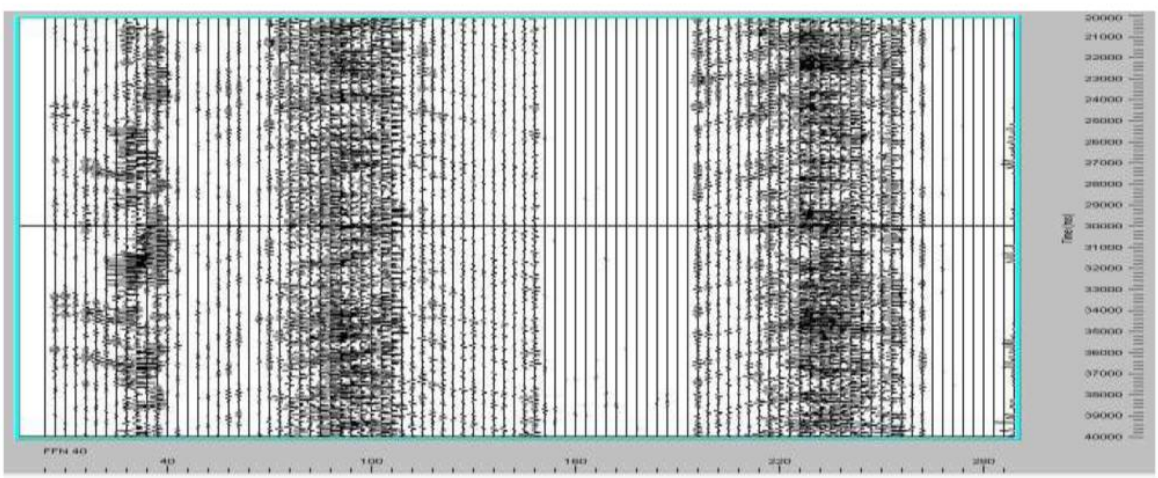

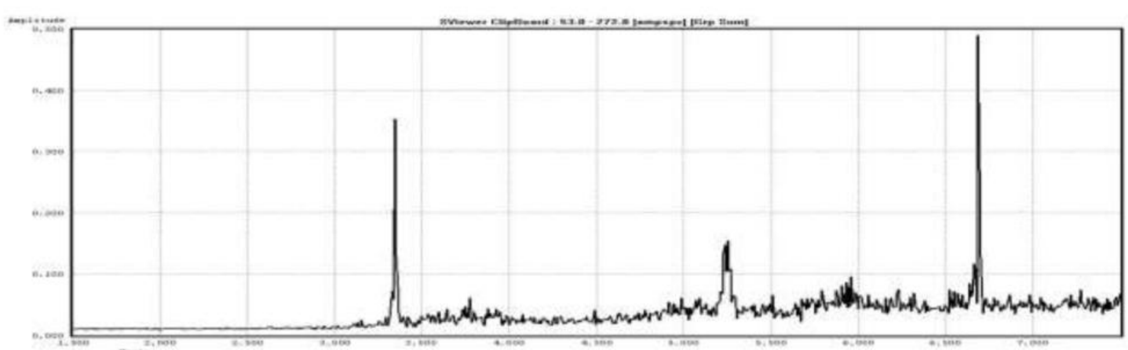

Record 41   Z Component   Flow noise test   Tool out of hole   Mud flow @ 365 gpm

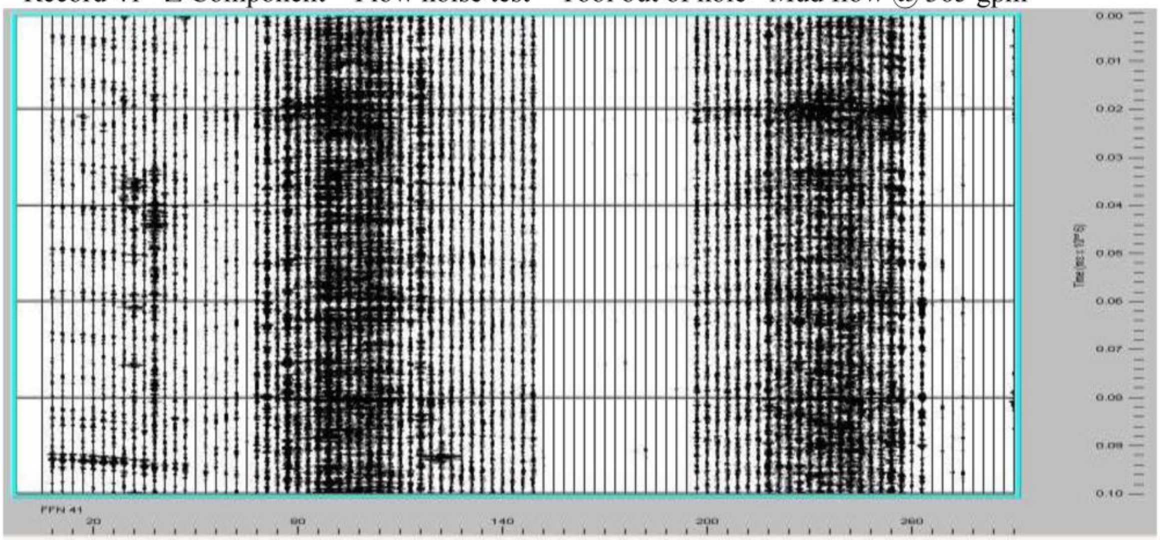

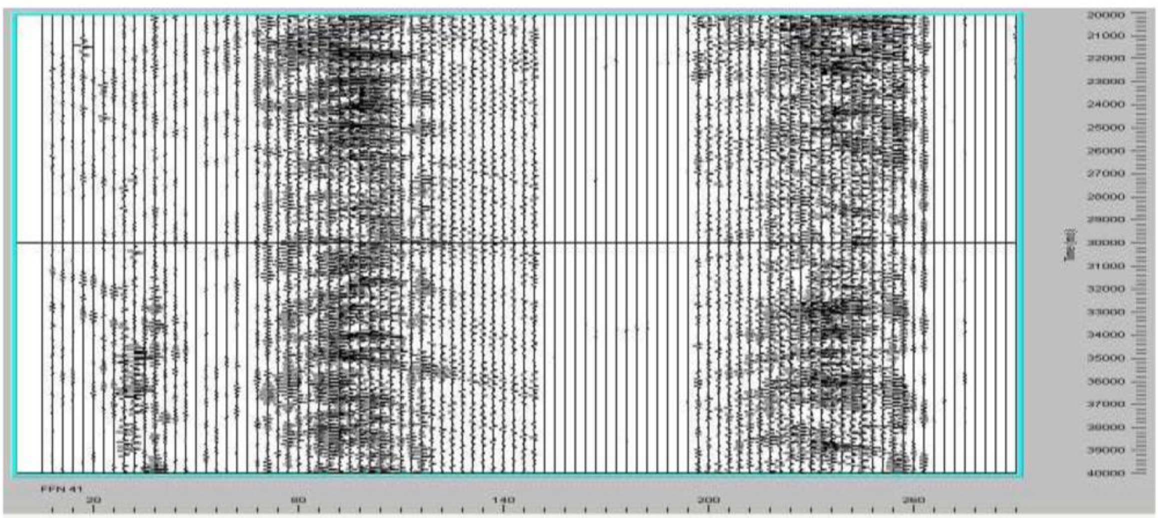

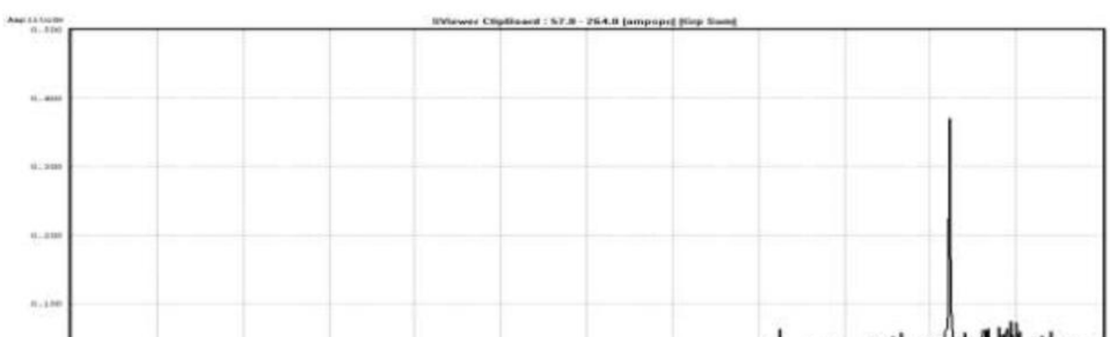

Record 41   HX Component Flow noise test   Tool out of hole Mud flow @ 365 gpm

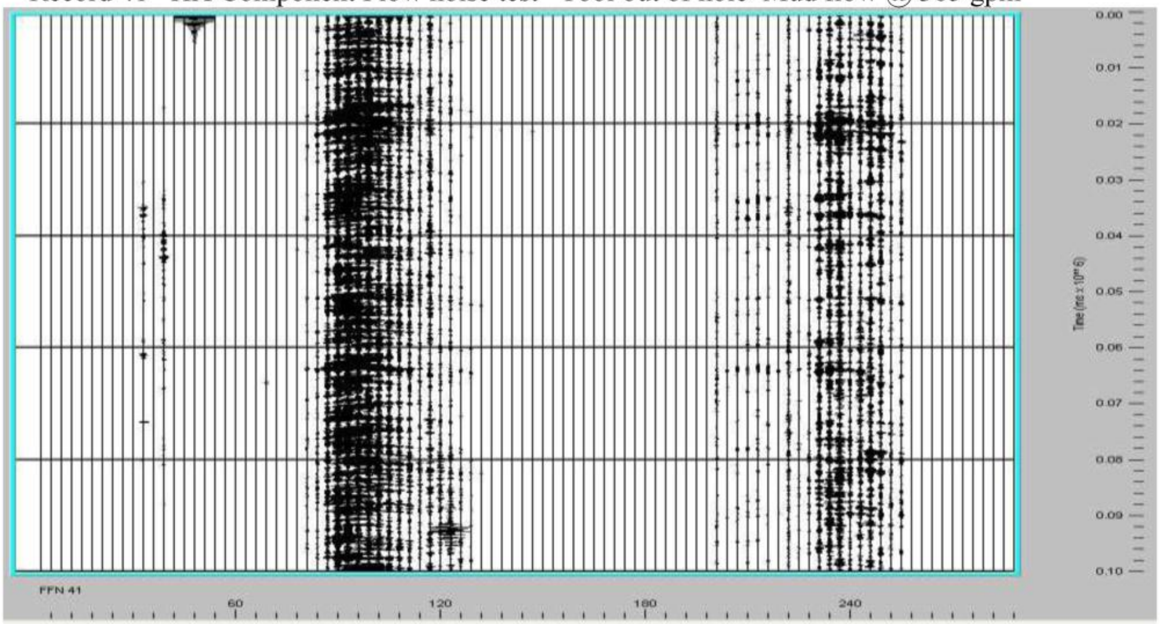

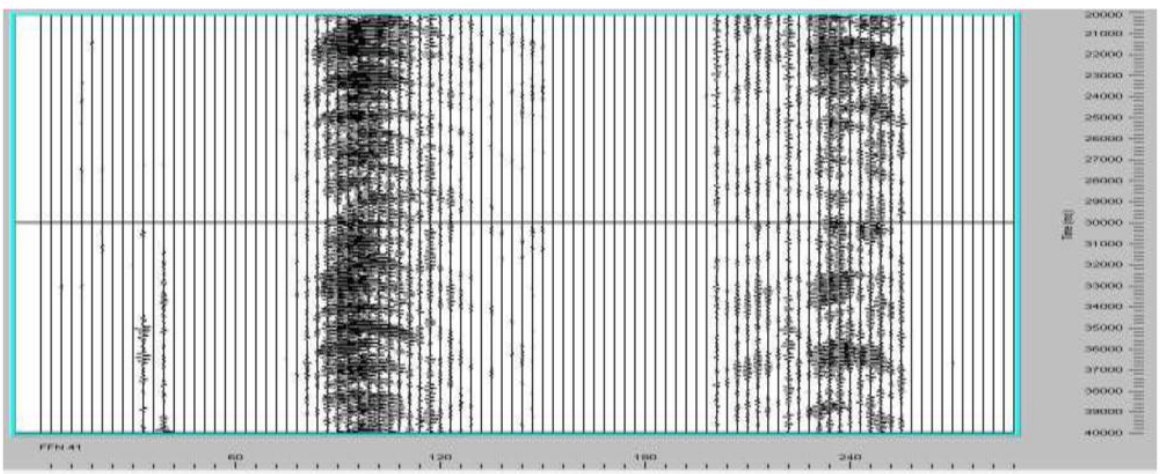

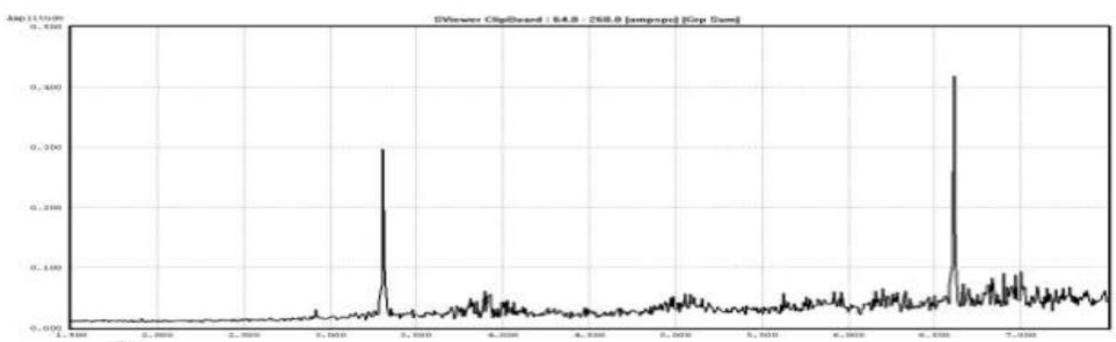

Record 41   HY Component Flow noise test   Tool out of hole Mud flow @ 365 gpm

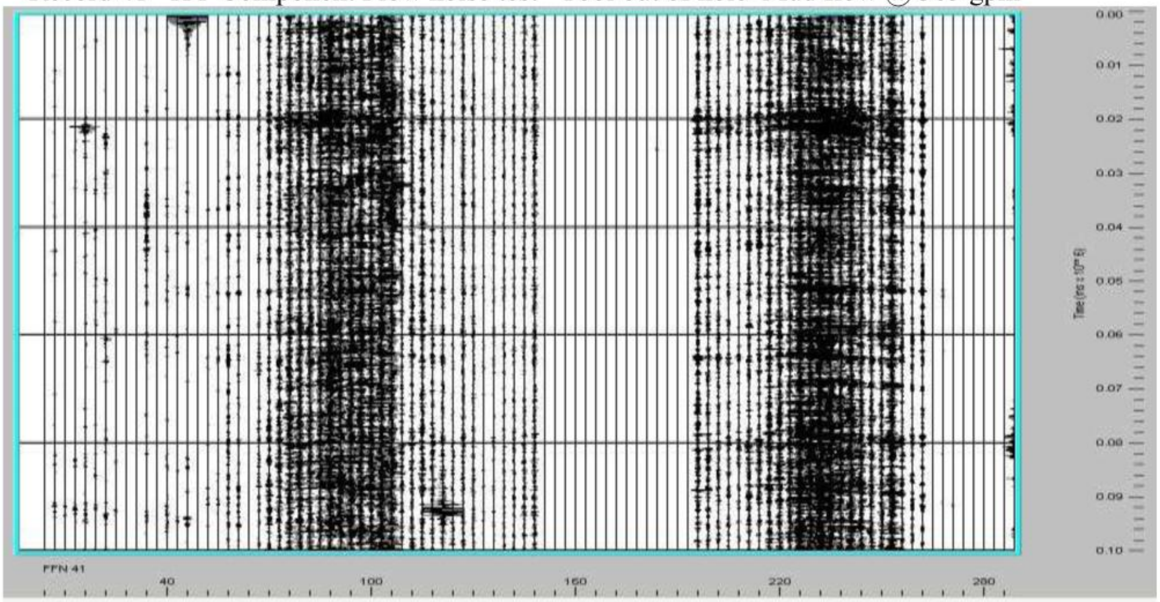

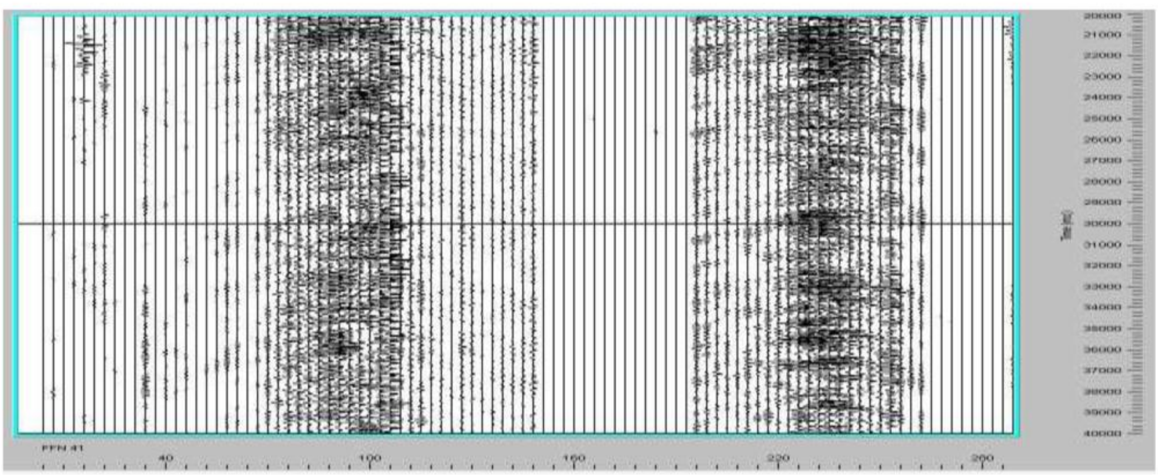

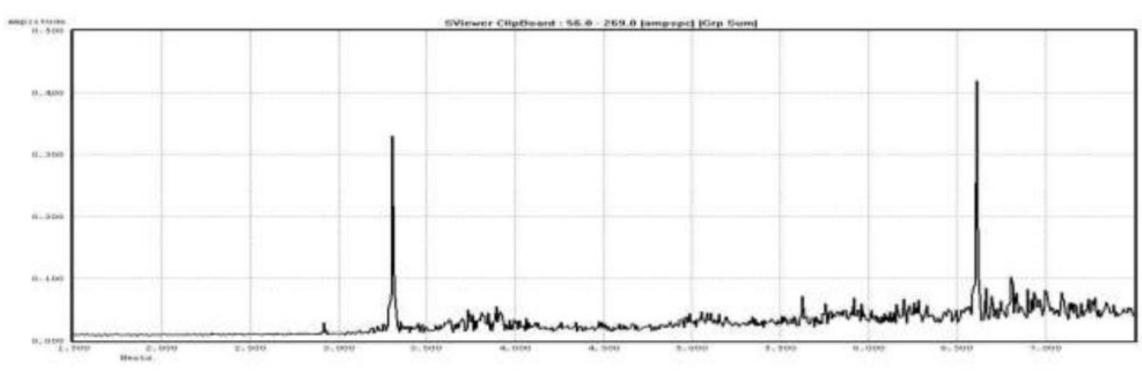

Autocorrelation analysis (windowed region shown)

Record 19 H2 Component Background noise test Mud flow @ 100 gpm

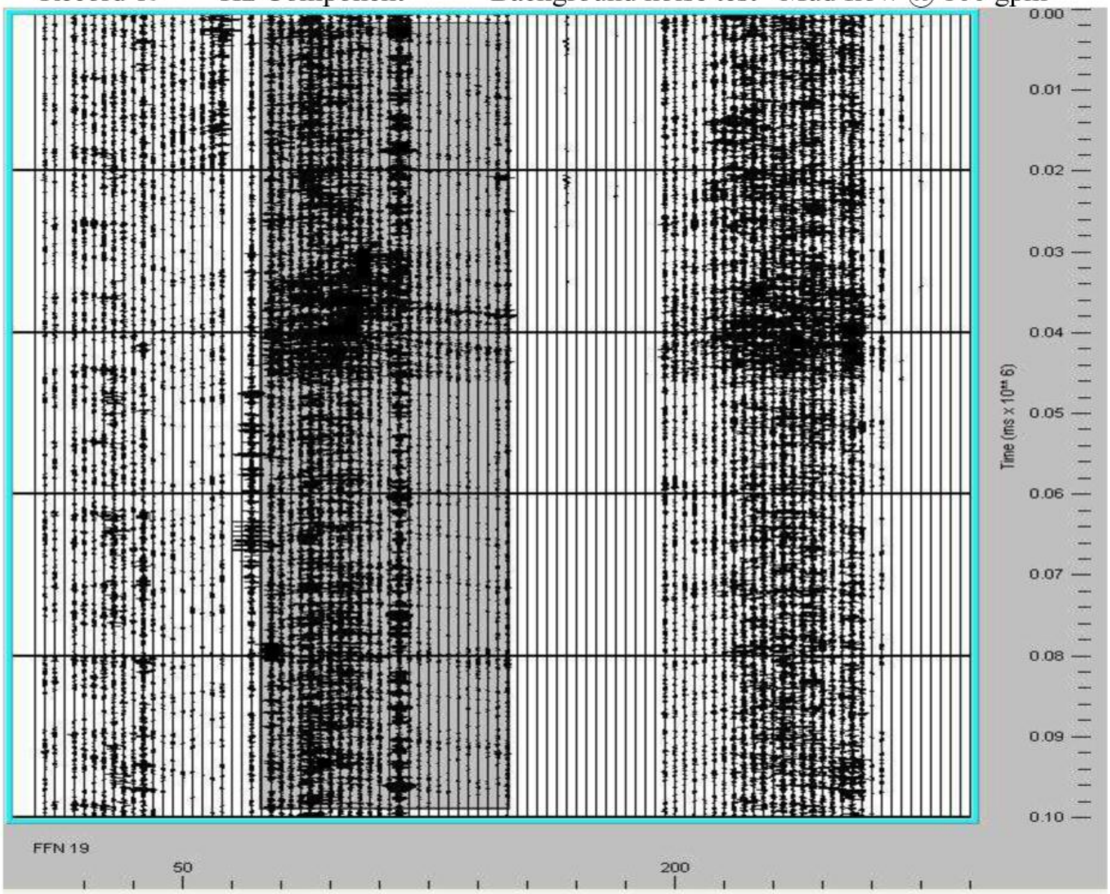

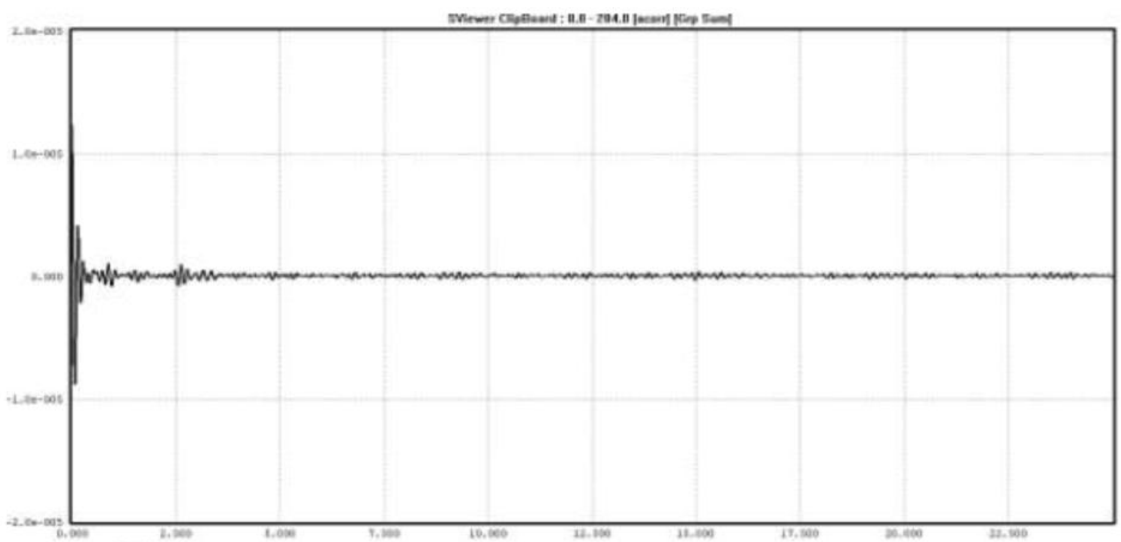

Record 12 Componnt H2 Hammer Test Mudflow @ 100 gpm

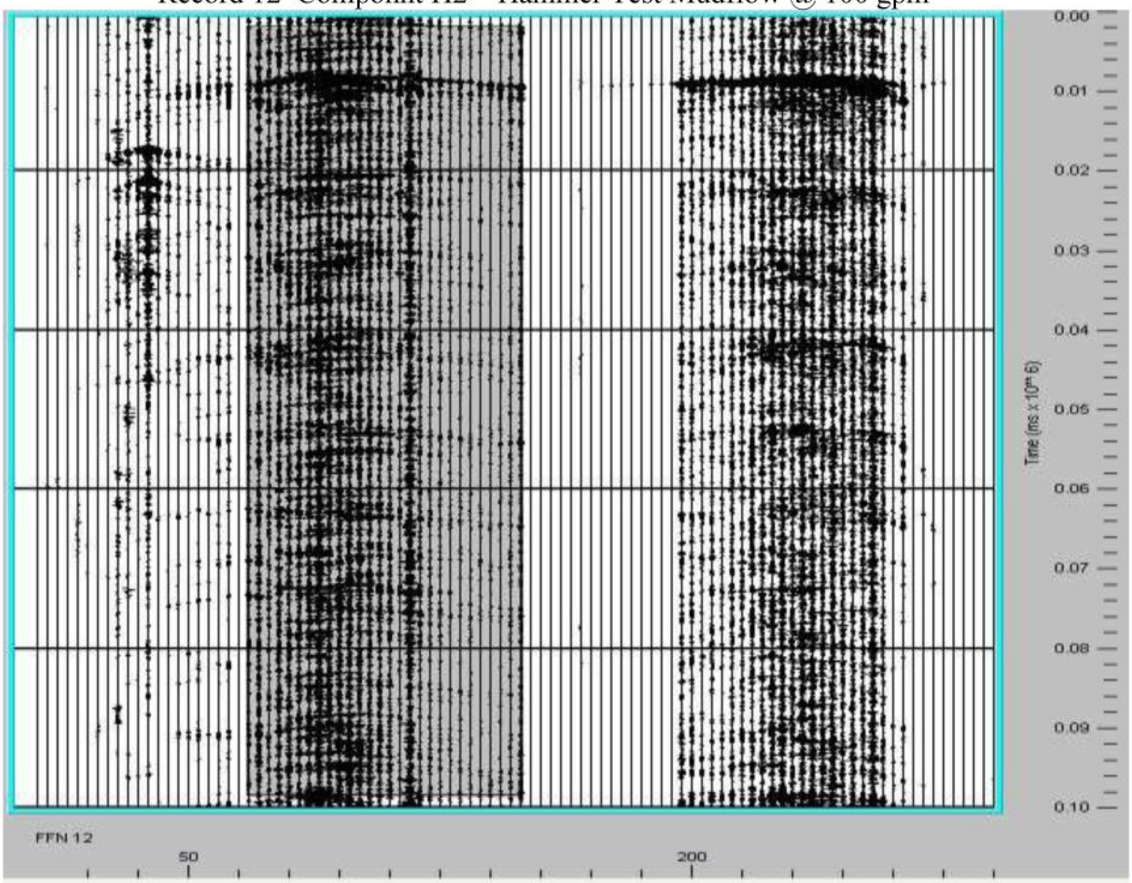

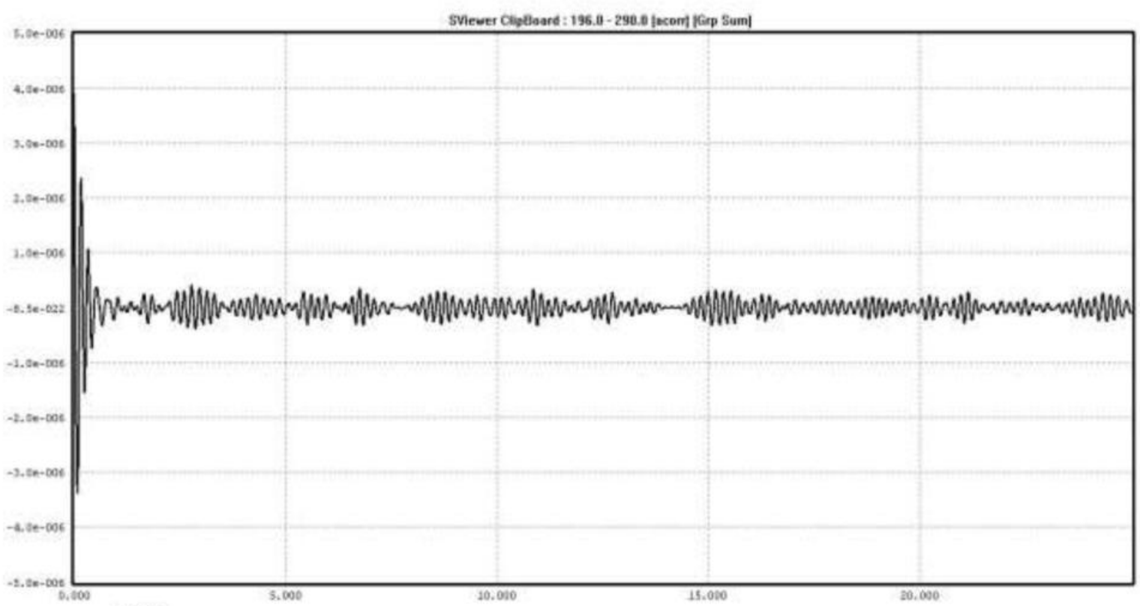

Record 31 H2 Component Pulse test Tool depth 775 ft Mud flow @ 365 gpm

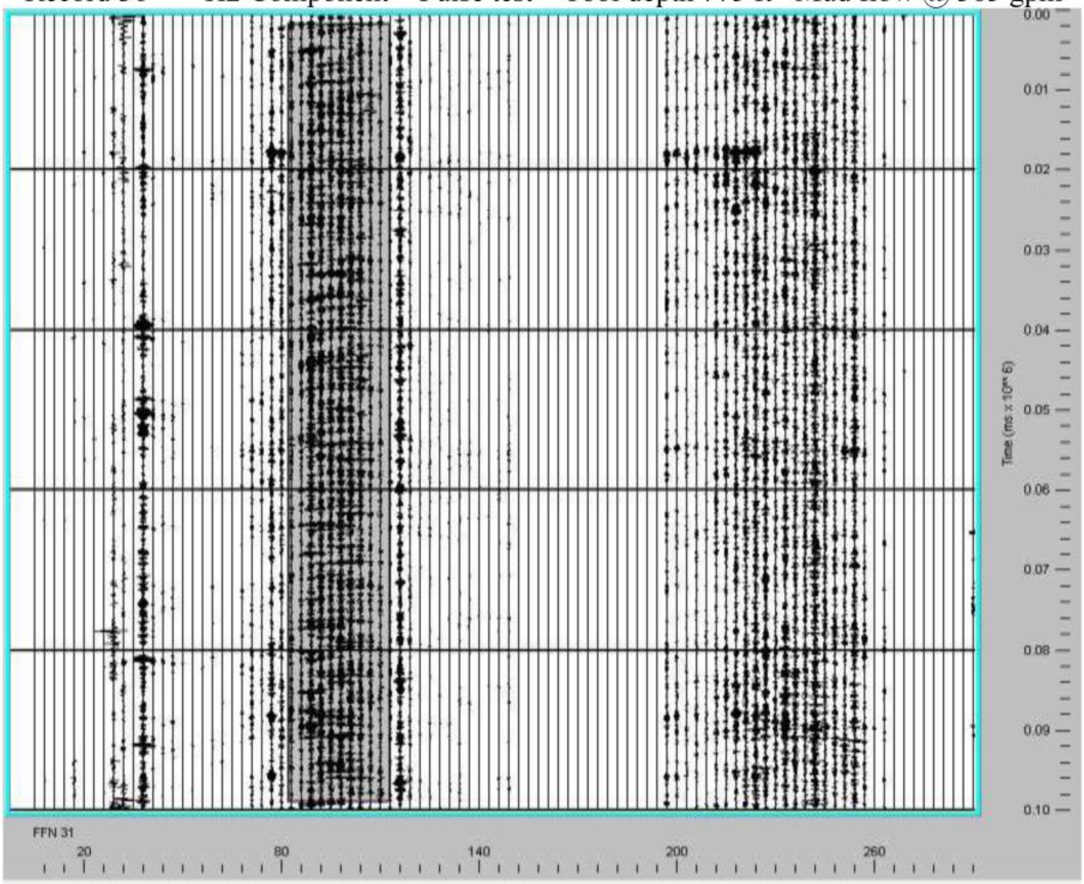

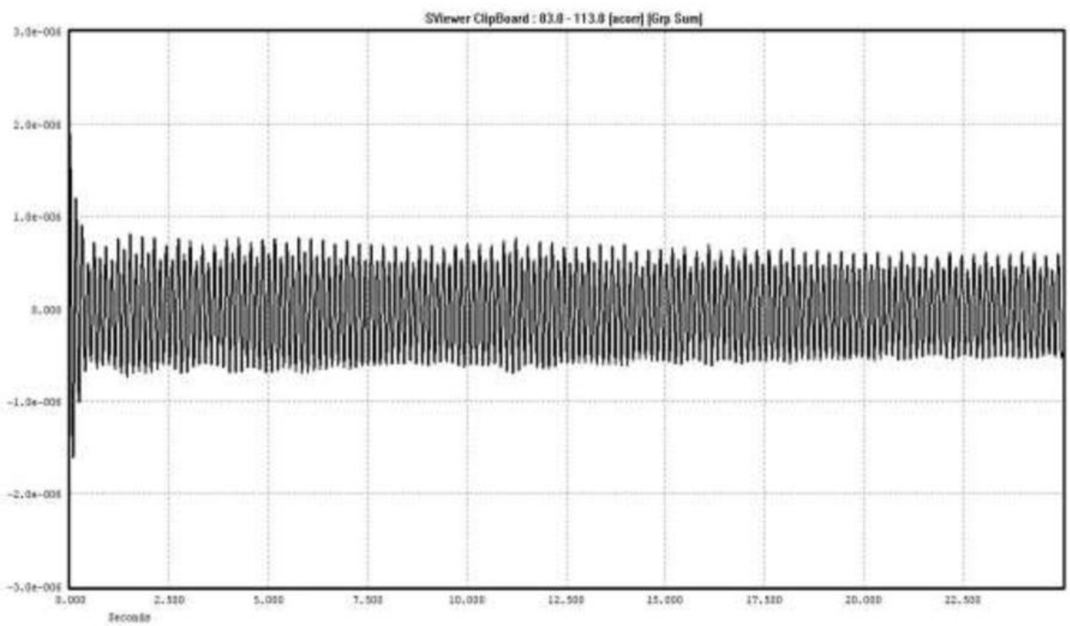

Record 40 H2 Component Pulse test Tool depth 2950 ft Mud flow @ 358 gpm

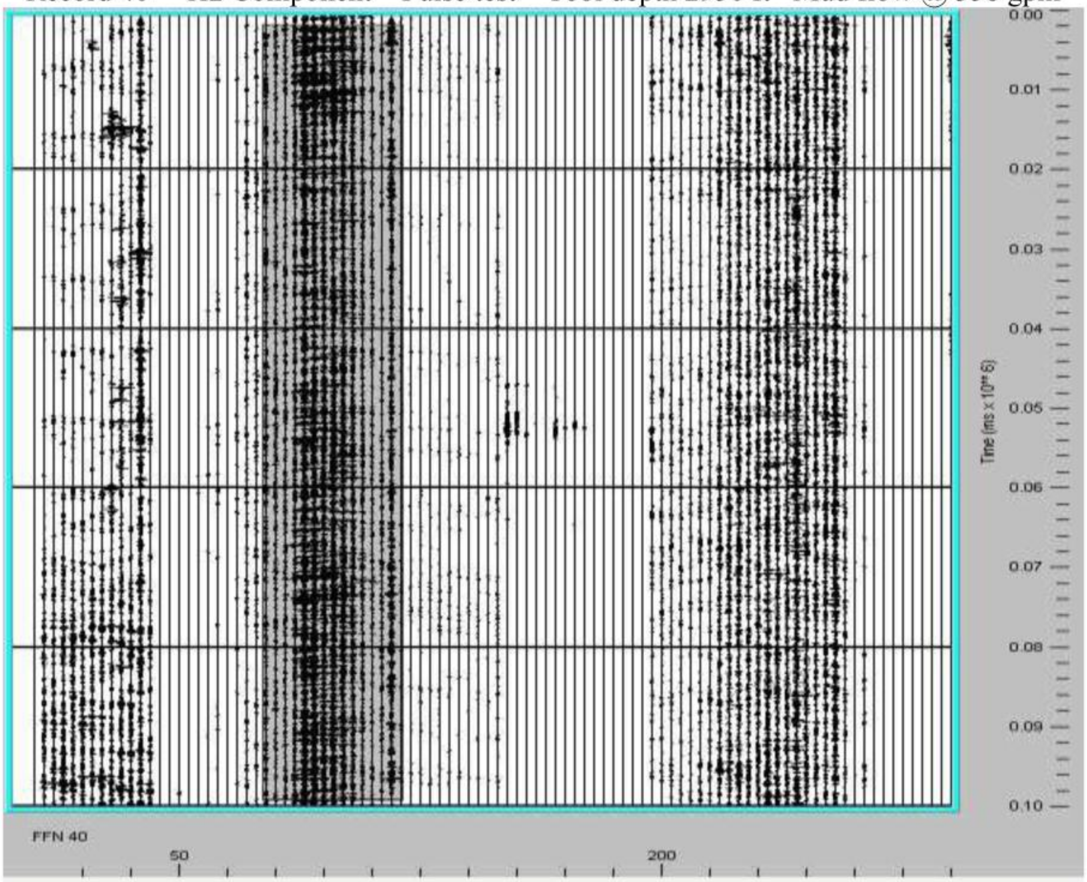

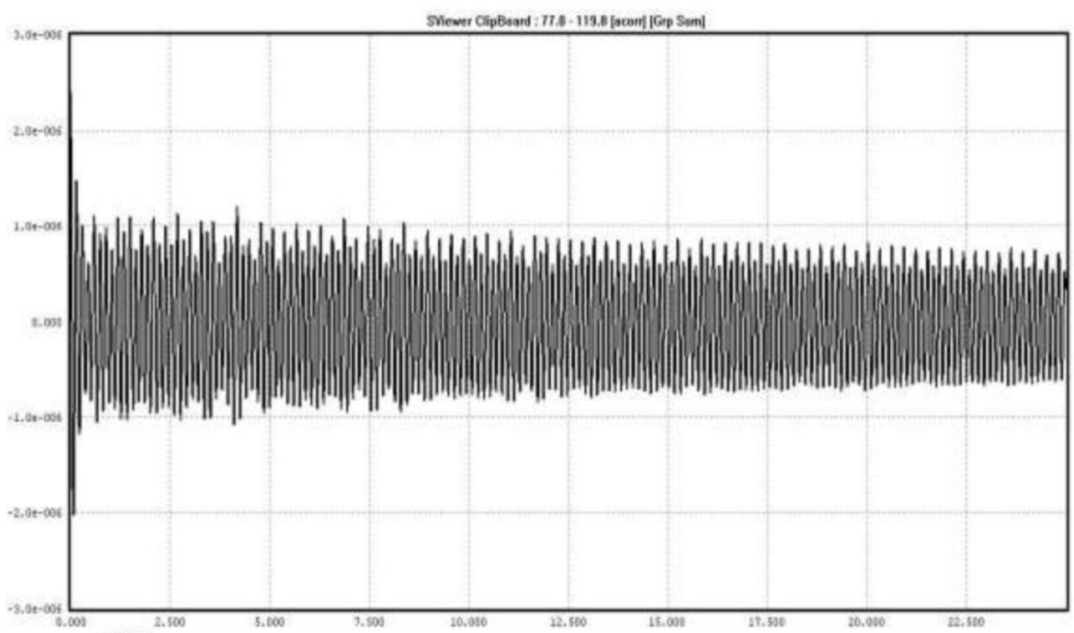

Record 41 H2 Component Flow noise test Mud flow @ 365 gpm

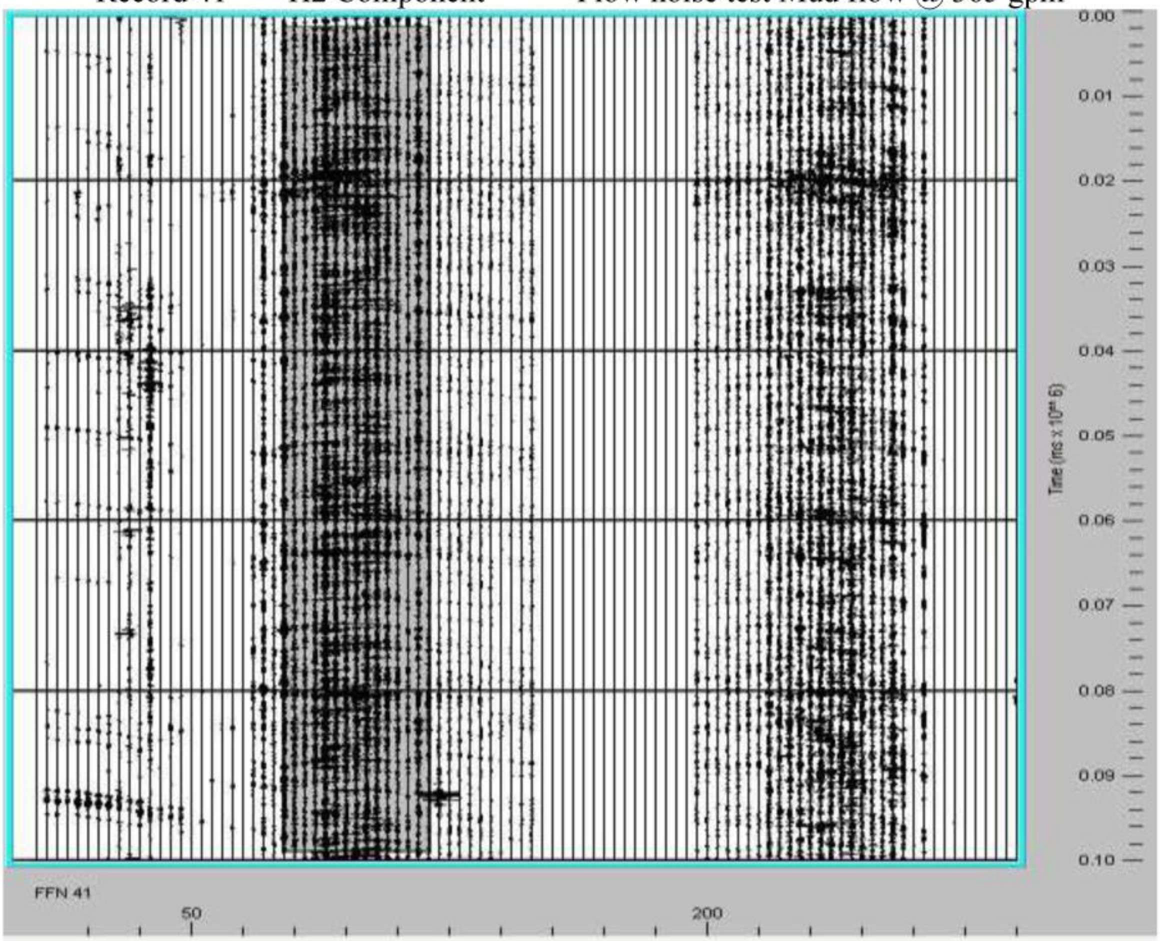

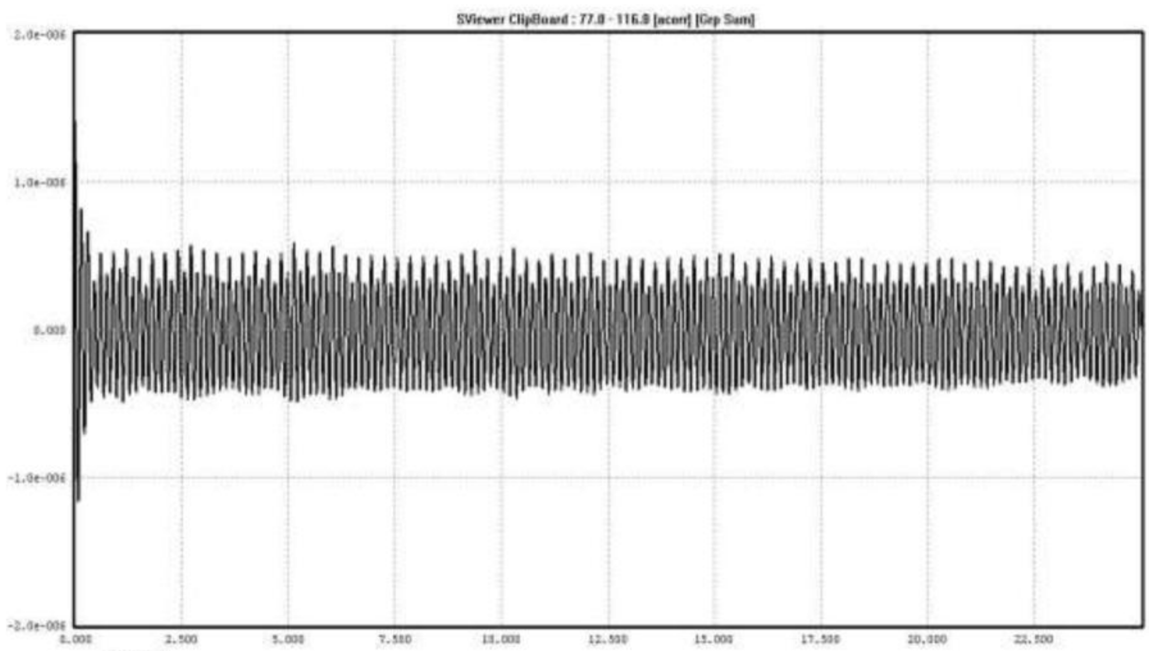

Low frequency spectral analysis (windowed region shown)

Record 19 H2 Component Background noise test Mud flow @ 100 gpm

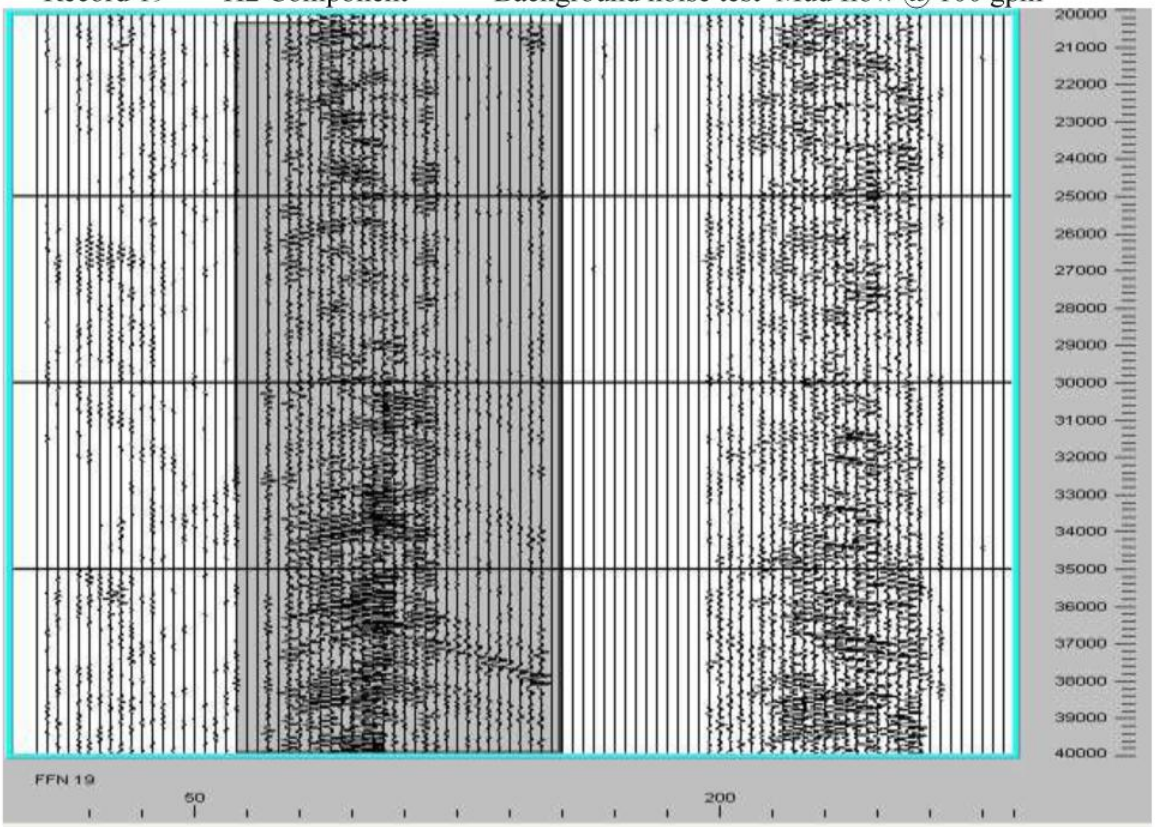

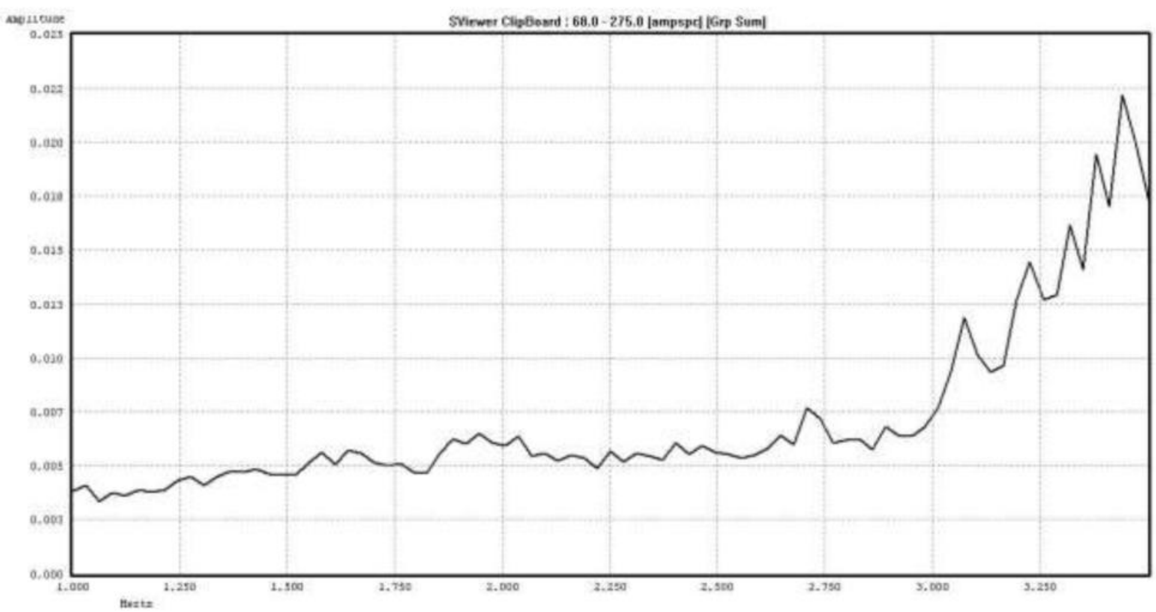

Record 12 H2 Component Hammer test Mud flow @ 100 gpm

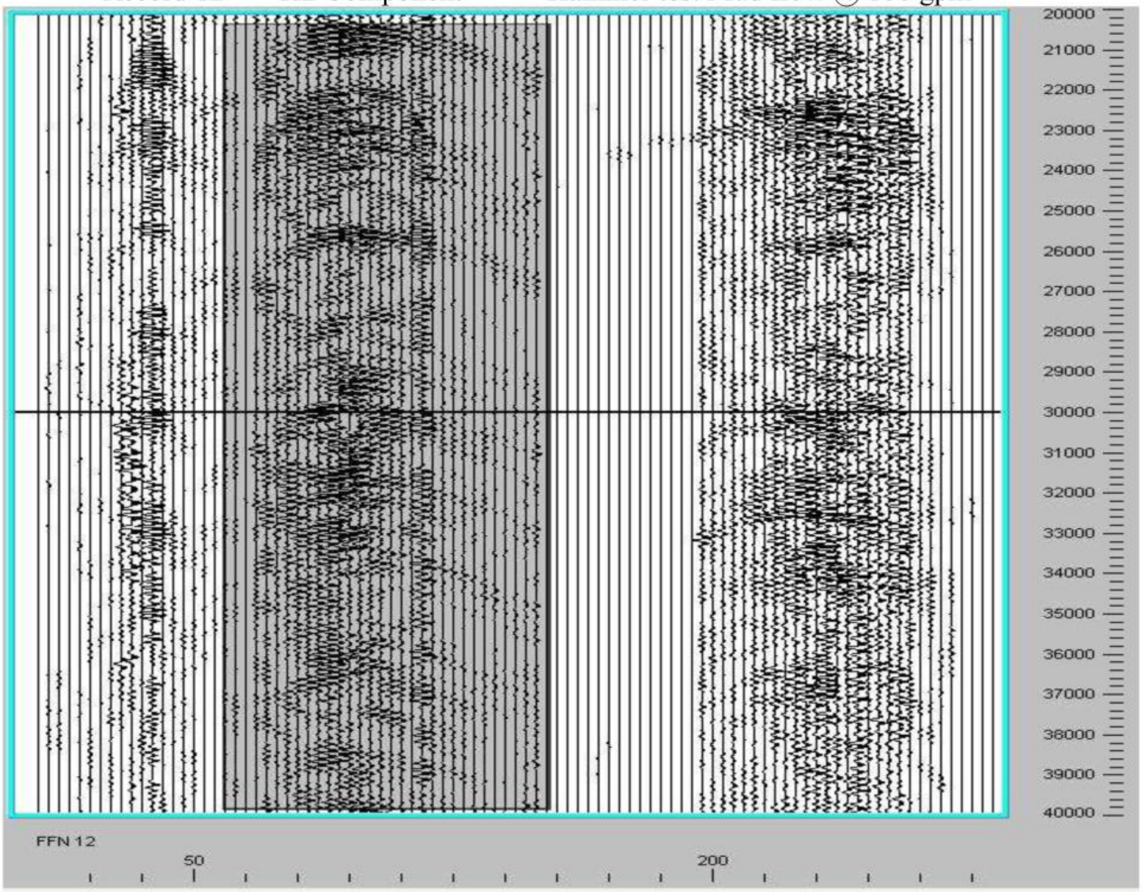

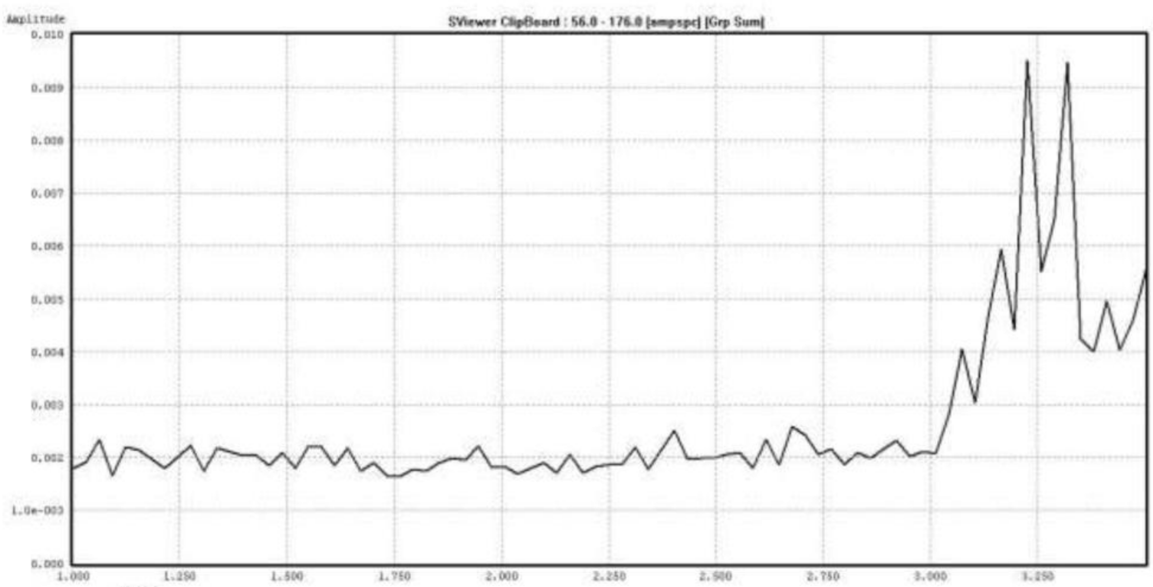

Record 31 H2 Component Pulse test Tool depth 775 ft Mud flow @ 365 gpm

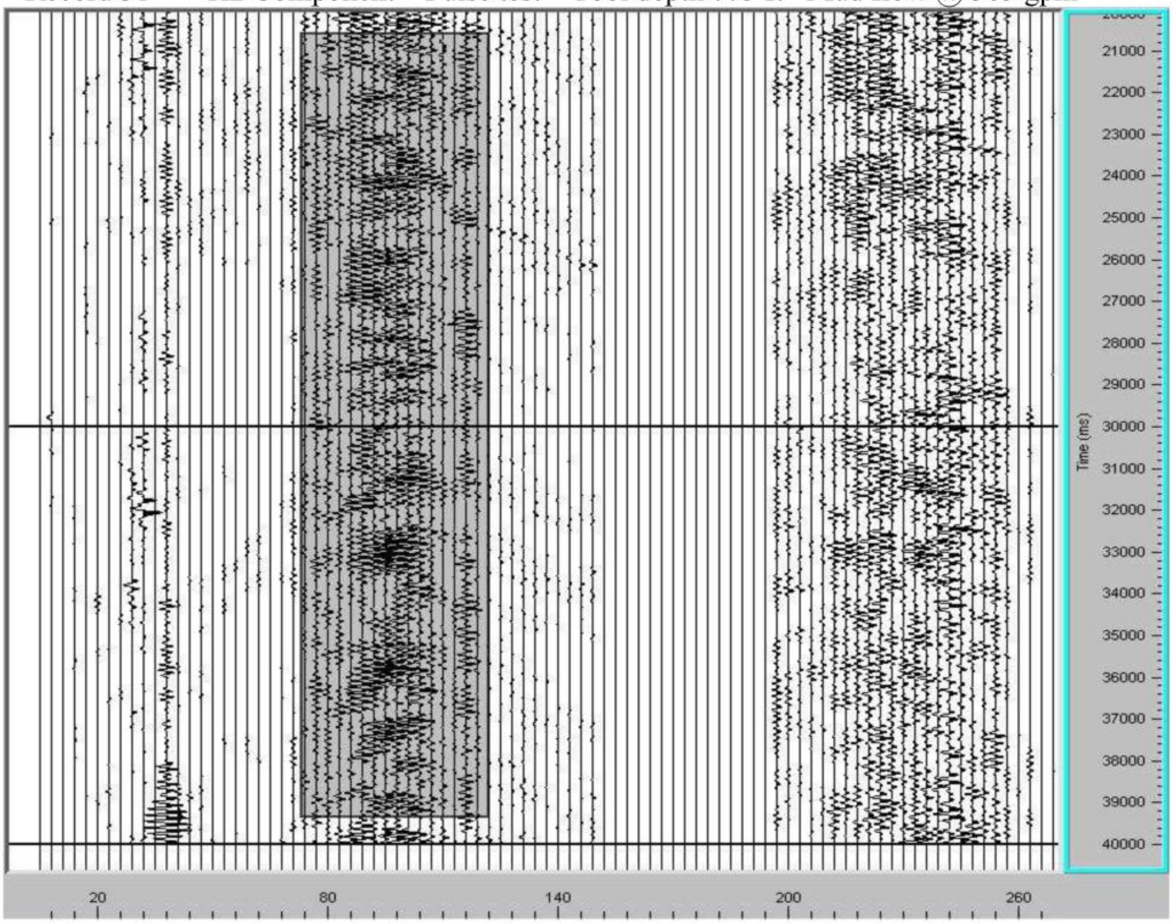

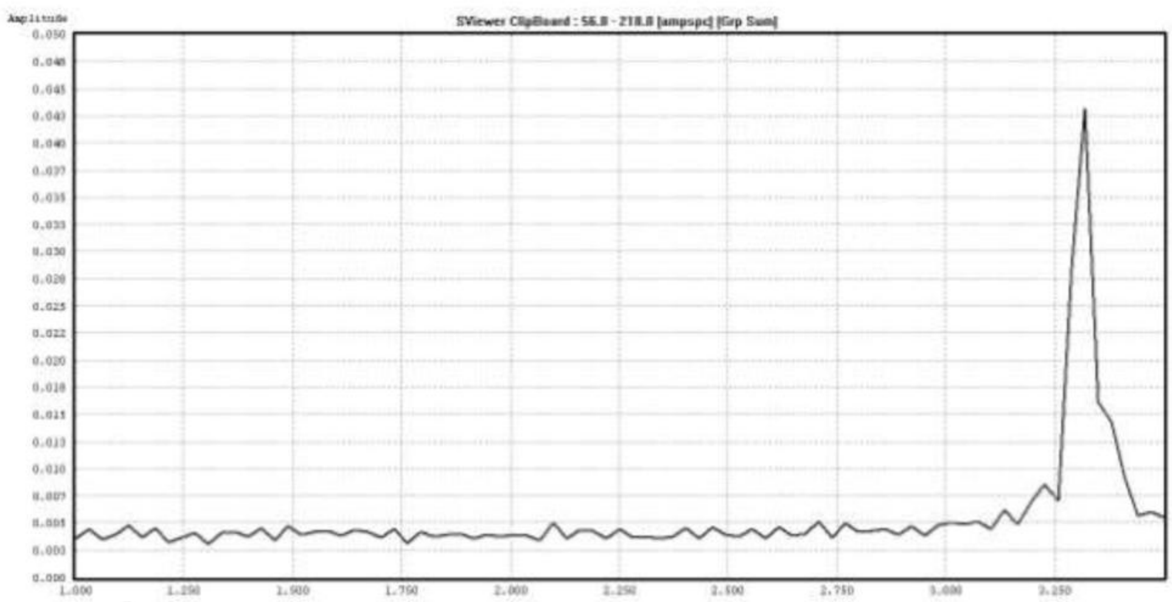

Record 40 H2 Component Pulse test Tool depth 2950 ft Mud flow @ 358 gpm

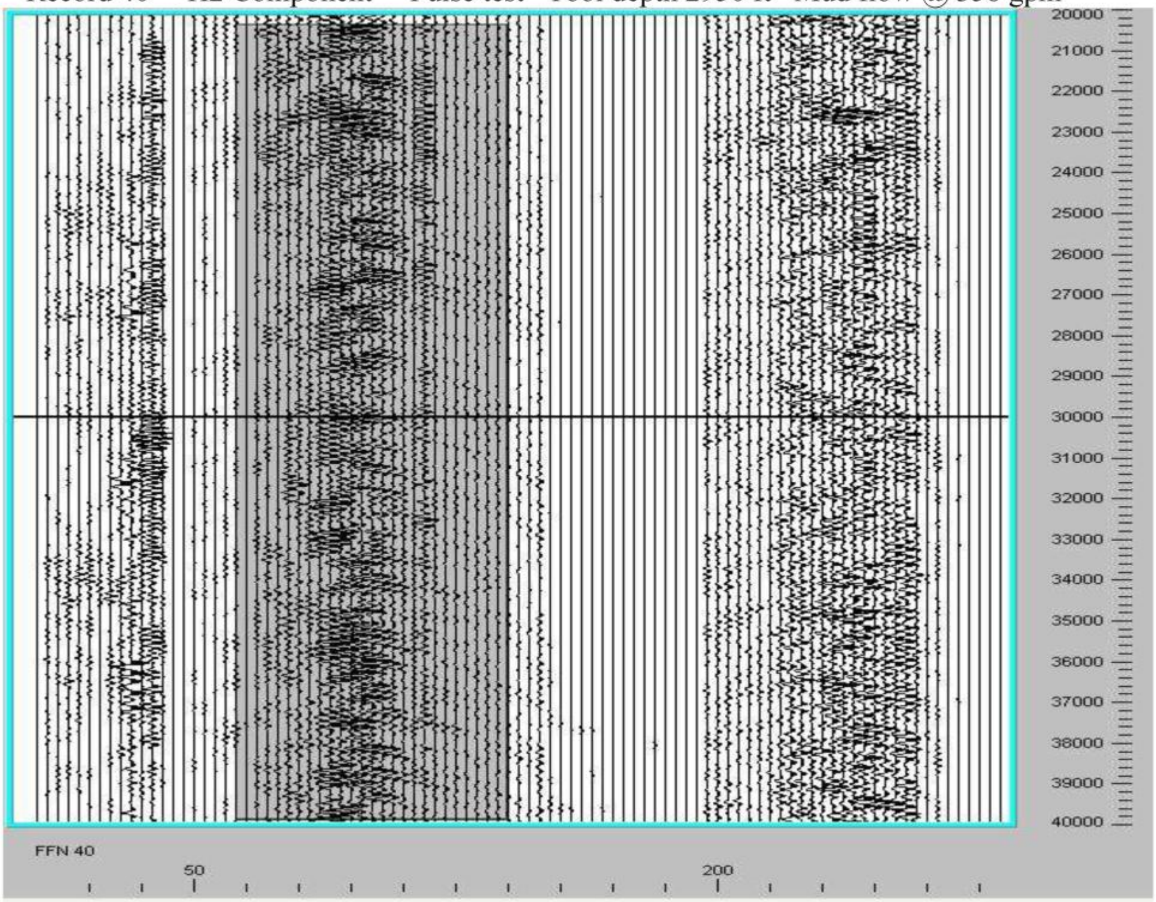

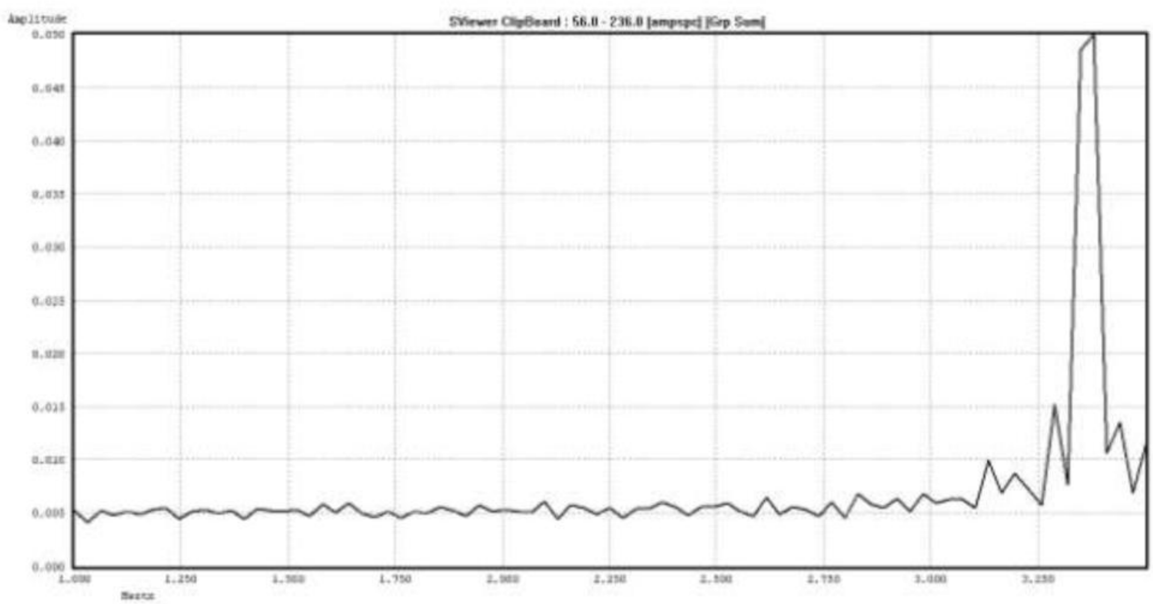

Record 41 H2 Component Flow noise test Mud flow @ 365 gpm

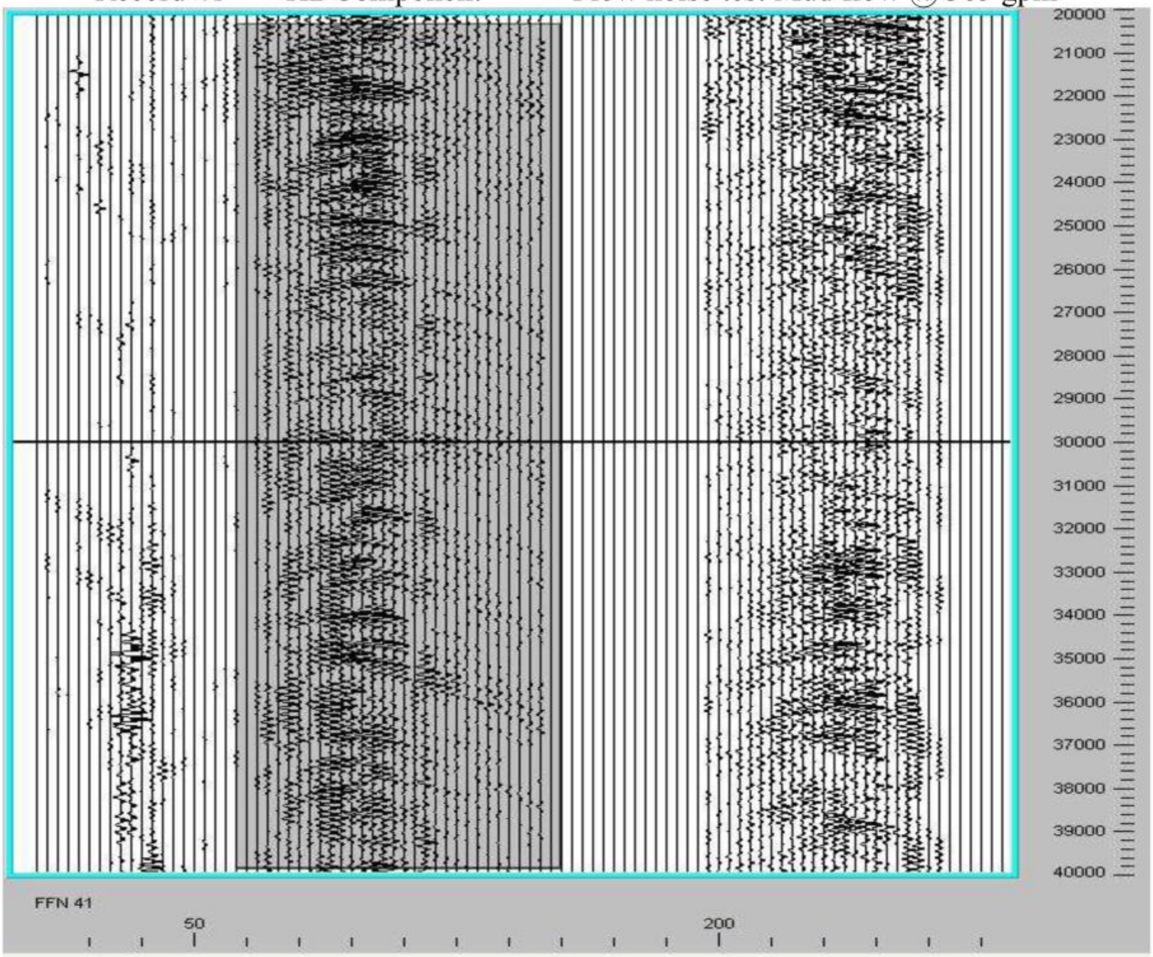

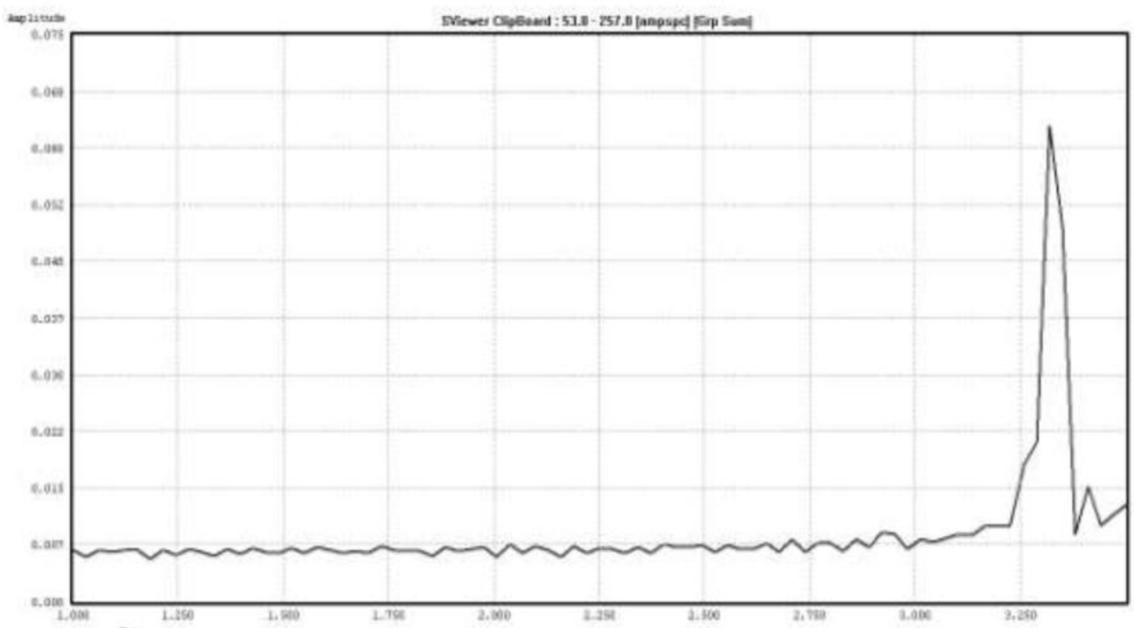

APPENDIX Db – SCORPION™ LAND SEISMIC RECORDING SYSTEM

ion
LAND IMAGING SYSTEMS

Scorpion® – The Right Tool for Cable-Based Land Recording

Scorpion, ION Land Imaging Systems' cabled recording system, maximizes seismic crew productivity, ensures error-free recording, enables full-wave imaging and is scalable to high channel count surveys. No matter what demands you encounter – increasing station counts, complex survey designs, 2D, 3D or 4D acquisition or hybrid analog and digital receiver spreads, Scorpion can handle the challenge.

Features and Benefits

Scorpion's telemetry architecture incorporates the latest transmission and switching technologies. Scorpion has been designed to employ four one-gigabit, Ethernet backbones, enabling the platform to handle high channel counts, high sampling rates and complex Vibroseis sweep schemes.

- A telemetry architecture and associated software that enables seismic crews to sustain data recording longer when operating in proximity to static and high energy pulse conditions.
- Built-in data path and bi-directional power deliver redundancy capabilities for continuous acquisition operations through most cable faults.
- Three port crossline units, DataBridge™ wireless backbones and spread anchor points provide spread flexibility to help overcome survey obstacles.

Scorpion's Vibroseis functionality enables increased productivity, flexibility, and reliability:

- Source-driven acquisition enables high productivity acquisition.
- Asynchronous timing and flexible source controller interface allows Scorpion to work seamlessly with third-party source controllers and various sources such as airguns.
- A choice of shooting modes to enable continuous Vibroseis operations even when GPS signal reception becomes unreliable.
- Support for multiple VPs on the same source point to facilitate recording of both p-wave and shear wave data.

Scorpion's user interface is based on Microsoft Windows® for ease of use and seamless access to management of all survey parameters from a single window.

- Start up wizards with automated and embedded intelligent survey parameters allow for accelerated start-ups.
- Robust layered map displays provide for efficient management of the spread and effortless troubleshooting

With significant improvements in A-unit and D-unit line wakeup, Scorpion enables the spread to be ready for acquisition in a shorter amount of time, increasing overall productivity.

Scorpion supports both synchronous and asynchronous start modes, which enables the system to work as a master or slave in a master-slave configuration.

Along with an optional internal tape drive, Scorpion supports higher capacity, higher bandwidth fiber-optic and SCSI tape drives, allowing for multiple choices for data output. Scorpion also supports plotters with SCSI and Ethernet interfaces.

Specifications

Central Recording System

Graphical User Interface (GUI)	64 bit AMD Opteron™ Multi-processor PC Runs all Windows®-based applications • Includes diagnostic tools that display spread status and faults • Includes CRS health monitoring and diagnostics Multi-monitor video support Microsoft® Windows® Server 2003
Real-Time Engine (RTE)	64 bit AMD Opteron™ Multi-processor PC Field Electronics Interface (FEI) with channel capacity up to 20,000 channels SUSE Linux Operating System, Version 10.1
Tape Drive	System supports dual LTO-2, external SCSI dual LTO-2, LTO-3, 3580, 3490, 3590 and 3592 (see Scorpion datasheet for details)

Ground Electronics

Crossline Unit (XLU)	Advanced network packet telemetry Ports: 3 each – crossline; 2 each - D-Unit or A-Unit line Crossline real-time telemetry capacity of 5,500 channels at 2 ms sample rate Multi-line capacity up to 120 lines. Quick-couple, mid-span connector Fiber optic crossline cable up to 15 km
Analog Line Unit (A-Unit)	Supports up to 3 analog receivers (channels) Built-in support for performing instrument and receiver tests in unit SmartNet™ redundant buffered data telemetry supports non real-time data transmission SmartPower™ power handling system provides redundant power capability
Digital Line Unit (D-Unit)	Supports up to 3 VectorSeis® receivers (3 components per VectorSeis receiver; 3 stations, 9 channels total) Built-in support for performing instrument and VectorSeis receiver tests SmartNet™ redundant buffered data telemetry supports non real-time data transmission SmartPower™ power handling system provides redundant power capability
Battery Booster Unit (BBU)	12 Volt nominal input, ± 24 Volt to earth nominal line output Powers 36 VectorSeis receivers using D-Units up to 33 m intervals Powers 48 analog receivers using A-Units up to 33m intervals SmartPower™ redundancy and switching (additional equipment may be required) Dual hot-swappable power inputs Serial port for connecting HDU (Hand-held Deployment Unit)
Crossline Cable	9 / 125 micron ruggedized, military grade, harsh environment fiber optic cable
Line Cable	Integral twisted-pair line cable with hermaphroditic Dynacon™ quick-couple, mid-span connectors 3-pair A-Unit or 4-pair Universal cable

United States – Stafford, TX
Phone 281.933.3339 Fax: 281.552.3150
Email: info@iongeo.com
Web Site www.iongeo.com

APPENDIX Dc – VECTORSEIS™ DIGITAL MEMS RECEIVERS

ion
LAND IMAGING SYSTEMS

VectorSeis® Receiver

VectorSeis multi-component seismic receivers use purpose-built digital accelerometers to accurately record full-wave seismic energy. Three orthogonally-configured digital accelerometers in a single-point receiver make it possible to accurately measure all seismic signal and noise with greater resolution than was possible with traditional technologies. The accelerometers enable VectorSeis deployment at any tilt angle by measuring the component of the gravitational field on each sensor axis. These measurements are used to automatically compute the angle of deployment. The ease of deployment allows for simple and efficient field operations while acquiring high quality data.

VectorSeis sensor technology has been rigorously proven in a wide range of geographic locations from North America to central Europe, Latin America, India, Russia/CIS and China. VectorSeis data has demonstrated excellent seismic signal resolution, bandwidth and vector fidelity.

Capabilities and Features

- VectorSeis 3-C digital receiver
  - Three identical accelerometers mounted orthogonally on a precision-machined aluminum cube for stability and industry-leading vector fidelity
  - Accelerometers mounted at the base of the module for optimum ground coupling and less wind noise susceptibility
  - Sensors decoupled from line cables for isolation from cable-transmitted noise and for ease of sensor handling
  - Used for multi-component and/or enhanced p-wave acquisition
  - Flat frequency and phase response yield accurate broad bandwidth data
  - Exceptional vector fidelity provides accurate multi-component images
- VectorSeis deployment – True Vertical™ data
  - Sensors maintain full dynamic range at all tilt angles
  - Module measures and records apparent gravity for each sensor axis
  - Apparent gravity angles for each axis recorded to tape header
  - Components rotated to True Vertical orientation

- True Digital™ performance
  - VectorSeis eliminates the need for analog filters and time-consuming analog circuit tests
  - Ultra-low distortion for unsurpassed linearity
  - No leakage
  - No high-line leakage

VectorSeis is designed to work with FireFly®, ION's next-generation cableless platform, and Scorpion®, ION's state-of-the-art, cable-based land seismic acquisition system.

VectorSeis Receiver Specifications

Technical	
Digital Quantization	24 Bits (23 + Sign), LSB = 0.39 μm/s² or 40 ng
Sample Rate	4 ms, 2 ms or 1 ms
Time Standard	Tied to Scorpion clock (*see Scorpion data sheet PN 1018-040016*)
Full Scale	**Normal Mode** +/- 3.3 m/s² or +/- 0.335 g peak, dynamic (*at all inclinations*) **Strong Motion Mode** +/- 6.9 m/s² or +/- 0.700 g peak, dynamic (*source radius enabled; at all inclinations*)
Noise (Normal Mode)	0.44 μm/s² or 44.7 ng²/Hz (-147 dBg²/Hz); 3 Hz to 375Hz
Equivalent Input Noise (EIN) (Normal Mode)	4.18 μm/s² or 426 ng rms @ 4 ms, 5.95 μm/s² or 607 ng rms @ 2 ms, 8.46 μm/s² or 862 ng rms @ 1 ms; 3 Hz to ¾ Nyquist
Instantaneous Dynamic Range (Normal Mode)	118 dB @ 4 ms, 115 dB @ 2 ms, 112 dB @ 1 ms; 3 Hz to ¾ Nyquist (*at all inclinations*)
Total System Dynamic Range	124 dB @ 4 ms, 121 dB @ 2 ms, 118 dB @ 1 ms; 3 Hz to ¾ Nyquist (*at all inclinations*)
Frequency Response	1.450 Hz @ 4 ms, 1.463 Hz @ 2 ms, 1.470 Hz @ 1ms; to ¾ Nyquist; +/-3 dB (*see 2ms Magnitude Response curves*)
Filters	**Digital Anti-Alias Filter** Linear or Minimum Phase Response 93.8 Hz @ 4 ms, 187.5 Hz @ 2 ms, 375 Hz @ 1 ms Rejection above Nyquist Frequency –128 dB Pass-band Ripple +/- 0.1 dB **Digital Low-Cut Filter** Low-Cut: Out or 1 of 32 Frequencies 3 to 90 Hz, 12 dB/octave **Digital Offset Filter** Either: Continuous Filter: 1.450 Hz @ 4ms, 1.463 Hz @ 2ms, 1.470 Hz @ 1ms, 6 dB/octave Fixed DC Offset Removal
Total Harmonic Distortion	Less than 0.002%* (@ 12 Hz, 68.4 mg peak acceleration or 0.01778 m/s (0.7 in/s) p.p. velocity)
Sensor to Sensor Matching	+/- 0.4% (at all inclinations)
Cross Axis Isolation	46 dB
Sensor Module Interface	Proprietary 2-wire interface
Deployment	Any Orientation (radial and axial cable entry options available)
Inclination Resolution	+/- 0.5° arc (relative to vertical)

* Measurement limited by mechanical test apparatus.

Technical specifications are typical values at 25° C

Testing

Embedded Power-up Self Test	Sensor wake-up and self-configuration checks Control loop validation Power consumption
Operator Controlled System Tests	• Vertical orientation (evaluates each sensor axis gravity magnitude and vector sum of all 3 sensors) • Spread noise • Sensor loopback (verifies module telemetry and digital filter performance) • Telemetry error count
End of Record Validation (Every Record)	• Overscale status • Vertical orientation (used to apply orientation correction) • Sensor orientation deviation (evaluates orientation after each acquisition) • Sensor offset • Digital fault flags

Physical

Dimensions	Body: 16.5 cm x 5.0 cm diameter (6.50 in x 1.97 in) Top: 6.9 cm diameter (2.72 in)
Weight	0.625 kg (1.38 lb, including 1.3 m cable and connector)

Environmental

Operating Temperature	-40°C to +75°C
Humidity	0 to 100%
Operating Altitude	-100 to +5500 m
Water Depth Rating	10 m

Related Products

Alignment Tool	For aligning all VectorSeis receivers along survey specific azimuth during deployment
Extraction Tool	For extracting VectorSeis receivers from the ground

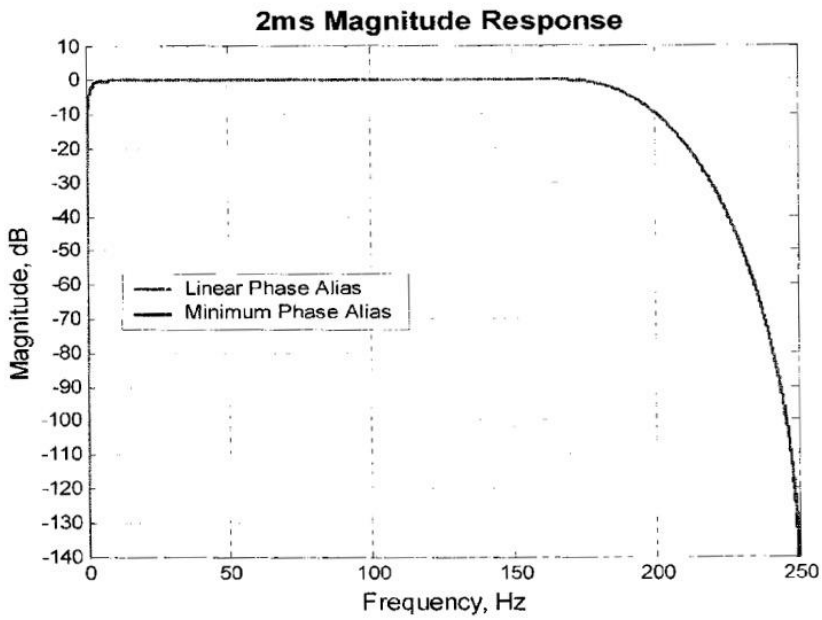
2ms Magnitude Response
Magnitude, dB
Frequency, Hz
Linear Phase Alias
Minimum Phase Alias
10
0
-10
-20
-30
-40
-50
-60
-70
-80
-90
-100
-110
-120
-130
-140
0
50
100
150
200
250

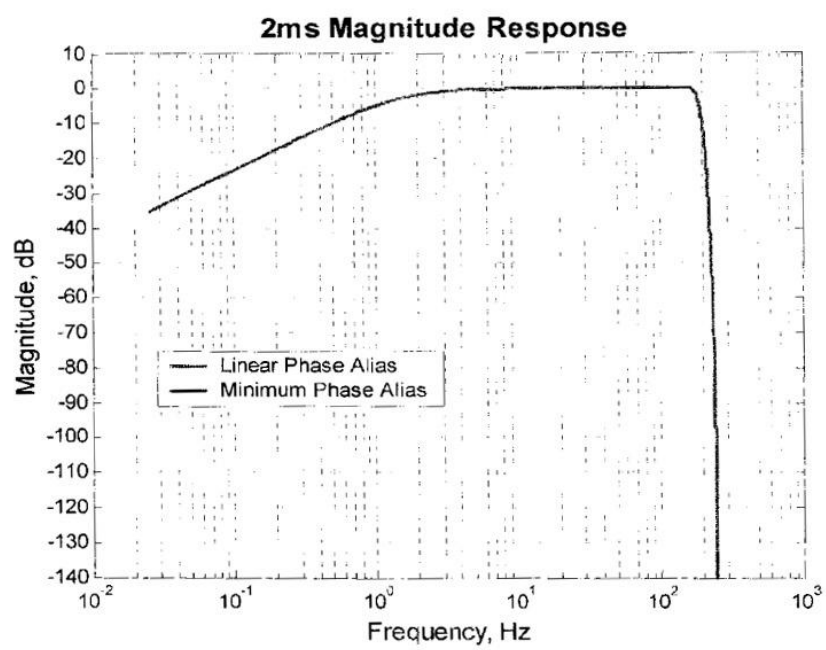
2ms Magnitude Response
Magnitude, dB
Frequency, Hz
Linear Phase Alias
Minimum Phase Alias
10
0
-10
-20
-30
-40
-50
-60
-70
-80
-90
-100
-110
-120
-130
-140
10^{-2}
10^{-1}
10^{0}
10^{1}
10^{2}
10^{3}

Response Curves

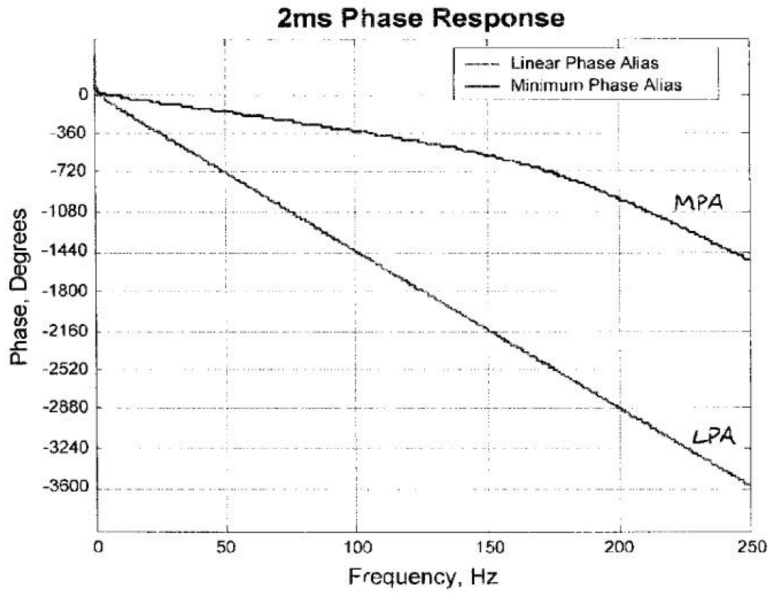

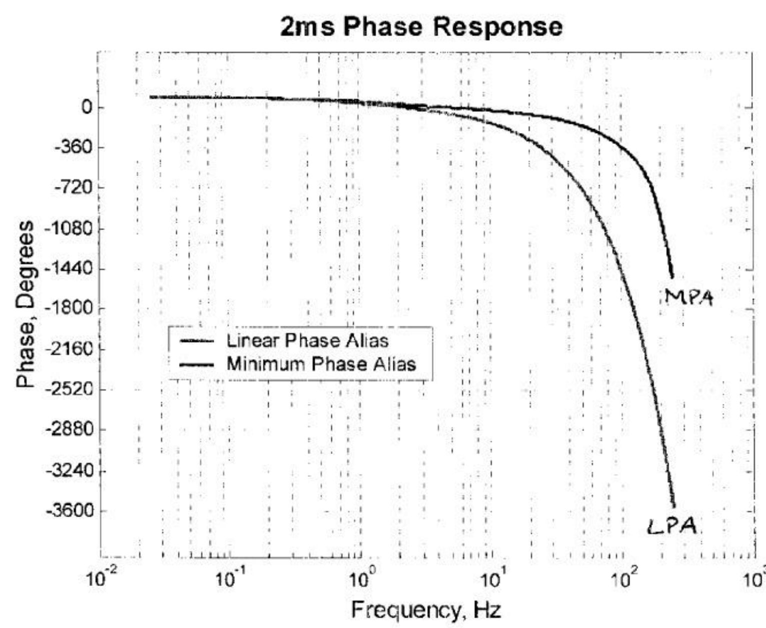

Response Curves

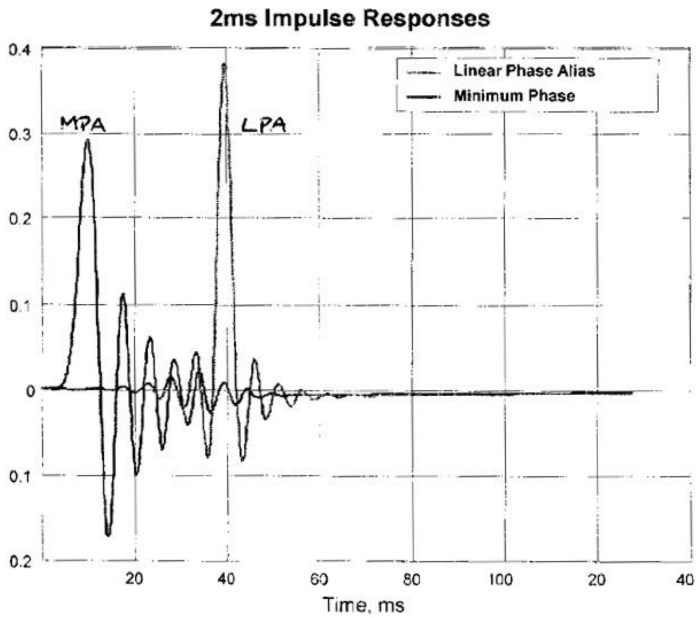

United States – Stafford, TX
Phone: 281.933.3339 Fax: 281.552.3150
Email: info@iongeo.com

Web Site
www.iongeo.com

 1018-040000C

LIST OF ACRONYMS

%	percent
AAPG	American Association of Petroleum Geologists
C	Centigrade
D	Depth
dB	Decibel
DOE	U.S. Department of Energy
DTS	Devine Test Site
E	Exponent
EGL	Exploration Geophysics Laboratory
F	Fahrenheit
FFT	Fast Fourier Transfer
Ft	Feet
G	Acceleration
Gpm	gallons per minute
HTHP	High temperature high pressure
Hz	Hertz
ID	inside diameter
In	inch
ION	Ion Geophysical, Inc.
J	Joule
K	Kilo
KHz	Kilohertz
LP	low pressure
M	Meter
Ms	Milliseconds
Msec	milliseconds
MWD	measurement while drilling

NETL	National Energy Technology Laboratory
NPR	Naval Petroleum Reserve
OD	Outside diameter
OTC	Offshore Technology Conference
Pa	Pascal
Psi	Pounds per square inch
Q	Flow rate
RMOTC	Rocky Mountain Oilfield Testing Center
RV	Recreational vehicle
RVSP	Reverse Vertical Seismic Profile
Sec	Second
SEG	Society of Exploration Geophysicists
SPW	Seismic Processing Workshop
SWD	Seismic While Drilling
TII	Technology International, Inc.
TOMEX®	Tomographic Exploration, a registered trademark of Baker Hughes, Inc.
TX	Texas
μ	Micro
μF	microfarad
V	Velocity
VP	velocity profile
VSP	Vertical Seismic Profile

This page intentionally left blank

U.S. Department of Energy
National Energy Technology Laboratory

626 Cochrans Mill Road
P.O. Box 10940
Pittsburgh, PA 15236-0940

3610 Collins Ferry Road
P.O. Box 880
Morgantown, WV 26507-0880

One West Third Street,
Suite 1400 Tulsa, OK 74103-3519

1450 Queen Avenue SW
Albany, OR 97321 -2198

2175 University Ave. South
Suite 201
Fairbanks, AK 99709

Visit the NETL Web site at:
www.netl.doe.gov

Customer Service:
1-800-553-7681